

TECHNISCHE UNIVERSITÄT MÜNCHEN

Lehrstuhl für Entwicklungsgenetik

Leucine-rich repeat kinase 2 (Lrrk2):
Functional characterization and interactome analysis
of a protein kinase associated with Parkinson's disease

Andrea Meixner

Vollständiger Abdruck der von der Fakultät Wissenschaftszentrum Weihenstephan für Ernährung, Landnutzung und Umwelt der Technischen Universität München zur Erlangung des akademischen Grades eines

Doktors der Naturwissenschaften

genehmigten Dissertation.

Vorsitzender: Univ.-Prof. Dr. S. Scherer

Prüfer der Dissertation:

1. Univ.-Prof. Dr. W. Wurst
2. Univ.-Prof. Dr. D. Langosch
3. apl. Prof. Dr. J. Adamski

Die Dissertation wurde am 23.05.2011 bei der Technischen Universität München eingereicht und durch die Fakultät Wissenschaftszentrum Weihenstephan für Ernährung, Landnutzung und Umwelt am 23.12.2011 angenommen.

Für meine Eltern

Table of Contents

Abbreviations	9
Summary	13
Zusammenfassung	15
I. INTRODUCTION	17
1. Parkinson's disease	17
1.1 Clinical definition	18
1.2 Pathology and pathophysiology of PD	19
1.3 Etiology and pathogenic mechanisms	22
1.3.1 Aging	22
1.3.2 Environmental factors	22
1.3.3 Genetic factors	23
1.3.3.1 <i>α-synuclein</i>	24
1.3.3.2 <i>Parkin</i>	26
1.3.3.3 <i>PINK1</i>	26
1.3.3.4 <i>DJ-1</i>	27
1.3.3.5 <i>UCHL1</i>	28
1.3.3.6 <i>Other PD genes</i>	29
1.3.4 Molecular pathogenesis	29
1.3.4.1 <i>UPS dysfunction and protein aggregation</i>	30
1.3.4.2 <i>Mitochondrial impairment and oxidative stress</i>	31
2. Leucine-rich repeat kinase 2 (Lrrk2)	34
2.1 Genetic aspects of Lrrk2-associated PD	34
2.2 Clinical and pathological implications of Lrrk2 mutations	35
2.3 Cellular and subcellular localization	35
2.4 Structure and enzymatic activity	36
2.4.1 Lrrk2 multidomain structure	36
2.4.2 Dual enzymatic properties of Lrrk2	39
2.4.2.1 <i>Kinase activity of Lrrk2</i>	39
2.4.2.2 <i>GTPase activity of Lrrk2</i>	40
2.5 Lrrk2 substrates, interactors and related signaling cascades	41
2.5.1 Kinase substrates	41
2.5.2 Interaction partners	43
3. The actin cytoskeleton	47
3.1 Actin dynamics	47
3.2 Regulation of actin cytoskeleton dynamics: Actin-binding proteins (ABPs)	48
3.3 The actin cytoskeleton in neurons	50
4. RNA interference	53
4.1 Mechanism of gene silencing by double-stranded RNA	53
4.2 RNAi as an experimental tool	54
II. AIM OF THE STUDY	59
III. MATERIAL AND METHODS	61
1. Material	61
1.1 Chemicals	61
1.2 General equipment	61
1.3 Molecular biology	62
1.3.1 Special equipment	62
1.3.2 Kits	62
1.3.3 Enzymes and special reagents	62
1.3.4 <i>Escherichia coli</i> strains	63
1.3.5 Oligonucleotides	63
1.3.6 Plasmids and constructs	64

Table of Contents

1.4 Mammalian cell culture	65
1.4.1 Special equipment.....	65
1.4.2 Media, reagents and supplements	65
1.5 Protein chemistry.....	66
1.5.1 Special equipment.....	66
1.5.2 Kits and special reagents.....	66
1.5.3 Protein complex purification.....	66
1.5.4 Mass spectrometry	66
1.6 Antibodies	67
1.7 Software and databases.....	69
1.7.1 Databases	69
1.7.2 Software	69
2. Methods	70
2.1 Protein chemistry.....	70
2.1.1 Protein extraction	70
2.1.1.1 <i>From cultured cells</i>	70
2.1.1.2 <i>From adult mouse brains</i>	70
2.1.2 Determination of protein concentration	71
2.1.3 SDS-polyacrylamide gel electrophoresis (SDS-PAGE).....	72
2.1.3.1 <i>Discontinuous SDS-PAGE</i>	72
2.1.3.2 <i>Gradient SDS-PAGE</i>	73
2.1.4 Staining of SDS gels	74
2.1.4.1 <i>Silver staining</i>	74
2.1.4.2 <i>Coomassie staining</i>	75
2.1.4.3 <i>Drying of SDS gels</i>	75
2.1.5 Western blot analysis	75
2.1.5.1 <i>Semi-dry blotting</i>	76
2.1.5.2 <i>Immunodetection</i>	76
2.1.5.3 <i>Multiscreen validation of antibodies</i>	77
2.1.6 Digitalizing of SDS gels and western blot films	77
2.2 Analysis of protein-protein interactions	78
2.2.1 Immunoprecipitation.....	78
2.2.1.1 <i>Validation of antibodies</i>	78
2.2.1.2 <i>Traditional (classic) IP</i>	79
2.2.1.3 <i>IP with coupled antibody</i>	79
2.2.1.4 <i>IP with cross-linked antibody</i>	81
2.2.2 Quantitative immunoprecipitation combined with knockdown (QUICK assay).....	82
2.2.2.1 <i>Sample preparation</i>	84
2.2.2.2 <i>Mass spectrometry</i>	84
2.2.2.2.1 <i>Prefractionation by SDS-PAGE</i>	85
2.2.2.2.2 <i>In-gel tryptic cleavage</i>	86
2.2.2.2.3 <i>LC-MS/MS analysis</i>	86
2.2.2.2.4 <i>Data analysis</i>	88
2.2.3 KEGG pathway enrichment and protein network analysis	89
2.3 Molecular biology.....	91
2.3.1 <i>Escherichia coli</i> cultures	91
2.3.1.1 <i>Liquid cultures</i>	91
2.3.1.2 <i>Plating cultures</i>	91
2.3.1.3 <i>Cryo-preservation of bacteria</i>	91
2.3.1.4 <i>Generation of chemically competent E. coli</i>	91
2.3.2 Chemical transformation of <i>E. coli</i>	92
2.3.3 Preparation of plasmid DNA.....	92
2.3.4 DNA sequencing.....	93
2.3.5 Separation of DNA on agarose gels.....	93
2.3.6 Purification of DNA	94
2.3.6.1 <i>From agarose gels</i>	94
2.3.6.2 <i>From enzymatic reactions</i>	94
2.3.7 Polymerase chain reaction (PCR).....	94
2.3.8 Annealing of synthetic oligonucleotides.....	95
2.3.9 Enzymatic treatment of DNA	95
2.3.9.1 <i>DNA restriction</i>	95
2.3.9.2 <i>Phosphorylation of DNA fragments</i>	95

2.3.9.3 Dephosphorylation of DNA fragments	96
2.3.9.4 Blunting of DNA fragments	96
2.3.9.5 Addition of 3'-A overhangs (A-tailing)	96
2.3.9.6 DNA ligation	97
2.3.10 TOPO cloning	97
2.4 Lentiviral vectors	99
2.4.1 Selection of target sequences	102
2.4.2 First generation silencing constructs	103
2.4.3 Second generation silencing constructs	104
2.4.4 Cloning procedure	105
2.4.5 Evaluation of knockdown efficiency	105
2.4.6 Viral production	106
2.4.7 Titration of lentiviruses	107
2.5 Gene expression analysis	108
2.5.1 Isolation of total RNA	108
2.5.2 Quantitative and qualitative analysis of RNA	109
2.5.3 Reverse transcription	109
2.5.4 Real-time PCR	110
2.6 Mammalian cell culture	112
2.6.1 Growth and maintenance of mammalian cell culture	112
2.6.2 Generation of cryo stocks	112
2.6.3 Stable isotope labeling with amino acids in cell culture (SILAC)	113
2.6.4 Transient transfection by calcium phosphate precipitation	113
2.6.5 Primary ventral mesencephalic (VM) progenitor cell cultures	114
2.6.5.1 Coating of chamber slides with poly-D-lysine and laminin	114
2.6.5.2 Preparation and maintenance	114
2.6.6 Lentiviral transduction	116
2.6.7 Immunofluorescence	116
2.6.8 Microscopy	117
2.6.9 Phenotypic analysis of mammalian cell culture	117
2.6.9.1 Transduction efficiency of dopaminergic neurons in primary VM cultures	117
2.6.9.2 Dopaminergic cell counts	117
2.6.9.3 Dopaminergic neurite length	118
2.6.9.4 Morphological analysis of NIH3T3 cells	118
2.6.10 Flow cytometry	119
2.7 Actin cosedimentation assay	120
2.8 Statistical analysis	121
IV. RESULTS.....	123
1. Experimental workflow	123
2. Implementation of immunological assays for the analysis of Lrrk2	124
2.1 Monoclonal anti-Lrrk2 antibody clones specifically detect Lrrk2 in western blot analysis	124
2.2 Establishment of the immunoprecipitation of endogenous Lrrk2	125
2.2.1 A streptavidin-biotin-based screening assay revealed specific precipitation of Lrrk2 by rat-monoclonal antibody clones	126
2.2.2 The rat-monoclonal anti-Lrrk2 clones 1E11 and 2E12 efficiently immunoprecipitate endogenous Lrrk2 in a classic IP approach	127
2.2.3 Lrrk2-specific immunoprecipitation using anti-Lrrk2 covalently coupled to CNBr- activated sepharose releases the antibody together with the precipitated proteins	130
2.2.4 Cross-linking of the Lrrk2-specific antibody to a Protein G affinity resin efficiently precipitates endogenous Lrrk2 without a considerable contamination by the antibody	131
2.3 Lrrk2 antibodies are non-specific in immunofluorescence labeling of cells	142
3. Lentiviral-mediated knockdown of Lrrk2 in vitro.....	145
3.1 Evaluation of shRNA sequences targeting murine Lrrk2 for their knockdown efficiency	145
3.2 Activation of a non-specific cellular innate immune response upon expression of first generation shRNAs against Lrrk2 in primary VM cultures	147
3.3 Second generation silencing constructs accomplish the efficient knockdown of Lrrk2 without the induction of an IFN response in primary VM cultures	150
3.4 Silencing of endogenous Lrrk2 affects cellular morphology	153

3.4.1 The knockdown of Lrrk2 in primary VM cultures leads to an impaired neurite outgrowth of developing DA neurons.....	153
3.4.2 Modifications in the cellular shape of NIH3T3 following Lrrk2 depletion.....	156
4. Analysis and evaluation of the Lrrk2 interactome	160
4.1 Lrrk2 interacts with components of the actin cytoskeleton	160
4.2 Lrrk2 binds F-actin and affects its polymerization <i>in vitro</i>	169
V. DISCUSSION	171
1. Performance of Lrrk2-specific antibodies in immunological assays	171
2. Second generation shRNA ^{mir} design of Lrrk2-specific RNAi triggers block immunostimulatory effects of simple hairpin-structured shRNAs	174
3. Lrrk2 as a modulator of the actin cytoskeleton	178
4. Perspectives.....	190
VI. REFERENCES.....	191
VII. ANNEX.....	211
1. Figure index	211
2. Table index	212
3. Publications and poster presentations	213
3.1 Peer-reviewed publications	213
3.2 Poster presentations	213
4. Acknowledgements	214
5. Curriculum vitae	217

Abbreviations

aa	amino acid(s)	ERM	ezrin/radixin/moesin
ABP	actin-binding protein	ETC	electron transport chain
AD	Alzheimer's disease		
ADP	adenosine 5'-diphosphate	F-actin	filamentous actin
Ago	Argonaute	FADD	Fas-associated protein with death domain
ANOVA	analysis of variance	FBS	fetal bovine serum
AP-MS	affinity purification combined with MS	FOG	freezing of gait
APS	ammonium peroxodisulfate	FSC	forward angle light scatter
Arp2/3	actin-related protein 2/3		
ATP	adenosine 5'-triphosphate	G-actin	globular actin
		GAP	GTPase-activating protein
bFGF	basic fibroblast growth factor	GAPDH	glyceraldehyde-3-phosphate dehydrogenase
BG	basal ganglia		
BioGRID	Biological General Repository for Interaction Datasets	GDP	guanosine 5'-diphosphate
		GEF	guanine exchange factor
bp	base pair	GFP	green fluorescent protein
BSA	bovine serum albumin	GIGYF2	Grb10-interacting GYF protein 2
		GPi	Globus pallidus pars interna
C_c	critical concentration	GTP	guanosine 5'-triphosphate
cDNA	complementary DNA		
C-domain	central domain	h	hour
CHIP	Hsp70-interacting protein	HBSS	Hank's balanced salt solution
CNBr	cyanogen bromide	HIV-1	human immunodeficiency virus-1
CNS	central nervous system	HPLC	high performance liquid chromatography
co-IP	coimmunoprecipitation		
COR	C-terminal of ROC	HPRD	Human Protein Reference Database
CRL	crown-rump-length		
C_t	threshold cycle	HRP	horseradish peroxidase
		Hsp	heat shock protein
Da	dalton (molecular mass)	HtrA2	high temperature requirement protein A2
DA	dopamine/dopaminergic		
DAPI	4',6-diamidino-2-phenylindole	I	protein intensity
dATP	2'-deoxyadenosine 5'-triphosphate	IFN	interferon
dCTP	2'-deoxycytidine 5'-triphosphate	IgG	immunoglobulin G
ddH₂O	ultra pure water	IP	immunoprecipitation
ddNTP	2',3'-dideoxynucleotide 5'-triphosphate	ISG	IFN-stimulated gene
		IU^{NIH3T3}	infectious units calculated in NIH3T3
dGTP	2'-deoxyguanosine 5'-triphosphate		
dH₂O	deionized water	JIP	JNK-interacting protein
DIK1	delta-like 1	JNK	c-Jun N-terminal kinase
DMEM	Dulbecco's modified Eagle medium		
DMP	dimethyl pimelimidate	kb	kilo base
DNA	deoxyribonucleic acid	kDa	kilo Dalton
dNTP	2'-deoxynucleotide 5'-triphosphate	KEGG	Kyoto Encyclopedia of Genes and Genomes
DOPA	3,4-dihydroxyphenylalanine		
dsRNA	double-stranded RNA	LB	Luria-Bertani
DTT	dithiothreitol	LC-MS/MS	liquid chromatography-tandem mass spectrometry
dTTP	2'-deoxythymidine 5'-triphosphate		
Dvl	dishevelled	LRR	leucine-rich repeat
		Lrrk2	leucine-rich repeat kinase 2
E	embryonic day	LTQ	linear quadrupole ion trap
ECL	enhanced chemiluminescence	LTR	long terminal repeat
EF1A	elongation factor 1-alpha		
EPLIN	epithelial protein lost in neoplasm	m/z	mass-to-charge ratio
		mAb	monoclonal antibody
ER	endoplasmic reticulum	MAPK	mitogen-activated protein kinase
ERK	extracellular signal-regulated kinase	MAPKK	MAPK kinase
		MAPKKK	MAPK kinase kinase

Abbreviations

min	minute	RLC	regulatory light chain
miR-30	microRNA-30	RNA	ribonucleic acid
miRISC	miRNA-induced silencing complex	RNAi	RNA interference
		ROC	Ras of complex
miRNA	microRNA	ROS	reactive oxygen species
MKK3/6	MAPKKs 3 and 6	rpm	rounds per minute
MKK4/7	MAPKKs 4 and 7	RRE	rev-responsive element
MLK	mixed-lineage kinase	rRNA	ribosomal RNA
MNE	mean normalized expression	RT	reverse transcription
MOI	multiplicity of infection		
MP	myosin phosphatase	S	supernatant
MPP ⁺	1-methyl-4-phenylpyridinium	SB	storage buffer
MPTP	1-methyl-4-phenyl-1,2,3,6-tetrahydropyridine	SDS	sodium dodecyl sulfate
		SDS-PAGE	SDS-polyacrylamide gel electrophoresis
M-RIP	myosin phosphatase-Rho interacting protein	sec	second
mRNA	messenger RNA	SF-TAP	Strep/Flag tandem affinity purification
MS	mass spectrometry		
MS/MS	tandem MS	SH3	Src homology 3
MSN	medium spiny neuron	shRNA	short hairpin RNA
MT	microtubules	shRNA ^{mir}	microRNA-designed shRNA
MYPT1	myosin phosphatase-targeting subunit	SILAC	stable isotope labeling with amino acids in cell culture
		SIN	self-inactivating
NP-40	Nonidet P-40	siRISC	siRNA-induced silencing complex
nt	nucleotide(s)	siRNA	short interfering RNA
		SNP	single nucleotide polymorphism
Oas	2',5'-oligoadenylate synthetase	SNpc	substantia nigra pars compacta
OD	optical density	SNr	substantia nigra pars reticulata
ORF	open reading frame	SSC	side angle light scatter
P	pellet	TBS	Tris-buffered saline
p.a.	pro analysi (reagent-grade)	TBST	TBS-Tween
P:A-ratio	perimeter to area ratio	TEMED	N,N,N',N'-tetramethylethylenediamine
pAb	polyclonal antibody		
PBS	phosphate-buffered saline	TFA	trifluoroacetic acid
PCR	polymerase chain reaction	TH	tyrosine hydroxylase
PD	Parkinson's disease	TH-ir	TH-immunoreactive
P-domain	peripheral domain	TLR	Toll-like receptor
pERM	phosphorylated ERM	T _m	melting temperature
PFA	paraformaldehyde	TM	tropomyosin
P _i	inorganic phosphate	Tmod3	tropomodulin 3
PI	propidium iodide	TOPO	topoisomerase I
PIE	physical interaction enrichment	T-zone	transition zone
PINK1	PTEN-induced putative kinase 1		
PKR	dsRNA-activated protein kinase R	U	Unit (enzymatic activity)
PNK	T4 polynucleotide kinase	UCHL1	ubiquitin carboxyl-terminal hydrolase L1
Pol II	RNA polymerase II		
Pol III	RNA polymerase III	UPS	ubiquitin proteasome system
PP1cδ	type 1 protein phosphatase	UTR	untranslated region
PPI	protein-protein interaction	UV	ultraviolet
pre-miRNA	miRNA intermediate		
pri-miRNA	primary miRNA	v/v	volume per volume
PRR	pattern recognition receptor	VM	ventral mesencephalon
PSP	progressive supranuclear gaze palsy	VSV-G	vesicular stomatitis virus G Glycoprotein
PTEN	phosphatase and tensin homolog	VTA	ventral tegmental area
PVDF	polyvinylidene difluoride		
		w/v	weight per volume
QUICK	quantitative immunoprecipitation combined with knockdown	wt	wildtype
		Y2H	yeast two-hybrid
RCR	replication competent retrovirus		
RIG1	retinoic acid-inducible gene 1	4E-BP	4E-binding protein
RIN	RNA integrity number		
RISC	RNA-induced silencing complex		

Amino acids:

Alanine	A	Leucine	L
Arginine	R	Lysine	K
Asparagine	N	Methionine	M
Aspartic acid	D	Phenylalanine	F
Cysteine	C	Proline	P
Glutamic acid	E	Serine	S
Glutamine	Q	Threonine	T
Glycine	G	Tryptophan	W
Histidine	H	Tyrosine	Y
Isoleucine	I	Valine	V

Purine and pyrimidine bases:

A	adenine	T	thymine
C	cytosine	U	uracil
G	guanine		

Summary

Parkinson's disease (PD) is the second most prevalent neurodegenerative disorder in modern societies, significantly impairing motor skills but also non-motor functions of affected individuals. On the cellular level, PD is characterized by a progressive loss of dopaminergic (DA) neurons in the Substantia nigra pars compacta as well as cytoplasmic proteinaceous aggregates (Lewy bodies) in the surviving neuronal cells. Though the disorder appears to be predominantly sporadic (idiopathic PD), e.g. with a complex etiology and devoid of any family history or known gene defects, a minority of cases present themselves as familial, monogenic inherited forms of the disorder. Mutations in the gene *leucine-rich repeat kinase 2* (*Lrrk2*) have been shown to be the single most common cause for autosomal-dominant inherited but also idiopathic PD. However, little is known about its involvement in the molecular pathogenesis of PD, primarily due to a limited understanding on the biological relevance of the protein. The present study thus focused on the analysis and characterization of the physiological function of *Lrrk2*.

As a prerequisite for functional studies on *Lrrk2*, the detection of the endogenous protein by western blot analysis and its immunoprecipitation from cellular lysates were successfully established at first as well as its lentiviral-mediated knockdown via expression of sequence-specific short hairpin RNAs (shRNAs). In order to gain knowledge on *Lrrk2*-associated cellular processes, the effects of *Lrrk2* protein depletion on cell morphology were determined in two different murine *in vitro* model systems. The delivery of *Lrrk2*-specific shRNAs to primary long-term cultures derived from the murine embryonic ventral mesencephalon (VM) by lentiviral vectors resulted in a significant reduction of *Lrrk2* on both mRNA and protein level. A potential induction of an innate immune response to shRNAs was monitored by expression of the interferon-stimulated gene *2',5'-oligoadenylate synthetase 1* (*Oas1*), which was not substantially altered in the genetically modified cultures. The knockdown of *Lrrk2* in developing DA neurons led on the cellular level to an impaired neurite outgrowth, a process critically dependent on proper actin cytoskeleton assembly and dynamics. When tested in the murine cell line NIH3T3, loss of endogenous *Lrrk2* caused, moreover, significant morphological alterations in these cells, being indicative of alterations in the underlying cytoskeletal organization. Collectively, the results obtained *in cellulo* imply an involvement of *Lrrk2* in the formation and/or modulation of actin-based cytoskeletal structures. This hypothesis was verified by a systematic analysis of the *Lrrk2* interactome. The protein, belonging to the ROCO protein superfamily, comprises various domains including a GTPase and kinase domain as well as several putative protein interaction domains, suggesting that protein-protein interactions could be crucial for the protein's biological function. Applying quantitative immunoprecipitation combined with knockdown (QUICK), a quantitative, mass spectrometry-based proteomic strategy, in NIH3T3 cells, I could show that endogenous *Lrrk2* at its physiological expression level interacts with

elements of the actin filament network. The identified interactome, which was validated *in silico*, revealed 36 proteins as robust interaction partners whose majority is functionally linked to the actin cytoskeleton, its assembly, organization, rearrangement and maintenance, thus implicating that the physiological role of Lrrk2 is related to actin-based cytoskeletal dynamics. In support of this hypothesis, cosedimentation assays of affinity-purified human Lrrk2 demonstrated that the protein binds specifically to filamentous actin and has at least a basal regulatory activity on actin polymerization.

Combining cellular and proteomic approaches for the analysis of Lrrk2 in its specific physiological context that were extended to a biochemical level, the study revealed novel and critical aspects on the biological function of Lrrk2. The findings suggest that the endogenous role of Lrrk2, as being part of a functional protein network that controls actin dynamics, is related to the organization of the actin-based cytoskeleton and associated cellular processes, whose impairment in neurons may underlie PD-associated neurodegeneration.

Zusammenfassung

Das Parkinson Syndrom (PS) ist die zweithäufigste neurodegenerative Erkrankung in unserer heutigen Gesellschaft, die sowohl die motorischen Funktionen Betroffener stark beeinträchtigt aber auch mit vegetativen, psychischen und kognitiven Störungen einhergeht. Auf zellulärer Ebene steht die Degeneration dopaminerger Neurone im Bereich der Substantia nigra pars compacta sowie das Auftreten charakteristischer Proteinablagerungen (Lewy Körperchen) in den überlebenden Neurone im Zentrum der Erkrankung. Obwohl die Erkrankung überwiegend sporadisch auftritt (idiopathisches PS), d.h. mit komplexer Ätiologie und ohne erkennbare Familienanamnese oder bekannten Gendefekten, sind auch seltene familiäre, monogen vererbliche Formen bekannt. Mutationen im Gen *leucine-rich repeat kinase 2 (Lrrk2)* stellen insgesamt die häufigste Ursache für ein autosomal-dominant vererbtes aber auch idiopathisches PS dar. Welche Rolle das Protein in der molekularen Pathogenese des PS spielt ist indes unklar und kann hauptsächlich auf ein fehlendes Verständnis seiner biologischen Funktion zurückgeführt werden. Der Fokus der vorliegenden Arbeit lag daher auf der Analyse und Charakterisierung der physiologischen Bedeutung von Lrrk2.

Als Voraussetzung für funktionelle Untersuchungen von Lrrk2 wurde zunächst die Detektion des endogenen Proteins durch Western Blot Analyse und dessen Immunopräzipitation aus Zelllysaten erfolgreich etabliert sowie sein lentiviral-vermittelter Knockdown durch die Expression Sequenz-spezifischer short hairpin RNAs (shRNAs). Um Erkenntnisse über Lrrk2-assoziierte zelluläre Prozesse zu erhalten, wurden die Auswirkungen eines Verlustes von Lrrk2 auf die Zellmorphologie in zwei verschiedenen murinen *in vitro*-Modellen untersucht. Die Expression Lrrk2-spezifischer shRNAs durch lentivirale Vektoren führte in primären ventral mesencephalen (VM) Langzeitkulturen aus embryonalem Mausgewebe zu einer signifikanten Reduktion von Lrrk2 auf mRNA- und Protein-Niveau. Eine mögliche Induktion einer nativen Immunantwort durch shRNAs wurde über die Expression des Interferon-stimulierten Gens *2',5'-oligoadenylate Synthetase 1 (Oas1)* kontrolliert, die in genetisch modifizierten Kulturen keine spezifischen Änderungen aufwies. Auf zellulärer Ebene führte der Knockdown von Lrrk2 in sich entwickelnden dopaminerger Neuronen zu einer Beeinträchtigung des Neuritenwachstums, ein Prozess, der insbesondere von einer korrekten Ausbildung und dynamischen Regulation des Aktin-Zytoskeletts abhängig ist. Auch in der murinen Fibroblasten Zelllinie NIH3T3 führte der Verlust von endogenem Lrrk2 zu signifikanten morphologischen Veränderungen, die auf Veränderungen in der zugrundeliegenden Zytoskelett-Organisation schließen lassen. Somit deuten die *in cellulo* erhaltenen Ergebnisse zusammengenommen auf eine Beteiligung von Lrrk2 am Aufbau und/oder der Modulation Aktin-basierender Zytoskelett-Strukturen hin. Diese Hypothese wurde durch eine systematische Analyse des Lrrk2 Interaktoms verifiziert. Lrrk2, das zur Familie der ROCO Proteinfamilie gehört, verfügt neben einer GTPase- und

Kinase-Domäne über verschiedene putative Protein-Interaktionsdomänen, die eine wesentliche Bedeutung von Protein-Protein-Interaktionen für die biologische Funktion von Lrrk2 nahelegen. Durch quantitative, Massenspektrometrie-basierte Proteinanalytik mit Hilfe des QUICK-Assays (quantitative immunoprecipitation combined with knockdown) in NIH3T3 Zellen konnte ich zeigen, dass endogenes Lrrk2 unter physiologischen Expressionsbedingungen mit Komponenten des Aktinfilament-Netzwerks interagiert. Das identifizierte und *in silico* verifizierte Interaktom wies 36 Proteine als robuste Interaktionspartner aus, die funktionell hauptsächlich in direktem Zusammenhang mit dem Aktin-Zytoskelett, dessen Aufbau, Anordnung, Reorganisation und Erhaltung stehen und somit einen Zusammenhang zwischen der physiologischen Funktion von Lrrk2 und zytoskeletaler Aktin-Dynamik implizieren. Unterstützt wird diese Hypothese durch Kosedimentations-Analysen von affinitäts-aufgereinigtem, humanen Lrrk2, die zeigten, dass Lrrk2 *in vitro* an filamentäres Aktin bindet und zumindest eine basale Fähigkeit besitzt, dessen Polymerisation zu beeinflussen.

Durch die Kombination von zellulären und proteomischen Strategien für die Analyse von Lrrk2 in dessen spezifischen physiologischen Kontext und deren Ergänzung durch biochemische Untersuchungen *in vitro*, konnten in der vorliegenden Arbeit neue und wesentliche Aspekte der biologischen Funktion von Lrrk2 herausgestellt werden. Die Ergebnisse legen nahe, dass Lrrk2 Teil eines komplexen Proteinnetzwerks ist, das die Dynamik und Organisation des Aktin-Zytoskeletts reguliert und an den davon abhängigen zellulären Prozessen beteiligt ist, deren Beeinträchtigung in Neuronen der Neurodegeneration im PS zugrunde liegen könnten.

I. INTRODUCTION

The natural process of human aging affects cells of the central nervous system (CNS) as much as cells of other organ systems. During senescence, the brain experiences a multitude of molecular, cellular, structural and functional changes (1, 2). To facilitate a successful aging of the brain, i.e. without severe deterioration of function, neurons as well as glial cells may compensate these changes by adaptive mechanisms. However, genetic and environmental factors that superimpose on the normal aging process and counteract or support cellular as well as molecular pathways of aging can influence whether high levels of brain function are preserved throughout life span of an individual or neural cells succumb degenerative cascades, leading to dysfunctions of the nervous system (1). The accelerated and selective loss of neurons is a hallmark of neurodegenerative diseases, such as Alzheimer's disease (AD) or Parkinson's disease (PD), each affecting different and specific areas of the adult brain. Herein, disease-related processes are thought to amplify the molecular alterations that are qualitatively similar to that present during normal aging in the respective vulnerable neurons, resulting in their dysfunction and death (2). Besides genetic predisposition and environmental factors, aging represents a major risk factor for the occurrence of neurodegenerative disorders in modern societies. As the average life expectancy in human populations worldwide shifts to upper age ranges (3), the number of people affected by these diseases increases considerable. To encounter the resulting staggering personal, societal and economic burden, effective or preventive therapies are needed that supersede the current symptomatic treatments. An improved understanding of the disorders and related pathophysiological pathways will be the key to the development of new pharmacological strategies for disease intervention.

1. Parkinson's disease

James Parkinson's classic monograph "An essay on the shaking palsy" (4) was the first clinical description of PD, today's second most prevalent neurodegenerative disease, which affects approximately six million people worldwide (5). It is predominantly a disorder of the elderly population, displaying a marked increase in the age-adjusted prevalence (the number of cases in a screened population) during senescence, with roughly 1-2% of the general population older than 65 years suffering from the disease, whereas 3-5% of people older than 85 years develop symptoms (6). Notably, there are several indications for gender differences in the risk to develop PD, although this appears to be ethnicity dependent. In Western populations, males hold a ~1.5-fold increased incidence rate towards females, with a neuroprotective effect of estrogen and gender-specific genetic predisposition as well as environmental influences as modifying factors being under discussion (6). The majority of PD cases are sporadic (idiopathic PD), i.e. without a familial history, but epidemiological studies

revealed that 5-10% of patients with a clinical picture of the disorder carry mutations in one of the genes causing monogenic forms of the disease (5). The underlying etiology and molecular pathogenesis is still poorly understood, but a complex interplay of age, genetic and non-genetic factors are thought to trigger the disease (6).

1.1 Clinical definition

PD is a chronic neurodegenerative disease that is clinically characterized by a large number of motor and non-motor features. The typical motor symptoms delineated by James Parkinson can, however, also appear in various combinations as part of other progressive neurodegenerative disorders or alternative causes account for their manifestation (reviewed in (7, 8)). Therefore, the clinical entity described by Parkinson has been referred to as “parkinsonism” or “parkinsonian syndromes”. Nevertheless, PD accounts for approximately 80% of the cases, thus representing the most common cause of parkinsonism (7).

The clinical assessment of PD utilizes four cardinal symptoms of the disorder, which can be grouped under the acronym TRAP: tremor at rest, rigidity, akinesia (or bradykinesia) and postural instability. Flexed posture and freezing of gait (FOG) are two additional features that are included in the diagnosis among the classic characteristics. Bradykinesia refers to the slowness of movements, which is manifesting itself such as decreased arm swinging and leg stride when walking. Similar to other PD symptoms, the degree of severity of this most characteristic clinical feature depends on the emotional state of the patient (9). Although bradykinesia is occasionally the initial symptom the disease starts with, tremor is the first clinical sign recognized by the patients (8). The tremor manifests as tremor at rest, being asymmetric (unilateral) with a frequency of 4-6 Hz. Commonly, rest tremor in PD is a supination-pronation (“pill-rolling”) tremor and most prominent in the distal part of an extremity, although it can also involve lips or chin but only very rarely neck/head or voice (9). Characteristically, the tremor is reduced during action and lost during sleep but accelerated in response to stress or excitement (8). Although rigidity is less common than rest tremor and bradykinesia, it is a frequent clinical sign at onset of PD. It is characterized by an increased resistance to passive movements of a limb and may result in postural deformities (9). During the course of disease, axial symptoms as well as gait disorders of the affected people become visible. As such, postural instability, which denotes the loss of postural reflexes where individuals have difficulties to keep their body in a stable or balanced position, occurs as one complication (9). Additionally, FOG, a form of akinesia and also referred to as motor blocks, represents a characteristic feature of PD but does not occur universally. It is one of the most disabling symptoms and becomes apparent in the insufficiency of patients to initiate or continue locomotion (9). Also FOG is influenced by cognitive factors such as stress and triggered by external stimuli like narrow spaces (6).

Although PD is predominantly characterized as a movement disorder, the clinical

spectrum of the disease also encompasses non-motor symptoms, which emerge during disease progression or might even antedate clinical manifestation of motor dysfunction (reviewed in (10, 11)). These non-motor symptoms frequently complicate the course of the disease and contribute markedly to the severe disabilities, impaired quality of life and decreased life expectancy of diseased persons. Death of PD patients is commonly due to complications during progress of the disease rather than from the disorder itself. As such, concurrence of unrelated infections (e.g. pneumonia or sepsis) or effects of impaired mobility, aspiration or increased falling with subsequent physical injuries contribute to mortality in PD (8).

1.2 Pathology and pathophysiology of PD

In the lifetime of patients, PD is defined on the basis of the clinical parkinsonian symptoms, but the definite diagnosis of the disorder requires postmortem analyses of the brain (7). A defining pathological characteristic of PD is the presence of intraneuronal proteinaceous cytoplasmic inclusions, appearing in the form of partially branched, spindle- or thread-like deposits within cellular processes (Lewy neurites) or globular structures in the perikarya (pale bodies or Lewy bodies) (Figure 1) (12). Lewy bodies are spherical eosinophilic protein aggregates comprised of a variety of proteins, with α -synuclein being the most prominent constituent, and are found in various neuronal cell types of the brain (12).

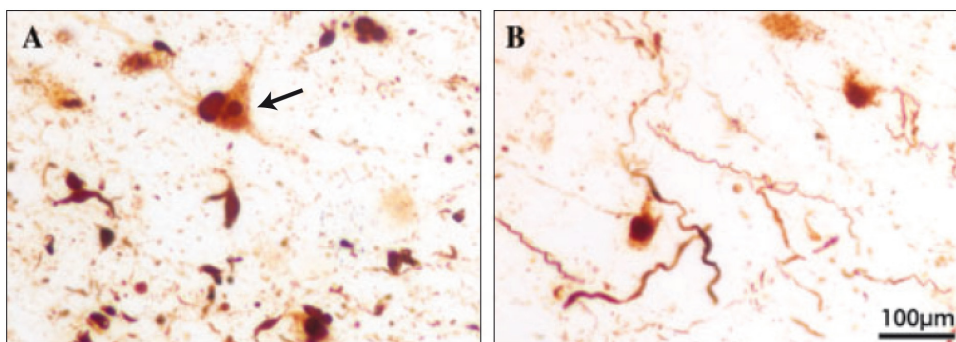


Figure 1: PD-related intraneuronal proteinaceous inclusion pathology.

Intracellular α -synuclein immunopositive spherical Lewy bodies (A) and thread-like Lewy neurites (B) are found in various neuronal populations in the brain of PD patients. The archetypical Lewy body reveals an intensely immunoreactive central core surrounded by a peripheral pale-staining halo (A, arrow). Reprinted by permission from John Wiley and Sons: *Annals of the New York Academy of Science* (13). © 2010.

During time course of the disease, the formation of proteinaceous aggregates is suggested to follow a specific sequence divided into six stages rather than evolving randomly (14, 15). Here, only specific neuronal populations are prone to develop the abnormal α -synuclein deposits while other cells, even in their close proximity, remain unaffected and maintain their morphological and functional integrity (15). The accumulation of α -synuclein thus spreads along certain vulnerable neuronal populations within distinct anatomical regions of the brain. During stages I and II, Lewy bodies and Lewy neurites occur in the olfactory

region and the lower brain stem and extend to the midbrain in stages III and IV. Stages V and VI involve the formation of the α -synuclein deposits in the higher order cortical association areas and finally a distribution to the entire neocortex (14, 15). The progression of aggregate pathology through these areas was well correlated with the appearance and worsening of motor and non-motor symptoms in PD (14, 15).

In PD, Lewy body pathology is accompanied by a region-specific selective loss of dopaminergic (DA), neuromelanin-containing neurons of the Substantia nigra pars compacta (SNpc), being apparent as the depigmentation of the SNpc in postmortem histological studies (7). The neuronal degeneration consequently results in a decreased DA-mediated innervation and functional modulation of the brain areas receiving their input from the DA neurons, especially the putamen and other basal ganglia (BG) nuclei (see below) (16). As the nigrostriatal pathway is involved in the control of motor functions, its progressive degeneration and the concomitant striatal DA deficit accounts mainly for the clinical cardinal symptoms of PD. However, a considerable degradation of the nigrostriatal pathway takes place before the initial appearance of motor dysfunctions in patients, with about 60% of the DA neurons in the SNpc lost and almost 80% of striatal DA depletion (7). This suggests the presence of successful compensatory mechanisms in the presymptomatic phase that counterbalance the deficiency in striatal DA and delay the clinical onset of the disease (reviewed in (17, 18)).

The progressive degeneration of DA neurons of the SNpc gives rise to a specific dysregulation of the BG circuitry. Together with cerebral cortical areas (associative, oculomotor, limbic and motor regions) and the thalamus, the BG nuclei (putamen, nucleus caudatus, globus pallidus, nucleus subthalamicus and substantia nigra) form a complex network of parallel, anatomically and functionally segregated loops. This functional network controls various operations depending on the cortical area that is involved, e.g. the initiation of voluntary movements or emotional and cognitive functions (19). The functional anatomy of the “motor circuit” within this complex provides the basis to elucidate the pathophysiologic features of movement disorders (20). The classical model (Figure 2A) proposes that the cortical afferent activity is modulated by the BG and then send back to the cortex, thus adjusting motor activity (reviewed in (19, 20)). Here, the striatum, especially the putamen as primary BG input nucleus, receives direct afferents from the cortical motor areas. The striatum “communicates” with the BG output nuclei Globus pallidus pars interna (GPi) and the Substantia nigra pars reticulata (SNr) through two different pathways, the so called “direct” and “indirect” pathway, which modulate the output function of the BG by opposing actions. Both the GPi and SNr exert an inhibitory effect on neurons in their target areas, e.g. the thalamus. Activation of striatal neurons by cortical input leads to the inhibition of the GPi/SNr via the direct pathway and sustains their inhibitory action through the excitatory input of the indirect pathway. The net result of both pathways on the BG output nuclei

therefore facilitates movement. In this context, the striatum receives additional input from the DA neurons located in the SNpc (Figure 2A) that establish synaptic connections to medium spiny output neurons (MSNs) as corticostriatal projections do. This anatomical architecture enables a modulation or gating of the corticostriatal transmission, and thus input into the BG, by the nigrostriatal pathway. The DA input into the striatum is assumed to exert a dual effect: excitation of the direct pathway via dopamine D1 receptors and inhibition of the indirect pathway via dopamine D2 receptors. The release of DA at the nigrostriatal nerve terminals thus promotes the transmission of corticostriatal synapses onto the MSNs of the direct pathway, whereas the input into the indirect pathway is reduced. The combination of both actions results in reduced activity of the BG output nuclei, increased transmission to the thalamus and finally in an enhanced activity of the cerebral cortex. Hence, the net result of DA action modulates movement (16). According to this scenario, DA denervation in the parkinsonian state disrupts the internal balance of the BG. It is assumed that the diminished activation of striatal receptors in consequence of DA deficiency causes an increased activity of the indirect pathway and decreased excitation of the direct pathway (Figure 2B). This results in an excessive activation of the BG output nuclei and consequently inhibition of the motor system, manifesting itself in the parkinsonian motor features.

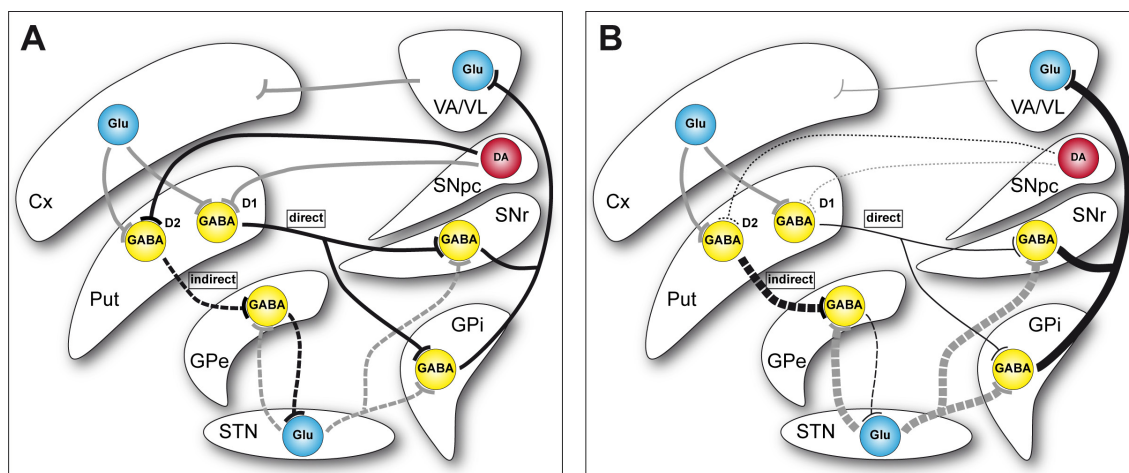


Figure 2: PD-related changes in the motor loop of the basal ganglia.

Schematic representation of the basal ganglia (BG) motor circuit (A) and its modification in the parkinsonian state (B). (A) Cortical motor areas project to the striatum, especially to the putamen (Put), terminating in excitatory synaptic connections to medium spiny neurons (MSNs). Two pathways that connect the putamen to the output nuclei of the BG, the Globus pallidus pars interna (GPi) and the Substantia nigra pars reticulata (SNr), originate from them. Their net result on the output nuclei facilitates movement. In the “direct” pathway (solid lines), MSNs directly project to the GPi/SNr where they exert an inhibitory effect. Hereby, the inhibitory effect of output nuclei on the thalamus (ventral anterior (VA) and ventrolateral (VL) nuclei) is decreased and movement via the cerebral cortex thus promoted. The “indirect” pathway (dashed lines) connects the putamen with the GPi/SNr via the Globus pallidus pars externa (GPe) and the Subthalamic nucleus (STN). Stimulation of the striatal projection neurons causes an activation of the BG output nuclei, increasing their inhibitory effect on the thalamus and finally evoking the suppression of movement. The striatum receives additional modulatory input from the dopaminergic (DA) neurons of the Substantia nigra pars compacta (SNpc) that is transduced via dopamine D1 (excitatory) and D2 (inhibitory) receptors on MSNs into the direct and indirect pathway, respectively. (B) PD-related depletion of DA (dotted lines) causes a disinhibition of the indirect pathway and decreased activity of the direct pathway. As a consequence, an excessive activation of the BG output nuclei provokes the clinical symptoms related to PD. Black bonds indicate inhibitory, gray bonds excitatory projections. Thickness of the connections denotes the degree of activation of each projection. Cx: cortex, GABA: gamma-aminobutyric acid, Glu: glutamate. Adapted from (16, 19).

1.3 Etiology and pathogenic mechanisms

The pathogenic mechanisms underlying PD are still incompletely understood, but mitochondrial dysfunction, impairments in the ubiquitin-proteasome system (UPS), accumulation of aberrant or misfolded proteins and oxidative stress have been proposed to represent the common molecular basics in the development of both sporadic and inherited forms of the disease (21). The specific causes for these defects are, however, poorly understood. A small fraction of PD patients show a clear family history and exhibit rather monogenetic forms of the disease with mutations in one of the causative genes, possessing a classical recessive or dominant Mendelian mode of inheritance. The majority of cases, however, emerge sporadic and several lines of evidence suggest a multifactorial etiology, resulting from three interactive events: environmental risk factors acting on each individual's inherited genetic predisposition, and age-related traits (22).

1.3.1 Aging

Aging is still considered to be the largest risk factor for the development of PD, although it is still a matter of debate whether the molecular mechanisms underlying the disease represent an exaggerated manifestation of those processes in normal aging or whether aging determines one's susceptibility for the disease or whether it is unrelated to PD (23). During aging of the brain, several molecular and cellular changes occur. As such, mitochondrial dysfunction, increased production of free radicals and oxidative stress cause a perturbed energy homeostasis, genomic instability and DNA mutations. Furthermore, a decline in proteasome and chaperone activity as well as an impairment of the autophagic cycle leads to the abnormal accumulation of damaged or misfolded proteins. Age-related changes in neuroprotective or neurorestorative mechanisms, e.g. microglia activity or response to neurotrophic factors, interfere with the ability of the brain to facilitate responses to environmental demands or to recover from damage (2, 23). In order to enable a successful aging of the brain, neuronal cells may respond to the age-related changes adaptively and compensate them by various mechanisms (1). Alterations linked to the aging process may form the basis for neurodegenerative diseases, triggered by failures in the cellular compensatory mechanisms, environmental factors and/or genetic predisposition (2, 23).

1.3.2 Environmental factors

Several epidemiologic studies indicate an environmental etiology for PD and identified, if not consistently and unambiguously, various environmental and occupational risk factors that may contribute to the disease. Here, a positive association of PD and exposure to chemical compounds of synthetic origin, including xenobiotics and pesticides, such as herbicides and insecticides, was found. The most prominent and best characterized example of environmental toxins linked to PD is 1-methyl-4-phenyl-1,2,3,6-tetrahydropyridine (MPTP),

which was initially identified as a neurotoxic contaminant of the illicitly manufactured synthetic opiate 1-methyl-4-phenyl-4-propionoxypiperidine (MPPP) and whose administration causes the development of an irreversible and severe syndrome resembling PD (7). MPTP crosses the blood-brain barrier and is ultimately converted to its active metabolite 1-methyl-4-phenylpyridinium (MPP⁺) within glial cells and serotonergic neurons followed by its release into the extracellular space. The subsequent uptake via the dopamine transporter (DAT) leads to the inhibition of complex I, causing mitochondrial electron transport chain (ETC) dysfunction and finally selective degeneration of DA neurons (7). MPP⁺ itself has been tested for its application as herbicide in the 1960s, and the structural resemblance to some pesticides, e.g. the herbicide paraquat, provides additional evidence for a functional link between increased risk for PD and pesticides (22).

A variety of individual habits have been investigated, including dietary factors, antioxidants intake, smoking, coffee and alcohol consumption, head injury and infections being considered. With the exception of tobacco, caffeine and alcohol ingestion that displayed an inverse association to PD, possessing a protective role, the relationship of the remaining factors to the disease's risk appears to be only tentative or predisposing (24, 25).

The evidence for many of the identified factors to play part in PD's etiology is still inconclusive, and no factor was identified to be solely responsible for the disease onset. One conceivable complication for the conclusive identification of risk factors that has been proposed is the possibility that the causal events leading to the disorder emerge many years prior to the disease onset. These events can even occur during early life, thereby determining increased susceptibility for PD in the adult life (24, 26).

1.3.3 Genetic factors

For a long time PD, was considered to be a non-genetic disorder of idiopathic origin and the influence of heredity controversial. The majority of cases are in fact sporadic and of unknown etiology, but within the last decade, disease-causing mutations have been identified in certain genes that give rise to monogenic forms of the disorder with autosomal-dominant or -recessive inheritance, confirming the role of genetics in the development of PD. Although sporadic and familial forms of the disease appear to be both clinically and pathologically different to various extents, the two entities share many features, including most importantly parkinsonism with nigrostriatal degeneration. Thus, common pathogenic mechanisms may underlie the disease and analysis of the gene products linked to familial forms of PD may elucidate the molecular pathways involved in the pathogenesis (27). Linkage studies revealed so far 15 PD loci and 11 genes for PARK loci (Table 1) (27, 28).

Table 1: Genetic loci and genes associated with PD.

Locus	Gene	Inheritance	Probable function
PARK1/4	<i>SNCA</i>	autosomal-dominant	Presynaptic protein
PARK2	<i>parkin</i>	autosomal-recessive	Ubiquitin E3 ligase
PARK3	Unknown	autosomal-dominant	Unknown
PARK5	<i>UCHL1</i>	autosomal-dominant	Ubiquitin C-terminal hydrolase
PARK6	<i>PINK1</i>	autosomal-recessive	Mitochondrial kinase
PARK7	<i>DJ-1</i>	autosomal-recessive	Chaperone, Antioxidant
PARK8	<i>Lrrk2</i>	autosomal-dominant	Protein kinase, scaffold
PARK9	<i>ATP13A2</i>	autosomal-recessive	Unknown
PARK10	Unknown	autosomal-dominant (?)	Unknown
PARK11	<i>GIGYF2</i>	autosomal-dominant (?)	IGF-1 signaling
PARK12	Unknown	X-linked	Unknown
PARK13	<i>HTRA2/OMI</i>	autosomal-dominant	Mitochondrial serine protease
PARK14	<i>PLA2G6</i>	autosomal-recessive	Phospholipase enzyme
PARK15	<i>FBXO7</i>	autosomal-recessive	Ubiquitin E3 ligase

Besides a number of genes that have been conclusively linked to monogenic forms of PD, recent studies revealed several genetic risk factors for the disease. Common variants in the two PD loci *leucine-rich repeat kinase 2 (Lrrk2)* and *α -synuclein (SNCA)* were shown to convey an increased risk for the disease as well as polymorphisms in two other genes not assigned to PARK loci, encoding the microtubule-associated protein tau (MAPT) and glucocerebrosidase (GBA). Genome-wide association studies established, moreover, three new putative susceptibility loci (PARK16-18) that, however, require further validation (29).

1.3.3.1 *α -synuclein*

α -synuclein (SNCA) was the first gene found to be associated with familial PD. Until today, three missense mutations (A30P, A53T and E46K) as well as duplication and triplication of the gene locus (referred to as PARK4) were identified that lead to rare autosomal-dominant forms of the disease (30-34). Here, the clinical and pathological features of patients carrying the A30P mutation resemble those of sporadic cases, whereas both the A53T and E46K mutations cause more severe phenotypes with atypical features. A similar situation prevails for the multiplication of gene copy numbers. Duplication causes the symptoms of classical PD and triplications an atypical form similar to A53T mutations, implicating that the gene dose is critical for the development of the disease. Thus, *α -synuclein* can evoke the disorder through both a toxic gain-of-function mechanism of the mutated protein or increased expression levels of the wildtype (wt) protein (28, 35).

The physiological function of *α -synuclein* is yet unclear. However, the protein has been found to be enriched in presynaptic terminals where it is closely associated with membrane and vesicle structures (35). *α -synuclein* has been linked to various cellular pathways that are critical to the integrity of DA neurons. Several studies provide evidence for a role of *α -synuclein* in the modulation of synaptic DA neurotransmission through the regulation of catecholamine metabolism, synaptic vesicle recycling and sorting as well as the compartmentalization of neurotransmitters (36-39). As fibrillar *α -synuclein* is the major

structural constituent of Lewy bodies and Lewy neurites, the protein is thought to acquire a central role in the pathogenesis of PD. Its accumulation is suggested to represent a key event in DA neuronal cell death during both sporadic and inherited PD (40, 41). In its native state, α -synuclein is a soluble and unfolded (intrinsically disordered) protein, exhibiting little or no ordered structure (42, 43). Due to a central hydrophobic region that contains the non-amyloid- β component (NAC) domain, the protein has a high propensity to aggregate. The monomers initially form β -sheet rich oligomers that constitute an intermediate population of protofibrils with heterogeneous structures, which remain soluble. These protofibrils are the predecessors for ultimately formed higher-order aggregates, where they are converted into stable and insoluble amyloid-like fibrils that precipitate along with other proteins to Lewy bodies and Lewy neurites (44). Several factors can trigger or modulate the formation of α -synuclein aggregates. As such, all pathogenic mutations increase the capacity of the protein to aggregate (44). As an equilibrium between the natively unfolded and partially folded (comprising the protofibrils) conformation of α -synuclein exists under physiological condition, increased amounts of the protein as caused by duplication and triplication of the gene locus shifts the balance towards the fibrillation-prone intermediates, thus promoting an increased rate of fibril formation (44). Besides genetic factors, numerous studies reported that various exogenous factors, including neurotoxicants linked to PD, accelerate the aggregation of α -synuclein (reviewed in (44)), thereby supporting a gene-environment interaction in the pathogenesis of PD. Additionally, post-translational modifications (e.g. phosphorylation, oxidation or truncation) modulate and/or contribute to fibrillation (44). It is still unclear, whether fibrils or protofibrils promote neurotoxicity, but both moieties are assumed to exert pathogenic functions through yet incompletely understood pathways. While protofibrillar, oligomeric forms of α -synuclein can form pore-like structures that cause inappropriate permeabilization of cellular membranes like vesicles (45), incompatible α -synuclein aggregates can interfere with the cellular physiology, including evocation of ER (endoplasmic reticulum) stress (46), mitochondrial dysfunction (47) and impairment of protein quality control systems (48, 49). The susceptibility of DA neurons towards α -synuclein toxicity and degeneration in PD might be due to the interaction of cytosolic DA and/or its metabolites with α -synuclein that was observed *in vitro*, forming adducts that stabilize α -synuclein protofibrils and thus inhibiting fibrillation (50-53). The emergence of inclusion bodies, however, may represent a protective response towards the formation of insoluble α -synuclein fibrils by sequestering the toxic protein aggregates and thus reducing their amount (35).

1.3.3.2 *Parkin*

Mutations in the *parkin* gene are the major cause for autosomal-recessive early-onset PD, where the disease becomes manifested before the age of 40 years. Here, missense and nonsense mutations, deletions of single or numerous nucleotides and genomic multiplications have been described. Pathologically, postmortem brains of affected patients displayed degeneration of DA neurons in the SNpc underlying their movement disorders but in the majority of cases without Lewy body formation (54).

Parkin functions as an E3 ubiquitin protein ligase that recognizes and thereby specifically targets misfolded proteins for degradation by the UPS (55-57). Although not all mutations affect obligatory the protein's enzymatic function, they all appear to manifest themselves in a loss-of-function of parkin. As a consequence, mutant protein variants are all ultimately deficient in their aptitude to facilitate the proteasome-dependent degradation of substrates, which subsequently accumulate in the cells and are potent to mediate cytotoxicity. Besides a differential disruption of solubility and intracellular localization, the mutants display defects in substrate binding, decreased catalytic activity, impairment of proteasomal degradation and/or destabilization *in vitro* (58). Concordantly, affected patients displayed a marked reduction in the protein's enzymatic E3 activity within brain areas succumbing degeneration and accumulation of several, non-ubiquitinated parkin substrates (59). A number of potential substrates has been identified, including proteins that are implicated in enhancing neuronal cell death and PD (60). Moreover, experimental evidence exists that implies a function of parkin different from the UPS. Studies on both mice and flies lacking the protein displayed mitochondrial defects as well as increased oxidative stress, which supports the notion that parkin plays a protective role in mitochondria (61-63). Parkin has been shown to mediate the maintenance of mitochondrial integrity. The protein regulates both transcription and replication of mitochondrial DNA in proliferating cells (64) and translocates to depolarized mitochondria where it promotes mitophagy, the selective clearance of these organelles through autophagic pathways (65). Furthermore, parkin participates in the autophagic clearance of proteins (66), operates in signaling pathways of cellular survival (27, 67) and its overexpression protects against a variety of toxic insults (60). This suggests a multipurpose neuroprotective role of parkin (27). The mechanisms by which parkin confers neuroprotection are still unresolved, but their elucidation may contribute to identify the role of parkin in PD pathogenesis. A selective vulnerability of DA neurons in PD might be linked to the ability of DA to covalently modify parkin, thereby inducing its functional inactivation by a decrease in solubility and E3 ligase activity (68).

1.3.3.3 *PINK1*

The second most common cause for autosomal-recessive early-onset PD is related to alterations in PINK1 (phosphatase and tensin homolog (PTEN)-induced putative kinase 1).

Clinically, homozygous mutations in the gene lead to a PD phenotype that resembles that of the idiopathic form, apart from its manifestation in early life, although some patients show atypical symptoms (69). Additionally, some PD cases of similar characteristics to the sporadic disease, including late onset, can be linked to heterozygous PINK1 mutations that may therefore also contribute to the development of sporadic PD (28).

PINK1 comprises an N-terminal mitochondrial targeting signal, which is sufficient to localize the protein to mitochondria, as well as a highly conserved kinase domain, sharing similarity to the serine/threonine kinase domain of the Ca^{2+} /calmodulin family and possessing autophosphorylation activity *in vitro* (70, 71). Disease-related mutations cluster to regions in or adjacent to the kinase domain, causing a loss of function of the protein's kinase activity and thus phosphorylation of its (mitochondrial) substrates. Additionally, they lead to modifications in the protein's autophosphorylation pattern and interfere with its mitochondrial localization (70, 72). The function of PINK1 as a putative mitochondrial serine/threonine kinase under normal conditions is yet obscure. Growing evidence indicates a crucial role in mitochondrial function and protection of cells against oxidative stress induced apoptosis (28, 73). Moreover, PINK1 was shown to act with parkin in a common pathway and to interact with DJ-1 (28). Therefore, the three proteins are assumed to form a functional E3 ligase complex that degrades parkin substrates via the UPS, with PINK1 and DJ-1 as putative regulators of parkin activity (74).

1.3.3.4 DJ-1

Another early-onset form of PD is caused by mutations (exonic and splice site deletions, missense mutations) in the *DJ-1* locus. The clinical phenotype of such rare familial cases is similar to that of *parkin* or *PINK1* mutation patients and is thought to be induced by a loss of function of the protein, being consistent with an autosomal-recessive trait of inheritance (69). Although several functions have been ascribed to DJ-1, the precise cellular role of the homodimeric protein, which belongs to the DJ-1/Thi/Pfpl superfamily, is largely opaque (69, 75). A putative active site close to the dimer interface resembles the catalytic triade of the active site of cysteine proteases (76). Nevertheless, it is assumed that DJ-1 exerts its most relevant function with respect to PD pathogenesis in the oxidative stress response. Here, it may act either as an antioxidant or sensor of oxidative stress (77, 78). The protein possesses an intrinsic capacity to eliminate hydrogen peroxide under oxidative stress conditions by oxidizing itself at cysteine residues, mainly C106, implicating that it acts as a direct scavenger of reactive oxygen species (ROS) (79, 80). Accordingly, an enhanced susceptibility towards oxidative stress was observed upon ablation of DJ-1 (27, 28). However, DJ-1 more likely acts as a sensor of cellular ROS levels than a simple antioxidant and has been found to be involved in several oxidative stress response pathways, including apoptosis and transcriptional regulation of antioxidant as well as survival genes (28, 75). As

such, DJ-1 is supposed to act in the phosphatidylinositol 3-kinase (PI3K) signaling pathway, which regulates cell survival, where it exerts its function as a negative regulator of PTEN through its redox sensor activity (81). Upon oxidative stress, DJ-1 was found to translocate to mitochondria (82) where it might exert an antioxidant and thereby cytoprotective function through its self-oxidizing characteristics by scavenging mitochondrial ROS (79). Loss of function therefore increases cellular ROS levels leading to oxidative stress.

DJ-1 might also be involved in the UPS, conferring its protective function against oxidative stress induced injuries as a redox-sensitive molecular chaperone or protease by refolding misfolded proteins or promoting their degeneration. Mild oxidation of DJ-1 promotes chaperone activity towards α -synuclein, thus preventing its fibrillation, which is, however, impaired by further, extensive oxidation (83, 84).

How mutations contribute to PD pathogenesis is also still elusive, but it has been shown that they disrupt the protein's activity either by destabilization of the protein or by affecting its subcellular localization (75).

1.3.3.5 UCHL1

UCHL1 (ubiquitin carboxyl-terminal hydrolase L1) was linked to autosomal-dominant PD by the identification of a heterozygous missense mutation (I93M) within the gene locus in a German sib-pair (85). The protein specifically localizes to neurons and testis/ovary and accomplishes three known functions: hydrolysis of polymeric ubiquitin chains from proteins intended for degradation by the UPS into monomers, dimerization-dependent ubiquitin ligase activity and maintenance of ubiquitin homeostasis by regulating the degradation of ubiquitin monomers (86). The mutation was shown to elicit a reduction in the catalytic hydrolase activity as well as in ubiquitin levels *in vitro*. Degradation of proteins might hence be prevented by an impaired deubiquitination that hampers proteasomal degradation of targeted proteins or limitation in the pool of ubiquitin monomers required for the clearance of proteins (59). Accordingly, mice lacking functional UCHL1 (*gad* mice) display an accumulation of abnormal proteins in the brain (87). However, a causal role of UCHL1 in the pathogenesis of PD is still controversial. Not least because the initial sib-pair is the only reported case of PD where the I93M mutation occurred, and no other pathogenic mutations have been reported to date. To the contrary, a common S18Y polymorphism was identified, which confers a putative positive effect and decreases the risk of idiopathic PD (88, 89). This variant was demonstrated to exhibit an increased hydrolase activity and reduced ligase activity compared to the wt enzyme (90, 91). Hence, a clear assignment of UCHL1's function is difficult to make, and its part in the UPS in the etiology of PD remains to be clarified.

1.3.3.6 Other PD genes

Mutations in the genes encoding the mitochondrial serine protease HtrA2 (high temperature requirement protein A2, or OMI) (92) and GIGYF2 (Grb10-interacting GYF Protein 2) (93) have been described to segregate with familial forms of PD. The latter protein is involved in insulin and insulin-like growth factor signaling, both exerting an important function in the CNS (93). HtrA2 was proposed to be involved in the mitochondrial protein quality control system (94), and several studies describe an association to PINK1 and parkin (28). The interaction with PINK1 is assumed to be involved in the regulation of HtrA2 protease activity (94). A recent study demonstrated that HtrA2 is able to cleave parkin, thereby disrupting its E3 ubiquitin ligase activity (95). However, the primary data sets concerning the involvement of both HtrA2 and GIGYF2 mutations in the pathogenesis of PD are equivocal (28) and their association with the disease has thus to be resolved.

Homozygous and compound heterozygous mutations in the lysosomal P-type ATPase gene *ATP13A2* were associated with recessive, juvenile-onset parkinsonism, although the pathogenicity of the heterozygous mutation is controversial. It might also act as a susceptibility factor for late-onset forms of the disease. The precise cellular function of *ATP13A2* is still unknown, but as α -synuclein aggregates can also be cleared from the cell via the lysosomal degradation pathway, its impairment by *ATP13A2* mutations may contribute to PD (5, 29).

Very recently, two other loci linked to parkinsonism were described: *PLA2G6* (96), which encodes a calcium-independent group VI phospholipase A2, and *FBXO7* (97), whose related protein is similar to parkin involved in the UPS as part of an E3 ubiquitin ligase (98). As the clinical symptoms caused by the mutations correspond to atypical parkinsonism different from the classical sporadic PD, their relation to the disease pathomechanisms remains unsolved and requires further studies (5).

1.3.4 Molecular pathogenesis

Although PD is clinically as well as pathologically well defined, the molecular pathways underlying the disorder are poorly understood. However, the identification of disease-causing mutations in monogenetically inherited genes and the remarkable consistent, specific phenotype of idiopathic and familial PD led to the assumption that both forms share a common pathogenesis and that the pathways underlying inherited PD may also have relevance in the sporadic disorder. Based on a variety of genetic, pathological and experimental analyses, two major pathways underlying the pathogenesis of PD have emerged (Figure 3). One claims that an aberrant accumulation and aggregation of proteins due to dysfunction of the UPS induces neurotoxicity, whereas the second expects oxidative stress as a consequence of mitochondria malfunction to be causative.

1.3.4.1 UPS dysfunction and protein aggregation

The UPS represents the major intracellular pathway for the degradation and clearance of regulatory as well as misfolded, mutant or damaged (e.g. oxidative injury) proteins, thereby taking the center stage in the regulation of various basic cellular processes (e.g. cell cycle, transcription factor regulation, gene expression, cell differentiation and immune response) and cellular quality control (99-101). This is accomplished by a series of enzyme-mediated reactions, where the target proteins are identified and linked with a polyubiquitin chain, serving as a proteolytic signal that assigns the proteins to degradation by the 26S proteasome (102). Perturbation of the balanced system of generation and clearance of aberrant proteins through either dysfunction of the UPS, impeding its ability to clear regular levels of abnormal proteins, or excessive production of such proteins, which exceeds the capacity of the UPS to degrade them or a combination of both results in the adverse state of proteolytic stress. As a consequence, proteins may aggregate and accumulate, which interferes with normal cellular function and viability (99, 101).

Several lines of evidence suggest a direct role of the UPS in sporadic and inherited PD, with mishandling of aberrant proteins affecting protein homeostasis and detrimental consequences for neuronal survival. As such, disease-causing mutations in the *parkin* gene compromise its normal function in the proteasome-dependent degradation of substrate proteins, ultimately leading to a toxic substrate accumulation that triggers neurodegeneration (see 1.3.3.2). A direct link of UPS aberration to neuronal survival is further encouraged by the association of mutated UCHL1 with familial parkinsonism (see 1.3.3.5). A critical role of protein aggregation in PD is supported by the accumulation of misfolded and aggregated α -synuclein due to mutations or multiplications of the corresponding gene (see 1.3.3.1). Wt α -synuclein is preferentially degraded by the proteasome (103). Pathogenic protein variants, however, are more resistant to proteasomal degradation and even impair the ubiquitin-dependent degradation system both *in vitro* and *in vivo*, with protein aggregates shown to be capable to inhibit proteasome activity (103-106). Mutation/overproduction of α -synuclein may thus induce a vicious cycle including misfolding of the protein, aggregation and proteasomal damage that results in turn in a generalized accumulation of a wide range of other cellular proteins and neurodegeneration (106, 107). Additional support for a role of UPS dysfunction and aberrant protein homeostasis in the pathogenesis of PD is provided by the evaluation of postmortem sporadic PD brain tissue that revealed both a structural and functional impairment of the UPS in these patients (108). Besides the overall propensity to develop proteolytic stress during the course of aging, cells within the SNpc are furthermore particularly prone to accumulation of aberrant proteins, which may account for their vulnerability to neuronal degeneration in PD: the proteasomal activity declines progressively (109), DA can interact with α -synuclein leading to aggregation (50, 51) and the oxidative metabolism of DA promotes free radical formation and oxidative damage of proteins (110).

Hence, growing evidence suggests that proteolytic stress is a common feature in the pathogenesis of both sporadic and inherited forms of PD. Protein aggregation as a consequence of impaired UPS and inhibition of proteasomal activity is then likely to cause oxidative stress (111), mitochondrial dysfunction (111), inflammatory reactions (112) and apoptosis (113), accelerating neurodegeneration.

1.3.4.2 Mitochondrial impairment and oxidative stress

Besides the notion that protein misfolding and UPS dysfunction are part of a significant pathway leading to the degeneration of DA neurons, there is ample evidence indicating that mitochondrial dysfunction, especially inhibition of ETC complex I and oxidative stress, represents another main upstream pathway to PD. The primary function of mitochondria is the generation of cellular energy in form of ATP by oxidative phosphorylation. But in addition to various other cellular functions (e.g. metabolism, Ca^{2+} homeostasis, free radical scavenging), mitochondria possess also a fundamental role in mediating cell death by apoptosis (114). Depolarization of the inner mitochondrial transmembrane potential, which results from an electrochemical gradient across the inner mitochondrial membrane generated as well as maintained by the ETC and drives ATP synthesis, is associated with opening of the mitochondrial permeability transition pore. This pivotal event in the mitochondrial mediated pathway of apoptosis leads to the release of several pro-apoptotic proteins from the mitochondrial intermembrane space that trigger the mitochondrial trace of apoptosis by both caspase-dependent and -independent mechanisms (114, 115). Moreover, mitochondria are the major source of ROS that arise as a byproduct of the oxidative phosphorylation (116). As these strong oxidants induce oxidative damage of proteins, lipids, polysaccharides and DNA, mitochondria possess a complex network of antioxidant defenses for detoxification, thereby maintaining a balance between production and removal of ROS to keep them at a low, non-toxic steady-state level (116). Mitochondrial insults, including ROS production itself or respiratory defects, interfere with this balance, with an excessive ROS formation and insufficient antioxidant defenses leading to a net production of ROS that initiates various deleterious processes, a state referred to as oxidative stress (116). DA neurons are inherently prone to oxidative stress, based on the cytosolic enzymatic oxidation or auto-oxidation of DA or its precursor L-DOPA (L-3,4-dihydroxyphenylalanine) that generates superoxide anions, hydrogen peroxide, DA quinone and DOPA quinone, respectively, contributing to DA neuron-specific pathogenicity and/or degeneration (117).

Evidence for the involvement of mitochondria dysfunction in the pathogenesis of PD first emerged upon the observation that accidental exposure of drug abusers to MPTP, whose neurotoxic metabolite MPP^+ selectively inhibits complex I of the ETC in DA neurons, induces an acute and irreversible parkinsonian syndrome (7). Additional support comes from reports on complex I deficiency (67) and identification of oxidative stress markers (118) in the

SN of PD patients. The finding that a variety of the genes associated with familial forms of PD, namely *parkin* (see 1.3.3.2), *PINK1* (see 1.3.3.3), *DJ-1* (see 1.3.3.4) and *HtrA2* (see 1.3.3.6), encode proteins exhibiting mitochondrial localization patterns and functioning further strengthens the link between mitochondrial dysfunction and PD. A number of pathogenic mutants were shown to have a direct or indirect impact on mitochondrial function and integrity that ultimately leads to mitochondrial failure and subsequently to neuronal dysfunction and death (reviewed in (67, 73, 75)), but the underlying mitochondrial pathways remain opaque. In addition to its cytosolic and vesicular localization, α -synuclein can also be translocated in an energy-dependent fashion to mitochondria by a cryptic mitochondrial targeting signal where it accumulates (119). Within the mitochondria, α -synuclein associates with the inner mitochondrial membrane where it specifically inhibits complex I of the ETC and increases ROS production, an effect that is enhanced by the mutant protein (119). Conversely, complex I deficiency initiates the aggregation of α -synuclein and the formation of inclusions in the cytosol (120). The ability of α -synuclein protofibrils to form pores capable of permeabilizing cell membranes (45) might account for the release of cytochrome c from mitochondria (121), mediated by the mitochondrial located protein, as well as of DA from synaptic vesicles into the cytosol (122), accomplished by the cytosolic aggregates, both ending in apoptotic cell death.

Given that PD is a multifactorial disease, it is worth to speculate that both mitochondrial dysfunction and UPS defects are involved in the pathogenesis of PD and might be interdependent, centering around oxidative stress and converge in vicious feedback or feedforward loops. Impairment of either of the two pathways may thus have deleterious effects on the other (75). As such, deficiency in the clearance of aberrant proteins caused by UPS dysfunction and leading to their accumulation can result in secondary mitochondrial damage and ROS production (123). Conversely, the proteasomal system is ATP dependent so that the depletion of ATP by disruption of the mitochondrial ETC can result in a decreased UPS activity. Additionally, mitochondrial dysfunction results in an accelerated production of ROS, thereby increasing the substrate load (oxidative damaged proteins) for the proteasome that in turn accumulate due to impairments in the UPS, inducing a feedforward amplification loop with adverse effects on cell function and survival (124). The exact mechanism of cell death is not definite, but the mitochondrial-mediated apoptosis pathway seems to play the major role in PD-associated neurodegeneration rather than necrosis or autophagic cell death (125, 126).

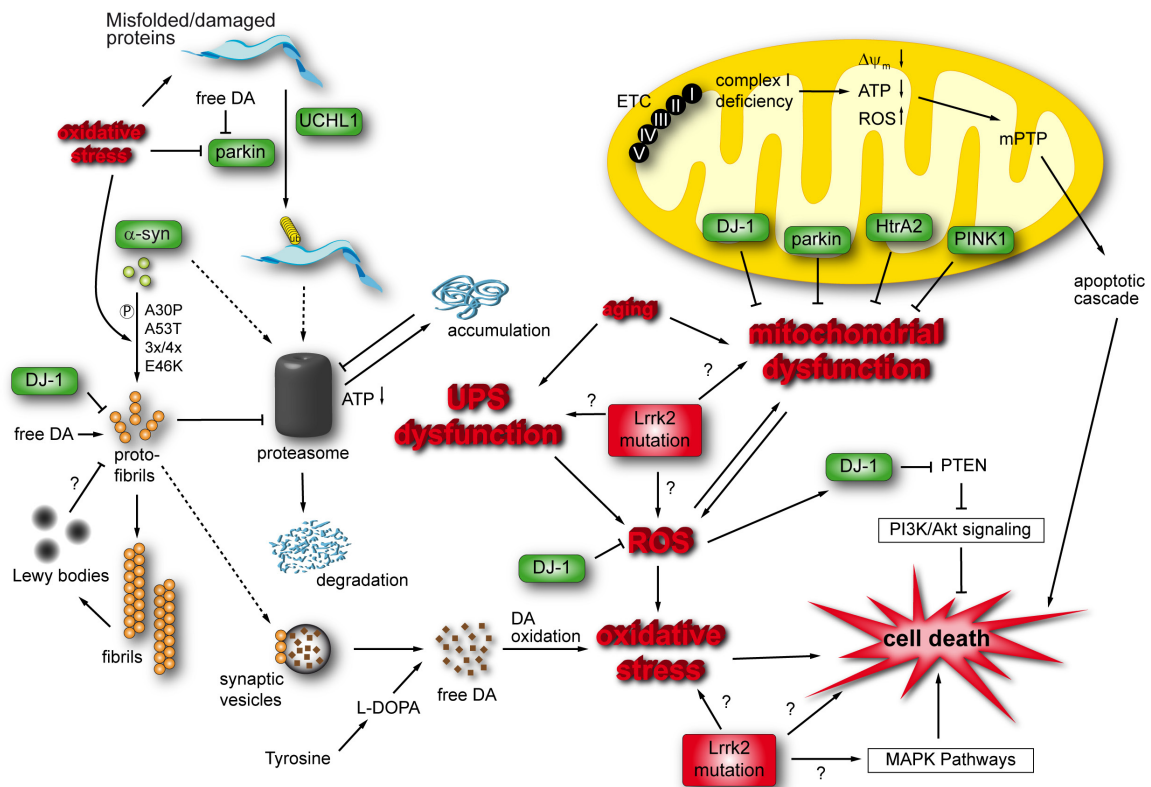


Figure 3: Molecular pathways implicated in the pathogenesis of PD.

Several pathogenic processes arose as putative contributors to neurodegenerative pathways in PD. Functional deficiency in the ubiquitin proteasome system (UPS) and subsequent protein accumulation as well as mitochondrial dysfunction and oxidative stress are thought of as the two major pathways underlying the molecular pathogenesis in both idiopathic and sporadic PD. Both are linked to each other at multiple levels, functioning as a network rather than independently, with pathogenic mutations in the disease-related genes affecting either of them. Parkin as an E3 ubiquitin (ub) ligase and UCHL1 that may function as a deubiquitinating enzyme, ubiquitin ligase or ubiquitin degrading enzyme can act in the clearance of proteins designated to proteasomal degradation via the UPS. UCHL1 and parkin mutations, ATP depletion due to mitochondrial failure or α -synuclein (α -syn) protofibrils result in disruption of the UPS function and thereby in the accumulation of proteins. Parkin function is also affected by oxidative stress, causing adverse alterations of its solubility and E3 ligase activity. α -synuclein protofibril formation and subsequent aggregation (fibrils) is promoted by pathogenic mutations, oxidative stress or post-translational modifications (e.g. phosphorylation). The formation of Lewy bodies might result from a cellular attempt to sequester aberrant proteins. Accumulation of α -synuclein is proposed to be prevented by the redox-sensitive chaperone activity of DJ-1. Additionally, DJ-1 exerts its neuroprotective function as a redox-sensitive regulator of the pro-survival PI3K/Akt signaling pathway and by scavenging reactive oxygen species (ROS), both cytoplasmic and mitochondrial. A protective effect on mitochondria is also assumed for PINK1, HtrA2 and parkin by regulating molecular pathways that protect cells from mitochondrial stress or maintaining mitochondrial integrity. Complex I dysfunction leads to an increased generation of ROS and decline in both ATP levels and mitochondria transmembrane potential ($\Delta\psi_m$). In turn, a decrease in $\Delta\psi_m$, extensive ROS production and low ATP cause membrane permeabilization via opening of the mitochondrial permeability transition pore (mPTP), initiating the mitochondrial (intrinsic) pathway of apoptosis. Whether and how mutations in Lrrk2 may contribute to the formation of ROS, mitochondrial and/or UPS dysfunction is still elusive. However, changes in MAPK-linked signal transduction pathways may contribute to Lrrk2-linked pathophysiology. The biosynthesis of dopamine (DA) as well as its α -synuclein protofibrils induced leakage from vesicles generates a pool of free cytoplasmic DA whose inherent instability entails its oxidation into detrimental ROS. Free DA furthermore significantly stabilizes α -synuclein protofibrils and inactivates parkin. Besides the specific interaction of PD-associated proteins with mitochondria and the UPS, the normal aging process contributes to the functional decline of both systems. See text for further details. Activating and inhibiting effects are depicted by arrows or bars. Dashed arrows indicate protein translocation; PD-related genes are highlighted in colored boxes. MAPK: mitogen-activated protein kinase, PI3K: phosphoinositide 3-kinase, PTEN: phosphatase and tensin homolog. Adapted from (21, 59, 67, 75, 117, 127, 128).

2. Leucine-rich repeat kinase 2 (Lrrk2)

The latest gene found to be related to autosomal-dominant familial PD is *Lrrk2* (*leucine-rich repeat kinase 2*, PARK8). In 2002, the PARK8 locus was initially mapped to chromosome 12q12 in a large Japanese kindred (Sagamihara family) presenting with dominant inherited parkinsonism (129). Two years later, the gene corresponding to PARK8 was identified, encoding the protein Lrrk2 (130, 131).

2.1 Genetic aspects of Lrrk2-associated PD

Although mutations in *Lrrk2* have originally been linked to familial PD, they are also found in patients with sporadic PD and account for up to 10% of inherited and approximately 4% of idiopathic cases, thus being collectively the most common cause of the disease (5). To date, more than 80 missense variants within the *Lrrk2* locus have been described, scattering over the entire protein and affecting any of the predicted functional domains, but neither gene multiplications nor deletions, as reported for other PD-related genes, have been identified (132, 133). However, genetic evidence for pathogenicity of most of the mutations remains so far unclear and is yet definitely established for only five of them. Namely, the R1441C, R1441G, Y1699C, G2019S and I2020T are proven to segregate with the disease (134). Additionally, the R1441H substitution is assumed to be pathogenic (135). Thus, with three missense mutations the R1441 codon is considered as a mutational hotspot within *Lrrk2* (136). Moreover, two other mutations (R1628P and G2385R) have been reported as common susceptibility variants among the Asian population (134).

The various Lrrk2 mutations occur with different frequencies in different ethnic populations. The most frequent substitution, G2019S, was found in 85% of PD patients carrying a Lrrk2 mutation (137) and accounts for 1-7% of hereditary PD in the European and North American population or 1-2% of sporadic cases within the Caucasians (136). However, remarkably ethnic differences of the G2019S variant are observed. Being very rare (less than 0.1% (138)) or even absent (139) among Asian populations for instance, it shows an exceptionally high frequency in other populations, ranging from 16% in Portuguese and 20% in Ashkenazi Jews to 42% in North African Arabs (133). These differences are most likely due to a common founder effect for the majority of the mutation carriers, originating in the Middle East or North Africa (140, 141). In contrast, both the R1628P and G2385R mutation, which were not identified in Caucasian individuals, are assumed to be a risk factor in the Asian population and also the I2020T substitution was found with a higher prevalence in the latter one (133). Furthermore, the penetrance of Lrrk2 mutations is age-dependent and varies among the different variants. As such, individuals inheriting Lrrk2 G2019S have a PD risk of about 28% at age 59 which increases to 74% at age 79 (137), whereas R1441C carriers have an age-specific penetrance of >90% at age 75 (142).

2.2 Clinical and pathological implications of *Lrrk2* mutations

The majority of *Lrrk2* mutation carriers exhibit clinical symptoms that are indistinguishable from those of idiopathic PD patients, where individuals present with the characteristic cardinal features of asymmetric late-onset, bradykinesia, rigidity, tremor at rest and postural instability, although a more benign course of the disease has been assumed (137). In addition, some rare patients are reported to show atypical features, including amyotrophy and fasciculation, autonomic dysfunction or dementia, and even appear with different clinical phenotypes, e.g. corticobasal syndrome, progressive supranuclear gaze palsy (PSP) or dementia with tremor (143). The yet predominant analogy of symptoms to classic PD is not always associated with a uniform neuropathology. Postmortem analysis of diseased individuals proven to carry *Lrrk2* mutations revealed heterogeneous findings, depending somewhat on the causal mutation and can be different for the same mutation, even varying within the same family. Besides the collectively observed compulsory neuronal loss in the SNpc, the majority of cases present with a standard Lewy body pathology typical for classic PD. Pathological manifestations include, however, also ubiquitin-positive inclusions, tauopathies reminiscent of PSP or AD as well as “pure” nigral degeneration without Lewy body formation (reviewed in (143, 144)). This pleomorphic pathology suggests that *Lrrk2* might be central to different neurodegenerative pathways associated with parkinsonism, where mutations in the protein primarily lead to loss of DA neurons and secondarily to the accumulation of aberrant proteins. Of note, *Lrrk2* itself is generally not perceived to reside in Lewy bodies in affected brains (145), implicating that *Lrrk2* may contribute to the formation of the cytoplasmic inclusions, although it is no obligate component of them.

2.3 Cellular and subcellular localization

Numerous studies analyzing the expression of *Lrrk2* on mRNA as well as on protein level demonstrate its ubiquitous distribution comprising the central nervous system as well as peripheral organs like heart, liver, lung, spleen and kidney (133). Neuroanatomically, *Lrrk2* is detected throughout the rodent and human brain where it localizes to various structures but with interregional differences in expression levels (145-151). Moderate to high levels were consistently reported in neurons within the cortex, striatum, hippocampus and cerebellum. Although two studies describe an absence of *Lrrk2* in the SNpc (147, 149), numerous other proved a detectable expression in this region and in particular in nigral DA neurons (145, 146, 148, 151, 152). Additionally, the protein was found in other distinct neuronal populations of the nigrostriatal pathway and is thus distributed to anatomical brain regions being of direct relevance to PD-associated neuropathology (145, 146, 148).

Expression profiling during murine development and in adult mice revealed that *Lrrk2* mRNA was detectable as early as at embryonic day (E) 8.5 in non-neuronal and E10.5 in

neuronal tissues, respectively (153). The overall expression increased from E15 to E17 and remained constant throughout adulthood. Whereas the biggest increase in *Lrrk2* mRNA levels proceeded between E15.5 and E19.5 in lung and kidney, a gain of expression in the brain was only observed to a nominal extent at an earlier time point (between E11.5 and E15.5) (154). Thus, *Lrrk2* expression appears to increase during organogenesis and maturation, which suggests along with its neuroanatomical expression pattern in the neonatal brain and in extra-neural tissues that *Lrrk2* is involved in proliferation, migration and differentiation of neuronal cells or morphogenesis of non-neuronal cells (153, 154).

On the subcellular level, *Lrrk2* appears to be a predominantly cytoplasmic protein, with a significant fraction being associated with membranous structures. The endogenous protein displays a punctuated cytoplasmic distribution pattern and was found to be associated with cytoskeletal as well as intracytoplasmic vesicular or membranous structures (146, 155). As such, *Lrrk2* was localized at Golgi- and microtubule-associated transport vesicles, mitochondria, lysosomal and endosomal vesicles, Golgi apparatus or ER, with a similar pattern observed by overexpression of the protein in cell lines (146, 155-157). Consistently, subcellular fractionation experiments on either rat brain tissue or cell lines with transient *Lrrk2* expression demonstrated a significant enrichment of *Lrrk2* in membrane-containing or -associated fractions (146, 156, 157). According to the lack of an obvious transmembrane domain (157), *Lrrk2* is not an integral membrane protein. Its association to lipid-based structures appears on their cytosolic side, such as the localization of *Lrrk2* to the outer mitochondrial membrane (146, 157). Furthermore, *Lrrk2* seems to be connected to lipid rafts and other membrane microdomains such as caveolae, microvilli/filopodia, intraluminal vesicles of multivesicular bodies (155, 158), which play an important role in various cellular processes, including signal transduction, cytoskeletal organization and membrane trafficking (159-161). *Lrrk2* may thus play a role in the biogenesis and/or regulation of vesicular structures, vesicular transport as well as membrane and protein turnover (128).

2.4 Structure and enzymatic activity

2.4.1 *Lrrk2* multidomain structure

The genomic region spanned by the *Lrrk2* gene encompasses approximately 144 kb, with an open reading frame (ORF) of 7581 bp in 51 exons (136). It encodes a large multidomain protein of 2527 amino acids with a molecular weight of about ~286 kDa belonging to the ROCO protein superfamily (162-164). As such, it comprises a characteristic combination of a ROC (Ras of complex protein) domain adjacent to a COR (C-terminal of ROC) domain (162), immediately followed by a kinase domain (mitogen-activated protein kinase (MAPK) kinase kinase; MAPKKK). This putative enzymatic region is flanked by several protein interaction domains (164) (Figure 4), each containing multiple sets of internal repeats that are predicted to adopt distinct configurations. Here, the 14 evolutionary

conserved repeats in the N-terminal region of Lrrk2, which are unique to this protein and absent from other Lrrk proteins such as Lrrk1, are predicted to constitute an Armadillo-like helical domain (165). Both the Lrrk2-specific and Armadillo repeats contain multiple hydrophobic residues in similar positions. The latter are one among other repeat structures that are able to form long alpha-helical structures (Armadillo-like helical domains) providing a structural interface for protein interactions (165, 166). Notion of the existence of ankyrin repeats following the Armadillo-like helical domain is controversial. Although some authors indicate the existence of such a domain (157, 164), this prediction could not be affirmed by domain searches (163). Nevertheless, ankyrin repeats are found in a wide range of eukaryotic, bacterial and viral proteins, including cytoskeletal proteins, transcription factors and developmental regulators, where they accomplish the interaction to a variety of protein classes (167). Preceding the ROC-COR-kinase motif, seven to eight leucine-rich repeats (LRRs) have been identified (163). LRR domains are known to mediate interactions with several different proteins and LRR-containing proteins are thus involved in many cellular processes, such as enzyme inhibition, cellular trafficking, signal transduction, neuronal differentiation and regulation of cytoskeletal morphology and dynamics (168). The last repeat domain associated with protein interactions within Lrrk2, the WD40 repeats, is located at the C-terminus and is predicted to encompass seven repeats (164). WD40 domains represent the most common repeat domains detected in human proteins and possess a highly symmetrical conformation, a structure that is also referred to as β -propeller (169). The donut-shaped structure of the domains exposes three surfaces, the upper, the lower and the circumference, that provide the platform for protein interactions, even simultaneous ones, with different proteins. Therefore, a common function of proteins belonging to the WD40 repeat family is the coordination of multiprotein complex assemblies, with the domain acting as a scaffold (169). As such, these proteins possess diversified functions, including signal transduction, cytoskeletal assembly and vesicular trafficking (169).

Besides the above described protein binding domains, Lrrk2 contains a putative “enzymatic core” that is comprised of a kinase domain and the ROC-COR motif. Based on sequence similarity, the kinase domain of Lrrk2 belongs to the MAPKKK proteins. It shares closest homology with their subclass of mixed-lineage kinases (MLKs) (157, 170), which pertain to the larger tyrosine kinase-like subfamily (TKL) of human protein kinases (171). Although members of this family resemble both serine/threonine and tyrosine kinases, the activity of all of them is, however, directed against serine and/or threonine residues but not tyrosine residues (172), which is also applicable to Lrrk2 (170, 173-175). MLKs control and participate in MAPK pathways, three-tiered kinase cascades where each kinase activates the successive one by phosphorylation. This leads to the activation of an effector kinase, which ultimately results in the phosphorylation of various proteins, including transcription factors and cytoskeletal proteins. MAPK pathways thus exhibit a great influence on many cellular

processes, e.g. gene expression, cell division, morphology, and survival (176). However, Lrrk2 exhibits some subdomain characteristics that delineate the protein from MLKs and other MAPKKs (157, 172).

The GTPase domain of proteins belonging to the ROCO family, ROC, appears as a separated monophyletic group of the Ras superfamily of small GTPases, showing closest homology to members of the Rab family (162, 163). Like other regulatory GTPases, Rab GTPases act as molecular switches that cycle between a GTP- (active) and GDP-bound (inactive) conformation, aided by guanine exchange factors (GEFs; conversion from GDP- to GTP-bound state through nucleotide exchange) and GTPase-activating proteins (GAPs; conversion from GTP- to GDP-bound state by hydrolysis) (177). In their inactive state, Rab GTPases are localized at the cytoplasmic face of intracellular membranes and function upon activation as regulators of distinct trafficking pathways. Following the recruitment of specific effector molecules, Rab GTPases regulate vesicle formation, actin- and tubulin-dependent vesicular transport and membrane fusion (177).

The COR domain is yet of unknown function and does not resemble any other described protein or domain. As such, it is currently regarded as a linker between the two putative catalytic domains, the GTPase and kinase domain (162).

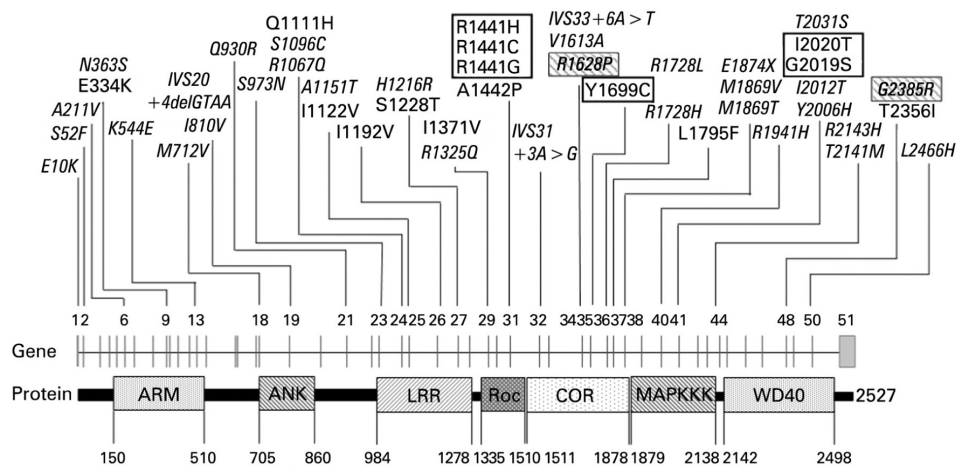


Figure 4: Lrrk2 multidomain structure.

Schematic representation of the predicted Lrrk2 domain structure and a subset of described variants. The protein comprises 2527 amino acids and contains, from N-terminal to C-terminal, several conserved domains: armadillo repeats (ARM), ankyrin-like repeats (ANK), leucine-rich repeats (LRR), Ras of complex protein (ROC), C-terminal of ROC (COR), mitogen-activated protein kinase kinase kinase (MAPKKK) and WD40. Numbers beneath the protein line indicate the amino acid residues of the estimated domain boundaries, those above the gene line the number of the variant-carrying exon. Mutations that have recurrently been proven to be pathogenic are shown in bold and boxed and those acting as risk factors are highlighted in italics and hatched boxes. Amino acid substitutions that are assumed to be putatively pathogenic, as they cosegregate with PD, are depicted in bold. Variants found in rare, single cases and therefore of unknown significance are outlined in italics. Adapted by permission from BMJ Publishing Group Limited (178). © 2009.

2.4.2 Dual enzymatic properties of Lrrk2

Lrrk2 and its paralog Lrrk1 are the only proteins presently known in the mammalian proteome that combine GTPase as well as kinase activity in one molecule, with both activities commonly holding an important role in the regulation of cellular processes. As such, several groups studied the enzymatic properties of Lrrk2 and the effects of PD-associated mutations.

2.4.2.1 Kinase activity of Lrrk2

Assessment of the kinase activity of Lrrk2 was so far focused on its ability to autophosphorylate or to phosphorylate generic substrates by *in vitro* kinase assays using the full-length recombinant protein (156, 157, 170, 179), as authentic substrates are not yet convincingly characterized (180). The protein possesses only a modest kinase activity *in vitro* compared to other MAPKKKs (181), suggested to be caused by the absence of proper cofactors, lack of an appropriate stimulus or proper protein folding under the assay condition (164). The studies, however, revealed that Lrrk2 is a functional kinase, considered to be efficient in comparison to other kinases within similar molecular weight ranges (180). Interestingly, Lrrk2 purified from transgenic mouse brains exhibits kinase activity, which was elevated in comparison with that from other transgenic organs or transfected cultured cells (182). Moreover, autophosphorylation activity of Lrrk2 was shown to target serine and threonine but not tyrosine residues, suggesting that the protein is, similar to MLK proteins, a true serine/threonine kinase (170, 173-175).

Discrepancy exists regarding the effect of PD-associated mutations on Lrrk2's kinase activity. Only the G2019S mutation, which is located within the conserved activation segment in the MAPKKK domain, was consistently shown to significantly increase the kinase activity compared to the wt protein in all related studies (183). In contrast, inconsistent effects were observed for the I2020T adjacent to G2019, where some studies reported a moderate but significant increase (156, 170, 184), while others described no effect (185, 186) or even a slight decrease (187). Conflicting results likewise exist for mutations outside the kinase domain that were either found to enhance the kinase activity up to 2.5-fold or to exert only minor effects as well as to inhibit the enzymatic activity (183). However, the studies differ in the expression systems, substrates, tags, construct length and assay methodology utilized which might contribute to the ambiguous results obtained (180, 188).

The mechanistic and/or structural mode of action by which the common G2019S substitution causes the universally reported activation of Lrrk2 kinase activity is postulated to be the conversion of the MAPKKK domain in a constitutively active state, keeping the catalytic side open. The glycine to serine exchange at residue 2019 significantly perturbs the local structure of the activation segment as revealed by structural analysis based on homology modeling (181). In contrast, the insertion of a threonine residue at I2020 has no

obvious effect on the predicted backbone structure of the kinase domain, correlating with the findings on the enzymatic activity of these mutants (181).

From *in vitro* studies using various cell lines as well as primary neuronal cultures, the kinase activity of Lrrk2 was suggested to contribute to the toxic effects of PD-associated protein variants (170, 179, 189, 190). Overexpression of both wt and mutant Lrrk2 (R1441C, Y1699C, G2019S, and I2020T) promoted cellular toxicity and cell death, but the latter exhibited a more pronounced effect on cell viability. Moreover, the mutants potentiated hydrogen peroxide (H₂O₂)-induced toxicity compared to the wt protein, which exhibited a protective effect (170, 190, 191). In contrast, expression of mutant Lrrk2 deficient in kinase activity (“kinase-dead”) was innocuous (170, 179, 189, 190).

2.4.2.2 GTPase activity of Lrrk2

The ROC motif of Lrrk2 was identified as an authentic and functional GTPase, able to bind (170, 179, 182, 192-194) and intrinsically hydrolyze (182, 192, 194) GTP *in vitro*. Displacement of GTP binding *in vitro* is only facilitated by competition with free GTP, GDP or the non-hydrolyzable analog GTP γ S but not by other related nucleotides (170, 179, 193), thus indicating that Lrrk2 is a *bona fide* GTPase. However, Lrrk2 displays only a poor ability to convert GTP to GDP *in vitro* (182, 192-194), which might be related to the absence of suitable GEFs or GAPs required for an efficient hydrolysis activity (170). Only recently, Häbig et al. described ARHGEF7 (Rho guanine nucleotide exchange factor 7) as a potential GEF for Lrrk2 *in vitro* (195). Given that a number of key residues that are essential for a robust GTPase activity are not well conserved in Lrrk2, it might also possess an intrinsically low rate of GTP hydrolysis (193). Concordantly, conversion of the Lrrk2 GTPase domain to a Ras-like form restored an adequate GTPase activity (193). Of note, Lrrk2 purified from transgenic mice brains also showed both GTP binding and hydrolysis activity, which exceeded those observed for the protein obtained from other transgenic tissues or cell lines (182).

The PD-linked mutations R1441C and R1441G within the ROC domain decreased the rate of GTP hydrolysis compared to the wt protein (182, 192, 194) but did not affect binding of GTP in the majority of studies (182, 192, 194), though one group observed elevated steady-state levels of GTP-bound Lrrk2 (170). Likewise, the Y1699C variant, situated in the COR domain, exhibited an increased binding of GTP (170) and is suggested to reduce GTPase activity (196). In contrast, mutations located in or adjacent to the kinase domain did not alter GTP binding (170), with their effects on GTP hydrolysis yet unknown. An increased amount of GTP-bound Lrrk2 at steady state might, however, be indicative for an impaired GTP hydrolysis. A decreased rate of GTP to GDP conversion is suggested to keep the associated variants (e.g. R1441C and R1441G) in a constitutively GTP-bound and thus active state (182, 192, 194).

As Lrrk2 is a modular protein containing both a GTPase and MAPKKK domain, it was

early on suggested that activation of the protein's kinase occurs in an intrinsic, GTPase-dependent fashion analogous to the hierarchically intermolecular mechanism exerted by small GTPases in controlling the activation of numerous cellular MAPK signaling pathways (162). Indeed, an intact GTPase activity was found to be critically required for Lrrk2 kinase activity, whereas reciprocally the GTPase activity functioned independent of the kinase domain (170, 179, 182, 192, 193). Moreover, Lrrk2's kinase activity was found as markedly increased *in vitro* by treatment with the non-hydrolyzable GTP analogs that presumably keep the protein in a GTP-bound active state (170, 179, 182, 193). Under *in vitro* cell culture conditions, transient expression of Lrrk2 "GTPase-dead" variants were equally well tolerated by cells like kinase-dead forms of the protein, lacking cell death and increased toxicity under H₂O₂-induced oxidative stress observed for the PD-associated mutants (see 2.4.2.1). This might be further indicative for the regulation of Lrrk2's kinase activity by its GTPase (170, 179, 189, 190). The observation that Lrrk2 forms a dimer (156, 197-199) led to the suggestion that the enzymatic domains within the protein form a self-regulatory module, defining the specificity and activity of the protein's own kinase domain (128, 180). The model hypothesizes that the dimerization of ROC or ROC-COR in the GTP-bound conformation entails an intermolecular interaction of the kinase domains, subsequently allowing autophosphorylation and activation of downstream kinase activity (196, 197, 200). Recent evidence exists for an autoregulation of Lrrk2 activity by autophosphorylation as known to exist for other kinases (173-175). The GTPase domain was observed to be a major cluster for autophosphorylation, with residues in close proximity to the GTP binding pocket including some within the guanine nucleotide phosphate-binding loop (P-loop) of ROC being targeted (173). This might be indicative for a kinase activity directed towards the GTPase domain and thereby modulating its activity. Mutations in the kinase domain that augment its catalytic activity (e.g. G2019S) may thus decrease GTPase activity by enhanced phosphorylation of the ROC domain and would be functional similar to R1441 mutations that have been shown to exhibit a decreased inherent GTPase activity (174). Regulation of small GTPases by phosphorylation of their corresponding kinases has previously been reported (201), but clearly further research is needed to assess the potential cross-regulatory mechanism of Lrrk2's GTPase and kinase activity.

2.5 Lrrk2 substrates, interactors and related signaling cascades

2.5.1 Kinase substrates

If the kinase activity of Lrrk2 is the critical component by which the protein exerts its cellular function and is linked to neurodegeneration in PD, the identification of its physiological substrates is crucial for the understanding of the biochemical and functional role of Lrrk2 and will ultimately help to clarify the pathological dysfunction in Lrrk2-linked PD. Numerous studies attempted to determine potential substrate proteins. Given the large size

of the Lrrk2 protein and its sparse homology to other characterized kinases, the tedious *de novo* identification of candidate substrates gets, however, further complicated and thus little is known about the physiological substrates of Lrrk2.

The cytoskeletal protein moesin was nominated as a putative target of Lrrk2-mediated phosphorylation (187). It belongs to the ERM (ezrin/radixin/moesin) family of proteins that link filamentous (F-) actin to the plasma membrane and are hence essential for many vital cellular processes, including neurite outgrowth (202, 203). Moesin was efficiently phosphorylated by the Lrrk2-G2019S variant at T558, which is known to be a physiologically relevant phosphorylation site, as it is involved in the modulation of moesin activation allowing binding to F-actin (202, 203). Lrrk2 was also found to phosphorylate ezrin and radixin at a residue equivalent to T588 in moesin (187). However, only denatured moesin served as a substrate for Lrrk2 *in vitro* and the proposed phosphorylation site on moesin, T558, is known to be efficiently phosphorylated by other kinases without denaturation (202). Hence, additional studies are required to confirm the physiological relevance. Nevertheless, it has been shown that the G2019S mutant of Lrrk2 increases the number of phosphorylated ERM (pERM)-positive filopodia in cultured neurons from transgenic mice. Additionally, a perturbed homeostasis of pERM and F-actin was observed in G2019S filopodia, suggesting that Lrrk2 is involved in the remodeling of F-actin through its modulation of ERM activities (204).

The eukaryotic initiation factor 4E-binding protein (4E-BP) was also efficiently phosphorylated *in vitro* by both the *Drosophila* paralogue dLrrk and human Lrrk2 (184). The unphosphorylated 4E-BP protein functions as a repressor of protein translation and is regulated by phosphorylation (205). Its phosphorylation through Lrrk2 at established sites of physiological relevance (T37/T46) is proposed to act as a stimulus for its phosphorylation by other kinases at secondary residues, thereby promoting the initiation of mRNA translation (184, 205). Whether Lrrk2 affects the biological function of 4E-BP as a mediator of responses to various stress stimuli, including oxidative stress (206-208), remains to be elucidated. While the Lrrk2-mediated phosphorylation of 4E-BP was confirmed *in vitro*, with the pathogenic mutants displaying an increased activity, Lrrk2 autophosphorylation was shown to be more efficient than 4E-BP phosphorylation by the wt protein under the respective assay conditions (209). Moreover, controversial findings were reported regarding the 4E-BP-phosphorylation in the cellular context where pT37/pT46 levels were found to be increased following the expression of Lrrk2 (wt or mutant) (184) or not to be altered in contrast to other kinases tested (MAPK14/p38 α) (209). The residues T37/T46 are known to be targeted by other kinases (205) as shown for MAPK14/p38 α (209) and indicated by the finding that RNA interference (RNAi)-mediated knockdown of Lrrk2 in cells does not completely abolish 4E-BP phosphorylation (184). It is therefore suggested that the impact of Lrrk2 on the phosphorylation of 4E-BP observed in some systems (184) might be related to p38-mediated cell stress pathways, possibly triggered by Lrrk2, rather than to a direct function of the protein

in stress resistance and neuronal maintenance (209).

The close sequence homology of Lrrk2 with MLKs, a subgroup of MAPKKK, that act upstream of canonical MAPKKs implicates a possible function of Lrrk2 within the MAPK cascade. *In vitro*, Lrrk2 was indeed shown to phosphorylate the highly homologous MAPKKs 3 and 6 (MKK3/6) as well as MKK4/7 that are known MAPKKK substrates and involved in cellular stress responses by activation of the MAPK p38 and c-Jun N-terminal kinase (JNK), respectively (181, 210). Here, PD-associated Lrrk2 variants displayed an increased activity towards MKK phosphorylation compared to the wt protein. Although MKKs act as substrates of Lrrk2 *in vitro*, its overexpression is not accompanied by an detectable increase in cellular phospho-JNK or phospho-p38 levels, indicating that the phosphorylation of MKKs does not occur with high efficiency within cells or arises in a locally restricted fashion that is not detectable in the overall cellular level (170, 172, 181, 210). Specificity of MAPK cascades is known to be achieved, at least in part, by the organization of MAPK modules, where scaffolding or anchoring proteins coordinate the assembly of appropriate kinases to signaling complexes for selective activation, sequestration and localization (211). Indeed, experimental evidence exists that indicates a role of Lrrk2 as part of a protein complex facilitating the localization of MKK/MAPK proteins to sites of stress (see 2.5.2) (210, 212, 213).

Lrrk2 was shown to crosstalk with the extracellular signal-regulated kinases 1 and 2 (ERK1/2) pathway where it may act as signal transducing kinase. Though specific substrates within the pathway are unidentified, this is consistent with both the sequence homology of Lrrk2 to MAPKKKs and its interaction with MKKs (see 2.5.2) (190, 191). ERK1/2 can function as a pro-survival factor as well as in a pro-apoptotic manner in response to oxidative stress (190, 214). Whether activation of the ERK1/2 pathway can be employed by wt Lrrk2 to confer a protective function against H₂O₂-induced toxicity or by the mutants to trigger cell death was conflictingly reported (190, 191).

Indications for a microtubule-linked function of Lrrk2 came from a study of Gillardon that assumes the stabilization of microtubules by phosphorylation of β -tubulin as one biological function of Lrrk2. Decreased dynamic properties of microtubules as observed for the Lrrk2 G2019S mutation may interfere with neuronal function and survival, which require the maintenance of tightly regulated microtubule dynamics within a physiological range (215).

2.5.2 Interaction partners

Besides the potential enzymatic activity of Lrrk2, protein-protein interactions (PPIs) may be likewise relevant to the physiological and pathological function of Lrrk2, given that Lrrk2 comprises a number of domains whose properties are linked to the formation of signaling complexes. Much effort has been spent to identify proteins acting as binding partners by using yeast two-hybrid (Y2H), protein pull-down, coimmunoprecipitation (co-IP) and mass spectrometry (MS) methodologies. Several interactions through a number of

domains, harboring also mutations that segregate with the disease, have been isolated whose biological relevance, however, requires further validation.

Consistent with the suggestion that Lrrk2 function is related to stress kinase signaling cascades (see 2.5.1) it has been shown that Lrrk2 is not only capable to phosphorylate MKKs but also to interact with MKK3/6 and MKK7 (210) as well as with a family of scaffolding proteins (JNK-interacting proteins (JIPs)) (213). They play an important role in the modulation of MAPK signaling cascades, with JIP1-3 regulating the specificity and localization of the JNK pathway and JIP4 of the p38 pathway (212, 213). Lrrk2 binds to JIP1-4 (213) and appears to affect, moreover, the localization of MKKs as co-overexpression of Lrrk2 with MKK6 increased the membrane association of MKK6 (213).

Whether Lrrk2 interacts with other proteins associated with familial PD and affects their function is of great interest. While Lrrk2 can specifically interact with parkin through the COR domain, it is not capable to bind to other PD-related proteins (e.g. DJ-1 or α -synuclein) (216). However, Lrrk2 does not serve as a substrate for parkin-mediated ubiquitination and proteasomal degradation (216). Although not ubiquitinated by parkin, the proper degradation of Lrrk2 was shown as mediated by the proteasomal rather than the lysosomal pathway (217-219). As such, the molecular chaperone heat shock protein (Hsp) 90 and its cochaperone p50^{cdc37}, specifically recruiting distinct protein kinase client proteins to the Hsp90 system (220), were found to associate with Lrrk2 *in vitro* and *in vivo* through its kinase domain (156, 217-219, 221). Being part of a multichaperone system, Hsp90 is involved in the proper folding, stabilization and activation of its client proteins, including various signaling proteins such as protein kinases (220). Although Hsp90 and its isoforms have been described to interact frequently with almost all proteins overexpressed in mammalian cells (172), several lines of evidence support a physiological relevance of the interaction with Lrrk2. Activity of the Hsp90 chaperone system appeared to stabilize Lrrk2, like other Hsp90 client proteins, against proteasome-mediated degradation and thus to be a crucial element in maintaining cellular Lrrk2 levels. Blocking Hsp90 activity was, moreover, shown to disrupt the interaction between Lrrk2 and Hsp90 as well as p50^{cdc37}, which might promote the interaction with other chaperone proteins linked to proteasomal degradation pathways (217, 219). An interaction of Lrrk2 and the Hsp70-interacting protein (CHIP) was demonstrated (217, 218), which functions as both cochaperone, interacting with the chaperones Hsp70 and Hsp90, and E3 ubiquitin ligase. It is thus crucial for the ubiquitination of several Hsp70/Hsp90 client proteins and serves as a molecular link between chaperone systems and protein degradation (222). Overexpression of CHIP was found to promote ubiquitination of Lrrk2, causing the latter to be degraded in a proteasome-dependent manner (217, 218). Moreover, wt and mutant Lrrk2 were degraded in a similar extent that prevents cellular toxicity of the PD-associated variants, indicating that it is not their diminished CHIP-mediated degradation that is pathogenic in Lrrk2-linked PD (217). The CHIP-mediated destabilization of Lrrk2 could,

however, be attenuated by co-overexpression of Hsp90 (217). In summary, the results suggest that the steady-state levels of Lrrk2 may be balanced by CHIP and the Hsp90 chaperone system, whose perturbation in the course of aging may interfere with a proper turnover of Lrrk2 (217, 218).

Lrrk2 was also reported to interact in a kinase-sensitive manner with the Fas-associated protein with death domain (FADD), a key death adaptor protein critical for the activation of the extrinsic pathway of apoptosis (223, 224). FADD transduces death signals by associating with the ligand-activated transmembrane death receptor, leading to the formation of the death-inducing signaling complex (DISC), which recruits and activates caspase-8 (224). PD-linked mutations increase the interaction of Lrrk2 and FADD but not with the tumor necrosis factor receptor-1-associated death domain protein (TRADD) and receptor-interacting serine/threonine kinase-1 (RIP1), the only death domain-containing proteins transducing extrinsic cell death signals that were additionally found to interact with Lrrk2 (223). It was thus suggested that Lrrk2 plays a role in the extrinsic apoptosis pathway which is activated by disease-triggering mutations that enhance the interaction between Lrrk2 and FADD, hence causing the recruitment and activation of caspase-8. Postmortem analyses of brain tissue from PD-patients bearing Lrrk2 mutations supported this notion, as they revealed increased levels of activated caspase-8 (223). Nevertheless, mutant Lrrk2-induced cell death has also been linked to mitochondria-dependent apoptosis (225). In conjunction with the assumed localization of Lrrk2 at mitochondrial membranes, mitochondrial dysfunction and related apoptotic pathways may underlie Lrrk2-induced toxicity, although the mechanisms in between overexpression and caspase activation are unknown. Lrrk2-dependent cell death may thus involve receptor-mediated apoptosis that can cause caspase activation in a mitochondria-dependent or –independent manner (226).

The described interaction of Lrrk2 with the dishevelled (Dvl) family of phosphoproteins (Dvl1-3) through the ROC-COR tandem domain links Lrrk2 to the Wingless/Int (Wnt) signaling pathway and suggests a further pathogenic pathway (227). Dvl1-3 constitute key regulators of the Wnt pathway, leading to multiple downstream effects, including the activation of small GTPases of structural similarity to the Lrrk2 ROC domain, and are important for several critical processes in neuronal development (227). PD-segregating mutations in the ROC or COR domain were shown to disrupt (Y1699C) or to strengthen (R1441C/G/H and R1728H/L) Dvl-Lrrk2 interactions. It has been suggested that the interaction with Dvls stabilizes the ROC-COR dimer which would according to the supposed model for Lrrk2 GTPase activity (see 2.4.2.2) positively affect the enzymatic activity of Lrrk2. Depending on the specific effects of ROC-COR mutations on the Lrrk2/Dvl-complex, the GTPase and kinase activity is either reduced or enhanced, implicating that aberrant levels of Lrrk2 activity might be involved in pathogenic mechanisms in Lrrk2-linked PD (227).

The LRR domain of Lrrk2 was described to interact with the small GTPase Rab5b that

is essential in synaptic endocytosis and microtubular-dependent vesicle transport (228, 229). Alterations in the expression level of wt Lrrk2 through knockdown or overexpression, but not the expression of mutant Lrrk2, significantly impaired synaptic vesicle endocytosis *in vitro*, which could be rescued by the co-overexpression of constitutive active Rab5b. In conjunction with the subcellular localization of Lrrk2 to membranous structures such as synaptic vesicles (see 2.3) and the protein's presence in the synaptosomes of neurites, a role of Lrrk2 in the regulation of synaptic vesicle endocytosis by its interaction with Rab5b was suggested (229). Moreover, Lrrk2 has been linked to microtubules by its interaction with α/β -tubulin mediated through the ROC domain (215, 230) and thus to a dynamic network that is critical for neuronal function, maintenance and survival (231, 232). Considering Lrrk2 found to colocalize with β -tubulin, Golgi transport vesicles, endosomes, lysosomes, and mitochondria previously (146) as well as its potential role in vesicle endocytosis, Lrrk2 might be involved in vesicular and/or microtubule-dependent transport (230). Although the R1441C substitution within the ROC domain retained the interaction, mutations may yet disrupt the microtubule-related function (230). Additionally, Lrrk2 was demonstrated to constrain microtubule assembly/stability mediated by elongation factor 1-alpha (EF1A), which was shown to regulate bundling as well as stabilization of microtubules (233). Here, Lrrk2 was assumed to impair microtubule assembly by EF1A through its binding/sequestering, but the effect of PD-linked mutations located within protein interaction domains of Lrrk2 on the association remains unknown. Furthermore, the interaction of EF1A and Lrrk2 appeared to reciprocally regulate their respective physiological function (233).

Recently, an interaction of Lrrk2 with 14-3-3 isoforms was demonstrated that appeared to be dependent on the phosphorylation of Lrrk2 at two conserved residues (S910 and S935) (234). 14-3-3 proteins form homo- or heterodimers that exert a widespread influence on diverse cellular processes by binding to phospho-serine/-threonine residues of proteins involved in transcription, biosynthesis, apoptotic signaling and cytoskeletal dynamics. Here, they operate by protecting regulatory sites of their target proteins from dephosphorylation or modulating dimer or multiprotein complex formation (235). The study of Nichols and colleagues suggests that the 14-3-3 binding may stabilize Lrrk2 and that its interferences by different Lrrk2 mutations might constitute a pathogenic output.

Although the Lrrk2-interacting proteins identified by the individual studies differ from each other, common themes regarding the associated biological processes are emerging, which were also reported in the study of Dachsel and colleagues (221). Combining immunoprecipitation (IP) of overexpressed Lrrk2 and tandem MS they identified several potent Lrrk2 binding partners that were grouped into three functional cellular pathways, found recurrently in the different studies: cytoskeleton and trafficking, chaperone system and kinase signaling. Yet, there is no knowledge which pathway is specifically perturbed as a consequence of Lrrk2 mutations.

3. The actin cytoskeleton

The physical integrity as well as numerous fundamental processes of an eukaryotic cell are largely dependent on the cytoskeleton, a framework of distinct, yet interconnected, cytosolic filaments composed of three types of protein fibers: actin (micro-) filaments (MFs or F-actin), microtubules (MTs) and intermediate filaments. Based on its highly dynamic properties, the cytoskeleton is modulated by various internal and external cues to adapt to demands on the cell and hence to execute its function in vital mechanisms critical to the development and function of a multicellular organism. Actin filamentous superstructures are essential for a wide variety of cell properties and function in the generation and maintenance of cell morphology and polarity, participate in endocytosis and intracellular trafficking, in cell division, contractility and motility, including neuronal outgrowth (236).

3.1 Actin dynamics

Actin is a highly conserved protein in eukaryotes, yet at least six different, functionally specialized and tissue-specific isoforms are known to be expressed: two smooth muscle actins (α -smooth and γ -smooth), two striated muscle actins (α -skeletal and α -cardiac) and two cytoplasmic actins (β -cytoplasmic and γ -cytoplasmic) (237). Actin monomers (globular (G-) actin) possess a high-affinity binding site for divalent cations (Mg^{2+} or Ca^{2+}) and nucleotides (ATP or ADP), whose complex stabilizes the molecule structure of G-actin (238, 239). Under physiological salt conditions, G-actin polymerizes into double-stranded, helical filaments (F-actin) by non-covalent head-to-tail assembly of the protomers, conferring structural polarity to the polymer with a so called barbed and pointed end (239). The polymerization principally proceeds in two phases, whose mechanisms were predominantly studied *in vitro*. Filament formation is initiated by self-association of actin monomers into trimer complexes (nucleation) that act as nuclei for further elongation. Due to the instability of the oligomers, this process is energetically unfavorable and represents the rate-limiting step (238). The following process of filament elongation involves the association as well as dissociation of monomers, with their rates at either filament end dependent on the concentration of available G-actin. Net polymerization proceeds when the monomer concentration exceeds the critical concentration (C_c) of the filament end - referring to the G-actin concentration where the rate of subunit addition to the end equals the rate of subunit dissociation at the same end – and net depolymerization when it falls below the C_c (238). In principle, association and dissociation of monomers can occur at either end. However, F-actin is asymmetric and the two extremities possess different kinetic characteristics. Due to the ATPase activity of actin, the polymerization of ATP-G-actin is accompanied by the irreversible hydrolysis of ATP to tightly bound ADP and inorganic phosphate (P_i). As nucleotide hydrolysis is uncoupled from polymerization, thus lagging behind the assembly of G-actin onto the filament end, and the rate of P_i release is slower than the hydrolysis, actin

filaments are heterogeneous in the relative content of ATP-actin, ADP-P_i-actin and ADP-actin subunits. The hydrolysis of ATP is, however, not random but occurs primarily at the barbed end of the filament, creating a serial arrangement of the different monomer species. The barbed end comprises ATP-bound monomers, followed by ADP-P_i intermediates and the pointed end is composed of ADP-bound subunits, with the distribution between the different G-actin species depending on the polymerization rate (240). The molecular polarity and irreversible nucleotide hydrolysis has implications for the rate and direction of filament growth (241). At steady state, where the monomer concentration falls between the C_cs of the two ends, barbed (“+”; fast growing) ends undergo constant ATP-G-actin association, whereas ADP-actin monomers dissociate from the pointed (“-“, slow growing) end at the same rate. Upon release from the filament, ATP is exchanged for ADP on the monomer, which can subsequently be added to the barbed end. The resulting continual steady-state flux of actin subunits through the filament from the barbed to the pointed end, referred to as treadmilling, gives rise to an unidirectional growth of the filament and represents the underlying principle that drives cellular motile events (239, 242).

3.2 Regulation of actin cytoskeleton dynamics: Actin-binding proteins (ABPs)

The treadmilling rate of monomeric actin under physiological conditions *in vitro* is very slow, as the rate limiting step of the process is the slow dissociation of monomers from the pointed end. With a growth rate of ~0.04 μm/min it is ~200-fold slower than observed *in vivo* (239). Thus, for treadmilling being the driving force for actin-based cellular processes, its intrinsic rate has to be increased. Moreover, the multiplicity of actin-related functions depends on distinct F-actin structures, each possessing unique and functionally significant biophysical and biochemical properties. The proper assembly and disassembly of actin filaments and their organization in structural higher-order networks is regulated by a plethora of actin-binding proteins (ABPs). Performing specific recognition and/or catalytic yet coordinated functions and serving as a target for various signaling pathways emanating from extracellular stimuli, they are essential to the coordination of dynamic actin mechanisms (239, 243). According to their function in the regulation of actin cytoskeleton dynamics, ABPs can be classified into seven main groups: (I) Monomer binders, proteins that bind to ADP- or ATP-actin, sequestering them and facilitating or preventing their polymerization. (II) Filament stabilizing proteins that laterally bind F-actin and prevent its depolymerization. (III) Proteins binding to the filament ends, thereby capping F-actin and avoiding the exchange of monomers either at the barbed or the pointed end. (IV) Proteins cross-linking actin filaments, thereby mediating the formation of filament bundles or nucleating branched filaments or three-dimensional networks. (V) Severing proteins that bind to the side of the filament and shorten its average length by splitting it into pieces. (VI) Filament depolymerizing proteins facilitate the transition of F-actin to G-actin. (VII) Motor proteins that use actin filaments as

tracks along which they move. Many ABPs are, however, not limited to one specific function and conversely, some of the proteins are not covered by the categorization (236, 239, 243). Figure 5 provides some examples of ABPs and illustrates their categorization corresponding to the proteins' function in non-muscular cells.

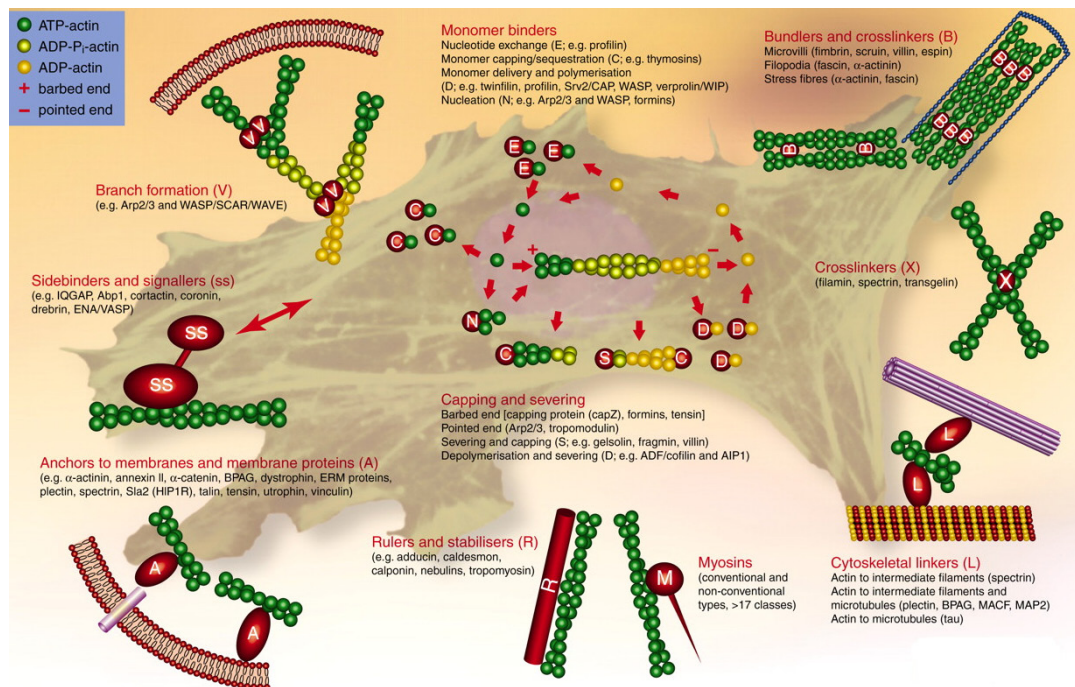


Figure 5: Actin-binding proteins.

The dynamic assembly of actin filaments and their spatial organization *in vivo* is controlled by a variety of actin-binding proteins (ABPs). F-actin assembly and disassembly (center) is regulated by proteins that bind either to G-actin to promote nucleotide exchange (E), nucleation (N), capping/sequestration (C), monomer delivery or polymerization (D), or to actin filaments and facilitate depolymerization and monomer sequestering (D), severing and capping (S) or capping of the barbed or pointed end (C). Depolymerization of filaments is prevented by rulers and stabilizers (R). Proteins engaged in branch formation (V), cross-linking (X), and bundling (B) mediate the assembly of filaments into two- or three-dimensional networks. Sidebinders and signalers (ss) act as linkers between signaling pathways that emanate from extracellular stimuli and the cytoskeleton. The nature of the actin cytoskeleton to function as a cellular scaffold involves proteins acting as anchors to membranes and membrane proteins (A), linkers to other cytoskeleton components (L) or using it as tracks (M). Reproduced with permission from The Company of Biologists Ltd: *Journal of Cell Science* (236). © 2005.

The size, localization and dynamics of the cytoplasmic monomer pool are of fundamental importance for the rapid reorganization and elongation of actin filaments in response to various stimuli that is thus subjected to a tight regulation at multiple levels. As such, ABPs can increase the dissociation of ADP-G-actin from the pointed end of the filaments, thereby providing a pool of monomeric actin available for polymerization at the barbed end. Prior to the entrance of the newly depolymerized monomers in a new round of polymerization, actin-monomer binding proteins mediate the recycling and conversion into ATP-bound G-actin. They deliver furthermore ATP-G-actin to the filaments' barbed ends and thus promote their elongation. Conversely, other actin-monomer binding proteins block the nucleotide exchange and prevent the assembly of actin monomers, thus generating a pool of actin, which cannot be polymerized. Such ABPs may contribute to actin dynamics as they sequester a proportion of G-actin in its "inactive", ADP-associated form that can be directed

to sides of rapid actin filament polymerization where the complex dissociates and the monomer becomes “activated” by nucleotide exchange for barbed end assembly (236, 239, 243). Stopping filament growth, barbed end capping proteins establish a high concentration of G-actin at steady state that derives from pointed end depolymerization and may in turn enter the directed growth of filaments (239, 243, 244). Conversely, capping of the pointed end can reduce the pool of monomeric actin and thus affects negatively the polymerization process (245).

Besides acting as regulators of the monomeric actin pool, ABPs affect actin assembly by mechanisms different from that. An important set of ABPs bypass the energetically unfavored process of spontaneous nucleation and initiate the *de novo* formation of actin filaments either from the sides of a pre-existing filament, creating a dendritic network, or monomers alone, generating straight filaments. Dynamics at the filaments’ ends is regulated by a number of proteins that specifically block the association and dissociation of actin monomers either at the pointed or barbed end (239, 243, 246). Other ABPs control the stability of actin filaments by binding to the filaments’ side and exerting their stabilizing properties by lowering the dissociation rate constant at the pointed end and regulating the access of depolymerizing proteins to F-actin (247, 248). Some filament side-binding proteins sever noncovalent bonds between the subunits in F-actin, thus producing short filaments (249, 250).

3.3 The actin cytoskeleton in neurons

Besides its critical role for a wide range of fundamental cellular processes, actin-based cytoskeletal dynamics is crucial for the development of the nervous system. Migration of neurons as well as extension of neurites, which involves processes similar to whole cell motility, rely on an organized actin polymerization, where cytoskeletal proteins represent the important endogenous factor for regulating neurite outgrowth (251).

Neurite outgrowth and pathfinding is directed by growth cones, specialized motile structures located at the tips of neuronal processes where signaling pathways emanating from extracellular cues converge and are interpreted. The growth cone structure is essential for its function. Based on the spatial organization of the different cytoskeletal elements, the growth cone is divided into three distinct yet contiguous domains (Figure 6A). The peripheral (P)-domain at the distal edge of the growth cone is dominated by actin filaments that are organized into either parallel bundles, forming dynamic, finger-like filopodia, or a branched dendritic network that underlies the lamellipodia, membranous flat, veil-like protrusions between the filopodia. In both structures, the filaments are oriented so that the growing barbed ends face the plasma membrane, whereas the pointed ends are inbound. MTs are the major cytoskeletal element in the central (C)-domain and enter from the axon shaft where they are organized into bundles and spread apart in the growth cone. At the interface

between the P- and C-domain, the transition (T)-zone is located. It is characterized by actin arcs, actomyosin contractile structures composed of anti-parallel bundles of F-actin and myosin II that lie perpendicular to the filament bundles of the radial filopodia. They can produce compressive forces that bring the MTs of the C-domain into a proximity range allowing their bundling at the growth cone wrist, a requirement for axon formation (252).

For neurite outgrowth, three iterative stages have to occur, with growth cone motility and protrusion of the leading edge membrane predominantly depending on the dynamic properties of actin. The steps involve extension and retraction (exploration), interaction between new extensions and the substrate (adhesion) and traction force generation (tension) (253, 254). Although neurite elongation can proceed without actin polymerization through MT-dependent processes, the extension rate is markedly reduced (251, 255). A combination of actin treadmilling and retrograde F-actin transport constitutes the “motor” that drives neurite extensions in response to guidance cues, and their sum determines whether filopodia as well as lamellipodia grow, retract or stay stationary. While actin filaments in the distal tips of both filopodia and lamellipodia are elongated by a constitutive assembly of actin monomers at the barbed end, thereby pushing the membrane in a forward direction, the entire filament is simultaneously dragged back in a myosin motor driven process (retrograde flow) towards the T-zone where it is depolymerized. The obtained actin monomers are subsequently recycled and enter a new round of polymerization. If the rate of the anterograde polymerization and the retrograde retraction are balanced, the growth cone neither retracts nor advances (Figure 6B). Both processes appear to be independently regulated, providing the opportunity of different responses in terms of speed, direction and duration. The forward movement of the growth cone is suggested to be accomplished by coupling the intracellular actin dynamics to the fixed extracellular matrix (“clutch” hypothesis or substrate-cytoskeletal coupling model). Here, receptors at the growth cone surface are thought to interact with an adhesive substrate or molecule, which leads in turn to a strong binding between the receptor and the actin cytoskeleton, establishing the molecular “clutch”. This mechanical linkage anchors the actin filaments and attenuates the retrograde flow, whereas actin polymerization proceeds at the leading edge, thus shifting the balance between the two processes towards forward protrusion of the growth cone (Figure 6C) (253, 254, 256).

The dynamic properties of actin structures in the growth cone are dependent on a wide variety of cytoskeletal proteins (see 3.2). In response to signaling cascades originating from extracellular cues, they direct the proper assembly of F-actin in an organized and localized fashion. As such, generation of the actin network underlying the lamellipodia is mediated by the well-orchestrated action of several ABPs (“dendritic nucleation model”) (reviewed in (257, 258)), bundling proteins facilitate the formation of F-actin bundles in the filopodia and sequestering/severing proteins promote the disassembly of actin filaments in the T-zone that

are subsequently recycled. Moreover, myosin motor proteins are indispensable as they drive the translocation of actin filaments in the course of retrograde flow (mainly myosin II) and accomplish vesicle transport along F-actin (myosin V). Although it is a widely accepted notion that the individual regulation of protein activities and their mutual interaction constitute the pivotal principle of actin-based motility processes, a comprehensive model has not yet been identified (251, 259, 260).

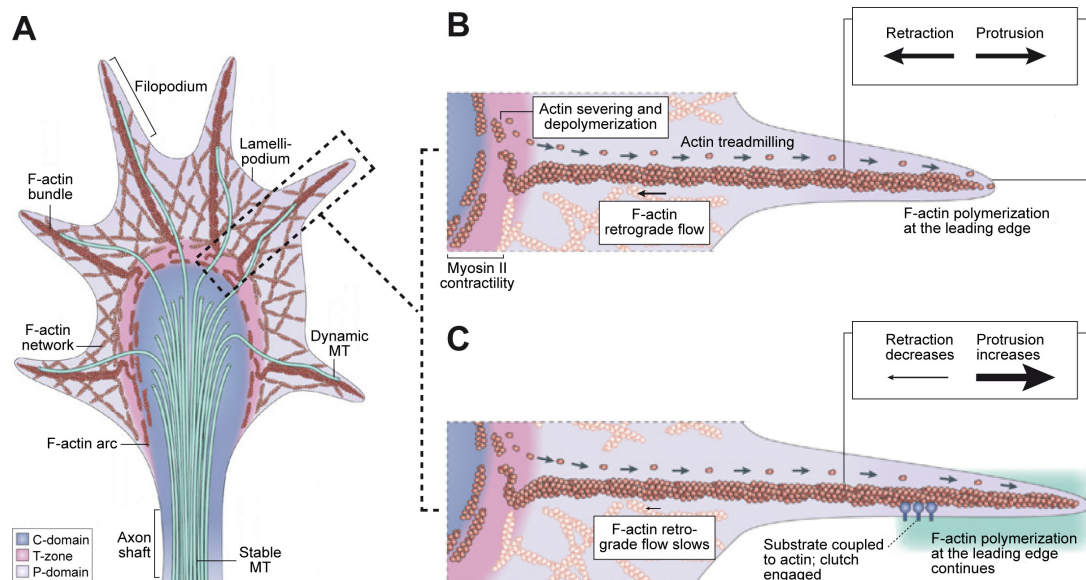


Figure 6: Cytoskeletal organization and actin dynamics in growth cones.

(A) The growth cone at the neurite tip can be divided into three different domains, characterized by the predominantly located cytoskeletal component therein. In the axon shaft, stable microtubules (MTs) are organized into parallel bundles that spread apart upon entering the growth cone into the central (C)-domain. Individual dynamic MTs extend through the transition (T)-zone into the peripheral (P)-domain where they align alongside to actin bundles. The P-domain at the distal end of the growth cone is rich in actin filaments that are organized into two different networks, giving rise to two distinct motile structures: F-actin in the filopodia is organized into long bundles, whereas lamellipodia are build up of a branched dendritic network. The T-zone at the interface between P- and C-domain contains actin arcs, which are composed of anti-parallel actin filaments and myosin II. (B) A combination of F-actin treadmilling (polymerization of filaments at the barbed end, severing/depolymerization of F-actin in the T-zone and recycling of actin monomers back to the leading edge) and F-actin retrograde flow (myosin motor-driven drawback of actin filaments towards the center of the growth cone) constitutes the “motor” underlying actin-based growth cone motility. If the forces generated by both processes are balanced, no protrusion occurs. (C) Upon encountering an attractive substrate, receptors at the growth cone surface bind to it and are coupled to the actin cytoskeleton, generating a molecular “clutch”. The mechanical link between cytoskeleton and the substrate is sufficient to overcome the force generated by retrograde F-actin flow, which consequently decreases. As actin polymerization at the leading edge continues, the membrane is pushed forward, resulting in protrusion of the growth cone. Adapted by permission from Macmillan Publishers Ltd: Nature Reviews Molecular Cell Biology (254). © 2009.

4. RNA interference

RNA interference (RNAi) is a natural mechanism of gene silencing that is conserved in a wide variety of eukaryotic organisms, including plants, invertebrates and vertebrates. It functions in many different cellular pathways, ranging from the defense against viral infections and mobile genetic elements (e.g. transposons) to the regulation of gene expression. RNAi-mediated silencing relies on cellular post-transcriptional gene regulatory mechanisms mediated by small non-coding RNAs to specifically guide recognition and ultimately degradation or translational repression of single-stranded target RNAs. More recently, RNAi has emerged as a powerful genetic tool to dissect function of numerous genes and bears a great potential as therapeutic agent to modulate gene expression.

4.1 Mechanism of gene silencing by double-stranded RNA

According to their origin, structure, associated effector proteins and biological role, three main categories of small RNAs have been described, which are only known to be present in eukaryotes: short interfering RNAs (siRNAs), microRNAs (miRNAs) and piwi-interacting RNAs (piRNAs). siRNAs and miRNAs represent the two primary categories of small RNAs, possessing a broad phylogenetic as well as physiological distribution and characterized by the double-stranded nature of their precursors. Conversely, piRNAs act most clearly in the germ line, appear to be generated from single-stranded precursors, although their origin is enigmatic, and associate to effector proteins different from those of siRNAs/miRNAs (261, 262). Although siRNAs and miRNAs share a common set of cellular proteins to elicit RNAi, the two populations differ in some aspects of their biogenesis pathways as well as in their gene silencing mechanisms. miRNAs are assumed to function as regulators of endogenous genes, playing a key role in controlling vertebrate differentiation and development, and as such to be endogenous and purposeful expression products of an organisms own genome. They are derived from precursor transcripts that are predicted to form an imperfect hairpin structure containing mismatches as well as bulges and target specific mRNAs of the cellular program. siRNAs, in contrast, are thought to act as “defender” of the genome’s integrity, protecting it against invading foreign nucleic acids, e.g. viruses, transposons and transgenes. Being directly derived from these triggers, they are primarily of exogenous origin and processed from long, fully complementary double-stranded (ds)RNAs, ultimately targeting the same transcript from which they arose (261).

The maturation of small RNAs is a stepwise process catalyzed by the dsRNA-specific RNase III-type endonucleases Droscha and Dicer (Figure 7). However, Droscha is only required for the processing of miRNAs in the nucleus but not of siRNAs. miRNAs are initially transcribed by RNA polymerase II (Pol II) as part of primary miRNA (pri-miRNA) precursors. pri-miRNAs typically consist of an imperfectly paired stem, a terminal loop and flanking segments. Within the nucleus, Droscha cuts the stem-loop out of the pri-miRNA, generating

the pre-miRNA hairpin intermediate. The pre-miRNA is subsequently transported into the cytoplasm by the nuclear export factor exportin-5 where the second RNase III, Dicer, carries out the cleavage reaction to remove the terminal loop, yielding the mature miRNA duplex of ~21 nucleotides in length. Likewise, the long, linear and perfect base-paired dsRNA precursors of siRNAs that are introduced directly into the cytoplasm or taken up from the environment are processed by Dicer. Both the mature miRNAs and siRNAs are characterized by a 5'-phosphate and 3'-dinucleotide overhang. The resultant duplexes are in the following unwound for the assembly into an effector ribonucleoprotein complex (RNP) (Figure 7), whose central catalytic component is a member of the Argonaute (Ago) protein family. siRNA-containing complexes are termed siRNA-induced silencing complexes (siRISCs), whereas miRNA-containing complexes are commonly referred to as miRISCs. In general, only the anti-sense strand (guide strand) of the RNA duplex is incorporated into RISCs that directs target recognition by Watson-Crick base pairing, while the other strand (passenger strand) is discarded. The single-stranded siRNA guides the siRISC complex to perfectly complementary RNAs, which are subsequently degraded. Here, Ago catalyzes the precise cleavage of the target RNA in the middle of the region spanned by the siRNA. After this initial cut, the target RNA fragments dissociate from the complex and are further degraded by cellular exonucleases, hence freeing siRISC for the cleavage of additional targets. While siRNAs can principally bind anywhere along the mRNA sequence, miRNAs primarily target the 3'-untranslated region (UTR). Although the mechanism of miRNA-directed post-translational regulation is not as well understood as the siRNA-mediated degradation, the extent of miRNA-mRNA complementarity is considered to direct the regulatory process: perfect base pairing, which occurs only rarely in animals, leads to the Ago-catalyzed cleavage of the target and its subsequent degradation, while central mismatches and bulges promote translational repression. Whether miRISCs suppress translation by inhibiting its initiation, preventing ribosome assembly, or stalling the elongation process is, however, still unclear (261, 263, 264).

4.2 RNAi as an experimental tool

The discovery of RNAi in mammalian cells provides a powerful tool for the specific silencing of any gene with a known sequence, hence representing a versatile tool for functional genomics. Different variants of artificial, small regulatory RNAs can trigger the innate RNAi pathway, which they enter at different points (Figure 7). Synthetic double-stranded siRNAs, small hairpin RNAs (shRNAs) and artificial miRNAs can be used as mediators. Here, miRNAs are expressed as pri-miRNA transcripts that are, as well as the shRNAs, processed by the endogenous biogenesis pathway into the mature silencing triggers (265, 266). Moreover, several methods for the delivery of efficient RNAi-triggers to the cellular target can be applied, which, however, fall into two main categories: (I)

exogenous delivery of chemically or enzymatically derived dsRNAs with a dinucleotide overhang at their 3'-end, thereby mimicking Dicer cleavage products, and (II) the promoter driven expression from plasmidal or viral vectors (267). For the former approach, classical gene transfer methods including liposome-mediated transfection, electroporation or microinjection are used to insert siRNAs into target cells. Within the cytoplasm, the siRNAs directly associate to RISCs and guide the degradation of the cognate mRNA. The major disadvantage of using synthetic siRNAs is the transient nature of this approach. Mammalian cells lack the mechanism present in fungi, plants, worms and *Drosophila* to amplify RNAi-trigger and thereby maintaining gene silencing. Depending on the turnover rate of the target protein, cell proliferation rate and siRNA dilution below a crucial threshold level needed to preserve gene silencing, the targeted protein levels recover within five to seven days after transfection (265, 266, 268). To achieve persistent gene silencing, DNA vector-mediated systems have been developed whose intracellular expression products are converted into mature siRNAs or miRNAs within the cells. As such, siRNAs can be expressed as fold-back stem-loop structures constituting simple hairpin-designed RNAs ("first generation" shRNA constructs) that get processed by Dicer after their export into the cytoplasm to yield functional siRNAs (Figure 7) (265, 268, 269). Alternatively, the gene specific silencing sequence can be inserted into the backbone of a naturally occurring miRNA precursor (266, 270), with the miRNA-30 (miR-30) primary transcript most often used as shuttle for siRNA expression (271). Resembling the stem loop structure of endogenous pri-miRNAs, these miRNA-designed or "second generation" shRNAs (shRNA^{mir}s) enter the RNAi pathway ahead of first generation shRNAs at the level of Drosha processing (Figure 7) (266, 271). Expression vectors can be introduced into cells by transient transfection methods, but expression of shRNA usually rely on viral delivery systems. Retroviral, lentiviral or adenoviral vectors can be used to infect a broad range of cell types depending on pseudotyping for the efficient delivery and stable integration of the shRNA expression cassette into the host's genome. Beyond that, lentiviral vectors, most commonly derived from the human immunodeficiency virus-1 (HIV-1), do not only transduce actively dividing cells but also efficiently integrate into primary and post-mitotic cells, thus making them the preferred system in neuronal applications (272).

Although RNAi-mediated gene silencing represents a useful tool in studying gene function, one has to take some obstacles into account that may compromise its specificity. Such off-target effects include the silencing of non-target mRNAs, caused either by a high degree of homology between the target and non-target sequence or by the ability of siRNAs to function through miRNA-like mechanisms (261, 273). Furthermore, dsRNAs are potent activators of the mammalian innate antiviral immune response, which virtually serves to recognize foreign RNA structures that are typical for viral infections, ensuring the survival of an infected organism (273, 274). Although it was initially thought that activation of the

antiviral defense network requires dsRNA molecules that are longer than 30 bp, synthetic 21-nucleotide (nt) siRNAs as well as shRNA expression constructs have been disclosed to induce an immune response (267, 275).

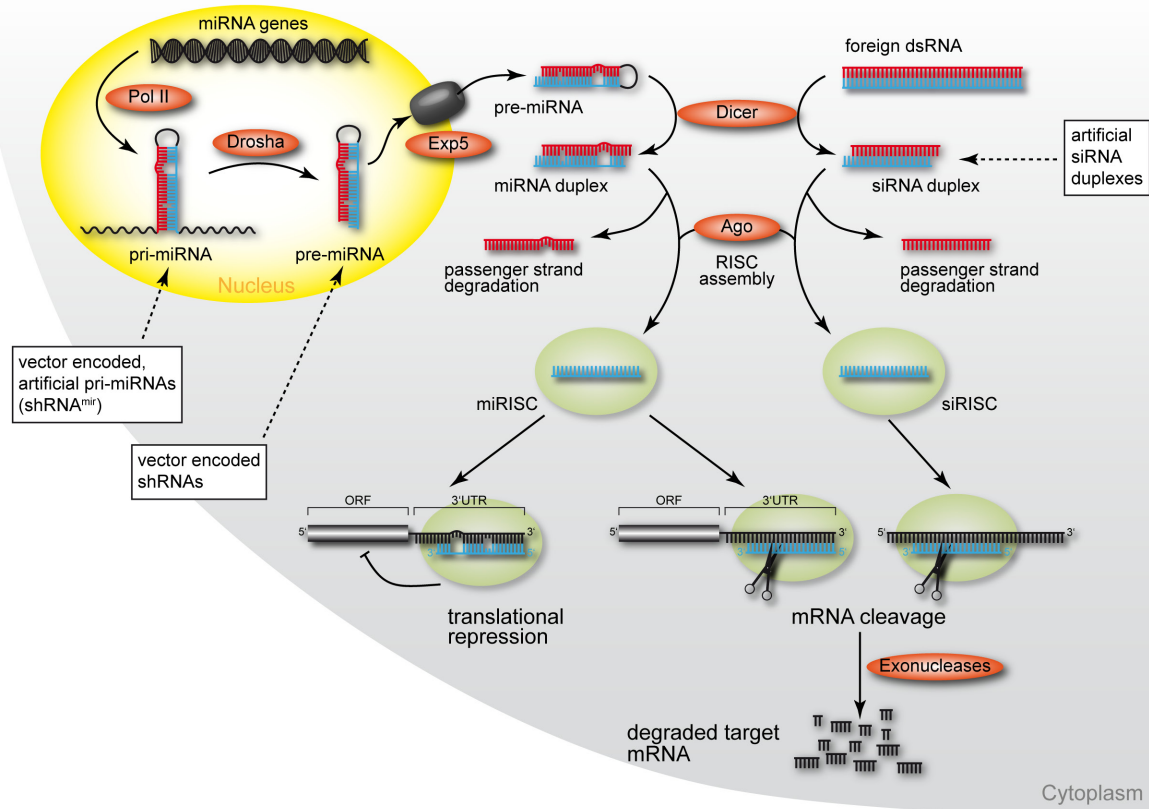


Figure 7: RNAi-mediated post-transcriptional regulation of gene expression and sites of intervention with RNAi technology tools.

miRNAs are expressed from RNA polymerase II (Pol II) promoters as part of pri-miRNA precursors, which are processed by the RNase III-type endonuclease Drosha in the nucleus to yield the stem loop pre-miRNA intermediates with imperfect base pairing. Following nuclear export by exportin-5 (Exp5), the pre-miRNAs are further processed by the RNase III enzyme Dicer into ~21-nt miRNA duplexes. Likewise, siRNA duplexes originate in the cytoplasm from Dicer-mediated cleavage of foreign, perfect base paired dsRNAs. Both miRNA and siRNA duplexes are unwound and the anti-sense (guide) strand (blue) is incorporated into a cytoplasmic RNA-induced silencing complex (RISC), referred to as miRISC or siRISC dependent on the origin of the integrated single-stranded RNA, while the passenger (sense) strand (red) is degraded. As a key component, these multiprotein-RNA complexes contain at least one member of the Argonaute (Ago) protein family, which contributes to their architectural and catalytic properties. The single-stranded siRNA/miRNA guides the sequence-specific recognition of target mRNAs by siRISC/miRISC. siRNAs usually hybridize with high complementarity to coding sequences and facilitate mRNA cleavage by Ago, whereas miRNA binding occurs predominantly at the 3'-UTR (untranslated region). Imperfect base pairing between miRNA and mRNA results in Ago-mediated translational repression, while complete complementarity leads to endonucleolytic cleavage of mRNA. After the initial cut, mRNA fragments are released and further degraded by various exonucleases. RNAi technologies deliver artificial small regulatory RNAs, which can enter the biogenesis pathway at different levels (white boxes). As such, synthetic siRNA duplexes can be introduced by classical gene transfer methods and are directly utilized for RISC assembly. Alternatively, plasmidal or viral vectors for the endogenous, promoter driven expression of artificial short hairpin RNAs (shRNAs), corresponding to the stem-loop structure of pre-miRNAs but with perfect base-pair matching, or artificial pri-miRNAs, which are processed by Drosha, can be applied. Both products are exported to the cytoplasm where they are further processed into mature siRNAs and miRNAs, respectively. Adapted from (261, 264, 266, 268, 271).

Upon detection of dsRNA by pre-existing cellular sensors, a series of cellular events is initiated that leads to a general inhibition of protein synthesis, translational activation of interferon (INF) and other cytokines, and ultimately to cell death (274). The induction of type I

INF, representing a key mediator in the antiviral defense system, is the most ubiquitous response to foreign dsRNA. IFN binds to cell surface receptors in an auto- and/or paracrine fashion, inducing signaling pathways that culminate in the nucleus with the upregulation of a plethora of IFN-stimulated genes (ISGs), which exert various functions, and thereby evoking a more global antiviral state (273, 276). ISGs are essential in mediating the intracellular antiviral activity. Many of these gene products constitute pattern recognition receptors (PRRs), recognizing viral RNAs and modeling signaling pathways, as well as transcription factors, thus promoting an amplification loop of enhanced INF production and restriction of viral spreading (276).

Cellular defense pathways are mediated by a variety of PRRs and can be classified as Toll-like receptor (TLR)-dependent or -independent. Receptors of the TLR protein family detect numerous molecules typically associated with viral, bacterial or fungal pathogens that enter the cell via the endosomal/lysosomal pathway. The non-TLR-mediated mechanisms in contrast recognize RNA species that are characteristic for viral infection and replication (273, 277). It is current opinion that endogenously expressed shRNAs predominately activate TLR-independent dsRNA sensors, while exogenous delivered siRNAs may activate both systems (267, 273). Out of the 13 known TLR sensors, three - TLR3, 7 and 8 - are known to be activated by siRNAs. The TLR-associated signaling pathways ultimately result in the release of pro-inflammatory cytokines and IFNs, thus causing significant immunotoxicity (274, 277). Cytoplasmic sensors of the TLR-independent mechanisms of dsRNA recognition include dsRNA-activated protein kinase R (PKR) and 2',5'-oligoadenylate synthetases (Oas'). Upon binding of dsRNAs, the INF-inducible Ser/Thr protein kinase PKR becomes autophosphorylated and thus activated, leading to the phosphorylation of the elongation and initiation factor (eIF)-2a, which blocks overall cellular protein synthesis and confers an antiviral state. Although translational inhibition is the prevalent role of activated PKR, it affects alternative signaling cascades (e.g. MAPK pathways) and can promote the downstream activation of transcription factors, including NF- κ B and IFN regulatory factor (IRF)-1, that trigger the expression of ISGs and IFN/pro-inflammatory cytokines, respectively (271). Three, INF-inducible members of the Oas family - Oas1, Oas2 and Oas3 - catalyze the conversion from ATP to 2',5'-oligoadenylates upon their dsRNA-mediated activation. These products bind to and activate the cellular endoribonuclease RNaseL, which clears single-stranded viral and cellular RNAs via their cleavage, resulting in a general inhibition of protein synthesis and apoptosis (271, 273, 274). A third cytoplasmic sensor within the TLR-independent pathway, retinoic acid-inducible gene 1 (RIG1), is activated by single-stranded or dsRNAs that contain uncapped 5'-triphosphates, which is a characteristic feature of some viral RNAs. RIG1-mediated signaling finally leads to the induction of IFN and other inflammatory mediators (277).

II. AIM OF THE STUDY

Mutations in the human *Lrrk2* gene have been identified as the most common cause of autosomal-inherited and sporadic PD. Patients with *Lrrk2*-associated forms of the disease present with a clinical syndrome indistinguishable from sporadic cases but display a pleomorphic pathology in postmortem analysis, depending somewhat on the mutation. Beyond that, nothing was known about either *Lrrk2*-associated cellular pathways or molecular pathomechanisms related to pathogenic protein variants at the beginning of the study. Gaining insights into the protein's normal physiological function was thought to contribute to the understanding of *Lrrk2*-associated PD and common pathways in the disorder. Characterized as a member of the ROCO protein superfamily, the domain structure of the encoded protein was known but its endogenous role remained elusive. The combination of a putative kinase and GTPase domain suggested that *Lrrk2* may exert both respective enzymatic activities. Comprising in addition several protein interaction domains, moreover, implied that *Lrrk2* may likely facilitate various protein-protein interactions contributing to the protein's function.

The aim of the work presented here was to analyze the physiological function of *Lrrk2*. Cellular, proteomic and biochemical approaches were employed to investigate the molecular basis of *Lrrk2*'s normal function and identify *Lrrk2*-related cellular pathways.

Objective 1: Characterization of *Lrrk2*-specific antibodies in immunological approaches.

At the beginning of the study, not only knowledge about the physiology of *Lrrk2* was missing but also basic experimental assays that are required for the protein's functional characterization. Therefore, the applicability of *Lrrk2*-specific antibodies generated within the laboratory to detect the endogenous protein in immunological approaches had to be validated at first, followed by an optimization of the respective assays.

Objective 2: Establishment of a lentivirus-mediated knockdown of *Lrrk2* in primary ventral mesencephalic cultures.

Selective gene silencing by RNAi represents a widely used technique for associating genes with biological processes in mammalian cells, based on the obtained loss-of-function phenotypes and their characterization. To dissect the function of *Lrrk2*, it was aimed to establish the stable and specific knockdown of *Lrrk2* via the expression of sequence-specific shRNAs, encoded by a lentiviral vector, in primary ventral mesencephalic (VM) cultures.

Objective 3: Evaluation of the consequences of Lrrk2 knockdown on DA neurons in primary VM cultures.

For the functional analysis of Lrrk2 via lentiviral-mediated RNAi, primary VM cultures derived from embryonic mice were selected as *in vitro* model, as the focus was laid on the impact of the protein's depletion in DA neurons, the prime cellular target site of defects in PD.

Objective 4: Evaluation of the consequences of Lrrk2 knockdown in the murine cell line NIH3T3.

The murine cell line NIH3T3 expresses Lrrk2 at experimentally trackable levels. As such, these easily manipulable cells were used to study the impact of Lrrk2 knockdown on cytoskeletal functions.

Objective 5: Identification of Lrrk2 interaction partners.

The analysis of associated protein complexes can indicate a protein's function. In the particular case of Lrrk2, its domain structure suggests that the protein requires specific protein-protein interactions to exert its biological role. The molecular interaction network of endogenous Lrrk2 was investigated by means of quantitative MS-based proteomics. For this purpose, NIH3T3 cells were utilized as they express significant levels of Lrrk2 protein and can be analyzed with high confidence.

Objective 6: Modeling of the Lrrk2-specific protein interaction network.

Information on the biological content of MS-based proteomic data can be gained if integrated and transferred to the context of biological pathways and networks. Network analysis can provide valuable information beyond a descriptive level and assists the assessment as well as validation of the dataset's biological significance. Towards this concept, and in cooperation with the group of Dr. J.A. Marto at Harvard Medical School, the identified Lrrk2 interaction partners were modeled into a Lrrk2-specific interaction network by integrating them with prevalidated protein interaction data provided by public databases.

III. MATERIAL AND METHODS

1. Material

1.1 Chemicals

All chemicals were purchased from Sigma-Aldrich (Sigma, Fluka, Aldrich; St. Louise, MO, USA) and VWR International (West Chester, PA, USA) if not otherwise stated. In this study dH₂O is referred to deionized water, ddH₂O is referred to ultra-pure water (Milli-Q Biocell, Millipore, Billerica, MA, USA).

1.2 General equipment

Analysis scales BP221S	Sartorius, Göttingen, Germany
ART Aerosol Resistant tips 20P/200/1000E	Molecular BioProducts, San Diego, CA, USA
Autoclave Bioclav	Schütt Labortechnik, Göttingen, Germany
Autoclave Systec 5075 ELV	Systec, Wettenberg, Germany
BD Falcon Blue Max 15 mL /50 mL high-clarity polypropylene conical centrifuge tubes	BD Bioscience, Franklin Lakes, NJ, USA
Biopure safe-lock reaction tubes 1.5 mL	Eppendorf, Hamburg, Germany
Diamond Tips DL10/D200/D1000	Gilson, Middleton, WI, USA
Disposable serological pipettes 5 mL/10 mL/25 mL	Greiner bio-one, Kremsmünster, Austria
Heating block thermostat HBT 130-2	HLC BioTec, Bovenden, Germany
Intelli-Mixer	Neolab, Heidelberg, Germany
L7-65 Ultracentrifuge with rotor (Type 45Ti; 45000 rpm)	Beckman Coulter, Brea, CA, USA
Magnetic stirrer RCT basic	IKA Labortechnik, Staufen, Germany
Milli-Q Biocell	Millipore
Multi-Axle-Rotating Mixer RM5	CAT Ingenieurbüro M. Zipperer GmbH, Staufen, Germany
MultiFlex round tips	Sorenson BioScience, Salt Lake City, UT, USA
Omnifix-50mL luer lock syring	B. Braun Melsungen AG, Melsungen, Germany
Omnifix-F1 syringe	B. Braun Melsungen AG
pH meter FE20-FiveEasy	Mettler Toledo, Greifensee, Switzerland
Platform shaker Duomax 1030	Heidolph Instruments, Schwabach, Germany
Polycarbonate bottle assembly with aluminum Caps (70 mL)	Beckman Coulter
Precision scales Basic Plus BP2100	Sartorius
Safe-lock reaction tubes 0.5 mL/1.5 mL/2 mL	Eppendorf
Shaking water bath 1083	GFL-Gesellschaft für Labortechnik GmbH, Burgwedel, Germany
Sigma Laboratory Centrifuges 6K15 and rotors 12500 and 11150/13350	Sigma Laborzentrifugen, Osterode, Germany
Sterican Insulin Needle – 0.40 Ø x 12 mm 27Gx¾” & 0.90 Ø x 40 mm 20Gx1½”	B. Braun Melsungen AG
Stuart Roller mixer SRT2	Bibby Scientific Ltd, Staffordshire, UK
Table top centrifuge 5415D, 5415R and 5424 with standard rotors	Eppendorf
Thermomixer comfort	Eppendorf
Ultra-low temperature freezer (-80°C) VIP™ series	Sanyo Biomedical, Wood Dale, IL, USA
Ultraspec 3300 pro UV/vis photometer	GE Healthcare, Waukesha, WI, USA
Vortex Genie 2	Scientific Industries, Bohemia, NY, USA
Water bath HRB 4 digital	IKA Labortechnik

1.3 Molecular biology

1.3.1 Special equipment

ABI Prism 3100 Genetic Analyzer for DNA sequencing	Applied Biosystems, Foster City, CA, USA
ABI Prism 384-well clear optical reaction plates	Applied Biosystems
ABI Prism 7900HT Sequence Detection System	Applied Biosystems
Absolute QPCR Seal	Thermo Fisher Scientific, Waltham, MA, USA
Agilent 2100 Bioanalyzer	Agilent Technologies, Santa Clara, CA, USA
BD Falcon 14 mL polypropylene round-bottom tubes	BD Bioscience
Incubator for <i>E. coli</i>	Memmert, Schwabach, Germany
Incubator Shaker for <i>E. coli</i>	GFL
Infors HT Multitron Incubator shaker for <i>E. coli</i>	Infors AG, Bottmingen-Basel, Switzerland
MicroAmp optical 96-well reaction plates	Applied Biosystems
MJ Research PTC-225 Peltier Thermo Cycler DNA Engine Tetrad	Bio-Rad, Hercules, CA, USA
QIAfilter Maxi Cartridges	Qiagen, Hilden, Germany
SubCell GT chambers for agarose gel electrophoresis	Bio-Rad
UV transilluminator UVT-40M	Herolab, Wiesloch, Germany

1.3.2 Kits

Agilent RNA 6000 Nano Kit	Agilent Technologies
Omniscript RT Kit	Qiagen
QIAGEN Plasmid Maxi Kit	Qiagen
QIAprep Spin Plasmid Miniprep Kit	Qiagen
QIAquick Gel Extraction Kit	Qiagen
QIAquick PCR purification Kit	Qiagen
QuantiTect SYBR Green PCR Kit	Qiagen
RNeasy Mini Kit	Qiagen
TOPO XL PCR Cloning Kit	Invitrogen, Carlsbad, CA, USA

1.3.3 Enzymes and special reagents

1 kb DNA ladder	New England Biolabs, Ipswich, MA, USA
2-log DNA ladder	New England Biolabs
ATP (100 mM)	Fermentas, Burlington, Canada
<i>Bgl</i> II and NEBbuffer 3	New England Biolabs
BigDye-Terminator v3.1 Cycling Sequencing Kit	Applied Biosystems
Bovine serum albumin (BSA; (100x)) for DNA restriction	New England Biolabs
<i>Cl</i> aI and NEBbuffer 4	New England Biolabs
dATP/ dGTP/ dCTP/ dTTP (100 μM each)	Stratagene, La Jolla, CA, USA
<i>Eco</i> RI and NEBbuffer <i>Eco</i> RI	New England Biolabs
Glycogen (20 mg/mL)	Roche, Penzberg, Germany
Klenow Fragment	New England Biolabs
PCR marker	New England Biolabs
<i>PfuTurbo</i> Hotstart DNA polymerase and reaction buffer	Stratagene
Protector RNase Inhibitor	Roche
Shrimp alkaline phosphatase and 10x reaction buffer	Roche
T4 DNA ligase and 10 x reaction buffer	Roche
T4 Polynucleotide-Kinase, 3'-phosphatase-free and 10x reaction buffer	Roche
<i>Taq</i> DNA polymerase and reaction buffer (with KCl and 25 mM MgCl ₂)	Fermentas
<i>Xba</i> I and NEBbuffer 4	New England Biolabs

1.3.4 *Escherichia coli* strains

DH5 α	Invitrogen
One Shot TOP10	Invitrogen

1.3.5 Oligonucleotides

All oligonucleotides were purchased from Metabion (Martinsried, Germany).

Table 2: Primer

Primer name	Sequence (5' - 3')	Application ^{a)}
Seq(pLVTH)_forward	AACCCGCTCCAAGGAATC	Sequencing
Seq(pLVTH)_reverse	CATACACATACGATTTAGGTGACAC	Sequencing
T3	AATTAACCCCTCACTAAAGGG	Sequencing
T7	TAATACGACTCACTATAGGG	Sequencing
Oligo-d(T) ₁₅	TTTTTTTTTTTTTTTT	RT
Lrrk2_3.5 kb fragment_forward	CTCTGAAGAAGTTGATAGTCAG	PCR
Lrrk2_3.5 kb fragment_reverse	TCATGCGAGCACTGAAACTC	PCR
GAPDH_forward	GACAAAATGGTGAAGGTCGGTG	Real-time PCR
GAPDH_reverse	AGGTCAATGAAGGGTCGTTG	Real-time PCR
Lrrk2_forward	GCTATCTTGCATTTTCGTTGTGC	Real-time PCR
Lrrk2_reverse	CCCAGGATTCCCAATGAACC	Real-time PCR
Oas1_forward	CCATCCTCAAGTGGACAAGAACTG	Real-time PCR
Oas1_reverse	TTGGGCTTTGGGCACCTTC	Real-time PCR

^{a)} RT: reverse transcription, PCR: polymerase chain reaction

Table 3: Oligonucleotides encoding first generation shRNA transcripts targeting Lrrk2.

The target sequence in Lrrk2 (AY792512) is shown in bold capital letters (stem sequence); lower case letters indicate the loop sequence. Underlined characters at the very 5'-end outline the pseudo-*Bgl*II and pseudo-*Xba*I restriction sites in the forward and reverse sequence, respectively.

Oligo name	Oligo Sequence (5' - 3')
sh1 forward	<u>GAT</u> CCCCAAGTTGATAGTCAGGCTGAATtcaagagaATTCAGCCTGACTATCAACTTTTTTTGGAAA
sh1 reverse	CTAGTTTCCAAAAAAGTTGATAGTCAGGCTGAATtctctgaaATTCAGCCTGACTATCAACTTGGG
sh2 forward	<u>GAT</u> CCCCAAACTGGGATGCAAAGCTTTAtcaagagaTAAAGCTTTCATCCAGTTTTTTTTGGAAA
sh2 reverse	CTAGTTTCCAAAAAAGCTGGGATGCAAAGCTTTAtctctgaaTAAAGCTTTCATCCAGTTTGGG
sh3 forward	<u>GAT</u> CCCCAAGAGGAAGACAGTGAGAAGCtcaagagaGCTTCTCACTGTCTTCTCTTTTTTTGGAAA
sh3 reverse	CTAGTTTCCAAAAAAGAGGAAGACAGTGAGAAGCtctctgaaGCTTCTCACTGTCTTCTCTTGGG
sh4 forward	<u>GAT</u> CCCCAATGCAGACCAAATGTGCTCAttcaagagaTGAGCACATTTGGTCTGCATTTTTTTGGAAA
sh4 reverse	CTAGTTTCCAAAAAATGCAGACCAAATGTGCTCAtctctgaaTGAGCACATTTGGTCTGCATTGGG
sh5 forward	<u>GAT</u> CCCCAAGAATTTCTGCATAGGGACAttcaagagaTGCCCTATGCAGAAATCTTTTTTTGGAAA
sh5 reverse	CTAGTTTCCAAAAAAGAATTTCTGCATAGGGACAtctctgaaTGCCCTATGCAGAAATCTTGGG
sh6 forward	<u>GAT</u> CCCCAAGTGCTCCGGTATCAGATGttcaagagaCATCTGATACCGGAGCACTTTTTTTGGAAA
sh6 reverse	CTAGTTTCCAAAAAAGTGCTCCGGTATCAGATGtctctgaaCATCTGATACCGGAGCACTTGGG
sh7 forward	<u>GAT</u> CCCCAAATACTGTCTTCAGATGAGTtcaagagaACTCATCTGAAGACAGTATTTTTTTGGAAA
sh7 reverse	CTAGTTTCCAAAAAATACTGTCTTCAGATGAGTtctctgaaACTCATCTGAAGACAGTATTTGGG
sh8 forward	<u>GAT</u> CCCCAATCTGTCTTATAACCAGCTtcaagagaGAGCTGGTTATAGGACAGATTTTTTTGGAAA
sh8 reverse	CTAGTTTCCAAAAAATCTGTCTTATAACCAGCTtctctgaaAGCTGGTTATAGGACAGATTGGG

Material and Methods

Table 4: Oligonucleotides encoding second generation shRNA (shRNA^{mir}) transcripts targeting Lrrk2.

The target sequence in Lrrk2 (AY792512) is shown in bold capital letters (stem sequence); lower case letters indicate the loop sequence. Underlined characters at the very 5'-end outline the pseudo-*Bgl*II and pseudo-*Xba*I restriction sites in the forward and reverse sequence, respectively.

Oligo name	Oligo Sequence (5' - 3')
shmiB3 forward	<u>GATCAGCGAAAGTTGATAGTCATCGGCTGAAT</u> ctgtgaagccacagatggg ATTCAGCCTGACTATCAACTTCTGCT
shmiB3 reverse	<u>CTAGTTTCCAAAAAGCAGAAAGTTGATAGTCAGGCTGAAT</u> ccccatctgtggcttcacag ATTCAGCCGATGACTATCAA CTTTTCGCT
shmiB4 forward	<u>GATCAGCGAAAAGTGCTCCGGTTCATCAGATG</u> ctgtgaagccacagatggg CATCTGATACCGGAGCACTTTCTGC
shmiB4 reverse	<u>CTAGTTTCCAAAAAGCAGAAAAGTGCTCCGGTATCAGATG</u> ccccatctgtggcttcacag CATCTGATGAACCGGAGCA CTTTTCGCT

1.3.6 Plasmids and constructs

Table 5: Plasmids

Plasmid name	Description	Resistance ^{a)}	Provider ^{b)}
pBC KS+(Clal)-H1	Subcloning vector	Chl	MB/Tronolab
pCMV-Gag/PolΔR8.92	Packaging construct	Amp	MB/Tronolab
pLVTH	Transfer vector	Amp	MB/Tronolab
pMD2.G	Envelope construct	Amp	MB/Tronolab
pRSV Rev	Packaging construct	Amp	MB/Tronolab
pLV(3'MCS)	Transfer vector (miR-30-based constructs)	Amp	MB
pEGFP-EK	Expression vector with 5' GFP reporter gene	Kan	MB/Tronolab
pCR-XL-TOPO	TOPO vector; TOPO XL PCR cloning kit	Kan	Invitrogen

^{a)} Amp: ampicillin (100 µg/mL); Chl: chloramphenicol (27 µg/mL); Kan: kanamycin (50 µg/mL)

^{b)} MB: Dr. M. Bauer (University of Tübingen); Tronolab: Laboratory of virology and genetics (EPFL)

Table 6: Constructs

Construct name	cDNA	Plasmid	Provider ^{a)}
pBC/H1-sh1	sh1	pBC KS+(Clal)-H1	AM
pBC/H1-sh2	sh2	pBC KS+(Clal)-H1	AM
pBC/H1-sh3	sh3	pBC KS+(Clal)-H1	AM
pBC/H1-sh4	sh4	pBC KS+(Clal)-H1	AM
pBC/H1-sh5	sh5	pBC KS+(Clal)-H1	AM
pBC/H1-sh6	sh6	pBC KS+(Clal)-H1	AM
pBC/H1-sh7	sh7	pBC KS+(Clal)-H1	AM
pBC/H1-sh8	sh8	pBC KS+(Clal)-H1	AM
pBC/H1-miB3	shmiB3	pBC KS+(Clal)-H1	MB
pBC/H1-miB4	shmiB4	pBC KS+(Clal)-H1	AM
pLVsh1	sh1	pLVTH	AM
pLVsh6	sh6	pLVTH	AM
pLVmiB3	shmiB3	pLV(3'MCS)	MB
pLVmiB4	shmiB4	pLV(3'MCS)	AM
pEGFP-EK-Lrrk2 (3.5kb)	Lrrk2 3.5kb fragment (AY792512: 50-3487)	pEGFP-EK	AM

^{a)} AM: A. Meixner (this study), MB: Dr. M. Bauer

1.4 Mammalian cell culture

1.4.1 Special equipment

Cell culture dishes and multidishes plates Nunclon Δ Surface 6-well/10 cm/14 cm	Nunc, Rochester, NY, USA
CO ₂ incubator MCO-17AIC	Sanyo
Cold light source Schott KL 1500 LCD	Schott, Mainz, Germany
FACSCalibur flow cytometer	BD Bioscience
Glass coverslips, Ø12mm	Assistent, Sondheim, Germany
Lab-Tek Chamber Slide System, 8-well	Nunc
Laminar Flow BDK-S 1200	BDK Luft- und Reinraumtechnik GmbH, Sonnenbühl-Genkingen, Germany
Liquid nitrogen tank Chronos	Messer Group GmbH, Sulzbach, Germany
Microscope Cover Slips (0.13 – 0.16 mm) 24 x 60 mm	Menzel-Gläser, Braunschweig, Germany
Microscope slides Superfrost Plus 25 x 75 x 1 mm	Menzel-Gläser
Millex-HV filter units 0.45 µm, PVDF, 33 mm	Millipore
Neubauer counting chamber, 0.100 mm, 0.0025 mm ²	Marienfeld, Lauda-Königshofen, Germany
Nikon SMZ-645 Stereo Zoom Microscope	Nikon Instruments Inc., Melville, NY, USA
Pasteur pipette 230/120 mm	Witeg Labortechnik GmbH, Wertheim, Germany
Rotana 46 RS centrifuge	Hettrich Lab Technology, Tuttlingen, Germany
Steritop-GP filter unit, 0.22 µm	Millipore
Surgical Disposable Scalpel	B. Braun Melsungen AG
Surgical/microsurgical instruments	FST, Heidelberg, Germany
Zeiss Axioskop 2 with AxioCam HRc	Zeiss, Göttingen, Germany

1.4.2 Media, reagents and supplements

¹³ C ₆ ¹⁵ N ₄ -L-Arginine and ¹³ C ₆ -L-Lysine	Silantes, Munich, Germany
4',6-diamidino-2-phenylindole (DAPI)	Sigma
Alexa Fluor 568 phalloidin	Invitrogen
B27	Invitrogen
Basic fibroblast growth factor (bFGF)	Miltenyi Biotech, Auburn, CA, USA
Distilled water, tissue culture tested	Invitrogen
Dulbecco's modified Eagle medium: Nutrient Mixture F-12 (DMEM/F12)	Invitrogen
DMEM containing 4.5 g/L glucose, L-glutamine, 25 mM HEPES	Invitrogen
DMEM-GlutaMAX	Invitrogen
Episerf	Invitrogen
Fluor Save reagent	Calbiochem, Merck KGaA, Darmstadt, Germany
Foetal bovine serum (FBS)	Invitrogen
FBS dialyzed	PAA, Pasching, Austria
Glucose (45%)	Sigma
Hank's balanced salt solution (HBSS)	Invitrogen
Insulin (4 mg/mL)	Invitrogen
L-Arginine and L-Lysine	Silantes
L-Glutamine (200 mM, 100x)	Invitrogen
Natural mouse laminin	Invitrogen
Penicillin (10000 U/mL)/streptomycin (10000 µg/mL)	Invitrogen
Phosphate-Buffered Saline (PBS)	Invitrogen
Poly-D-lysine homobromide (mol wt 70000-150000)	Sigma
Pyruvate (100 mM, 100x)	Invitrogen
SILAC DMEM	PAA
Sodium bicarbonate (7.5%)	Invitrogen
Trypsin-EDTA (0.05%, 1x)	Invitrogen

1.5 Protein chemistry

1.5.1 Special equipment

Agfa Curix 60 Developer	Agfa, Cologne, Germany
Amersham Hyperfilm ECL	GE Healthcare
Cell scraper 25 cm	Sarstedt, Nümbrecht, Germany
Cellophane foils	Deti GmbH, Meckesheim, Germany
Electrophoresis systems Mini-Protean 3 and Protean II	Bio-Rad
Gradient maker	VWR
GS-710 calibrated imaging	Bio-Rad
Hybond PVDF membranes	GE Healthcare
Hypercassette 18 x 24 cm	GE Healthcare
IKA shaker MTS4	IKA Labortechnik
Multiscreen apparatus Mini-Protean II	Bio-Rad
Power Supply Power Pac 300/Basic/HC	Bio-Rad
Power Supply Power Pac 3000	Bio-Rad
Semi-dry transfer cell Trans-Blot SD	Bio-Rad
SpeedVac SPD111V	Fisher Scientific, Hampton, NH, USA
V96 MicroWell™ Plates and standard lids	Nunc
Whatman chromatography papers	Th. Geyer, Renningen, Germany
XCell SureLock Mini-Cell	Invitrogen

1.5.2 Kits and special reagents

Bio-Rad Protein Assay Kit	Bio-Rad
Blotting Grade Blocker non-fat dry milk	Bio-Rad
Bovine serum albumin (BSA)	PAA
Dimethyl pimelimidate (DMP)	Thermo Fisher Scientific
Enhanced chemiluminescence kit, ECLplus	GE Healthcare
NuPAGE MOPS SDS running buffer (5x)	Invitrogen
NuPAGE NOVEX Bis-Tris gels	Invitrogen
PageRuler™ Prestained Protein Ladder	Fermentas
Precision plus protein standard, dual color	Bio-Rad
Trypsin, sequencing grade modified	Promega, Fitchburg, WI, USA

1.5.3 Protein complex purification

BioBind strip assembly, Streptavidin Coated Microplates	Thermo Fisher Scientific
Cyanogen bromide-activated sepharose 4B	Sigma
Illustra MicroSpin columns	GE Healthcare
Laemmli sample buffer	Bio-Rad
Microcon Centrifugal Filter Devices YM-3	Millipore
Poly-Prep Chromatography Columns	Bio-Rad
Protein G PLUS-Agarose	Santa Cruz
Protein G Sepharose 4 Fast Flow	GE Healthcare
Surgical blades, sterile, carbon steel	Schreiber Instrumente, Fridingen, Germany

1.5.4 Mass spectrometry

LTQ Orbitrap XL	Thermo Fisher Scientific
Ultimate 3000 Nano-LC	Dionex, Sunnyvale, CA, USA

1.6 Antibodies

Table 7: Commercial primary antibodies

Antibody	Species	Dilution ^{a)}	Provider
<i>Western blotting</i>			
Anti-Arp3 (clone FMS338)	mouse, monoclonal	1:100000 – 1:500000 (5% (w/v) nonfat dry milk in TBST)	Sigma
Anti-GAPDH (clone 6C5)	mouse, monoclonal	1:2000 – 1:500000 (5% (w/v) nonfat dry milk in TBST)	Millipore
Anti-GFP	rabbit, polyclonal	1:5000 – 1:10000 (5% (w/v) nonfat dry milk in TBST)	Invitrogen
Anti-Myosin Id	rabbit, polyclonal	1:5000 (5% (w/v) nonfat dry milk in TBST)	Santa Cruz, Santa Cruz, CA, USA
Anti-Myosin IIa	rabbit, polyclonal	1:1000 – 1:5000 (5% (w/v) BSA in TBST)	Cell Signaling, Danvers, MA, USA
Anti-Myosin IIb	rabbit, polyclonal	1:1000 – 1:5000 (5% (w/v) BSA in TBST)	Cell Signaling
Anti-Tropomyosin (clone TM311)	mouse, monoclonal	1:10000 – 1:250000 (5% (w/v) nonfat dry milk in TBST)	Sigma
<i>Immunofluorescence</i>			
Anti-Tyrosine Hydroxylase (clone LNC1)	mouse, monoclonal	1:500	Millipore
Anti-Lrrk2	rabbit, polyclonal	Tested 1:100 - 1:500	Alexis, Farmingdale, NY, USA
Anti-Lrrk2	rabbit, polyclonal	Tested 1:100 - 1:1000	Lifespan, Seattle, WA, USA
Anti-Lrrk2	rabbit, polyclonal	Tested 1:100 - 1:500	Cell Signaling
Anti-Lrrk2	rabbit, polyclonal	Tested 1:100 - 1:500	Abcam, Cambridge, UK
Anti-Lrrk2	goat, polyclonal	Tested 1:100 - 1:500	Santa Cruz

^{a)} Antibodies used in western blot analysis were diluted in the buffer given in parentheses.

Table 8: Rat-monoclonal and rabbit-polyclonal antibody clones against Lrrk2.

Rat-monoclonal antibodies were generated against the peptide antigen encompassing the amino acids 2025 to 2055 of the human protein (UniProt-ID: Q5S007) (Dr. C.J. Gloeckner, Helmholtz Zentrum München) and produced in house by Dr. E. Kremmer (Helmholtz Zentrum München). In cooperation with Eurogentec, rabbit-polyclonal antibodies were produced, using peptides spanning amino acids (aa) 2501-2514 (146) and 2513-2527 (Dr. C.J. Gloeckner) of murine Lrrk2 (UniProt-ID: Q5S006).

Species	Clone	Status	Application ^{a)}	Provider
Rat	3G6	Hybridoma supernatant	Tested in WB: 1:1 – 1:100 Tested for IP	E. Kremmer
Rat	6F8	Hybridoma supernatant	Tested in WB: 1:1 – 1:100 Tested for IP	E. Kremmer
Rat	2E12	Hybridoma supernatant	Tested in WB: 1:1 – 1:100 Tested for IP	E. Kremmer
Rat	4B7	Hybridoma supernatant	Tested in WB: 1:1 – 1:100 Tested for IP	E. Kremmer
Rat	3A6	Hybridoma supernatant	Tested in WB: 1:1 – 1:100 Tested for IP	E. Kremmer
Rat	3E11	Hybridoma supernatant	Tested in WB: 1:1 – 1:100 Tested for IP	E. Kremmer
Rat	1E11	Hybridoma supernatant	Tested in WB: 1:1 – 1:100 Tested for IP	E. Kremmer
Rat	4H9	Hybridoma supernatant	Tested in WB: 1:1 – 1:100 Tested for IP	E. Kremmer
Rat	2D8	Hybridoma supernatant	Tested in WB: 1:1 – 1:100 Tested for IP	E. Kremmer
Rat	5A3	Hybridoma supernatant	Tested in WB: 1:1 – 1:100 Tested for IP	E. Kremmer
Rat	8A3	Hybridoma supernatant	Tested in WB: 1:1 – 1:100 Tested for IP	E. Kremmer

^{a)} WB: western blotting (dilutions in 5% nonfat dry milk in TBST), IP: immunoprecipitation

Material and Methods

Table 8 (continued): Rat-monoclonal and rabbit-polyclonal antibody clones against Lrrk2.

Species	Clone	Status	Application ^{a)}	Provider
Rat	1E11	Affinity Purified	WB: 1:500 – 1:5000 IP Tested in IF: 1:250	E. Kremmer
Rat	2E12	Affinity Purified	Tested in WB: 1:1 – 1:100 Tested in IP Tested in IF: 1:250	E. Kremmer
Rat	3A6	Affinity Purified	Tested in WB: 1:1 – 1:100 Tested in IF: 1:250	E. Kremmer
Rabbit	820 (aa 2501-2514)	Affinity Purified	Tested in IF: 1:50 – 1:100	Eurogentec
Rabbit	821 (aa 2513-2527)	Affinity Purified	Tested in IF: 1:50 – 1:100	Eurogentec

^{a)} WB: western blotting (dilutions in 5% nonfat dry milk in TBST), IP: immunoprecipitation, IF: immunofluorescence

Table 9: Secondary antibodies

Antibody	Species	Dilution ^{a)}	Provider
Anti-mouse IgG HRP-conjugated	goat, polyclonal	1:15000 WB	Jackson ImmunoResearch, West Grove, PA, USA
Anti-rabbit IgG HRP-conjugated	goat, polyclonal	1:15000 WB	Jackson ImmunoResearch
Anti-rat IgG HRP-conjugated	goat, polyclonal	1:15000 WB	Jackson ImmunoResearch
Anti-rat IgG AlexaFluor 568-conjugated	goat, polyclonal	1:200 IF	Invitrogen
Anti-rabbit IgG AlexaFluor 568-conjugated	goat, polyclonal	1:200 IF	Invitrogen
Anti-goat IgG AlexaFluor 568-conjugated	goat, polyclonal	1:200 IF	Invitrogen
Anti-mouse IgG AlexaFluor 568-conjugated	goat, polyclonal	1:200 IF	Invitrogen
Biotin-SP-AffiniPure Anti-Rat IgG (H+L)	mouse, polyclonal	1:200 IP screen	Jackson ImmunoResearch

^{a)} WB: western blotting, IP: immunoprecipitation, IF: immunofluorescence

Table 10: Immunoglobulins

Name	Provider
IgG from rat serum, reagent grade, ≥95% (SDS-PAGE)	Sigma
Purified rat IgG2a	E. Kremmer

1.7 Software and databases

1.7.1 Databases

BioGRID	http://www.thebiogrid.org/
HPRD	http://www.hprd.org/
KEGG	http://www.genome.jp/kegg/
Mouse specific IPI database version 3.52	http://www.maxquant.org/
NCBI	http://www.ncbi.nlm.nih.gov/
NCBI Blast	http://blast.ncbi.nlm.nih.gov/Blast.cgi
NCBI Nucleotide	http://www.ncbi.nlm.nih.gov/sites/entrez?db=nucleotide
NCBI Protein	http://www.ncbi.nlm.nih.gov/sites/entrez?db=protein
NCBI PubMed	http://www.ncbi.nlm.nih.gov/sites/entrez
Swiss-Prot	http://www.expasy.ch/sprot/
UniProt	http://www.uniprot.org/

1.7.2 Software

Adobe Illustrator CS3	Adobe Systems, San Jose, CA, USA
Adobe Photoshop CS3	Adobe Systems
Agfa FotoLook 36 V3.60.0	Agfa-Gevaert Group, Mortsel, Belgium
Agilent 2100 Expert Software V3.01.02.SI136 and V3.02.07.SI532	Agilent Technologies
AxioVision V4.0 - 4.7.2.0	Carl Zeiss Imaging Solutions, Göttingen, Germany
CellQuest Pro	BD Bioscience
EndNote 9	Thomson Reuters, New York, NY, USA
GraphPad Prism 4	GraphPad Software, La Jolla, CA, USA
ImageJ 1.41	W. Rasband, National Institutes of Health (NIH), Bethesda, MA, USA (http://www.hhs.gov)
ImageJ plug-in NeuronJ	W. Rasband
Mascot version 2.2	Matrix Science, Boston, USA
MaxQuant V1.0.13.8	J. Cox, M. Mann, Max-Planck Institute for Biochemistry, Martinsried, Germany (http://www.maxquant.org)
MS Office 2003 (Word, Excel, PowerPoint)	Microsoft, Redmond, WA, USA
Pathway Palette	Dana-Farber Cancer Institute, Boston, MA, USA (http://blaispathways.dfci.harvard.edu/Palette.html)
SDS Software 2.3	Applied Biosystems
SigmaPlot 8.02	Systat, Chicago IL, USA
siRNA Target Finder	Applied Biosystems (http://www.ambion.com/techlib/misc/siRNA_finder.html)
Vector NTI Suite 9.0/10.0	Invitrogen
WinMDI 2.8	J. Trotter (http://facs.scripps.edu/software.html)
XCalibur V 2.07	Thermo Fisher Scientific

2. Methods

2.1 Protein chemistry

2.1.1 Protein extraction

2.1.1.1 *From cultured cells*

For the generation of protein extracts from cultured cells, growth medium was completely removed and cells were washed once with PBS. Plates and 8-well chamber slides were placed on ice and an appropriate volume of freshly prepared ice-cold lysis buffer (30 mM Tris-HCl, pH 7.4, 150 mM NaCl, 1% (v/v) Nonidet P-40 (NP-40) (Roche), 10% (v/v) glycerol, 1x Roche complete protease inhibitor mixture (Roche), 1x phosphatase inhibitor cocktail 1 and 2 (Sigma)) was added. For 15 cm plates 1 mL buffer was used, for 6-well plates 50 μ L and cells on 8-well chamber slides were lysed in 10 μ L buffer per well. Cells were detached from the surface of the dishes using a cell scraper. Extracts were transferred to 1.5 mL tubes and kept on ice for 30 min with intermittent vortexing. To remove intact cells and cell debris, lysates were centrifuged at 16000 $\times g$ and 4°C for 10 min, and the supernatants were transferred into fresh tubes. The protein concentration of the lysates was determined by using the Bradford method (see 2.1.2) before they were aliquoted and snap-frozen in liquid nitrogen. Samples were stored at -80°C until further use.

In some cases (see 2.4.5), the cells were detached from the cell plate surface by trypsinization and harvested by centrifugation for 5 min with 90 $\times g$ at room temperature. The growth medium was removed, cells were washed once with PBS before 100 μ L ice-cold lysis buffer (6-well format) was added to the pellet. Cells were dissolved immediately by vortexing and extracts were processed as described above.

2.1.1.2 *From adult mouse brains*

Adult mouse brains were obtained from the CD-1 mother animals (animal breeding facility, Helmholtz Zentrum München, Munich, Germany) of E12.5 embryos that were used for the preparation of primary ventral mesencephalic (VM) cell cultures (see 2.6.5.2). After removal from the skull, the brain was stored in ice-cold PBS and transferred to a cell culture dish containing PBS to remove blood vessels and meninges. PBS was carefully removed from the tissue by placing the brain on a filter paper before the brain was cut into small pieces. The tissue pieces were individually transferred into a precooled mortar filled with liquid nitrogen, snap-frozen and collected into a 50 mL tube, which was stored at -80°C until extraction of brain proteins.

For the preparation of protein extracts, the brain pieces were successively put frozen into a mortar that was placed into a box containing liquid nitrogen and grinded with a precooled pestle to a fine powder. The grinded material was transferred completely to two 2 mL tubes and weighed. 50 μ L Brij-buffer (30 mM Tris-HCl, pH 7.4, 150 mM NaCl, 0.25%

(v/v) Brij-96, 10% (v/v) glycerol, 1x Roche complete protease inhibitor mixture, 1x phosphatase inhibitor cocktail 1 and 2) was added per mg tissue, which was immediately dissolved by vigorously pipetting up and down followed by vortexing. The extracts were subsequently homogenized by passing them first three times through a 20G (0.9 mm) and then two times through a 27G (0.4 mm) needle attached to a 1 mL sterile plastic syringe. Lysates were kept on ice for 30 min with intermittent vortexing and cleared from intact cells as well as cell debris by centrifugation for 10 min at 16000 x *g* and 4°C. The supernatants (first lysate) were pooled in one tube, and the pellets were each resuspended in additional 500 µL Brij-buffer. After incubation for 30 min on ice, the samples were again centrifuged (10 min, 16000 x *g*, 4°C), and the supernatants (second lysate) were combined with the first one. Protein concentration was determined using the Bradford assay (see 2.1.2), and 500 µL aliquots of the brain lysates were snap-frozen in liquid nitrogen. Samples were stored at -80°C until further use.

2.1.2 Determination of protein concentration

The total protein concentration in a given solution was determined according to Bradford (278). This colorimetric assay is based on an absorbance shift of the dye Coomassie brilliant blue G-250 from 465 nm to 595 nm upon binding to proteins under acidic conditions. The dye forms complexes with the proteins by binding non-covalently to their cationic and non-polar, hydrophobic side chains (preferentially arginine and aromatic amino acids), whereby its protonated cationic form ($A=465$ nm) is converted to the stable unprotonated anionic sulfonate form ($A=595$ nm). The spectral shift is proportional to the amount of bound dye and thus to the amount of protein in a sample. Within a range of 2-120 µg protein/mL, the Bradford assay is linear, so that a sample concentration can be determined based on a standard regression curve. This highly sensitive assay (detection limit between 0.05-0.5 µg/µL) is sparsely susceptible to interference by various chemicals except detergents, such as sodium dodecyl sulfate (SDS), strong basic reagents and high urea concentrations.

The Bio-Rad protein Assay Kit was used for the Bradford assay according to manufacture's instructions. The Dye Reagent Concentrate was diluted 1:5 with ddH₂O. 1 mL of the diluted reagent was mixed with an appropriate amount of protein sample and incubated for 5 min at room temperature. The absorption was measured at 595 nm, with the diluted reagent used as a blank. For the determination of protein concentration, a standard regression curve with 2-8 µg BSA, diluted in the corresponding lysis buffer, was generated.

2.1.3 SDS-polyacrylamide gel electrophoresis (SDS-PAGE)

SDS-polyacrylamide gel electrophoresis (SDS-PAGE) is a widely used technique for the separation of proteins according to their size (molecular mass). Therefore, proteins are denaturated with SDS and reducing agents, such as β -mercaptoethanol. The anionic reagent SDS binds, moreover, in a constant weight ratio of 1.4 g per g polypeptide to proteins, thereby conferring a high negative charge density to the proteins, which masks their intrinsic charge. This leads to a nearly constant charge-to-mass ratio of the SDS-protein complexes, which can thus be separated by electrophoresis in a SDS-containing gel according to their molecular masses, with small proteins moving faster through the polyacrylamide matrix.

2.1.3.1 Discontinuous SDS-PAGE

For the standard separation of protein mixtures, discontinuous one-dimensional SDS-PAGE according to Laemmli (279) was used. This gel system offers an improved separation resolution by the combination of a large-pored stacking gel, which uses the principle of isotachopheresis to concentrate the SDS-protein complexes, on top of the separating gel, where the negatively charged complexes are separated (zone electrophoresis). The pH value of the stacking gel (pH 6.8) is in the range of the pI value (isoelectric point) of glycine, a major component of the running buffer, which is therefore predominantly present in its net-uncharged zwitterionic state and moves very slowly in the electric field. On the other hand, the chloride ions of the stacking gel buffer form a quickly moving front migrating ahead of the glycine, whereby creating a narrow zone in which the SDS-protein complexes with an intermediate electrophoretic mobility are concentrated. Passing the alkaline separating gel, (pH 8.8) glycine becomes mostly negatively charged, thus increasing its mobility towards the SDS-protein complexes. The latter are then separated in the small pores of the separating gel according to their molecular masses.

Gels were poured separately by using the casting chambers of the Mini-Protean 3 system for mini gels and the Protean II system for 18 cm gels, respectively. Depending on the application of the gel, 0.75 or 1 mm spacers were selected. The casting chamber was filled with the separating gel solution (Table 11), which was overlaid with isopropanol. The acrylamide matrix was formed by copolymerization of acrylamide and bisacrylamide induced by the polymerization starter ammonium peroxydisulfate (APS) and accelerated by addition of N,N,N',N'-tetramethylethylenediamine (TEMED). Depending on the size of the separated proteins of interest, different concentrations of acrylamide (8-12%) were used (Table 11). After polymerization, isopropanol was removed and the top of the separating gel was rinsed with ddH₂O. Residual water was removed with Whatman paper before the stacking gel (Table 12) was poured on top of the separating gel and suitable combs (10-well, 15-well or Prep/2-D-well) were inserted.

Table 11: Gel solutions for SDS separating gels (10 mL).

	8%	10%	12%
Acrylamide:bisacrylamide (37.5%:1%)	2.7 mL	3.3 mL	4 mL
1.5 M Tris-HCl pH 8.8	2.5 mL	2.5 mL	2.5 mL
ddH ₂ O	4.5 mL	4 mL	3.3 mL
10% (w/v) SDS	100 μ L	100 μ L	100 μ L
TEMED	20 μ L	20 μ L	20 μ L
10% (w/v) APS	50 μ L	50 μ L	50 μ L

Table 12: Gel solution for SDS stacking gels (5 mL).

	4%
Acrylamide:bisacrylamide (37.5%:1%)	700 μ L
1.5 M Tris-HCl pH 6.8	700 μ L
ddH ₂ O	3.5 mL
10% (w/v) SDS	50 μ L
TEMED	20 μ L
10% (w/v) APS	50 μ L

For electrophoresis, gels were placed into the gel chambers (Mini-Protean 3 or Protean II), and the buffer chambers were filled with SDS electrophoresis buffer (50 mM Tris, 384 mM glycine, 0.2% (w/v) SDS). The comb was removed, and the wells were rinsed with electrophoresis buffer. Before loading the protein extracts, Laemmli buffer (5x buffer: 250 mM Tris-HCl, pH 6.8, 5% (w/v) SDS, 50% (v/v) glycerol, 500 mM β -mercaptoethanol and 0.025% (w/v) bromophenol blue) was added to the samples in a 1:5 ratio, and proteins were denatured by incubation for 1 h on ice or heating to 96°C for 5 min. After loading the protein extracts onto the gel, electrophoresis was done 15 min with 60 V (Mini-Protean 3) or 16 mA (Protean II) and subsequently changed to 100-120 V and 10 W, respectively. The electrophoresis was stopped after the bromophenol blue front reached the end of the separating gel. For the determination of protein size, prestained protein standards (e.g. Precision Plus Protein Standard Dual Color) were used.

For the prefractionation of protein samples prior to MS (see 2.2.2.2.1), precasted 12% NuPAGE Bis-Tris gels were used. Therefore, gels were placed in the NuPAGE chamber, which was filled with 1x NuPAGE MOPS SDS running buffer.

2.1.3.2 Gradient SDS-PAGE

In contrast to standard SDS-PAGE, where the separating gel has a homogeneous acrylamide concentration, gradient gels are specially prepared to have low percent-acrylamide at the top and high percent-acrylamide at the bottom of the separating gel. This enables the separation of a broader range of protein size in the same gel.

Gels were poured separately as described (see 2.1.3.1) except that for the casting of the separating gel two solutions of different acrylamide concentration (Table 13) were mixed by gravity flow using a gradient maker positioned above the casting chamber.

Table 13: Gel solutions for SDS gradient separating gels (30 mL).

	6%	12%
Acrylamide:bisacrylamide (37.5%:1%)	6 mL	12 mL
1.5 M Tris-HCl pH 8.8	11.25 mL	11.25 mL
ddH ₂ O	12.6 mL	3.6 mL
10% (w/v) SDS	150 μ L	150 μ L
80% (v/v) glycerol	-	3 mL
TEMED	2 μ L	2 μ L
10% (w/v) APS	8 μ L	8 μ L

2.1.4 Staining of SDS gels

Following electrophoretic separation, proteins can be detected in SDS gels by complexing with silver ions or by employing organic dyes, such as Coomassie brilliant blue R-250.

2.1.4.1 Silver staining

Silver staining for the detection of proteins following gel electrophoresis was first reported by Switzer et al. (280) and is based on the complex formation of ionic silver with proteins followed by the reduction to its metallic form. Thus, protein bands are visualized where the reduction occurs. The method is around 100 times more sensitive than methods using Coomassie brilliant blue R-250 (see 2.1.4.2), being able to detect proteins in the nanogram range.

For the silver staining of SDS gels, all steps were carried out at room temperature with gentle shaking. After electrophoresis, gels were incubated twice for 30 min or overnight in fixation solution (50% (v/v) methanol, 12% (v/v) acetic acid, 0.1% (v/v) 37% formaldehyde). The combination of low pH, a high organic solvent and the cross-linker formaldehyde was used to insolubilize the proteins within the gel matrix (fixation process). To remove SDS and methanol from the gel matrix, gels were incubated three times for 20 min in 50% (v/v) ethanol. The incubation in the methanol and ethanol solutions led to a dehydration of the gels. Therefore, gels were rehydrated for 1 min in an aqueous 0.02% (w/v) sodium thiosulfate (STS, Na₂S₂O₃) solution followed by two washing steps in dH₂O. Treatment of the gels with the sulfiding reagent STS increased the sensitivity of silver staining (sensitization). It forms a noncovalent complex with the proteins by ionic binding and yields, in the presence of an excess of silver, Ag₂S (silver sulfide), which acts as a catalytic center for the reduction of silver ions into metallic silver (281). Thus, gels were incubated for 20 min in silver nitrate (AgNO₃) solution (0.2% (w/v) AgNO₃, 0.075% (v/v) 37% formaldehyde) and subsequently washed twice with dH₂O. Development of the staining was induced by placing the gels in developer solution (6% (w/v) sodium carbonate (Na₂CO₃), 0.005% (w/v) Na₂S₂O₃, 0.1% (v/v) 37% formaldehyde). This led to a shift from an acidic towards alkaline pH range, where formaldehyde was able to reduce the silver ions complexed by the proteins. Furthermore, the addition of micromolar amounts of sodium thiosulfate reduced the background by preventing

the deposition of silver or insoluble silver salts. After obtaining the desired staining degree, the reaction was stopped by placing the gels for 10 min or overnight in fixation solution. The gels were equilibrated in storage solution (20% (v/v) ethanol, 2% (v/v) glycerol) for at least 15 min before they were scanned (see 2.1.6) and dried (see 2.1.4.3).

2.1.4.2 Coomassie staining

The staining of protein gels with Coomassie dyes is based on its stoichiometric binding to proteins under acidic conditions, where the dye's anions are linked to the protonated amino groups of the proteins through ionic interactions and Van der Waals forces. Staining of proteins with Coomassie brilliant blue R-250 is faster but less sensitive (about 100 ng of protein per band) compared to silver staining (see 2.1.4.1).

The Coomassie staining of SDS gels was accomplished at room temperature with gentle agitation. Following electrophoresis, gels were incubated for 15 min in fixation solution (50% (v/v) methanol, 12% (v/v) acetic acid). Visualization of protein bands was achieved by placing the gels in staining solution (50% (v/v) methanol, 12% (v/v) acetic acid, 0.04% (w/v) Coomassie brilliant blue R-250) until an appropriate staining of the protein bands was acquired. As this method was only used to stain gels for the prefractionation of complex protein mixtures prior to MS (see 2.2.2.2.1), a decreased amount of Coomassie brilliant blue R-250 compared to the standard protocol (0.1% (w/v)) was used. Thereby, the risk of strong staining was reduced, circumventing time consuming destaining procedures and ensuring a complete destaining of excised gel bands prior to tryptic cleavage (see 2.2.2.2.2). Background staining was removed by washing the gels in fixation solution, which was changed several times until a clear band pattern was observed.

2.1.4.3 Drying of SDS gels

The gels were packed air bubble-free between two wet cellophane foils and dried at room temperature.

2.1.5 Western blot analysis

Western blot analysis represents a further method for the detection and identification of proteins. SDS-protein complexes separated by SDS-PAGE can be electrophoretically transferred to an absorbent membrane (blotting), forming an exact replica of the gel with the high-resolution of the protein pattern, where they can be individually detected using specific antibodies (282).

2.1.5.1 *Semi-dry blotting*

In this study, blotting of SDS gels to polyvinylidene difluoride (PVDF) transfer membranes was performed with a semi-dry blotting apparatus. The fast and efficient transfer of proteins to the immobilizing membrane by semi-dry blotting uses two plate electrodes generating a uniform electric field over a short distance and horizontally sandwiching the gel and membrane between two stacks of buffer-soaked filter papers. This method requires considerably less buffer than the tank blotting method and allows the use of a discontinuous buffer system, ensuring a faster and optimized electrotransfer (283).

Following electrophoresis, SDS gels were incubated in anode buffer II (0.3 M Tris) for 30 sec. PVDF membranes, cut to size of the gels, were activated with methanol, washed twice with dH₂O and equilibrated with anode buffer II. Three filter papers (Whatman) were soaked in anode buffer I (25 mM Tris) and placed onto the anode plate. On their top, two filter papers imbued with anode buffer II were placed, followed by the PVDF membrane and the gel. Three filter papers soaked with cathode buffer (40 mM ϵ -aminocaproic acid, 0.01% (w/v) SDS) were placed on the gel before the cathode plate was installed. The whole setting was assembled air bubble-free and up to four mini gels could be blotted in parallel. Proteins were transferred with 0.8 mA/cm² gel for 2.5 h.

2.1.5.2 *Immunodetection*

After blotting, the efficiency of the protein transfer was checked using Ponceau S staining. Therefore, membranes were incubated for 15 min in Ponceau staining solution (0.5% (w/v) Ponceau S, 1% (v/v) acetic acid). Background staining was removed by washing the membranes three times for 10 min with Ponceau destaining solution (10% (v/v) acetic acid, 40% (v/v) ethanol), and the protein band pattern was digitalized (see 2.1.6). Membranes were destained in TBST (30 mM Tris-HCl, pH 7.4, 150 mM NaCl, 0.1% (v/v) Tween20), and non-specific binding sites were blocked for 1h at room temperature in 5% (w/v) nonfat dry milk in TBST. Probing of the membranes with primary antibodies in an appropriate dilution was performed overnight at 4°C in either 5% nonfat dry milk/TBST or 5% (w/v) BSA in TBST (see 1.6, Table 7 and Table 8). Unbound antibodies were removed by washing three times for 10 min in TBST before membranes were incubated with the appropriate horseradish peroxidase (HRP)-coupled secondary antibody (see 1.6, Table 9) diluted 1:15000 in 5% nonfat dry milk/TBST for 1 h at room temperature. Following washing of the membranes (three times, 10 min, TBST), immunoreactive signals were visualized with the enhanced chemiluminescent detection system plus (ECLplus) on Hyperfilm ECL according to manufacture's instructions. 2 mL of solution A was mixed with 50 μ L of solution B immediately before use and added to the membranes for 5 min at room temperature. Subsequently, membranes were placed into a developer cassette, and Hyperfilm ECL films were exposed under red light conditions for an appropriate time before they were developed

using the Agfa Curix 60 developer and digitalized (see 2.1.6). In order to reprobe the membranes, bound antibodies were removed by incubating the membranes for 20 min at 55°C in 62.5 mM Tris-HCl buffer, pH 6.8, containing 10 mM β -mercaptoethanol and 2% (w/v) SDS.

2.1.5.3 Multiscreen validation of antibodies

Specificity of rat-monoclonal anti-Lrrk2 antibody clones (see 1.6, Table 8) obtained after stable recloning in hybridoma cells was analyzed on NIH3T3 cell lysates by western blot analysis using the Mini-Protean II multiscreen apparatus. 100 μ g total protein was separated by SDS-PAGE (Prep/2D comb) (see 2.1.3.1) and electroblotted onto a PVDF membrane (see 2.1.5.1). After blocking non-specific binding sites in 5% nonfat dry milk/TBST for 1 h at room temperature, the membrane was clamped between the gasket and the sample template of the multiscreen apparatus. The apparatus' channels were loaded air bubble-free with 500 μ L of 10-fold serial dilutions (1:1-1:100) of the antibody-containing hybridoma supernatants (see 1.6, Table 8) in 5% nonfat dry milk/TBST. Following incubation for 3 h at room temperature with agitation, the antibody solutions were removed by vacuum aspiration and the membrane was washed 10 min by applying 500 μ L TBST/channel to remove unbound antibody. Then, the membrane was placed into a vessel and washing with TBST was repeated twice for 10 min at room temperature before the membrane was incubated for 1 h at room temperature with the HRP-conjugated anti-rat secondary antibody (see 1.6, Table 9; 1:15000 in 5% nonfat dry milk/TBST). The membrane was washed three times for 10 min with TBST, and antigen-antibody complexes were subsequently visualized as described (see 2.1.5.2).

2.1.6 Digitalizing of SDS gels and western blot films

Silver stained SDS gels and immunosignals on Hyperfilms were digitalized using a GS-710 Calibrated Imaging Densitometer, Agfa FotoLook 36 and Adobe Photoshop 7.0 software. Scans were performed at a resolution of 300 dpi.

2.2 Analysis of protein-protein interactions

The analysis of PPIs represents a crucial element for the functional annotation of proteins, e.g. the identification of specific interaction partners of a given target protein provides significant evidence for its physiological function and related cellular signaling networks. A multitude of methods for the detection and analysis of PPIs have been developed (reviewed in (284-287)), but the combination of affinity purification and mass spectrometry (AP-MS) represents a key technique in the identification and characterization of protein complexes (288). Protein complexes are purified directly from cellular lysates by affinity-based methods and their components are subsequently identified by MS.

2.2.1 Immunoprecipitation

For the affinity purification of protein complexes, either an antibody recognizing the target protein can be used or the affinity-tagged recombinant protein. co-IP utilizes suitable antigen-specific antibodies for the extraction of functional protein complexes from cellular lysates. Three different approaches for performing a co-IP are available: the traditional (classic) method, the antibody coupling method and the antibody cross-linking method (289). The advantage of immobilizing the antibody to a matrix compared to the classic method is the reduction of coeluted antibody, which can interfere with the downstream analysis of protein complexes for which two main techniques can be used. The extracted protein complexes can be separated by SDS-PAGE and analyzed by western blotting. This approach, however, depends on the identification of proteins that are suspected to interact with the target protein and is thus hypothesis-driven. In contrast, discovery-driven approaches apply MS-based techniques for the analysis of the extracted target protein and its binding partners.

A lack of specific and suitable antibodies for the target protein often favors the overexpression of the tagged protein, but this approach entails some drawbacks. It can induce potentially deleterious overexpression phenotypes and can alter the protein's properties, thereby affecting the composition of the related complex (290). Thus, co-IP, which targets PPIs from an unaltered *in vivo* setting, still represents the gold-standard for the analysis of PPIs.

2.2.1.1 Validation of antibodies

To obtain antibodies applicable for IP, the rat-monoclonal anti-Lrrk2 antibody clones (see 1.6, Table 8) were tested for their suitability in an IP by using a streptavidin-biotin-based approach. Streptavidin coated microtiter plates (BioBind Microtiter microplates) were washed once with 400 μ L PBS per well and incubated for 30 min at room temperature under agitation with 50 μ L biotin-conjugated mouse-polyclonal anti-rat IgGs (Biotin-SP-conjugated AffiniPure Mouse Anti-Rat IgG (H+L); see 1.6, Table 9) diluted 1:200 in PBS per well. Due to the high

biotin-binding affinity of streptavidin, the biotinylated anti-rat antibodies were immobilized on the plates, and unbound IgGs were subsequently removed by washing the wells twice with 400 μ L PBS. Then, 100 μ L of the anti-Lrrk2 antibody subclones were added to the wells and incubated for 30 min at room temperature under agitation, thereby binding to the anti-rat IgGs. The wells were washed two times with 400 μ L PBS to remove unbound antibodies and incubated overnight at 4°C under agitation with 100 μ L protein extracts derived from NIH3T3 cells (0.3 μ g/ μ L total protein, diluted in PBS) per well to form an antigen-antibody complex. After washing the wells with 400 μ L PBS, bound proteins were eluted by incubating the wells for 1 h at 4°C under agitation with 20 μ L 5x Laemmli buffer (see 2.1.3.1). Eluted proteins were separated by SDS-PAGE (see 2.1.3.1) and analyzed by silver staining (see 2.1.4.1) and western blotting (see 2.1.5). Antibodies showing a clear immunosignal for Lrrk2 were considered as positive and selected for further immunoprecipitation experiments.

2.2.1.2 Traditional (classic) IP

In the traditional IP approach, the antigen-antibody complex is formed in a sample solution and subsequently captured by an IgG-binding protein (Protein A or Protein G) that is immobilized on a solid support. The precipitated immune complex can be analyzed by SDS-PAGE, often followed by western blot detection to verify the identity of the antigen and bound interaction partners.

Total NIH3T3 cell lysates were precleared by adding Protein-G-Plus-Agarose in a 1:20 ratio for 10 min at 4°C. The precleared lysates were adjusted with PBS to a final protein concentration of 1 μ g/ μ L and 500 μ L were incubated overnight at 4°C with a final concentration of 4, 8 or 10 μ g/mL anti-Lrrk2 antibody (purified clone 1E11 and 2E12, respectively; see 1.6, Table 8) at a time. Bead control samples without antibody were prepared in parallel. Immune complexes were precipitated by adding 50 μ L Protein-G-PLUS-Agarose for 2 h at 4°C, and unbound proteins were removed by washing the resin three times with 800 μ L ice-cold PBS. To elute bound proteins, the resin was incubated with 60 μ L Laemmli sample buffer (62.5 mM Tris-HCl, pH 6.8, 2% (w/v) SDS, 25% (w/v) glycerol, 0.01% (w/v) bromophenol blue; Bio-Rad) for 10 min at 60°C with shaking. Prior to SDS-PAGE, β -mercaptoethanol was added to a final concentration of 700 mM to the samples. Protein complexes were separated on SDS gels (see 2.1.3.1) and subsequently analyzed by silver staining (see 2.1.4.1) and western blotting (see 2.1.5).

2.2.1.3 IP with coupled antibody

One drawback of the classic IP method is the coelution of the IP antibody with immune complexes, which can interfere with downstream analyses (289). Immobilization of the IP antibody by its covalent conjugation to an activated support represents one approach to prevent eluate contamination. This method utilizes the activation of a chemically inert

polysaccharide resin like sepharose by cyanogen bromide (CNBr) to which proteins and other primary amines can covalently bind.

The anti-Lrrk2 antibody (clone 1E11) was covalently coupled to Cyanogen Bromide Activated Sepharose 4B according to the manufacture's instructions with minor modifications. An appropriate amount of freeze-dried matrix was incubated for 30 min on ice with intermitted panning in 200 mL swelling buffer (1 mM HCl) per g resin to remove bound lactose, which serves as stabilizer for the beads during the freeze-drying process, and for swelling the matrix. 0.5 g of matrix yields approximately 1.75 mL soaked resin. The use of HCl additionally stabilizes the reactive cyanate ester groups, which hydrolyze rapidly to inert carbamates under alkaline conditions. After transferring the soaked matrix to a Büchner funnel, the swelling buffer was removed by gentle suction, and the matrix was washed once in 10-fold matrix volume ddH₂O. Subsequently, the resin was equilibrated in coupling buffer (0.1 M sodium hydrogen carbonate, pH 8.5, 0.5 M NaCl; 5 mL per g dry matrix) and immediately transferred to a 4-fold matrix volume of PBS containing the rat-monoclonal anti-Lrrk2 antibody to prevent hydrolysis of the reactive groups. The antibody was coupled at a density of 4 mg per mL resin overnight at 4°C. A control matrix was prepared in parallel by incubating the resin in PBS containing 4 mg/mL total rat IgGs (see 1.6, Table 10). The next day, the coupling solution was removed by gentle suction on a Büchner funnel, and the binding efficiency of the ligand was monitored by determining the solutions' optical density (OD) at 280 nm (OD₂₈₀) before and after coupling. Unbound ligands were removed by washing the matrix three times in a 5-fold matrix volume coupling buffer, and unreacted groups were blocked for 2.5 h at room temperature in blocking buffer (0.2 M glycine). The matrix was extensively washed four times, alternating between coupling buffer and acetate buffer (0.1 M acetic acid, pH 4, 0.5 M NaCl) and subsequently stored as 1:4 slurry in 1 M NaCl containing NaN₃ at 4°C.

For immunoprecipitation, NIH3T3 cell lysates were precleared using the rat IgG-coupled control matrix. Thereto, the control matrix was added at a 1:10 ratio to the lysate and incubated for 30 min at 4°C under rotation. The protein concentration of the precleared lysate was determined using the Bradford method (see 2.1.2) and was subsequently adjusted with lysis buffer to a final concentration of 2 µg/µL. 500 µL of the precleared lysate were then incubated with either the anti-Lrrk2- or the IgG-coupled resin in a 1:10 ratio overnight at 4°C and agitation. The next day, matrices were washed six times with 500 µL ice-cold lysis buffer (see 2.1.1.1) prior to the elution of the protein complexes in 1x Laemmli sample buffer (see 2.2.1.2) supplemented with 10 mM dithiothreitol (DTT) for 10 min at 60°C and 900 rpm. Precipitated proteins were separated by SDS gels (see 2.1.3) and visualized by silver staining (see 2.1.4.1) as well as analyzed by western blotting (and 2.1.5).

2.2.1.4 IP with cross-linked antibody

In addition to the direct covalent coupling to a chemically activated support matrix, the IP antibody can be immobilized by cross-linking. This method utilizes a chemical cross-linker to conjugate the antibody to an IgG-binding protein (Protein A or Protein G) resin by a covalent bond. In contrast to direct coupling, where primary amines are randomly bound to the matrix and hence randomly orientated, covalent cross-linking is site-directed. Protein G binds preferentially to the Fc portions of the antibody, therefore preserving the antigen-binding domain.

The rat-monoclonal Lrrk2 specific antibody (clone 1E11) was covalently cross-linked to Protein G Sepharose 4 Fast Flow beads as outlined by Thermo Fisher Scientific and described elsewhere (291). Therefore, the matrix was equilibrated by washing two times with a 2.5-fold matrix volume of binding/wash buffer (50 mM sodium borate, pH 8.2) and subsequently incubated for 30 min at room temperature under gentle agitation with a 2-fold matrix volume of the antibody, diluted 1:1 in binding/wash buffer. Binding of the antibody was performed at a density of 1 mg per mL matrix. The antibody solution was removed, and binding efficiency was verified by determining the absorption of the solution before and after incubation with the matrix at OD₂₈₀. Then, the beads were washed twice with a 2.5-fold matrix volume of binding/wash buffer, and a small sample of the matrix was removed to analyze the cross-linking efficiency (see below). The antibody was cross-linked by incubating the beads with a 2-fold matrix volume of 25 mM dimethyl pimelimidate (DMP) in cross-linking buffer (0.2 M triethanolamine, pH 8.2) for 1 h at room temperature. This homobifunctional imidoester cross-linker reacts with primary amines under alkaline conditions to form amidines, resulting in a covalent attachment of the antibody to Protein G. Surplus DMP was removed by washing the matrix two times with a 2.5-fold matrix volume of cross-linking buffer, and remaining active sites were blocked in 1-fold matrix volume 0.1 M ethanolamine (pH 8.2) for 10 min at room temperature. The beads were washed twice with a 2.5-fold matrix volume of elution buffer (200 mM glycine, pH 2.5, 500 mM NaCl, 0.1% NP-40) to remove unbound antibody and subsequently with binding/wash-buffer for use. Beads were stored as 50% slurry in PBS with 0.01% (w/v) Thimerosal in PBS at 4°C. In parallel, a control matrix was prepared by cross-linking rat IgG2as (see 1.6, Table 10) at the same density as the IP antibody to Protein G sepharose.

The efficiency of the cross-linking reaction was analyzed by incubating equal amounts of the matrix before and after the incubation with DMP with a 2-fold matrix volume of elution buffer for 10 min on ice (first eluate) followed by Laemmli buffer (see 2.1.3.1, diluted 1:5 in ddH₂O), which was neutralized by the addition of 5% (v/v) 2 M Tris-HCl (pH 9), for 15 min at 37°C with shaking (second eluate). After neutralization of the glycine eluates with 5% (v/v) 2 M Tris-HCl (pH 9), both eluted proteins and equal volumes of the antibody or rat IgG solution before and after binding to the matrix were separated by SDS-PAGE (see 2.1.3.1)

and subsequently analyzed by silver staining (see 2.1.4.1).

For IP, total cellular lysates derived from NIH3T3 cells or mouse brains were adjusted with lysis buffer to a total protein concentration of 0.5 mg/mL and 1 mL was precleared by incubation with Protein G Sepharose in a ratio of 1:10 for 30 min at 4°C under gentle agitation. For immunoprecipitation, the precleared lysate was incubated with anti-Lrrk2-Protein G Sepharose matrix in a ratio of 1:40 overnight at 4°C with rotation. As a control for non-specific protein binding, IP negative controls were performed by incubation with the rat IgG2a-control matrix at the same ratio. The matrices were washed three times with 500 µL ice-cold HEPES buffer (20 mM HEPES, pH 7.5, 50 mM NaCl, 0.1% (v/v) NP-40, 1x Roche complete protease inhibitor mixture, 1x phosphatase inhibitor cocktail 1 and 2). Subsequently, protein complexes were eluted in a 2-fold matrix volume Laemmli buffer (see 2.1.3.1, diluted 1:5 in ddH₂O) for 15 min at 37°C and gentle agitation. Precipitated proteins were subjected to SDS-PAGE (see 2.1.3) followed by silver staining (see 2.1.4.1) and western blotting (see 2.1.5), respectively.

2.2.2 Quantitative immunoprecipitation combined with knockdown (QUICK assay)

A major challenge in the analysis of PPIs using affinity purification methods such as immunoprecipitation to isolate protein complexes is the identification of *bona fide* interacting partners versus non-specific contaminants. Immunoprecipitates comprise not only the target protein itself and related complex partners but also proteins that bind non-specifically to the antibody or to the matrix as well as proteins with cross-reactivity to the antibody, generating a significant background. Therefore, an appropriate negative control has to be employed in parallel to discriminate specific and non-specific binding. Proteins identified in the control can be used to subtract the background from the experimental protein complex by two different approaches. Gel-based separation and visualization of individual proteins of the experimental and control IP reveal proteins that are present in both and thus not specific to the target complex. Intrinsic protein bands of the experimental IP can be recovered for further analysis by MS. Alternatively, peptides derived from both immunoprecipitates can be directly analyzed by liquid chromatography-tandem mass spectrometry (LC-MS/MS) and those identified in both can be considered as background (287, 292). However, for the identification of complex components, the purity of the samples should be enhanced to a maximum. Even though the incorporation of a negative control allows discrimination between specific and non-specific interactions, a lack of quantitative information impedes the validation of PPIs with accuracy.

The QUICK (quantitative immunoprecipitation combined with knockdown) assay reported by Selbach and Mann (293) represents an adaptation to standard AP-MS strategies. This approach assesses interactions between endogenous proteins at their normal cellular level by a combination of stable isotope labeling with amino acids in cell

culture (SILAC) (294), RNAi, co-IP and quantitative MS (Figure 8). Therefore, two cell populations are labeled by SILAC, whereby the incorporation of either a normal amino acid or its heavy isotope-substituted counterpart leads to a distinct labeling of the proteins from both populations, constituting the basis for the quantitative analysis of protein interactions by MS. RNAi is used to knockdown the expression of the target protein in one of the two cultures, leading to a significant decrease in its abundance. This population represents the negative control in the following immunoprecipitation of endogenous protein complexes. Precipitated proteins from both samples are combined in equal parts, proteolytically cleaved and analyzed by LC-MS/MS. In principle, experimental and control sample contribute equally to background proteins that bind non-specifically to the antibody or the matrix, and the resulting peptides should be represented in the mass spectra by doublets in a 1:1 ratio. Genuine components of the protein complex will appear in doublets in which the peptide peaks derived from the RNAi-treated samples occur with a decreased intensity, leading to a ratio >1 (287, 293).

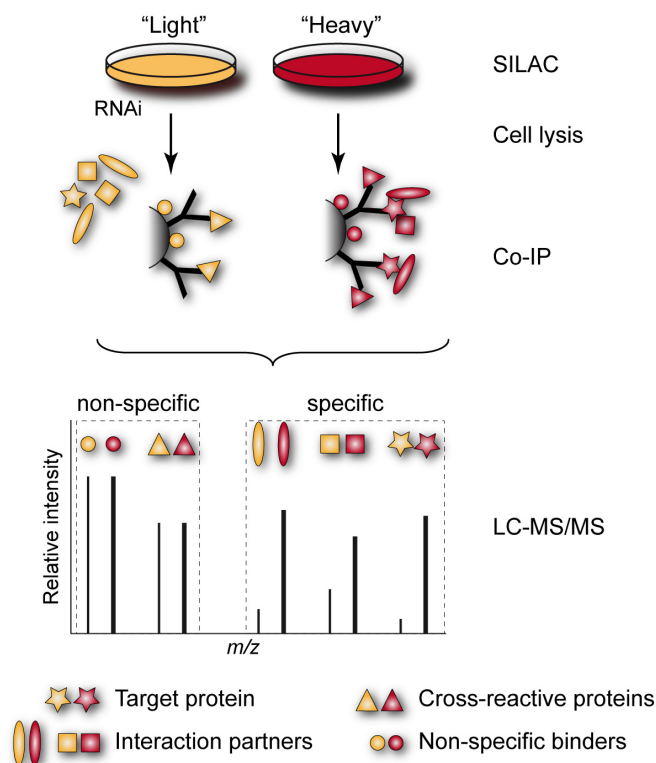


Figure 8: Strategy to screen for endogenous PPIs by QUICK.

Two cell populations are differentially labeled with stable isotopes by culturing them in medium containing normal (light) amino acids or their heavy isotope-substituted counterparts (SILAC). Expression of the target protein is knocked down by RNAi in one of the cultures and protein complexes are precipitated by IP. In principle, four different classes of proteins are found within an IP: the target protein, its specific complex partners, proteins that cross-react with the IP antibody and those binding non-specifically to antibody and matrix. Knockdown of the target protein by RNAi leads to a significant decrease in its amount. Consequently, only non-specific background proteins remain in the IP. Prior to LC-MS/MS, IP samples derived from both conditions are combined and subjected to the analysis. The schematic mass spectrum displays that non-specifically bound proteins will be represented by peaks of equal intensity, whereas the target protein itself and its complex partners are detected by higher intensities in the heavy form. As a further control, cross-over experiments are conducted where the knockdown is placed in the heavy labeled condition. This should yield reciprocal abundance ratios. Adapted from (287, 293).

2.2.2.1 Sample preparation

The QUICK approach was applied for the systematic analysis of the Lrrk2 interactome. Therefore, SILAC labeling of wt and LVmiB3 transduced NIH3T3 cells (see 2.6.6) was done as described in 2.6.3. Immunoprecipitation was conducted with the rat-monoclonal anti-Lrrk2 antibody clone 1E11 covalently cross-linked to Protein G Sepharose (see 2.2.1.4) with some modifications. Crude lysates from heavy and light labeled cells were adjusted with lysis buffer to a total protein concentration of 1 mg/mL and 1 mL was precleared by incubation with Protein G Sepharose in a 1:10 ratio. In order to investigate possible global changes in protein abundance ratios induced by lentiviral-mediated RNAi, samples of the whole cell lysates were kept. For immunoprecipitation, precleared lysates were incubated with anti-Lrrk2-Protein G Sepharose matrix in a ratio of 1:40 overnight at 4°C. Matrices of the two separated IPs were combined, unbound proteins were removed by washing with HEPES buffer and protein complexes were eluted in a 1-fold matrix volume Laemmli buffer (see 2.1.3.1, diluted 1:5 in ddH₂O). Both precipitated proteins and whole cell lysates were subsequently analyzed by LC-MS/MS (see 2.2.2.2).

2.2.2.2 Mass spectrometry

Mass spectrometry represents an indispensable analytical tool for protein-protein interactions. Within the AP-MS workflow, protein complexes are purified by affinity-based approaches and subsequently characterized by MS. The identification of proteins by MS is fundamentally premised on the determination of the mass-to-charge ratio (m/z) of ions in a gas phase, which serves as a basis for various protein identification and characterization strategies. Thereto, different types of highly sensitive mass spectrometers are currently used with various ionization techniques (295). In principle, mass spectrometers consist of three essential parts: in the ion source, neutral sample molecules are converted into ions, transferred to the gas phase and accelerated into the mass spectrometer where the ions are separated according to their m/z value by the mass analyzer and are finally detected by the ion detector, which amplifies each ion impact to an electric signal. The signals are subsequently converted to a graphic output (mass spectrum) by the readout electronics, with the ion abundance (signal intensity) plotted against the m/z value. The set of measured peptide masses (peptide mass fingerprint) can be used for the identification of proteins by matching them with theoretically calculated proteolytic peptide masses for each protein within a database. However, MS can be utilized to determine additional structural features of peptides, including the amino acid sequence, and thus provides a more specific and sensitive method for the identification of proteins. Therefore, a tandem MS setting is applied, where the peptides are separated according to their m/z ratio and particular isolated ions (parent ions) are subsequently fragmented. A mass spectrum of the resulting fragments (tandem MS; MS/MS) is generated and utilized for the identification of peptides/proteins by

database search (296).

MS per se is not a quantitative technique. Quantification is, however, critical when using MS as the final identification method for PPIs. AP-MS can be a challenging assay, as the endogenous expression level of the target protein and/or its interaction partners can be low, interactions might be transient and a large background of coprecipitated proteins might be present. Therefore, the biochemical purification of protein complexes has always to compromise on specificity and selectivity, and the high sensitivity of MS-based protein identifications can result in a large number of identified false-positive interactions. However, despite protein identification, MS-based techniques allow a quantitative profiling of differentially labeled protein samples, improving the analysis of PPIs based on affinity purification. Here, true interactors or complex components are identified by a quantitative comparison between samples of the specifically enriched protein complex and an appropriate negative control. Non-specific bound proteins emerge with an equal abundance in both conditions, while significantly enriched proteins compared to the control are considered as interaction partners. This is even applicable to samples with a low degree of enrichment and/or a substantial amount of non-specific background proteins (297).

The success of protein mixture analysis by MS depends on a proper sample preparation, compatible with the downstream analysis. A prefractionation of the precipitated proteins prior to their proteolysis and MS analysis decreases the sample complexity and increases the yield of protein identifications. The different fractions are proteolytically cleaved, representing the essential step within the sample preparation, as the analysis of intact proteins is by far not as efficient as the analysis of peptides. Following proteolytic cleavage, the peptides are subjected to the analysis. Within the present study, MS-based proteomic analyses were performed in cooperation with Dr. K. Boldt (University of Tübingen).

2.2.2.2.1 Prefractionation by SDS-PAGE

The single dimension separation of peptides by a high performance liquid chromatography (HPLC) column LC-MS/MS analysis (see 2.2.2.2.3) might not provide an efficient resolution for the analysis of complex protein samples. Therefore, proteins are divided into fractions that are analyzed separately, thereby decreasing the sample complexity. Separation of the samples increases, moreover, the dynamic range of the measurement (296).

Protein samples were prefractionated by SDS-PAGE on precasted 10% NuPAGE gels (see 2.1.3.1). For the analysis of whole cell lysates, a sample volume corresponding to 100 µg total protein from heavy and light labeled cells was combined and 5x Laemmli buffer (see 2.1.3.1) was added in a 1:5 ratio. From the IP eluates, a volume of 35 µL was subjected to the fractionation. Both samples were denaturated by incubation for 5 min at 96°C before they were loaded and separated at a constant voltage on SDS gels. The run was stopped

after a separation distance of 1-2 cm and proteins were visualized by Coomassie staining (see 2.1.4.2). Gels were washed three times for 30 min with ddH₂O to remove substances that interfere with the following in-gel proteolytic cleavage, such as methanol and formaldehyde, before stained gel lanes were excised with a clean scalpel. The excised lanes were fractionated to 6 bands (IP samples) or 18 bands (whole cell lysates) that were subsequently cut into plugs of 1 mm³. For further treatment, plugs were transferred to 96 well plates.

2.2.2.2.2 In-gel tryptic cleavage

To prepare protein samples after prefractionation for MS analysis, they have to be cleaved within the gel followed by an extraction of the peptides.

Coomassie stained gel plugs, obtained after prefractionation of the proteins by SDS-PAGE (see 2.2.2.2.1), were destained by washing them twice for 15 min in 200 μ L 50% acetonitrile followed by incubation for 15 min in 100% acetonitrile. The destaining procedure was repeated if the staining was still visible. Subsequent to complete destaining of the gel plugs, 100 μ L 5 mM DTT was added, and the samples were incubated for 15 min at 60°C to reduce disulfide bonds within the proteins. After cooling to room temperature, the DTT solution was removed and replaced with 100 μ L of 25 mM 2-iodoacetamid for protein alkylation. After 45 min incubation in the dark, the gel plugs were washed twice for 15 min with 100 μ L 50% (v/v) acetonitrile, dehydrated with 100 μ L of 100% acetonitrile for 5 min and air dried for 15 min at room temperature. Subsequently, the samples were subjected to in-gel proteolysis in 10-30 μ L 50 mM ammonium bicarbonate containing 10 ng/ μ L trypsin overnight at 37°C. On the next day, a sequential extraction of the peptides from the gel plugs was performed at room temperature, ensuring the release of peptides with different physicochemical properties. Therefore, peptides were acidified by adding 5-15 μ L 2% (v/v) trifluoroacetic acid (TFA) to gain a final concentration of 0.5% (v/v) TFA in the trypsin solution. After incubation for 15 min under agitation, the supernatant was removed and transferred to a fresh 96 well plate. Elution was repeated with 70 μ L of 40% (v/v) acetonitrile containing 0.5% TFA for 15 min. The second supernatant was pooled with the first one and followed by a third extraction step in 99.5% (v/v) acetonitrile/0.5% TFA. After incubation for 15 min, the supernatant was combined with the first two, and samples were dried in a speed vac to near-complete dryness. The samples were then either stored at -20°C or 2% (v/v) acetonitrile with 0.5% TFA were directly added to a final volume of 40 μ L prior to LC-MS/MS analysis.

2.2.2.2.3 LC-MS/MS analysis

In an LC-MS/MS analysis, the peptides resulting from a proteolytic cleavage of a protein sample are separated by reverse phase HPLC and analyzed on-line by MS/MS. The

peptides loaded onto the HPLC column are eluted using a solvent gradient of increasing organic content, so that the peptides elute according to their hydrophobicity with hydrophilic peptides first and hydrophobic last. Following elution, the peptides are ionized and vaporized by electrospray ionization (ESI). The following mass spectrometric analysis generates mass information with high accuracy in the MS spectra, and further amino acid sequence information can be deduced from fragment ion information in the MS/MS spectra. The combination of these data is used for a confidential identification of peptides and thus protein matching from sequence databases. These tandem MS analyses were performed on an LTQ-Orbitrap. In principle, this hybrid mass spectrometer links two types of mass analyzer capable of detecting ions and recording mass spectra in tandem, a linear quadrupole ion trap (LTQ) and an Orbitrap, and thus combining the guiding, trapping and detection properties of the LTQ with the high accuracy m/z detection ability of the Orbitrap. A key feature of the LTQ-Orbitrap is that both mass analyzers work in parallel. The precursor ion masses are measured in the Orbitrap (MS scan) with very high accuracy and resolution and the following fragmentation profiles are obtained in the LTQ with low resolution (MS/MS scan). A true parallel operation is achieved by a selection of precursor ions from the quick initial scan in the Orbitrap analyzer that are fragmented while the MS scan is still acquired, leading to a rate close to 1 sec per cycle, with one cycle containing 1 Orbitrap spectrum acquired at a resolution of 60,000 FWHM (full width at half maximum) and 3-5 LTQ fragmentation spectra. The high mass accuracy of the Orbitrap of just 1 ppm (parts per million) for the precursor ions constrains peptide candidates to just a few sequences in the database, thereby reducing the identification of false-positives and facilitating peptide identification (298).

LC-MS/MS analysis was performed on an Ultimate3000 nano HPLC system coupled to a LTQ OrbitrapXL mass spectrometer by a nano spray ion source. Tryptic peptide mixtures were automatically injected and loaded at a flow rate of 30 $\mu\text{L}/\text{min}$ in 95% (v/v) buffer C (2% (v/v) acetonitrile, 0.1% (v/v) trifluoro acetic acid in HPLC grade water, Merck) and 5% (v/v) buffer B (98% (v/v) acetonitrile, 0.1% (v/v) formic acid in HPLC grade water) onto a nano trap column (100 μm i.d. x 2 cm, packed with Acclaim PepMap100 C18, 5 μm , 100 \AA , LC Packings). After 5 min, peptides were eluted and separated on the analytical column (75 μm i.d. x 15 cm, Acclaim PepMap100 C18, 3 μm , 100 \AA , LC Packings) by a linear gradient from 5% (v/v) to 40% (v/v) of buffer B in buffer A (2% (v/v) acetonitrile and 0.1% (v/v) formic acid) at a flow rate of 300 nL/min over 140 min. Remaining peptides were eluted by a short gradient from 40% (v/v) to 100% buffer B in 5 min. The eluting peptides were analyzed in the LTQ OrbitrapXL using XCalibur software (version 2.07). From the high resolution MS prescan with a mass range of 300 to 1500, the ten most intense peptide ions were selected for fragment analysis in the linear ion trap if they exceeded an intensity of at least 200 counts and if they were at least doubly charged. The normalized collision energy for CID (collision induced dissociation) was set to a value of 35 and the resulting fragments were detected with

normal resolution in the linear ion trap. The lock mass option was activated and a background signal with a mass of 445.120020 was used as lock mass (299). Every ion selected for fragmentation, was excluded for 30 sec by dynamic exclusion.

2.2.2.2.4 Data analysis

The identification of PPIs within the QUICK assay is based on the quantification of immunoprecipitated proteins by LC-MS/MS. Therefore, a stable isotope signature was introduced into proteins by SILAC (see 2.6.3). MS quantification on the basis of differential isotopic labeling of proteins and peptide is based on the stable isotope dilution theory, which states that a stable isotope-labeled peptide is chemically identical with its native counterpart and thus both peptides behave identical in an LC-MS/MS analysis. As the isotope mass tag induces a distinct, predictable mass shift into the peptides, which is recognized by the mass spectrometer, differentially labeled samples can be combined at an early stage of sample processing, thereby additionally excluding variations due to sample treatment. MS analysis can be performed jointly, facilitating the direct comparison of the samples in the same analysis. Quantification is obtained by matching signal intensities or peak areas of isotope-labeled peptide pairs within the respective mass spectra (Figure 9). The introduced mass difference is dependent on the isotopes and amino acids used. The heavy form of lysine, $^{13}\text{C}_6$ lysine, consists of six carbon atoms of the ^{13}C isotope, whereas its light counterpart contains 6 ^{12}C atoms. $^{13}\text{C}_6$ lysine adds therefore 6.020129 Da to the monoisotopic mass of lysine. The heavy isoform of arginine, $^{13}\text{C}_6^{15}\text{N}_4$ arginine, induces a mass shift of 10.008269 Da.

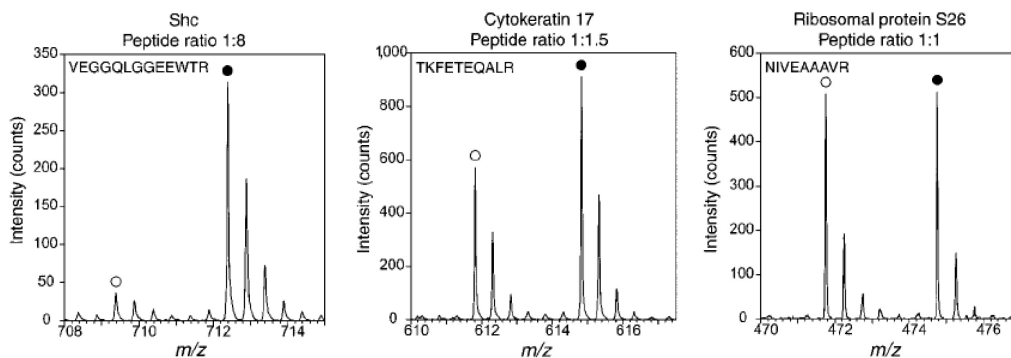


Figure 9: Representative MS spectra of SILAC peptide doublets.

The panels show three examples of SILAC peptide pairs, with the lower-mass peak cluster derived from the peptide composed of normal amino acids and the higher-mass peak cluster resulting from labeling of the same peptide with a heavy isotope amino acid (here $^{13}\text{C}_6$ -arginine). Peptide quantification doublets shown in the left and middle panel display an increased peak intensity of the labeled peptide (solid dot) over its unlabeled form (unfilled dot) (ratio of 8 and 1.5, respectively), reflecting a specific enrichment of the proteins in the respective experimental condition. In contrast, proteins of equal abundance result in a 1:1 ratio of the light and heavy peptide in the spectrum (right panel). Reprinted by permission from Macmillan Publishers Ltd: Nature Biotechnology (300). © 2003.

For quantification, all acquired spectra were processed and analyzed using the MaxQuant software (version 1.0.13.8) (301) and the mouse specific IPI database version 3.52 (number of sequences: 83947) in combination with Mascot version 2.2. Trypsin/P was selected as enzyme for cleavage with two missed cleavages allowed. Fragment ion tolerance was set to 0.5 Da and the top six MS/MS peaks per 100 Da were used. A maximum of three labeled amino acids per peptide was allowed. The precursor ion tolerance was automatically set by the MaxQuant software. Cysteine carbamidomethylation was selected as fixed modification, and methionine oxidation, phosphorylation on serine, threonine or tyrosine as well as protein acetylation were allowed as variable modifications. The peptide false discovery rate was set to 5%, the protein false discovery rate to 1%. All contaminants included in the MaxQuant contaminant database, with the exception of β -actin, as well as proteins that showed high variability (> 100%) were removed and only proteins identified and quantified in at least two of five experiments were considered for further analysis. If the identified peptide sequence set of one protein was equal to or contained the peptide set of another protein, these two proteins were grouped together by MaxQuant and not counted as independent protein hits. All details for the peptide and protein identifications and quantifications including all parameters used for MaxQuant analysis are given in Supplementary File 1 for the QUICK assay and in Supplementary File 2 for the proteome comparison. MaxQuant normalized protein ratios were utilized for the downstream analyses and a *p*-value of 0.05 was selected as threshold for significant enrichment of Lrrk2 complex components.

2.2.3 KEGG pathway enrichment and protein network analysis

For the identification of significant over-represented biological process categories within a set of proteins as well as for the analysis and visualization of PPIs, Pathway Palette (302) was used. Thereto, the genes corresponding to the significant enriched proteins within the QUICK assay (QUICK query set) were uploaded to the Pathway Palette website. In the case of protein hits with ambiguous assignment by the MaxQuant software, one gene was selected at random under the assumption that similar proteins share interaction partners.

Pathway enrichment analysis was performed based on annotations in the Kyoto Encyclopedia of Genes and Genomes (KEGG) (303) database using the respective analysis function provided by Pathway Palette. Functional terms were identified for their significant enrichment levels using the supplied *p* values.

Interaction networks were abstracted as graphs, where proteins are represented as nodes and their direct interactions as edges. Known interactions between the proteins were retrieved from the Human Protein Reference Database (HPRD) (304) and the Biological General Repository for Interaction Datasets (BioGRID) (305). Interactions were evaluated as

well as prioritized according to their “evidence”, referring to the experimental systems used for the detection, provided by the database and utilizing the following categorization: (I) “BioGRID: Low-Throughput” or “HPRD: in-vivo”, (II) “BioGRID: HTP/complex” or “HPRD: in-vitro” and (III) “BioGRID: HTP/Pairwise” or “HPRD: yeast 2-hybrid”. Within HPRD, annotations pertaining to experiments such as co-IP are designated “in vivo”, whereas GST fusion and similar “pull-down” types of experiments are summarized as “in vitro”. Experimental evidences for an interaction obtained by yeast two-hybrid are denoted as “yeast two-hybrid” (306). Unfortunately, a more detailed description of experimental techniques that constitute each of the three annotation groups is not provided. In contrast, BioGRID maintains a very detailed ontology of “evidence classes”, which are represented by coarser definitions in Pathway Palette (Table 14).

Table 14: Subdivision of BioGRID experimental evidence codes represented in Pathway Palette.

Pathway Palette interaction category	Experimental technique for interaction validation
BioGRID:HTP/complex	Affinity Capture-Western
BioGRID:HTP/complex	Affinity Capture-MS
BioGRID:HTP/pairwise	Two-Hybrid
BioGRID:Low-Throughput	Reconstituted Complex
BioGRID:Low-Throughput	Biochemical Activity
BioGRID:Low-Throughput	Copurification
BioGRID:Low-Throughput	Cocrystal Structure
BioGRID:Low-Throughput	Far Western
BioGRID:Low-Throughput	Cofractionation
BioGRID:Low-Throughput	Protein-peptide
BioGRID:Low-Throughput	Affinity Capture-Luminescence
BioGRID:Low-Throughput	Colocalization
BioGRID:Low-Throughput	FRET
BioGRID:Low-Throughput	Protein-RNA
BioGRID:Low-Throughput	Affinity Capture-RNA
BioGRID:Low-Throughput	PCA

To assess the physical cohesiveness of the resulting protein network, a Physical Interaction Enrichment (PIE) analysis (307) was implemented (in collaboration with Dr. M. Askenazi, Harvard Medical School). Thereto, a custom Python script was used to select random query sets from the reference network consisting of the 29377 mouse Entrez Gene IDs, with 51460 known interactions between them, represented in Pathway Palette. In total, a million sets, having the same size and node degree distribution as the QUICK set, were analyzed for the number of interactions within the sets to obtain a frequency distribution used for the calculation of physical cohesiveness (PIE score) and significance.

To further investigate the connectivity between the proteins of the QUICK set, interaction data from the HPRD and BioGRID database were used to construct an extended network by adding only first-order shared neighbors of the proteins, where two proteins from the QUICK set are linked by one interconnecting (intermediate) protein. Network complexity was reduced by removing edges between the first-order neighbors.

2.3 Molecular biology

2.3.1 *Escherichia coli* cultures

2.3.1.1 Liquid cultures

Liquid cultures, either small-scale (3 mL, mini-preparation) or large-scale (200 mL, maxi-preparation), were used for the expansion of *Escherichia coli* (*E. coli*) clones prior to plasmid DNA preparation (see 2.3.3). Thereto, single colonies of transformed bacteria were transferred to 3 mL LB medium (Luria-Bertani; 1% (w/v) tryptone, 0.5% (w/v) yeast extract, 1% (w/v) NaCl, pH adjusted to 7.0 with NaOH) supplemented with the appropriate antibiotics (e.g. ampicillin, kanamycin, chloramphenicol; see 1.3.6, Table 5) and grown over day at 37°C under shaking with 220 rpm in 14 mL Falcon tubes. For large-scale cultures, 200 mL LB medium containing the antibiotics were inoculated with 200 µL from the mini-preparation culture and incubated overnight at 37°C under agitation with 110 rpm in baffled flasks.

2.3.1.2 Plating cultures

Plating cultures were used for clonogenic selection (see 2.3.2) or were generated from cryo cultures (see 2.3.1.3). The *E. coli* suspension was streaked out on LB agar plates (LB medium with 1.5% (w/v) agar, supplemented with the appropriate antibiotics; see 1.3.6, Table 5) and incubated overnight at 37°C. The plates could be stored at 4°C for several days.

2.3.1.3 Cryo-preservation of bacteria

Bacteria clones carrying an appropriate DNA construct were preserved as cryo cultures. Thereto, 500 µL of an *E. coli* overnight culture were mixed with an equal volume of 80% (v/v) glycerol. After snap-freezing in liquid nitrogen, cryo cultures could be stored at -80°C for several years.

2.3.1.4 Generation of chemically competent *E. coli*

E. coli competent for chemical transformation using the rubidium chloride (RbCl₂) method (308) were generated from the *E. coli* strains DH5α and TOP10 as described elsewhere (309) with some modifications. DH5α and TOP10 cryo cultures were streaked out on LB agar plates without antibiotics and incubated overnight at 37°C. Single colonies were expanded in 2.5 mL LB medium at 37°C with constant agitation. The next day, the overnight culture was diluted 1:100 in LB medium supplemented with 20 mM magnesium sulfate and grown to an OD₆₀₀ of 0.4-0.6. After centrifugation at 5000 x *g* for 5 min at 4°C, the pellet was gently resuspended in a 0.4-fold original volume ice-cold TFB1 buffer (30 mM potassium acetate, 100 mM rubidium chloride, 10 mM calcium chloride, 50 mM manganese chloride, 15% (v/v) glycerol, pH was adjusted to 5.8 with acetic acid). The suspension was incubated for 5 min on ice before the bacteria were pelleted by centrifugation for 5 min at 5000 x *g* and

4°C. The pellet was gently resuspended in ice-cold TFB2 buffer (10 mM MOPS (3-(N-morpholino)propanesulfonic acid), 75 mM calcium chloride, 10 mM rubidium chloride, 15% (v/v) glycerol, pH was adjusted to 6.5 with potassium hydroxide solution) and incubated for 15 min on ice. The solution was then dispensed in 100 µL aliquots and snap-frozen in liquid nitrogen. The aliquots were stored at -80°C prior to use for transformation (see 2.3.2).

2.3.2 Chemical transformation of *E. coli*

For chemical transformation, competent bacteria (see 2.3.1.4) were gently thawed on ice. 30-50 ng plasmid DNA (see 2.3.3) or 5 µL of a ligation product (see 2.3.9.6) were added to 50 µL of *E. coli* suspension and incubated for 30 min on ice. The mixture was exposed to a heat pulse for 30 sec at 42°C, which induced the incorporation of DNA-salt complexes into the bacteria, and subsequently cooled down on ice for 1 min. 250 µL of SOC medium (2% (w/v) tryptone, 0.5% (w/v) yeast extract, 0.05% (w/v) sodium chloride, 20 mM glucose) were added and bacteria were grown for 1 h at 37°C with agitation at 225 rpm. For clonogenic selection, transformed bacteria were plated onto LB agar plates supplemented with the appropriate antibiotics (see 2.3.1.2) and incubated overnight at 37°C. Single colonies were expanded in liquid cultures (see 2.3.1.1) and used for plasmid DNA preparation (see 2.3.3) or cryo cultures (see 2.3.1.3).

2.3.3 Preparation of plasmid DNA

Single transformed *E. coli* colonies (see 2.3.2) were expanded in LB medium containing the appropriate antibiotics (see 2.3.1.1). Mini-preparation of plasmid DNA was carried out according to manufacture's instructions (QIAprep Spin Plasmid Miniprep Kit) applying 2 mL of a small-scale culture. For preparative purposes, 200 mL of a large-scale culture were used for the preparation by means of the QIAGEN Plasmid Maxi Kit as described in the manufacture's protocol. Both kits are based on the lysis of bacteria under alkaline conditions in the presence of SDS and the subsequent binding of plasmid DNA to a DNA-binding resin. In case of mini-preparations, DNA was eluted in 50 µL ddH₂O. For purifications applying the QIAGEN Plasmid Maxi Kit, plasmid DNA was eluted and precipitated according to manufacture's instructions before it was air-dried and dissolved in 150 µL ddH₂O. The concentration and purity of plasmid DNA preparations was determined by UV-spectrometry. Thereto, the DNA was diluted 1:100 in ddH₂O and absorption at 260 nm and 280 nm was measured. An OD₂₆₀:OD₂₈₀ ratio of 1.8 indicated a pure DNA preparation. DNA concentration was calculated according to the following equation:

$$\text{DNA concentration } [\mu\text{g}/\mu\text{L}] = \text{OD}_{260} \cdot 50 \cdot \text{dillution factor}$$

2.3.4 DNA sequencing

DNA sequencing was performed according to Sanger (310) on a capillary-based automated sequencer (ABI Prism 3100 Genetic Analyzer) using the BigDye-Terminator v3.1 Cycle Sequencing Kit. This method takes advantage of the ability of the DNA polymerase to incorporate analogues of nucleotide bases by using 2',3'-dideoxynucleotide 5'-triphosphates (ddNTPs) as substrates. The DNA template is amplified linearly by a DNA polymerase using sequence specific primers and a dNTP (2'-deoxynucleotide 5'-triphosphate) mixture that is supplemented with ddNTPs, differentially labeled by fluorescent tags referring to the four bases (A, T, G and C). Upon incorporation of a ddNTP at the 3'-end of the growing chain, the elongation is selectively terminated at an A, T, C or G. Hence, the cycle-sequence reaction results in a mixture of fluorescent labeled products of various lengths that can be resolved according to the DNA fragments' size by capillary electrophoresis and analyzed for their tags. Based on this data, the DNA sequence can be deduced.

200-500 ng of plasmid DNA template were mixed with 2 μ L BigDye Terminator Mix, containing the DNA polymerase, dNTPs and fluorescence-labeled ddNTPs, and 1 μ L primer (100 μ M, dissolved in HPLC grade H₂O; see 1.3.5, Table 2). HPLC grade H₂O was added to a final volume of 10 μ L. The sequencing reaction was performed on a thermal cycler using the following cycling program with 40 cycles from step 2 to 4:

1. 96°C 1 min denaturation of dsDNA template
2. 96°C 30 sec denaturation of dsDNA template
3. 50°C 15 sec annealing of primers
4. 60°C 4 min elongation of the primers
5. 60°C 4 min final elongation

After the cycle-sequence reaction, the DNA was precipitated by the addition of 8 μ L HPLC grade H₂O and 32 μ L 95% (v/v) ethanol (p.a.) in HPLC grade H₂O. After 15 min incubation at room temperature in the dark, the mixture was centrifuged (15 min, 16000 x g, room temperature). The DNA pellet was washed by the addition of 200 μ L 70% (v/v) ethanol in HPLC grade H₂O and centrifuged for 10 min at 16000 x g and room temperature. The DNA pellet was air-dried and resuspended in 75 μ L HPLC grade H₂O. For analyzes on the automated sequencer, 25 μ L of the dissolved DNA was applied. The resulting data were analyzed using the Vector NTI Suite 9.0 software package.

2.3.5 Separation of DNA on agarose gels

Linearized DNA fragments were separated by agarose gel electrophoresis according to their size. Dependent on the fragment size, 0.8-1.2% (w/v) DNA agarose was dissolved in TAE buffer (40 mM Tris-acetate, pH 8.0, 1 mM EDTA) by boiling in a microwave. The agarose solution was supplemented with 0.5 μ g/mL of the fluorescent DNA-intercalating ethidium bromide, poured into a gel tray and stuffed with a comb. After solidification, the

comb was removed and the tray placed into an electrophoresis chamber where it was overlaid with TAE buffer. Before loading the DNA samples into the gel wells, 6x loading buffer (0.25% (w/v) bromophenol blue, 40% (w/v) sucrose) was added in a 1:6 ratio. Electrophoresis was performed with 50-100 V until the bromophenol blue dye front reached the end of the gel. DNA fragments were visualized by UV-light irradiation and digitalized. For the determination of DNA fragment size, specific size standards were used (see 1.3.3).

2.3.6 Purification of DNA

2.3.6.1 From agarose gels

Following electrophoresis (see 2.3.5), DNA fragments were excised with a scalpel. Purification was carried out using the QIAquick Gel Extraction Kit as recommended by the manufacturer. The DNA was eluted in 30 μ L ddH₂O.

2.3.6.2 From enzymatic reactions

To remove salts, enzymes and unincorporated nucleotides from DNA fragments, the QIAquick Gel Extraction Kit or QIAquick PCR Purification Kit was used according to manufacturer's instructions. The DNA was eluted in 30-40 μ L ddH₂O.

2.3.7 Polymerase chain reaction (PCR)

PCR was used for the preparative amplification of specific DNA sequences and essentially done according to a standard procedure (311). Here, two sequence specific primers that hybridize to the sense and antisense strand of the DNA template, respectively, define the DNA region that is enzymatically amplified by a DNA polymerase. A cyclic repetition of denaturation (separation of DNA strands), annealing (hybridization of the primers to their complementary sequence) and elongation (synthesis of the complementary strand by the DNA polymerase) results in an exponential replication of the DNA template.

A *Pfu* thermostable DNA polymerase (purified from *Pyrococcus furiosus*) with 3'-5' exonuclease activity (proofreading) was used for preparative DNA amplification. The reaction mixture (50 μ L) contained 100 ng plasmid DNA template, 1x *Pfu* reaction buffer, 250 μ M dNTPs (each), 0.25 μ M sense and 0.25 μ M antisense oligonucleotide primer (see 1.3.5, Table 2) and 2.5 U *PfuTurbo* Hotstart DNA Polymerase in ddH₂O. PCR reaction was performed on a thermal cycler with the following amplification program:

- | | | | |
|----|------|--------|------------------------------------|
| 1. | 95°C | 2 min | denaturation of the dsDNA template |
| 2. | 95°C | 30 sec | denaturation of the dsDNA template |
| 3. | 55°C | 30 sec | annealing of the primers |
| 4. | 72°C | 4 min | elongation of the primers |
| 5. | 72°C | 10 min | final elongation |

The amplification stage comprised 30 cycles of stage 2 to 4. Conditions of the PCR reaction were optimized according to the size of the PCR product and primers properties. Therefore, the annealing temperature (stage 3) was set as the mean value of the melting temperature (T_m) of sense and antisense primer. Primers were designed using the Vector NTI Suite 9.0 software package so that (I) the T_m was between 50°C and 65°C, (II) the differences in the T_m was below 3°C and (III) hairpin structures and dimerization were unfavorable. The elongation time (stage 4) correlated with the length of the expected DNA fragment, with 1 kb amplified by *PfuTurbo* Hotstart DNA polymerase per minute.

2.3.8 Annealing of synthetic oligonucleotides

Lyophilized oligos (see 1.3.5, Table 3 and Table 4) were dissolved at 100 μ M in ddH₂O as indicated by the manufacturer. For annealing, 2 μ L of each complementary oligo were added to 16 μ L ddH₂O and linearized for 4 min at 94°C. After incubation for 10 min at 70°C (annealing), reactions were cooled down to 4°C.

2.3.9 Enzymatic treatment of DNA

2.3.9.1 DNA restriction

Restriction endonucleases cleave dsDNA at specific sites or adjacent to the recognition sequence by catalyzing the hydrolysis of phosphodiester bonds in the DNA backbone. Resulting products possess either blunt or sticky ends, depending on the enzyme's nature, and have a free 3'-hydroxyl group and 5'-phosphate group.

Empty plasmid vectors (5 μ g) and complementary DNA (cDNA) containing plasmid vectors (5 μ g) were digested for 3 h with 10-40 U of the appropriate sequence-specific enzyme under optimal buffer and temperature conditions defined by the manufacturer in a 50 μ L reaction mixture for further cloning (see 2.3.9.6). Restriction of vectors with two enzymes that need different buffer conditions was performed as sequential digestion, where the DNA was purified after the first reaction using the QIAquick Gel Extraction Kit (see 2.3.6.2). Restricted plasmid DNA was analyzed by agarose gel electrophoresis (see 2.3.5) and the fragments of interest were excised and purified (see 2.3.6.1).

2.3.9.2 Phosphorylation of DNA fragments

Synthetic oligos possess a hydroxyl group at their 5'-end, thus requiring the generation of a reactive 5'-phosphate group for subsequent ligation into plasmid vectors. For this purpose, T4 polynucleotide kinase (PNK) was used, which catalyzes the transfer of the γ -phosphate from ATP to 5'-hydroxyltermini of polynucleotides.

5 μ L of the annealed oligos (see 2.3.8) were incubated in a reaction volume of 10 μ L with 1x PNK reaction buffer, 10 U PNK and 0.1 mM ATP for 90 min at 37°C. Subsequently, PNK was heat-inactivated by incubation for 10 min at 70°C.

2.3.9.3 Dephosphorylation of DNA fragments

Digestion of dsDNA with restriction enzymes generates a reactive phosphate group at the 5'-end of the linearized plasmids which readily ligates with the corresponding 3'-hydroxyl group of a compatible cohesive or blunt end of the same plasmid during subsequent ligation. This relegation competes with the insertion of an insert during the ligation reaction and thereby strongly reduces the yield of desired ligation product. In order to prevent relegation of a linearized plasmid, the 5'-phosphate group was removed utilizing alkaline phosphatase.

Dephosphorylation was achieved by incubation of 1-2 μg of the linearized plasmid DNA with 2 U shrimp alkaline phosphatase (SAP) in 1x SAP reaction buffer in a total volume of 20 μL for 10 min at 37°C. Salts and enzyme were subsequently removed by purification of the DNA using the QIAquick Gel Extraction Kit (see 2.3.6.2).

2.3.9.4 Blunting of DNA fragments

For ligation of DNA fragments with non-compatible cohesive ends, 5'- and 3'-protruding termini were blunted by the Klenow (large) fragment of DNA polymerase I from *E. coli*, a DNA-dependent DNA polymerase that combines a 5'-3' polymerase and 3'-5' exonuclease activity. In the presence of dNTPs it is therefore used to fill in 5'-protruding ends with dNTPs (5'-3' polymerase activity) and to generate blunt ends from 3'-overhangs due to its 3'-5' exonuclease activity.

Degradation of 3'-single-stranded (ss) overhangs was conducted in a final volume of 40 μL containing 3-5 μg of linearized template DNA, 5 U Klenow fragment and 1x reaction buffer (NEBbuffer EcoRI) and incubation of the mixture for 3 min at 37°C. For the subsequent fill in reaction of 5'-protruding ends, dNTPs were added to a final concentration of 4 mM each as well as 1 μL of 10x reaction buffer and 5 U Klenow fragment. The reaction mixture was adjusted to a final volume of 50 μL with ddH₂O and incubated for additional 30 min at 37°C. DNA was purified using the QIAquick Gel Extraction Kit (see 2.3.6.2).

2.3.9.5 Addition of 3'-A overhangs (A-tailing)

PCR products obtained with the *Pfu* DNA polymerase (see 2.3.7) possess blunt ends due to the enzyme's 3'-5' exonuclease activity, which prevents the addition of 3'-A overhangs necessary for TA-cloning (e.g. TOPO-cloning, see 2.3.10). However, taking advantage of the nontemplate-dependent terminal transferase activity of a *Taq* polymerase (from *Thermus aquaticus*), single A overhangs can be added to the 3'-end of the PCR products.

The post-amplificational addition of 3'-A overhangs was carried out in a final reaction volume of 50 μL containing 1x *Taq* polymerase buffer, 0.2 mM dATP, 0.5 U *Taq* polymerase, 1.25 mM MgCl₂ and approximately 100 ng of the purified PCR product. The reaction mixture was incubated for 15 min at 72°C, cooled down to room temperature, and DNA fragments were purified using the QIAquick PCR purification kit (see 2.3.6.2).

2.3.9.6 DNA ligation

DNA ligation generates phosphodiester bonds between the 3'-hydroxyl and 5'-phosphate group of two DNA segments having blunt or complementary cohesive ends, catalyzed by a DNA ligase.

Purified restricted and dephosphorylated plasmid vectors (about 10-150 fmol; see 2.3.9.1 and 2.3.9.3) and purified restricted DNA inserts (see 2.3.9.1) or phosphorylated synthetic double-stranded oligos (see 2.3.8 and 2.3.9.2) were combined and incubated with 1 U T4 DNA ligase and 1x T4 DNA ligase buffer in a final volume of 20 μ L overnight at 16°C. The molar ratio of vector to insert DNA was optimized for the different ligations and varied from 1:7 (fragments > 3 kb) to 1:50 (synthetic oligonucleotides). Reactions lacking the insert DNA served as negative controls (vector control).

Before transformation of *E. coli*, the whole ligation reaction was precipitated with isopropanol to remove salts and enzymes. Therefor, 1 μ L glycogen (20 μ g/ μ L), 20 μ L 8 M LiCl and 500 μ L isopropanol (p.a.) was added to 20 μ L ligation reaction mixture and adjusted to a final volume of 1 mL with ddH₂O. Glycogen was used as a carrier to reduce the loss of DNA when precipitating small amounts of DNA. The mixture was incubated for 20 min at -20°C and subjected to centrifugation for 10 min at 16000 x *g* and room temperature. Precipitated DNA was washed in 200 μ L 70% (v/v) ethanol (p.a.) and centrifuged at 16000 x *g* and room temperature for 10 min. The DNA pellet was air-dried and dissolved in 10 μ L ddH₂O for 30 min at 4°C. 5 μ L of the precipitated ligation product was transformed into competent *E. coli* (see 2.3.2). Plasmid DNA was isolated (see 2.3.3) and constructs were validated by restriction analysis (see 2.3.9.1) and DNA sequencing (see 2.3.4).

2.3.10 TOPO cloning

Cloning of long (> 3 kb) PCR products was performed by TOPO-based cloning using the TOPO XL PCR Cloning Kit. This method is based on an improved TA cloning approach, using the linearized plasmid vector pCR-XL-TOPO with 3'-T overhangs generated by *Vaccinia* DNA topoisomerase I (TOPO), which remains covalently bound to the DNA after restriction ("activated plasmid"). 3'-A overhangs of respective PCR products complementary to the 3'-T overhangs of the vector can be efficiently ligated, catalyzed by the already present topoisomerase I.

TOPO-based cloning was done according to manufacturer's instructions. After the addition of 3'-A overhangs to *Pfu* amplified PCR products (see 2.3.7 and 2.3.9.5), 4 μ L of the purified DNA fragments (about 20 ng/ μ L) were mixed with 1 μ L pCR-XL-TOPO vector and incubated for 5 min at room temperature. The reaction was stopped by the addition of 1 μ L 6x TOPO Cloning Stop Solution. 5 μ L of the reaction were transformed into *E. coli* (see 2.3.2), cells were plated on LB agar plates containing 50 μ g/mL kanamycin and grown

overnight. As the pCR-XL-TOPO vector encodes for the lethal *E. coli* gene *ccdB* that is fused to the C-terminus of the LacZ α fragment, recombinants can be directly selected. Insertion of a long PCR product disrupts the expression of the *lacZ α -ccdB* gene fusion, permitting growth of only positive recombinants upon transfection. Plasmid DNA was isolated from single colonies (see 2.3.3) and validated by restriction analysis (see 2.3.9.1) and DNA sequencing (see 2.3.4). The pCR-XL-TOPO-cDNA was then used for further subcloning.

2.4 Lentiviral vectors

Cellular Lrrk2 expression was down-regulated using a lentiviral-mediated shRNA expression system derived from HIV-1. Since their first application, lentiviral vectors were strongly developed in design to decrease the biohazard potential and optimize both the production yields and gene transfer efficiency. To increase biosafety, lentiviral vectors were engineered to be replication-defective, thus restricting the infection process to a single round without spreading. The general concept of genetic modification for this purpose persists in a split genome vector system associated with a reduction in the number of viral sequences. Therefore, the *trans*-acting sequences, encoding only proteins that are essential for lentiviral vector assembly and function, are separated from the *cis*-acting sequences, required for the transfer of the viral genome to the target cell. The assembly of lentiviral vectors thus necessitates (I) “packaging/helper constructs” that provide the viral proteins in *trans*, and (II) a “transfer vector”, expressing the *cis*-acting sequences linked to the transgene expression cassette. Only the latter will be packed into viral particles by the producer cells and can be subsequently transferred to the target cell. However, the odds are that replication competent retroviruses (RCRs) can be generated by recombination, either at the level of DNA input in the producer cell line or within heterozygous particles that contain RNAs from the packaging and transfer vectors. This would recreate a single viral genome that contains both *cis*- and *trans*-acting sequences and thus replication competent recombinants. Such events are dependent on residual *cis*-acting sequences in the packaging constructs allowing residual levels of encapsidation and on the extend of homology between packaging and transfer vectors (312-314).

Here, the gene transfer vector LVTH (315) was used, which contains in addition to the transgene expression cassette, merely all *cis*-acting sequences required for packaging, reverse transcription, integration, transcription, polyadenylation and efficient nucleocytoplasmic transport of the vector RNA, but lacks all viral protein coding sequences (Figure 10). Several modifications have been engineered into the vector to improve both efficiency and biosafety (Figure 10). As such, the integration of a regulatory element of the woodchuck hepatitis virus (WPRE) downstream of the transgene enhances its expression from the heterologous promoter (316). Moreover, the vector belongs to the type of self-inactivating (SIN) transfer vectors (317). These constructs encompass an intact 5'-long terminal repeat (LTR) but harbor a promoter-disabling deletion in the U3 region of the 3'-LTR (Figure 10). During reverse transcription in the target cell, both U3 regions of the provirus are generate from the 3'-LTR of the viral genome, thus transferring the deletion to the 5'-LTR of the resulting proviral DNA. The SIN-configuration of the gene transfer vector results therefore in a transcriptionally inactive provirus. The abolished intrinsic promoter/enhancer activity of the HIV-1 5'-LTR decreases the likelihood of insertional activation of adjacent cellular genes as well as vector mobilization and consequently reduces the risk of RCRs being formed

(317). Furthermore, a potential transcriptional interference between the LTR and heterologous promoters driving transgene expression is prevented (314).

Within the LVTH transfer vector, the shRNA expression cassette is located in the 3'-LTR (Figure 10), leading to its duplication in the integrated provirus. This double-copy configuration results in higher rates of siRNA synthesis and thereby to a maximal silencing efficiency accomplished by the lentiviral vector (315). The general composition of the shRNA-encoding DNA sequence (see also Figure 12) incorporates a sense siRNA sequence derived from the target transcript which is linked to its reverse complementary anti-sense siRNA sequence by a short spacer (loop). A following five nucleotide poly-T tract (T5) serves as the transcription termination signal for RNA polymerase III (Pol III), which drives the expression of the shRNAs via a H1-promoter located upstream of the coding sequence. The resulting transcripts lack a poly-A tail at their 3'-end and carry, due to the Pol III termination modalities at T5, a short poly-U tail. The transcripts are predicted to fold back, forming a stem-loop structure (shRNA) that thus resembles the structure of endogenous pre-miRNAs and are processed by the RNAi machinery, yielding siRNAs that trigger gene silencing (318, 319).

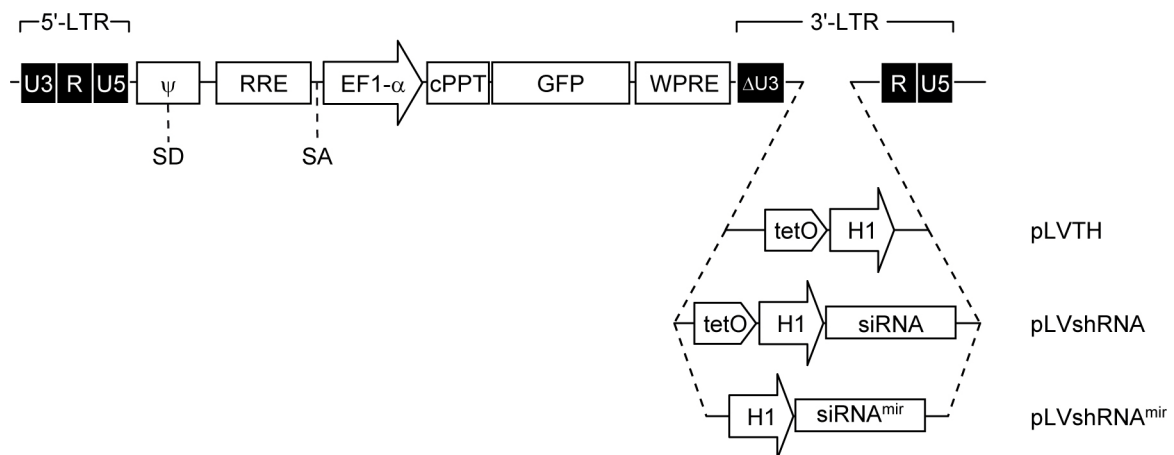


Figure 10: Lentivirus vector-based delivery system for stable shRNA expression.

Schematic representation of the HIV-1-based transfer vector pLVTH (315) and derived shRNA expression vectors (LVshRNA and LVshRNA^{mir}). Transfer vectors contain all HIV-1 sequences necessary for transfer and integration of the genome into target cells as well as a reporter gene under the control of a heterologous promoter. Coexpression of shRNA is achieved by insertion of the corresponding expression cassette in the 3'-long terminal repeat (LTR). Transcription of the transfer vector genomic RNA in the producer cell line by RNA polymerase II (Pol II) occurs from the 5'-LTR, which consist of the unique 3 (U3), repeat (R) and unique 5 (U5) regions, and requires the trans-activation of Pol II by the Tat (trans-activator) protein (Tat-dependent expression). A major deletion in the U3 region of the 3'-LTR (Δ U3) completely inactivates its promoter/enhancer activity, thus generating self-inactivating (SIN) transfer vectors (see text for details). Transport of the full-length vector RNA from the nucleus to the cytoplasm within the producer cell line is mediated by the nucleocytoplasmic transport signal RRE (rev-responsive element). The viral protein Rev (regulator of expression of virion proteins) binds to the RNA motif and targets it for nuclear export via the nuclear core complex. Subsequent incorporation of the vector RNA into assembling virus particles requires the encapsidation signal ψ , which interacts with the nucleocapsid (NC) protein within the Gag/Gag-Pol polyproteins. Improved SIN vectors contain the central polypurine tract (cPPT) sequence from the HIV-1 *pol* gene, improving gene transfer performance, and the post-transcriptional regulatory element of the woodchuck hepatitis virus (WPRE) positioned downstream of the of the reporter gene GFP (green fluorescent protein), increasing its expression. The expression of the GFP reporter is under the control of the internal promoter EF1- α (elongation factor 1 alpha). For the coexpression of shRNAs, the expression cassette, comprising the RNA polymerase III (Pol III)-dependent promoter H1 and the shRNA encoding sequence, is inserted in the 3'-LTR. tetO: tetracycline-responsive regulatory element, SD: splice donor site, SA: splice acceptor site, shRNA: short hairpin RNA (first generation silencing constructs), shRNA^{mir}: microRNA-30-based shRNAs (second generation silencing constructs).

Lentiviral vectors are generated by trans-complementation, whereby packaging cells are cotransfected with the transfer vector and helper constructs, providing the packaging system (Figure 11). The packaging cassettes encode all lentiviral vector *trans*-elements that comprise structural and enzymatic proteins required for vector particle production and efficient transduction of target cells. Removal of *cis*-elements (e.g. packaging signal and LTRs) curtails generation of RCRs by preventing the packaging of full-length mRNAs that encode *trans*-acting sequences into vector particles and their subsequent transfer to the target cell. Only *cis*-acting elements pertinent to post-transcriptional mRNA processing events (e.g. the Rev-responsive element (RRE)) are maintained within the packaging constructs. In this study, lentiviral vectors were packed by three non-overlapping expression constructs, two expressing the viral proteins and the other encoding for an exogenous viral envelope glycoprotein (third generation packaging system; Figure 11) (320). The first plasmid (pCMV-Gag/Pol Δ R8.92) contains the *gag-pol* reading frame together with RRE for an optimized Rev-dependent expression and the *tat* gene. Tat is required for the regulation of viral genome expression on the transcriptional level by stimulating transcriptional elongation by Pol II (312). The *gag-pol* coding region encodes for the structural proteins of the viral core and viral enzymes, respectively (312). The regulatory protein Rev is expressed by the second packaging construct (pRSV-Rev) and is known to bind the *cis*-acting element RRE. The Rev/RRE system is important for the efficient transport of the unspliced *gag-pol* mRNA and transfer vector genomic RNA from the nucleus to the cytoplasm and therefore for the proper assembly of lentiviral vectors (321). Providing Rev on a separate plasmid makes the expression of the packaging functions conditional on complementation available only in the producer cells (conditional packaging system) (322). The third component of the packaging system is the envelope expression construct (pMD2.G), where the wildtype (wt) HIV-1 envelope protein was replaced by the heterologous G glycoprotein of the vesicular stomatitis virus (VSV-G). The VSV-G pseudotyped vectors display a wider host range and allow gene transfer into a broader variety of target cells. Moreover, the VSV-G envelope confers the viral particles high stability, allowing their concentration by ultracentrifugation (312, 313). Partitioning of the remained packaging components on separate expression constructs improves the biosafety of a lentiviral vector by decreasing the homology between the packaging and transfer vector and thus risk of recombination. Moreover, various lentiviral vector elements that afford wt HIV-1 its pathological capabilities have been omitted or replaced by heterologous sequences, thus leaving only the minimal set of sequences required for the generation of efficient vectors (312, 321).

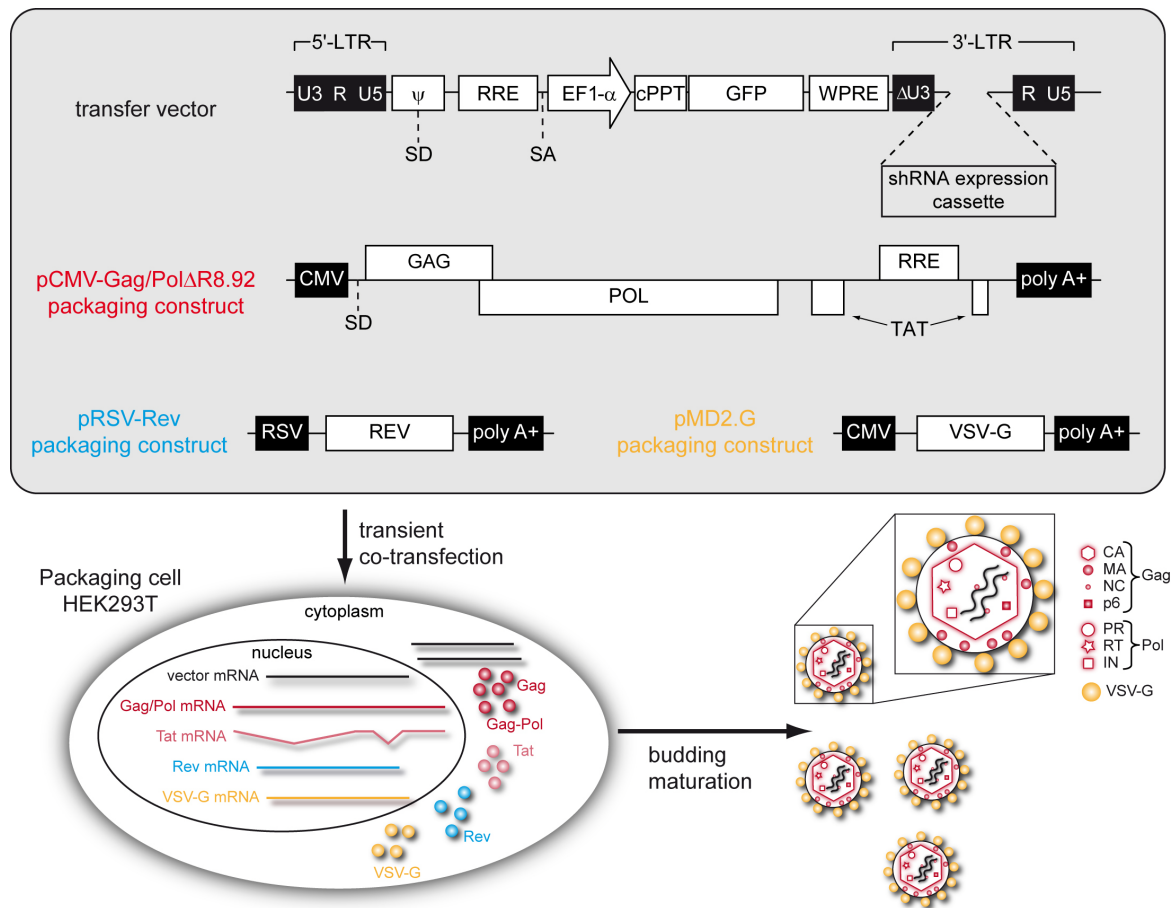


Figure 11: Generation of multiple-attenuated and SIN HIV-1-derived lentiviral vectors based on a four-plasmid (third generation) system.

Schematic diagram of lentiviral vector production by *trans*-complementation. Packaging cells (HEK293T) are transiently cotransfected with the SIN lentiviral vector plasmid (transfer vector; pLVTH/pLVshRNA/pLVshRNA^{mir}) and three packaging constructs (pCMV-Gag/PolΔ8.92, pRSV-Rev and pMD2.G). The transfer vector contains the reporter gene (GFP) and the shRNA expression cassette to be delivered in the lentiviral backbone and comprising all *cis*-acting sequences required for genomic RNA production and packaging. All *trans*-acting factors required for the assembly of viral particles, i.e. Gag, Gag-Pol, Rev, Tat and the heterologous envelope protein (vesicular stomatitis virus G protein; VSV-G), are provided by the three additional packaging plasmids. The 5'- and 3'-LTR of these constructs are replaced with heterologous promoter (human cytomegalovirus, CMV, or rous sarcoma virus, RSV) and polyadenylation signals, respectively. Additionally, the packaging signal ψ as well as unnecessary accessory genes that are required for a productive infection/replication of the parental wt virus in host cells are deleted from the constructs (multiple-attenuated vectors). Tat is required for the expression of the transfer vector RNA from the viral LTR promoter by transcriptional transactivation. Rev is needed for the nucleocytoplasmic transport of both the gene transfer vector RNA and Gag/Pol-transcript, thus promoting the subsequent expression of the latter. The internal proteins of the virion are derived from the Gag and Gag-Pol polyprotein precursors. Both precursors are translated from the unspliced RNA containing the *gag* and *pol* coding sequences. Gag-Pol results from a ribosomal frameshift from the *gag* into the partially overlapping *pol* ORF. Two copies of the transfer vector RNA, the Gag and Gag-Pol polyproteins are packed into viral particles, whose surface is decorated with the envelope glycoprotein. Pseudotyping with the VSV-G broadens the vector tropism and stabilizes the vector particles, thus supporting vector concentration by ultracentrifugation. Concomitant with the final stages of budding, the viral protease (PR) is activated by dimerization within the released immature particles, leading to proteolytic processing of Gag and Gag-Pol into their mature protein products and viral particle maturation. The Gag precursor yields the viral matrix (MA), nucleocapsid (NC), capsid (CA) and p6 protein. Cleavage of the Gag-Pol polyprotein results in reverse transcriptase (RT), integrase (IN) and protease (PR). The mature lentiviral vectors accumulate in the cell culture supernatant and high-titer viral preparations can be obtained by ultracentrifugation. Adapted from (312, 313, 320-322).

2.4.1 Selection of target sequences

siRNA sequences targeting within the murine Lrrk2 transcript (AY792512) were identified and selected according to guidelines published by Tuschl (269) using the Ambion-web-based oligo-search software (siRNA target finder). Putative 21-nt siRNA sequences had

to meet the following requirements: the sense strand contains two adenines at its 5'-end, the overall G/C content does not exceed 50% and does not possess more than four consecutive T/Us, which are recognized as transcription termination signal by the Pol III. To reduce the risk of cross-reactivity with other genes, all putative target sequences were checked for homology to both murine expressed sequence tags (ESTs) and mRNA sequences by performing a BLAST search. Sequences with more than 15-16 contiguous base pairs of homology to other coding sequences were excluded from consideration. From the remaining sequences, only those with a minimal number of homologies were kept among which a total of 8 sequences targeting the *Lrrk2* transcript at different positions (exons) were selected (Table 15).

Table 15: siRNA target sequences for the specific knockdown of *Lrrk2* expression.

Name	Target sequence in <i>Lrrk2</i> (<i>Mus musculus</i>) (5' - 3') ^{a)}	Targeting region ^{b)}	Exon
sh1	5'-AAGTTGATAGTCAGGCTGAAT-3'	60-78	1
sh2	5'-AAACTGGGATGCAAAGCTTTA-3'	540-558	5
sh3	5'-AAGAGGAAGACAGTGAGAAGC-3'	1027-1045	9
sh4	5'-AATGCAGACCAAATGTGCTCA-3'	1582-1600	14
sh5	5'-AAGAATTTCTGCATAGGGACA-3'	1851-1869	16
sh6	5'-AAAGTGCTCCGGTATCAGATG-3'	2526-2544	20
sh7	5'-AAATACTGTCTTCAGATGAGT-3'	2854-2872	22
sh8	5'-AATCTGTCCTATAACCAGCTC-3'	3267-3285	24

^{a)} GenBank accession number: AY792512

^{b)} Position in *Lrrk2* cDNA (AY792512) indicated in bps.

2.4.2 First generation silencing constructs

The general structure of sense target sequence, connecting loop, and antisense target sequence of the first generation shRNA silencing constructs was entirely based on the selected *Lrrk2* transcript specific target sequences. Therefore, the shRNA expression cassette was designed such that the 21-nt target sequences (sense) (see 2.4.1, Table 15) were separated from their reverse complement (antisense) by a spacer sequence of nine unpaired nucleotides (323). The coding sequence was followed by a run of five thymidines serving as Pol III transcription termination signal (T5). A pseudo-*Bgl*II (*pBgl*II) and pseudo-*Xba*I (*pXba*I) site were added to the 5'- and 3'-end, respectively, (see 1.3.5, Table 3) that allow cloning of the shRNA expression cassette into the lentiviral expression vector (see 2.4.4). Figure 12A illustrates the generic structure of the expression cassette using the example of sh1 (see 1.3.5, Table 3). Following transcription by Pol III, the RNA transcript is predicted to fold back, forming a stem-loop structure that is processed by Dicer to generate functional siRNAs (Figure 12A).

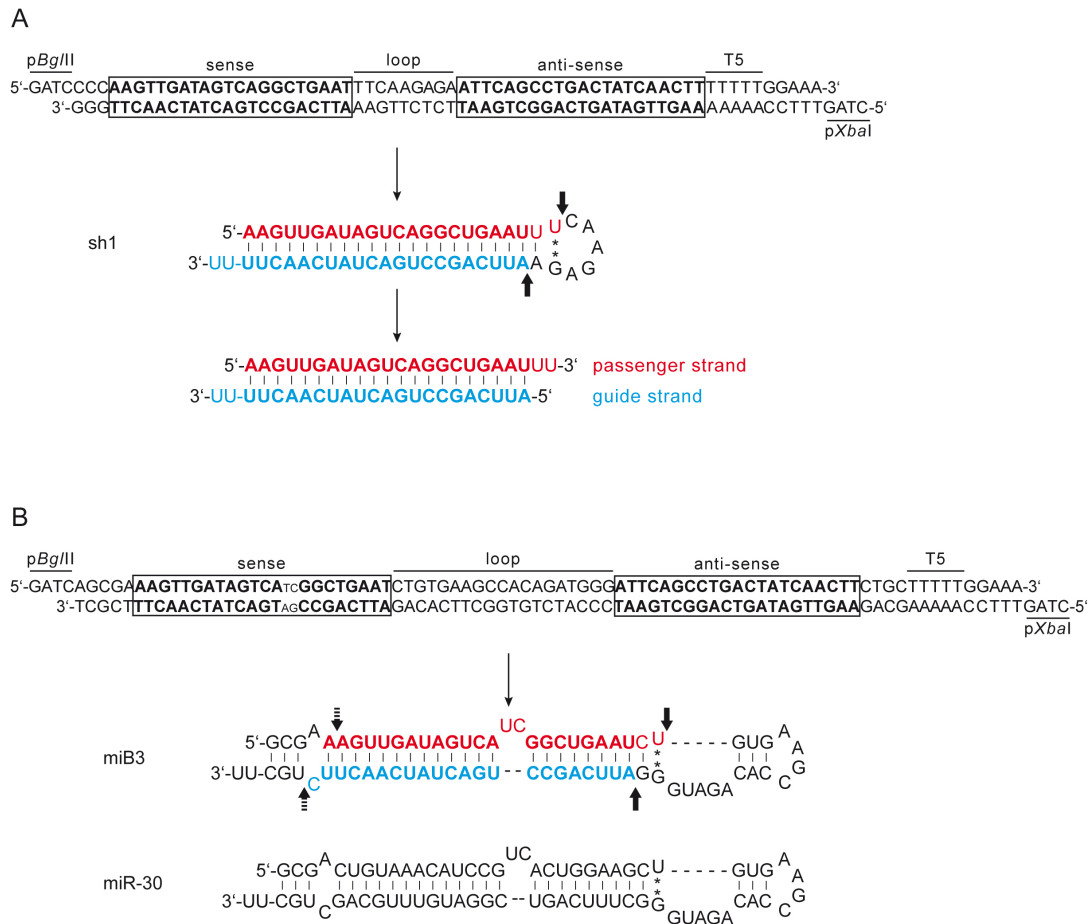


Figure 12: Structure and design of shRNA-based silencing constructs (first and second generation).

(A) First generation silencing constructs (shRNA) using the example of sh1. The expression cassette was designed such that the Lrrk2 transcript specific 21-nt target sequence (sense) was separated by a 9-nt loop from its reverse complementary sequence (antisense), followed by the Pol III transcription termination signal T5. A pseudo-*Bgl*III (*pBgl*III) and pseudo-*Xba*I (*pXba*I) restriction site was added to the 5'- and 3'-end, respectively, enabling cloning of the cassette into the lentiviral expression vector. The RNA transcript generated by Pol III folds back, forming a pair stem-loop structure (shRNA). The 3'-U overhang results from the Pol III properties to terminate transcription when the enzyme encounters a run of 4-5 thymidines after incorporation of several uridines. The shRNA is processed by the RNase III enzyme Dicer, which removes the terminal loop, yielding functional siRNA, triggering gene silencing. (B) Second generation silencing construct (shRNA^{mir}) of the Lrrk2 targeting sequence sh1. Design features of the naturally occurring microRNA-30 (miR-30) transcript were implemented in Lrrk2 shRNA constructs by replacing the stem sequence of the primary miR-30 transcript (pri-miR-30) with siRNA duplex sequences targeting Lrrk2 mRNA. As in the miR-30 transcript, a dinucleotide bulge was integrated into the passenger strand. The general structure of the shRNA^{mir} expression cassette resembles that of first generation constructs, comprising the shRNA^{mir} coding sequence (sense target sequence-loop-antisense target sequence) followed by the Pol III transcription termination motive. The 5'-*pBgl*III and 3'-*pXba*I site enables cloning of the expression plasmid. Bold characters represent target specific sequences, with the passenger strand (sense orientation) shown in red and the target mRNA complementary guide strand (antisense orientation), which is incorporated into the RISC complex, in blue. Arrows in bold indicate Dicer cleavage sites and dashed arrows Drosha cleavage sites. G:U wobble base pairing is indicated by stars.

2.4.3 Second generation silencing constructs

Second generation silencing constructs (shRNA^{mir}) were designed that resembled the stem-loop structure of the endogenous miR-30. Thereto, the siRNA encoding sequences targeting Lrrk2 were incorporated into the backbone of the primary miR-30 transcript (pri-miR-30) by replacing the pri-miR-30 stem sequence with Lrrk2-specific siRNA duplex sequences (Figure 12B) (324-326). As in the native miRNA transcript, a dinucleotide bulge was inserted into the passenger strand (Figure 12B). The corresponding expression cassette

encompassed, analogous to that for first generation constructs, the shRNA^{mir} coding sequence (sense target sequence - loop - antisense target sequence) followed by the T5 motive and was flanked by a 5'-p*Bgl*II and 3'-p*Xba*I site (see 1.3.5, Table 4). The resulting transcripts enter the RNAi pathway where they are sequentially processed by the RNase III enzymes Drosha and Dicer (Figure 12B) into functional siRNAs.

2.4.4 Cloning procedure

Lentiviral expression vectors encoding Lrrk2 specific shRNA or shRNA^{mir} constructs were constructed by cloning the corresponding expression cassette first into the pBC KS+(*Clal*)-H1 vector (327) under the control of an H1 promoter. H1-shRNA or H1-shRNA^{mir} cassettes were subsequently ligated in the lentiviral expression vector pLVTH (315) and pLV(3'MCS), respectively.

For the cloning of expression cassettes encoding the different shRNA or shRNA^{mir} constructs, dsDNA fragments were generated from single-stranded synthetic oligonucleotides (see 1.3.5, Table 3 and Table 4, and 2.3.8) at first, followed by their phosphorylation (see 2.3.9.2). The fragments were cloned 3' to the H1 promoter of pBC KS+(*Clal*)-H1 by insertion in the *Bgl*II/*Xba*I site of the plasmid (327), resulting in the respective insert carrying pBC/H1 clones (see 1.3.6, Table 6). Fidelity of the sequence encoding the silencing constructs was insured by sequencing (see 2.3.4) before H1-shRNA and -shRNA^{mir} cassettes were cloned into the lentiviral expression vector. The H1-shRNA cassette, with the exception of H1-sh1, was isolated from their pBC/H1 clone with *Eco*RI and *Clal* and cloned into the *Eco*RI/*Clal* site of the pLVTH (315), generating the respective lentiviral expression vectors pLV (see 1.3.6, Table 6). In the case of the shRNA construct sh1, the 9-nt loop sequence and the 3' adjacent antisense target sequence form together an *Eco*RI restriction site, so that the H1-shRNA cassette was removed from the pBC/H1 clone by *Clal* solely, blunted and cloned into the blunted *Eco*RI/*Clal* site of the expression vector. H1-shRNA^{mir} cassettes were subcloned with *Eco*RI and *Clal* into pLV(3'MCS), which is a modified lentiviral expression vector derived from the original pLVTH plasmid: the tetO-H1 fragment was excised using *Bam*H1 and *Clal* and replaced by a 66 bp fragment containing a *Eco*RI and *Clal* restriction site (engineered by Dr. M. Bauer).

2.4.5 Evaluation of knockdown efficiency

To evaluate the silencing efficiency of the selected first generation shRNA constructs, HEK293T cells were plated at a density of 5×10^5 cells per well onto 6-well plates. The next day, cells were transiently cotransfected with 4.91 μ g pBC/H1 vector carrying the shRNA construct (pBC/H1-sh1 – pBC/H1-sh8; see 1.3.6, Table 6, and 2.4.4) and 0.546 μ g pEGFP-EK-Lrrk2 (3.5 kb) (see 1.3.6, Table 6) in a 9:1 ratio by calcium phosphate precipitation (see 2.6.4). The latter vector encodes for the expression of a 3.5 kb fragment of murine Lrrk2

(AY792512: 50-3487), encompassing the specific siRNA targeting regions, fused 3' to the reporter GFP (green fluorescent protein). Cells transfected with peGFP-EK-Lrrk2 (3.5 kb) and the empty pBC KS+(ClaI)-H1 plasmid in the same ratio, with either of the vectors solely and untransfected cells served as controls. Two days after transfection, cells were trypsinized (see 2.6.1) and one half was subjected to flow cytometric analysis (see 2.6.10), the second half to western blot analysis (see 2.1.5).

For the analysis by flow cytometry, samples were centrifuged at 90 x *g* for 5 min at room temperature. The cells were resuspended in 0.5 or 1 mL PBS supplemented with 10% FBS and 10 µg/mL propidium iodide (PI) and subsequently subjected to the analysis to determine the amount of GFP positive cells within the different samples.

For western blot analysis, cells were pelleted under the same conditions and lysed as described in 2.1.1.1. Proteins were separated by standard SDS-PAGE (see 2.1.3.1), and GFP expression levels were analyzed (see 2.1.5).

2.4.6 Viral production

Recombinant lentiviruses were produced according to standard protocols (315, 320). Thereto, HEK293T were plated at a density of 3×10^6 cells in 10 mL growth media onto 10 cm plates (see 2.6.1). The next day, cells were transiently cotransfected at 70% confluence with 13 µg transfer vector (see 2.4.4), 13 µg pCMV-Gag/Pol Δ R8.92, 3 µg pRSV-Rev and 3.75 µg pMD2.G by calcium phosphate precipitation (see 2.6.4). At least 16 plates were transfected with one of the different transfer vectors. After 16 h the medium was changed to 6 mL Episerf containing 4 mM glutamine, 100 U/mL penicillin and 100 µg/mL streptomycin, thus removing an excess of calcium phosphate precipitates that interfere with the virus collection. Furthermore, the viral production under serum-free conditions limits a systemic immune response in the target cell. 24 h later, the supernatants, including the recombinant virus, were collected, with the medium arising from eight plates of the same lentiviral construct pooled at a time. Supernatants were cleared of cells and cell debris by centrifugation for 10 min at 600 x *g* and room temperature, followed by filtration through a 0.45 µm pore size syringe filter. Subsequently, the virus was sedimented by ultracentrifuged at 50000 x *g* and 4°C for 1.5 h. The supernatant was completely removed, taking care of leaving the pellet undisturbed, before the virus was resuspended, 160-fold concentrated, in Episerf. Thereto, 300 µL medium was added and the virus was redissolved for 3 h at 4°C. Finally, the concentrated virus suspensions of two identical settings were combined, aliquoted into 50 µL aliquots and frozen at -80 °C.

2.4.7 Titration of lentiviruses

As all lentiviral vectors coexpress GFP, titering of concentrated viral supernatants was performed by flow cytometric analysis of transduced NIH3T3 cells. Therefore, cells were plated at a density of 1×10^5 cells per well on 6-well plates. 16 h later, cell counts were obtained from one well and serial volumes of each recombinant lentivirus (10, 1 and 0.1 μL) were added. The cells were cultured for 3 days, divided and 24 h later the percentage of GFP-positive cells was determined by flow cytometry (see 2.6.10). For this, cells were trypsinized (see 2.6.1), harvested by centrifugation at $60 \times g$ and resuspended in 0.5 or 1 mL 0.5 % (v/v) paraformaldehyde (PFA) in PBS before they were subjected to the analysis.

Wells containing less than 10% GFP-positive cells were used to calculate the amount of infectious units ($\text{IU}^{\text{NIH3T3}}$) per μL using the following equation:

$$\text{IU}^{\text{NIH3T3}}/\mu\text{L} = \frac{F \cdot \text{Cn}}{V}$$

F refers to the frequency of GFP-positive cells determined by flow cytometry and was calculated by dividing the percentage of GFP-positive cells by 100. Cn is the total number of target cells that was available for infection and V denotes the volume of the inoculum. The multiplicity of infection (MOI) used hereafter for the infection of cells represents the ratio of input $\text{IU}^{\text{NIH3T3}}$ to the number of cells available for transduction.

2.5 Gene expression analysis

For the evaluation of RNAi experiments, gene expression levels were analyzed by quantitative real-time PCR. This method is based on the technique of PCR (see 2.3.7) but allows monitoring of the reaction process as it occurs, i.e. in real time, by combining amplification and detection into a single step. This is achieved by the use of different fluorescence chemistries that enable a correlation of the PCR product amount to fluorescence intensity. There to, fluorescent molecules are included into the reaction that can be both dye-labeled, sequence specific oligonucleotide primer or probes and dsDNA-binding dyes (e.g. SYBR Green I). As the dsDNA PCR product accumulates during reaction progression, fluorescence increases proportionally to the concentration of the amplicon and fluorescence intensity thus reflects the amount of amplified product in each PCR cycle. The reactions are characterized by the time point (i.e. PCR cycle) where target amplification is first detected. This value is referred to as cycle threshold (C_t), the cycle at the early exponential phase where the amount of fluorescence has reached a threshold where it significantly exceeds (in general 10 times the standard deviation of the baseline) the background level. The C_t value is inversely correlated to the amount of nucleic acids in the input sample and is used for target copy number quantification. The quantity of DNA in the sample can be calculated either absolute, giving a concentration, or relative, displaying changes in sample gene expression to an external standard or control. In both cases, data obtained from the real-time PCR experiment have to be normalized against a control gene to correct sample to sample variations, facilitating an accurate comparison of mRNA transcripts across different samples.

Here, a two-step SYBR Green-based real-time PCR approach was used, where reverse transcription (RT) and PCR amplification occurred in different reactions. Gene expression levels were determined by relative quantification based on the normalization of expression level to the internal control gene glyceraldehyde 3-phosphate dehydrogenase (GAPDH).

2.5.1 Isolation of total RNA

Total RNA was isolated from cells using the RNeasy Mini Kit as described by the manufacturer. In brief, cells were lysed in a total of 600 μ L RLT buffer supplemented with β -mercaptoethanol, which inactivated RNases to insure purification of intact RNA. The lysates were subsequently homogenized to reduce sample viscosity by shearing of genomic DNA. There to, samples were passed five times through a 27G (0.4 mm) needle attached to a 1 mL sterile plastic syringe until homogeneous lysates were received. After the addition of ethanol, providing appropriate conditions for the binding of RNA to the RNeasy silica membrane, homogenates were applied to RNeasy Mini Spin columns and contaminants were washed away. RNA was eluted in 30 μ L RNase free ddH₂O and stored at -80°C for further

processing. The RNeasy procedure provides an enrichment for mRNAs, as RNAs < 200 bp, such as 5.8S rRNA, 5S rRNA and tRNAs, which comprise together 15-20% of total RNA, are selectively excluded.

2.5.2 Quantitative and qualitative analysis of RNA

RNA integrity and quantity was determined with the RNA 6000 Nano assay kit on an Agilent 2100 Bioanalyzer according to manufacture's instructions. The technique is based on the principle of capillary gel electrophoresis that has been transferred to a chip format. Chips accommodate a set of 12 interconnected microchannels that are filled with a sieving matrix containing a fluorescent dye. Due to their constant mass-to-charge ratio, nucleic acid fragments are electrophoretically separated by their size. Dye molecules intercalate with the RNA strands and complexes are detected by laser-induced fluorescence. The obtained data are translated into electropherograms and/or densitometry plots (gel-like images) by plotting the fluorescence intensity versus the migration time. With the help of a defined ladder that contains fragments of known size and concentration, a standard curve of migration time versus fragment size is generated and utilized for the calculation of sample fragments. A marker fragment is run with each sample and the ladder. It serves as an internal standard and is used to align the ladder data with those obtained from the samples, thus compensating for drift effects during the course of chip run. Quantification is done with help of the area under the ladder, which is compared with the sum of sample peak areas. An indication on the RNA integrity is given by the ribosomal ratio (328). RNA is considered of high quality, if the ratio of 28S rRNA to 18S rRNA is about 2.0 or higher. More recent software versions include an algorithm that assigns the "RNA integrity number" (RIN) as an estimation for the integrity of total RNA (329). It is based on a combination of different features of the entire electrophoretic trace of the RNA sample and reflects the degree of RNA degradation, providing a more robust universal measure than the ribosomal ratio.

For gene expression analysis by quantitative real-time PCR, only RNA samples with a 28S:18S ratio of ≥ 1.8 or RIN values of at least 8 were used.

2.5.3 Reverse transcription

Production of single-stranded cDNA from RNA was accomplished by RT reactions primed with oligo-d(T)s. The extracted total RNA was utilized as template.

First strand cDNA synthesis was performed using the Omniscript RT Kit according to manufacturer's instructions. Thereto, RNA was denatured by incubation of 5 min at 65°C and 1-2 μg were subjected to RT in a final reaction volume of 20 μL , containing 1x Buffer RT, 0.5 mM each dNTP, 1 μM oligo-d(T)₁₅ primer, 10 U RNase inhibitor and 4 U Omniscript reverse transcriptase. The RNA-dependent DNA polymerase activity of the enzyme transcribes cDNA from the RNA template, whereas the hybrid-dependent exonuclease

(RNase H) activity catalyzes the specific degradation of RNA in the RNA:DNA hybrid, leaving single-stranded cDNA. After incubation of the reaction for 1 h at 37°C, primers, salts, dNTPs and enzymes were removed from the samples by purification using the QIAquick PCR Purification Kit as described by the manufacturer. Samples were eluted in 40 µL RNase free ddH₂O and stored aliquoted at -20°C before they were used as a template for real-time PCR amplification reactions.

2.5.4 Real-time PCR

Gene expression was analyzed by real-time PCR using SYBR Green I chemistry, a cyanine dye that binds specifically to dsDNA. In solution, the unbound dye exhibits very little fluorescence. Binding to dsDNA leads to a conformational change and thus substantial enhanced fluorescence which is utilized for the detection of PCR products as they accumulate during cycling. For each analyzed gene, a primer pair was designed using the Vector NTI software with one of the primers spanning an exon boundary and yielding PCR products of 100-150 bp. These short amplicons are likely to reach optimal amplification efficiency. Primers are designed as 19-25 oligo nucleotides in length with T_m set to a range from 54-56°C or 61-63°C for high binding specificity and GC content set to a range of 40-60% for optimal PCR efficiency. To ensure specific target amplification, primer pairs were analyzed by BLAST search. For primer sequences see 1.3.5, Table 2. Real-time PCR reactions were performed in 384-well clear optical reaction plates using the ABI Prism 7900HT Sequence Detection System. Reactions possessed a total volume of 10 µL composed of 1/20 or 1/40 volume of the purified cDNA depending on whether 1 µg or 2 µg RNA was applied to the RT reaction (see 2.5.3), 1 µM (GAPDH and Oas1) or 10 µM (Lrrk2) forward and reverse primer and 1x SYBR Green PCR Master Mix comprising SYBR Green I dye, HotStarTaq DNA Polymerase, dNTPs including dUTP, the passive reference dye ROX, 5 mM MgCl₂ and QuantiTect SYBR Green PCR Buffer. Additional 1 mM MgCl₂ was added to reactions with GAPDH primers. 10-fold serial dilution series (1:10¹-1:10³) of purified cloning vectors or cDNA obtained from appropriate cell cultures were included to calculate the amplification efficiency of the respective target based on the resulting “standard regression curve”. To rule out any DNA cross-contamination, blank samples were included. Each sample was analyzed in triplicate or quadruple wells. Amplification was done on the ABI Prism 7900HT Sequence Detection System using the following cycling conditions, with the amplification stage comprising 40 cycles of stages 2 to 4:

- | | | | |
|----|---------|--------|---|
| 1. | 95°C | 15 min | initial activation of HotStarTaq DNA Polymerase |
| 2. | 94°C | 15 sec | denaturation of the DNA template |
| 3. | 54/65°C | 30 sec | annealing of the primers |
| 4. | 72°C | 30 sec | extension of the primers |
| 5. | | | dissociation stage |

A melting curve was obtained for each PCR product (stage 5) to confirm correspondence of SYBR Green signals to a unique and specific amplicon. Thereto, the reaction mixture was heated to 95°C for 15 sec and then cooled down (1.6°C/s) to 60°C for additional 15 sec. During the subsequent slowly heating of the samples to 95°C with a ramp rate of 1.6°C/s, fluorescence was continuously measured to monitor the dissociation of SYBR Green. The resulting melting peak represents the characteristic T_m of a particular DNA product (where 50% of the DNA is double-stranded and 50% is single-stranded). If the PCR generates one amplicon, the analysis reveals one melting peak, whereas primer dimers and non-specific products yield additional melting peaks. Specificity of PCR amplicons was verified by melting curve analysis and gel electrophoresis (see 2.3.5).

For the relative quantification of gene expression levels, real-time PCR data were processed according to Simon (330). Here, absolute expression values of the target genes were normalized to those of the reference gene GAPDH within the same sample and the “mean normalized expression” (MNE) for the triplicate or quadruple measurements was calculated (equation 1).

$$\text{Equation 1} \quad \text{MNE} = \frac{(E_{\text{reference}})^{C_{t_{\text{reference,mean}}}}}{(E_{\text{target}})^{C_{t_{\text{target,mean}}}}}$$

The process of normalization takes the different efficiencies of PCR amplification for the target (E_{target}) and the reference ($E_{\text{reference}}$) into consideration (efficiency correction) and transforms the logarithmic scaled raw data unit C_t into the linear unit of normalized expression. Therefore, C_t values for a sample triplicate or quadruple were averaged (C_t reference, mean and C_t target, mean). Amplification efficiencies were estimated from the “standard regression curve” based on equation 2.

$$\text{Equation 2} \quad E = \left(10^{-1/\text{slope}} - 1 \right) \times 100$$

By applying the differential equation of Gauss for error propagation, related standard errors (SE) for MNE levels (SE_{MNE}) were calculated according to equation 3.

$$\text{Equation 3} \quad SE_{\text{MNE}} = \sqrt{(\ln(E_{\text{target}}) \cdot SE_{C_{t_{\text{target,mean}}}})^2 + (\ln(E_{\text{reference}}) \cdot SE_{C_{t_{\text{reference,mean}}}})^2}$$

Standard error of the averaged C_t values for each sample triplicate and quadruple, respectively, is referred to as $SE_{C_{t_{\text{target, mean}}}}$ or $SE_{C_{t_{\text{reference, mean}}}}$.

Gene expression data are represented as relative values compared to the corresponding wt samples. If not stated otherwise, results from at least three independent biological replications were pooled.

2.6 Mammalian cell culture

2.6.1 Growth and maintenance of mammalian cell culture

Cell cultures (NIH3T3 and HEK293T) were started from cryo cultures (see 2.6.2). Thereto, cryo cultures were thawed quickly in a water bath at 37°C and transferred to a 10 or 15 cm culture dish with 10 and 20 mL of the prewarmed (37°C) cell-line specific medium (see below), respectively. Culture dishes were gently shaken and incubated at 37°C in a humidified atmosphere with 5% CO₂ in air (CO₂ incubator). Confluent cells were subcultured by detaching them with trypsinization solution and seeding them onto new plates with a ratio of 1:5 – 1:20 or defined density. To this end, the medium was removed and cells were washed once with prewarmed PBS (37°C). Cultures were treated with 3 mL (10 cm dish) or 6 mL (15 cm dish) prewarmed trypsin/EDTA at 37°C until the cells detached. After addition of 7 or 14 mL of serum-containing growth medium to stop trypsinization, the cell suspension was transferred to a 15 mL or 50 mL tube and centrifuged for 3 min at 700 x g and room temperature. The sedimented cells were resuspended in 5 mL fresh growth medium, counted by using a Neubauer counting chamber where required, and transferred into new cell culture dishes at a proper density.

NIH3T3 cells were grown in DMEM containing 10% (v/v) FBS, 2 mM glutamine, 50 U/mL penicillin and 50 µg/mL streptomycin. As NIH3T3 cells gradually lose to react on serum-starvation (see 2.6.9.4) during prolonged culturing, cells were not cultured longer than 8 weeks (331).

For the generation of lentiviral vectors, low-passage HEK293T cells were used, with freshly thawed cells for each round of production. Thawed cells were plated at a density of 3x10⁶ cells per 15 cm culture dish in 20 mL D-MEM-GlutaMAX supplemented with 10% FBS, 50 U/mL penicillin and 50 µg/mL streptomycin. Cells were expanded by replating them at the same density 2 and 4 days (80% confluence) after thawing. At day 6 after starting the cell culture, cells were seeded at a density of 3x10⁶ cells per dish onto 10 cm plates containing 10 mL growth medium and transfected the next day (see 2.4.6).

2.6.2 Generation of cryo stocks

For the preparation of cryo stocks, cells at 80% confluence were trypsinized and sedimented as described (see 2.6.1). The pellet was resuspended in 50% (v/v) cell culture medium and 50% (v/v) 2x Freeze medium (fresh growth medium containing additional 20% (v/v) FBS and 15% (v/v) dimethyl sulfoxide (DMSO)). Density of the cell suspension was determined, adjusted to 1.5x10⁶ or 3x10⁶ cells/mL and 1 mL of the suspension was transferred to a cryo tube at a time. The tubes were placed overnight at -80°C and transferred the next day into liquid nitrogen for long term storage.

2.6.3 Stable isotope labeling with amino acids in cell culture (SILAC)

SILAC (294) has emerged as a simple and straightforward approach in MS-based quantitative proteomics. It relies on the labeling of cellular proteomes through normal metabolic processes, incorporating non-radioactive, stable isotope-containing amino acids in newly synthesized proteins and thus allowing a differential quantification of two proteomes. Thereto, two cell populations of different experimental conditions are grown in the same type of growth medium, except that one of them contains amino acids with the natural isotopes (light medium) and the other containing the isotopically heavy form of a particular amino acid. Heavy amino acids can contain ^{13}C instead of ^{12}C or ^{15}N replacing ^{14}N . To ensure that cells only incorporate the added, labeled amino acids into their proteome, essential amino acids are chosen and cells are grown with dialyzed serum. Most commonly used applications of the method use media containing heavy isotope-labeled arginine and -lysine, which ensures that all tryptic cleavage products of a protein, except the very C-terminal peptide, carry a least one labeled amino acid, resulting in a constant mass-increment over the non-labeled counterpart. Complete labeling of the proteins, i.e. each instance of the natural light amino acid is replaced by its isotope-labeled analog, is achieved by cultivation of the cells for at least five cell doublings. Incorporation of the mass tags introduces a distinct, predictable mass shift into the proteins or peptides compared to those containing the natural amino acid isotopes (see 2.2.2.2.4) but does not change any other chemical property. Thus, the different isotope labeled samples can be combined and jointly processed for subsequent MS-analysis facilitating their direct comparison in the same analysis.

For SILAC, wt NIH3T3 and analogue Lrrk2 knockdown cells were grown in SILAC medium containing either normal L-lysine and L-arginine for the light condition or the heavy isotope-labeled counterparts (arginine: $^{13}\text{C}_6^{15}\text{N}_4$; lysine: $^{13}\text{C}_6$) for the heavy condition three days after transduction (see 2.6.6). Media were prepared by adding the amino acids (SILAC or natural) to a final concentration of 0.1 mg/mL to L-lysine and L-arginine deficient DMEM. Additionally, the medium was supplemented with 0.23 mg/mL proline to prevent arginine to proline conversion, which could impair the quantification accuracy (332). After sterile filtration, 50 U/mL penicillin and 50 $\mu\text{g}/\text{mL}$ streptomycin were added as well as dialyzed FBS to a final concentration of 10% (v/v). Lrrk2 knockdown cells were grown in light medium, whereas the wt control was cultured in heavy medium. In parallel, crossover experiments with an inverted isotopic labeling were conducted. To achieve complete SILAC incorporation, cells were grown in the SILAC medium for five passages prior to further processing (see 2.2.2).

2.6.4 Transient transfection by calcium phosphate precipitation

Calcium phosphate (CaPO_4)-based transfection represents an efficient method for DNA transfer to mammalian cells (333). It is premised on the spontaneous formation of

insoluble DNA-CaPO₄ coprecipitates in a supersaturated solution (334) that attach to the cell surface and are brought into the cells by endocytosis (335).

To prepare the DNA-CaPO₄ coprecipitates, plasmid DNA was combined with 0.5 M CaCl₂ in a sterile tube and adjusted with sterile ddH₂O to the respective volume (Table 16). A second tube containing 2x HBS (280 mM NaCl, 100 mM HEPES and 1.5 mM Na₂HPO₄) was prepared. The DNA-mixture was added dropwise to the HBS solution under continuous bubbling through air flow to mix. The DNA-CaPO₄ suspension was incubated for 20 min at room temperature before 1 mL or 200 µL were added to the cells.

Table 16: DNA amount and reagent volumes for calcium phosphate precipitation on different cell culture surface areas.

	6 well	10 cm plate
Culture media	2 mL	10 mL
Total DNA	5.46 µg	32.75 µg
0.5 M CaCl ₂	50 µL	250 µL
Final volume of DNA/CaCl ₂ -mixture adjusted with ddH ₂ O	100 µL	500 µL
2x HBS	100 µL	500 µL

2.6.5 Primary ventral mesencephalic (VM) progenitor cell cultures

2.6.5.1 Coating of chamber slides with poly-D-lysine and laminin

8-well chamber slides were coated for plating of primary neurons (see 2.6.5.2) with poly-D-lysine and laminin. Thereeto, 2 µg/cm² poly-D-lysine was added to each well in a final volume of 200 µL cell culture grade ddH₂O and incubated for 3 h at 37°C. Then, the poly-D-lysine solution was removed and the culture wells were washed once with ddH₂O. For the subsequent coating with laminin, 1 µg/cm² mouse laminin in a final volume of 200 µL was added to the wells and incubated overnight at 37°C. Prior to plating of the cells, the chamber slides were washed twice with ddH₂O and once with D-MEM/F12.

2.6.5.2 Preparation and maintenance

For the preparation of primary progenitor cultures of DA neurons, all experiments were carried out in accordance with the European Community Council Directive (86/609/EEC) for care and use of laboratory animals. Primary embryonic mouse VM cells were isolated and cultured as previously described (336). CD-1 mice (animal breeding facility, Helmholtz Zentrum München) were mated overnight and the day after was defined as E0.5. Time pregnant mice were sacrificed by cervical dislocation at gestation day 12.5 (E12.5) and embryos were obtained by caesarian section. Here, the removed uterine horns were collected in ice-cold PBS before they were transferred to a clean 10 cm dish containing ice-cold HBSS supplemented with 0.45% (v/v) glucose (dissection buffer) where the embryos were dissected from the uterine sac and the amniotic membrane was removed. To confirm and monitor the gestational age, crown-rump-length (CRL) of the embryos was measured (expected CRL at E12.5: 8-9 mm). Embryos were collected in clean ice-cold dissection

buffer, where those that did not meet the CRL criteria or were malformed were excluded. The VM region was dissected in ice-cold dissection buffer as shown in Figure 13, and the pericranium as well as meninges were carefully removed. Isolated VM tissue from 30-40 mouse embryos (3-4 adult mice) was stored and pooled in ice-cold dissection buffer on ice. After transfer of the ventral mesencephali to a 1.5 mL tube, HBSS was removed and the tissues were mildly triturated with a fire-polished Pasteur pipette (80% diameter) in 750 μ L titration buffer (HBSS supplemented with 0.45% (v/v) glucose, 1 mM sodium pyruvate and 1 mM sodium bicarbonate). Non-dissociated tissues were precipitated on ice by gravity before the supernatant was transferred to a new 15 mL tube. Then, another 750 μ L titration buffer was added to the VM tissues that were dissociated using a 60%-diameter fire-polished Pasteur pipette. The remaining bits of tissue were settled on ice by gravity before the second supernatant was pooled with the first one. Dissociated cells were harvested by centrifugation at 100 x g for 5 min at 4°C. The cell pellet was resuspended with ice-cold standard medium consisting of DMEM/F12 supplemented with 2% (v/v) B27, 2 mM glutamine, 0.45% (v/v) glucose, 1 mM sodium pyruvate, 20 μ g/mL insulin, 0.5 U/mL penicillin and 0.5 μ g/mL streptomycin and plated at a final density of 1×10^5 viable cells in 200 μ L prewarmed standard medium on 8-well chamber slides precoated with poly-D-lysine and mouse laminin (see 2.6.5.1). For the expansion of neuronal progenitor cells, bFGF was added to the cultures at the day of dissection and the following two days to a final concentration of 20 ng/mL. From day 3 on, VM cells were cultured without bFGF. The cells were incubated at 37°C in a water-saturated atmosphere with 5% CO₂ for 9 or 14 days and maintained in standard medium, which was changed every second day, during the first 7 days in vitro. From DIV7 on, 10% FBS was added to the standard medium.

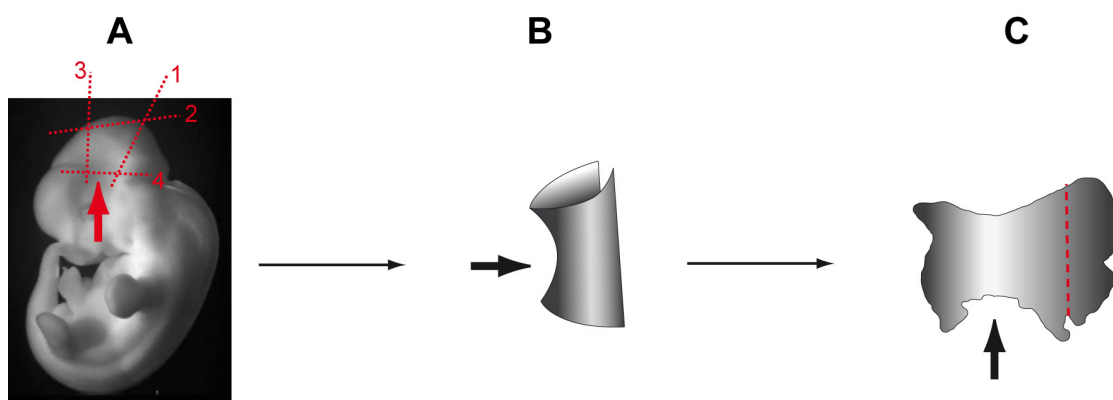


Figure 13: Dissection of the ventral midbrain (VM) region from embryonic mouse brain.

E12.5 embryos from time pregnant CD-1 mice were isolated from the uterine sac and freed from any remaining placental and amniotic membranes. (A) Dissection of the midbrain. Dashed lines outline the single surgical cuts used for the isolation of the midbrain with their chronological order numbered. The bold arrow indicates the anterior midline and VM region. Cuts 1 and 3 remove the rostral forebrain and caudal hindbrain region, respectively. The posterior region was removed with cut 2 and cut 4 was used to extract the tissue from the embryo. The picture was taken from the EMAP eMouse Atlas Project (<http://www.emouseatlas.org>) (337). (B) Careful removal of the pericranium and meninges provide the tube-like structure of the midbrain with their posterior region deleted (bold arrow: anterior midline and VM region). (C) Open up of the isolated tissue results in a butterfly-shaped structure, which was trimmed by removing the posterior/lateral tissue on each side (dashed line). The bold arrow indicates the anterior midline of the VM.

2.6.6 Lentiviral transduction

Lrrk2 expression in both NIH3T3 cells and primary VM cultures was depleted by transduction with lentiviruses encoding Lrrk2 silencing shRNA-constructs. Non-transduced (wt) or LVTH-transduced were prepared in parallel and served as negative controls.

To this end, NIH3T3 cells were seeded at a density of 2.5×10^4 cells per well onto 6-well plates and transduced the following day using a MOI of 5. The corresponding volume of concentrated virus (control or second generation shRNA-encoding vectors) was added to the culture wells and scattered by gentle shaking of the plate.

Primary VM cultures plated at a density of 1×10^5 cells per well onto 8-well chamber slides (see 2.6.5.2) were transduced at the first day *in vitro* (DIV1). For the transduction with the different first generation silencing constructs, the applied MOI ranged from 0.5 to 2, whereas a MOI of 0.5 was used for all second generation constructs. The empty transfer vector LVTH was always transduced at a MOI of 0.5. For a single experiment, each condition was run in triplicate or quadruple wells.

2.6.7 Immunofluorescence

NIH3T3 cells and VM cultures were fixed by adding 2 mL or 200 μ L prewarmed 4% (w/v) PFA in PBS and subsequent incubation for 15 min at 37°C. PFA was then discarded and replaced by prewarmed PBS. Fixed cultures were stored at 4°C until further processing.

For immunofluorescence (IF) staining, fixed cells were permeabilized and concomitantly blocked in PBS containing 10% (v/v) horse serum and 0.4% (v/v) Triton X-100 (blocking buffer) for 1 h at room temperature. Cells were incubated for 3 h at room temperature or overnight at 4°C with the primary antibody directed against the protein of interest in an appropriate dilution (see 1.6, Table 7 and Table 8) in PBS containing 2.5% (v/v) horse serum and 0.1% (v/v) Triton X-100. To remove unbound antibodies, cells were washed three times for 10 min (8-well chamber slides) or six times for 5 min (coverslips) with PBS. Fluorescent labeling was done with Alexa Fluor 568-conjugated secondary antibodies (see 1.6, Table 9) diluted in 2.5% (v/v) horse serum in PBS/0.1% (v/v) Triton X-100 containing 1 μ g/mL 4',6-diamidino-2-phenylindole (DAPI) for nuclear staining. Following incubation for 3 h at room temperature, cells were washed three times for 10 min with PBS.

For labeling of the actin cytoskeleton, permeabilized and blocked cells were incubated with Alexa Fluor 568 phalloidin diluted 1:500 in PBS containing 2.5% (v/v) horse serum and 0.1% (v/v) Triton X-100 for 90 min at room temperature. Nuclei were visualized by the addition of DAPI (see above).

Following IF labeling, 8-well chamber slides were briefly rinsed with ddH₂O before both the media chamber and silicone gasket was carefully removed. About 5 μ L of mounting medium (FluorSave) was added in each chamber section and the slide covered with a glass coverslip, avoiding trapping of any air bubbles. The slides were dried overnight and sealed

the next day with nail polish. Coverslips were washed six times for 5 min with PBS, rinsed briefly in ddH₂O and mounted upside-down onto a droplet of FluorSave on a glass slide. Mounted chamber slides and coverslips were stored at 4°C for several weeks.

2.6.8 Microscopy

Immunostained cell cultures were analyzed by fluorescence microscopy using an Axioscope2 fluorescence microscope equipped with an AxioCam HRc digital camera. Images were obtained using a FITC optical filter set for GFP autofluorescence, a Rhodamine optical filter set for Alexa Fluor 568 staining, a DAPI optical filter set for DAPI staining and a Nomarski optical filter set (Plan-Neofluar 20x/0.50 and 40x/0.75 objectives). Image acquisition was carried out using the AxioVision4 software package.

Camera lucida drawings for tyrosine hydroxylase (TH)-immunoreactive (TH-ir) neurons were obtained from original images captured with a 20x objective. Representative, randomly selected neurons from each condition were manually traced using NeuronJ. Tracings were saved as a 16-bit TIFF file and converted utilizing ImageJ.

2.6.9 Phenotypic analysis of mammalian cell culture

For the phenotypic analysis of shRNA expressing NIH3T3 cells as well as primary VM cultures, cells were fixed, visualized by IF staining (see 2.6.7) and examined by microscopy using an Axioscope2 fluorescence microscope (see 2.6.8). In case of lentiviral transduced cultures, only GFP-positive cells were analyzed.

2.6.9.1 Transduction efficiency of dopaminergic neurons in primary VM cultures

To evaluate the transduction efficiency of DA neurons in primary VM cultures with lentiviral vectors encoding Lrrk2 shRNAs or the empty transfer vector alone (see 2.6.6), the fraction of TH-ir neurons that have been infected by viral particles was calculated at DIV9 or DIV14. Owing to the (co-)expression of GFP by pLVTH-based vectors, quantification of the transduction efficiency was assessed by determining the percentage of TH-ir cells exhibiting GFP expression. Thereto, a total of 100 randomly selected TH-ir cells were analyzed per well under microscopical observation using a 20x objective. Data obtained from all wells per experimental condition were pooled over at least three independent biological repeats.

2.6.9.2 Dopaminergic cell counts

To determine the amount of dopaminergic neurons in the mesencephalic neuronal cultures at DIV9 and DIV14, total numbers of TH-ir cells were counted within the culture wells by microscopic analysis utilizing a 20x objective. Cell counts are expressed as a percentage of the corresponding wt culture per 8-well chamber (equal to 81 mm²). Data obtained from all wells per treatment group of at least three independent biological replications were pooled.

2.6.9.3 Dopaminergic neurite length

To quantify the neurite length of DA neurons in VM cultures at DIV9 and DIV14, digital images of twelve randomly selected fields per well from TH-immunostained cultures were captured using a 20x objective. Cultures were analyzed by manually tracing each individual process of a neuron from the cell body to the neurite tip utilizing the NeuronJ plug-in of the ImageJ software. The length of neurites was calculated according to a calibrated scale using Excel software. Only individual processes without contacts to other neurites or cells were chosen for quantification. If a neurite branched, the longer of the branches was traced. As it was not possible to distinguish between axons and dendrites in the cultures, all processes were considered equivalent and were referred to as neurites. To measure neurite length, a mean of 55 to 73 and 38 to 46 neurons per well was used for the analysis at DIV9 and DIV14, respectively, and data represent the total neurite length. For every experimental condition, the average neurite length was determined. Additionally, the relative frequency distribution of the neurite length was generated by grouping the length into consecutive bins increasing by 40 μm , ranging from 40 to $>200 \mu\text{m}$, and the percentage of neurites with a given length was calculated. Data obtained from all wells per condition, three to four per experiment, were pooled over at least three independent experiments.

2.6.9.4 Morphological analysis of NIH3T3 cells

For the analysis of cell morphology, wt and transduced NIH3T3 cells (see 2.6.6) were divided and replated at 5-10% density in DMEM/10% FBS (see 2.6.1) on glass coverslips five days after transduction. 4 h post-splitting, the cells were washed in prewarmed DMEM without FBS and serum starved with 0.5% FBS for 24 h. Then, the cells were fixed and immunostained for F-actin (see 2.6.7) to visualize cell shape. Ten randomly selected fields per coverslip were imaged using a 10x objective. Subsequently, the images were analyzed using ImageJ software. A binary mask was created by setting a threshold brightness that distinguished the fluorescent cells from the black background. Cell outlines were traced automatically and single cell's area and perimeter of at least 500 cells per coverslip were measured. As a quantitative measure of cell shape, the ratio of perimeter to area (P:A-ratio) (338) of each cell was determined. The average P:A-ratio and the frequency distribution of P:A-ratios in consecutive bins increasing by $0.05 \mu\text{m}^{-1}$ and ranging from 0.05 to $>0.4 \mu\text{m}^{-1}$ was calculated for each coverslip. Data obtained from all coverslips per experimental condition, with three coverslips per treatment group within one experiment, from four independent biological replications were pooled.

2.6.10 Flow cytometry

Flow cytometry is a widely used laser-based technique to measure and analyze biophysical, biochemical and molecular characteristics of cells, thus allowing discrimination of different cell populations in a heterogeneous cell suspension. It is based on the light scattering properties of the cells being analyzed and emission of fluorescence as light from the excitation source strikes the moving cells. Thereto, a single-cell suspension passes in a fluid stream through a laser beam, and light scattering as well as fluorescence is measured for each individual cell that passes the laser source by a set of distinct detectors. The scattering of light is due to diffraction, refraction and reflection, with its amount and direction influenced by the physical characteristics of the cells. Here, two types of light scatter are measured. The forward angle light scatter (FSC) results from diffraction and is used for the estimation of cell size. Refraction and reflection are the underlying basis for the side angle light scatter (SSC) and is an indicator of cell granularity and surface characteristics. In addition to FSC and SSC measurements, various wavelength of fluorescence can be detected. Fluorescence is emitted by fluorochrome-labels as cells pass the laser excitation beam and detected by separate fluorescence (FL) channels. The specificity of detection is controlled by optical filters, defining ranges of transmitted wavelengths. In general, three major filter types are used. “Longpass” filters allow detection of light above a cut-off wavelength, “shortpass” filters permit light below a cut of wavelength and “bandpass” filters transmit light within a specified narrow range of wavelength (band width).

Here, the percentage of GFP-positive cells within a given sample, used to evaluate the silencing efficiency of different shRNA constructs (see 2.4.5) or titration of concentrated lentiviruses (see 2.4.7), was analyzed by flow cytometry using a 488 nm argon-ion laser equipped BD FACSCalibur flow cytometer. Data acquisition was obtained using the BD CellQuest Pro software. The samples were excited and analyzed for GFP fluorescence using a 530/30 nm bandpass filter. In cases of samples supplemented with PI to stain for dead cells, fluorescence of the fluorochrome was collected through a 650 longpass filter. Cells were gated on the basis of FSC, SSC and, if present in the sample, PI, thus defining the population of viable cells analyzed for GFP expression. FSC signals were recorded in the linear mode, whereas SSC and fluorescence signals were acquired in the logarithmic mode.

At first, the homogenous cell population free of cell debris and cluster was determined based on cell size (FSC) and granularity (SSC) (R1). For the titration of lentiviruses, R1 was used to define the population of viable cells (G1=R1, light scattering gate). To evaluate the silencing efficiency of shRNA construct, viable cells were identified by gating on the homogeneous cell population (R1) and the population of PI-negative cells (R2) (G1=R1 and R2). In both cases, 30000 events were recorded and analyzed for GFP expression. The amount of GFP-positive cells within the samples was determined using the CellQuest Pro or WinMDI 2.8 software. Results obtained from three independent experiments were pooled.

2.7 Actin cosedimentation assay

Actin cosedimentation is an *in vitro* assay commonly used to analyze the binding of a target protein to F-actin (Figure 14). The underlying principle of the assay is that actin monomers (G-actin) can be polymerized into F-actin *in vitro* that can be sedimented by ultracentrifugation. If the protein of interest, present during polymerization, is able to associate with F-actin, it will be sustained in the pellet along with F-actin after ultracentrifugation, whereas it remains in the supernatant when it cannot bind F-actin.

F-actin binding of Lrrk2 was assessed in cooperation with Prof. M. van Troys (Ghent University). Actin (Ca-ATP-G-actin) was purified from rabbit skeletal muscle according to Spudich and Watt (339), further purified over a Sephadex G-200 gel filtration column in G-buffer (5 mM Tris-HCl, pH 7.7, 0.1 mM CaCl₂, 0.2 mM ATP, 0.2 mM DTT) and stored on ice. For F-actin cosedimentation assays, affinity purified SF-TAP (Strep/Flag tandem affinity purification) tagged Lrrk2 (173, 340) in storage buffer (SB; desthiobiotin elution buffer, 20% glycerol) (kindly provided by Dr. C.J. Gloeckner) was added to a final concentration of 150 nM or 300 nM to 3 μM actin in G-buffer, supplemented with Roche complete protease inhibitor mixture. In all samples the combined volume of SB and protein in SB was always constant, i.e. 15 μL per 25 μL sample volume, thus ensuring constant buffer conditions. Polymerization was induced by the addition of KCl and MgCl₂ to 100 mM and 2 mM, respectively. After incubation for 45 min at room temperature and 2 h at 4°C, samples were subjected to ultracentrifugation at 100000 x *g* for 10 min at room temperature. The supernatants (S) were removed and pellets (P) were washed once with F-buffer (G-buffer containing 100 mM KCl and 2 mM MgCl₂) before they were resuspended in Laemmli buffer. To take into account any effects of the storage buffer on actin polymerization, samples containing only 3 μM actin and SB were included. A potential sedimentation of Lrrk2 irrespective of F-actin was monitored by incubating the protein at a concentration of 300 nM solely under actin polymerization buffer conditions.

Equal amounts of both the pellets and supernatants from each reaction were analyzed by SDS-PAGE followed by Coomassie brilliant blue staining to mainly visualize actin or western blotting using an anti-Flag antibody to show the presence of Lrrk2. Western blot analysis of F-actin cosedimentation samples was based on IRDye infrared dye technology (Li-COR Biosciences, Lincoln, NE, USA) on an Odyssey Infrared Imaging System (Li-COR Biosciences) following the manufacturer's guidelines. In brief, proteins separated by SDS-PAGE were electrophoretically transferred onto Hybond-C nitrocellulose membranes (GE Healthcare). The blots were blocked in 50% Odyssey buffer (Li-COR Biosciences) in PBS and subsequently incubated with rabbit-polyclonal anti-Flag antibody (Sigma) diluted in 50% Odyssey buffer in PBS containing 0.01 % Tween20. For detection of the Flag-epitope, membranes were probed with an IRDye 800CW goat-polyclonal anti-rabbit secondary antibody (Li-COR Biosciences) and signals were detected using an Odyssey Infrared

Imaging System.

Protein intensities (I) on Coomassie gels and western blots were quantified by densitometric analysis using ImageJ after background subtraction. The distribution of G- vs. F-actin was determined from the intensity ratios $I_{(S)}/I_{(S)}+I_{(P)}$ and $I_{(P)}/I_{(S)}+I_{(P)}$, respectively, and expressed in percentages. To allow comparison over different western blots, the signals for Lrrk2 intensities in the pellet fractions at different concentrations were normalized for each blot to the protein's intensity in the supernatant at 150 nM Lrrk2.

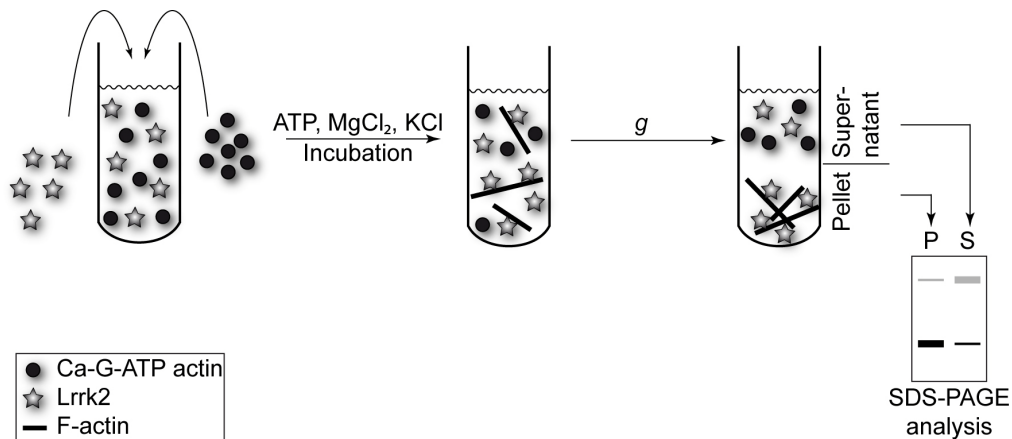


Figure 14: Actin cosedimentation assay.

The actin cosedimentation assay is an *in vitro* assay routinely used to analyze the F-actin binding capacity of specific proteins. There to, G(globular)-actin and the target protein are mixed in the presence of ATP and polymerization is induced by the addition of MgCl₂ and KCl. G-actin is allowed to polymerize until equilibrium is reached and sedimented by ultracentrifugation. The pellet (P) and supernatant (S) is analyzed by SDS-PAGE.

2.8 Statistical analysis

All data are expressed as mean \pm standard error of the mean (SEM). n indicates the number of independent experiments. Multiple group analyses were made by one-way analysis of variance (ANOVA) followed by Tukey's or Holm-Sidak post-hoc test as well as by two-way ANOVA with Bonferroni's post-hoc analysis using GraphPad Prism 4 software. Means were assumed to be significantly different when the P value for the null hypothesis was less than 0.05. The Chi-Square test (χ^2) was applied to analyze the distributions of frequencies using Excel. Differences among the distributions were considered significant if $p < 0.05$. The p -value of physical cohesiveness of the Lrrk2 interaction network was calculated as described (307).

IV. RESULTS

1. Experimental workflow

A participation of Lrrk2 in the etiology of PD was revealed just before the beginning of this study. The emphasis of the work presented here was to discover biochemical pathways and cellular functions associated with Lrrk2, thus providing a basis for studies focusing on perturbed activities in these pathways possibly linked to PD. Figure 15 presents a schematic overview of the experimental workflow that was established to elucidate the endogenous role of Lrrk2 within the cellular context.

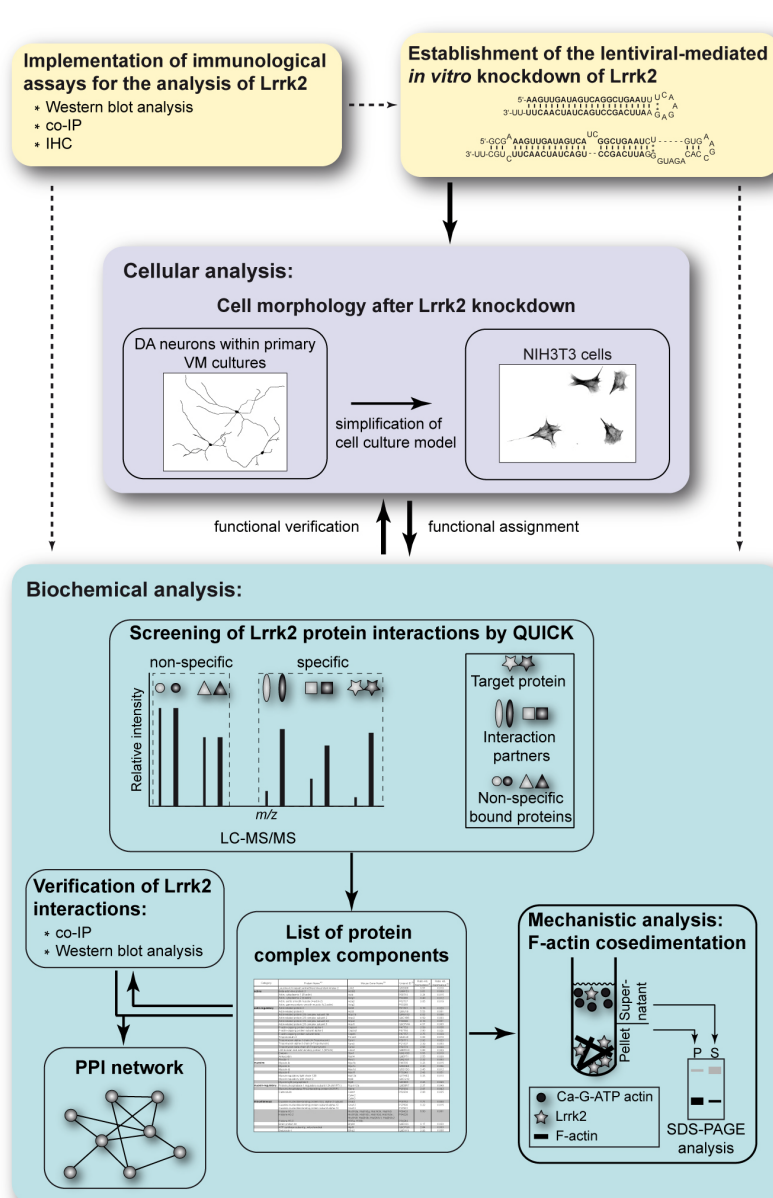


Figure 15: Schematic overview of the experimental procedure.

The present study aimed to gain insights into the endogenous function of Lrrk2 and Lrrk2-mediated signaling pathways. As a prerequisite (dashed arrows) for the analysis of Lrrk2, immunological assays were implemented. Moreover, the lentiviral-mediated *in vitro* knockdown of Lrrk2 by the expression of shRNAs was established, which represented a central approach within the study. The phenotypic implication of a Lrrk2 knockdown was investigated by determining changes in the cellular morphology using DA neurons within primary VM cultures derived from E12.5 mouse embryos and NIH3T3 cells as a simplified cell culture model. In order to assign the physiological function of Lrrk2, its interactome was systematically analyzed by QUICK using NIH3T3 cells. A list of putative Lrrk2 complex components was obtained and a selected subset was verified by western blot analysis following co-IP. The identified Lrrk2 interacting proteins were mapped into a PPI network, integrating interaction data stored in the HPRD and BioGRID database as well as interactions implied by the experimental results. The found interaction partners suggest that the biological role of Lrrk2 is associated with the actin cytoskeleton. The physiological relevance of the hypothesis was analyzed by an F-actin cosedimentation assay as an *in vitro* mechanistic approach. Further support was revealed by the cellular analyses.

2. Implementation of immunological assays for the analysis of Lrrk2

At the beginning of this study, Lrrk2 was merely known to be associated with PD's etiology. Thus, besides knowledge about the physiological role of Lrrk2, basic experimental assays were missing. Various immunological assays such as western blot analysis, IP and IF represent indispensable tools for the analysis of a protein's function and were thus aimed to be established. Due to the initial lack of specific commercial antibodies that could recognize (endogenous) Lrrk2 in such approaches, monoclonal (mAb) and polyclonal (pAb) antibodies against Lrrk2 that were produced in the laboratory (see below) were verified for their specificity in western blot, IP and IF followed by an optimization of the respective method if necessary. The mAbs tested here were generated in house by Dr. E. Kremmer using a peptide encompassing the amino acids 2025 to 2055 of human Lrrk2 (UniProt-ID: Q5S007) selected by Dr. C.J. Gloeckner. The epitope is located in the kinase domain of the protein and displays 100% sequence homology to murine Lrrk2. Stable hybrid myeloma cells (hybridomas) producing the mAbs were generated based on prescreens by Dr. E. Kremmer, A. Schumacher (Helmholtz Zentrum München) and Dr. C.J. Gloeckner. In the present study, only stable subcloned antibodies were tested for their suitability in western blot analysis, IP and IF. In addition to mAbs, polyclonal antibodies were produced against murine Lrrk2 in cooperation with Eurogentec using two different peptides. Both epitopes are located at the C-terminus of the protein, spanning the amino acids 2501 to 2514 (146) and 2513 to 2527 (selected by Dr. C.J. Gloeckner). The purified antibodies were primarily monitored for their aptitude in IF.

2.1 Monoclonal anti-Lrrk2 antibody clones specifically detect Lrrk2 in western blot analysis

Monoclonal antibodies against Lrrk2 produced from stable hybridomas were tested for their specificity in western blot analysis on NIH3T3 cell lysates using the conditioned media of the generated cell clones. 8 out of the 11 tested antibodies detected an immunoreactive signal at ~280 kDa, corresponding to the expected molecular mass of Lrrk2 (Figure 16A). Additionally, a second immunosignal in the molecular mass range above Lrrk2 was detected (Figure 16A) which does not appear after denaturation of the protein samples in Laemmli buffer by incubation for 1 h on ice instead of heating to 96°C for 5 min (Figure 16B). Thus, the second band might arise from a dimerization of the protein upon boiling of the sample. Many of the tested antibodies displayed a strong background staining and additional immunosignals in the lower molecular mass range. The best results in terms of a strong signal at ~280 kDa and low non-specific background staining were obtained with the clones 1E11, 2E12 and 3A6 (Figure 16A). The antibody 1E11 was selected and its specificity in western blot analysis was confirmed using lysates of NIH3T3 cells whose Lrrk2 expression was knocked down by lentiviral-mediated expression of target-specific, first generation

shRNAs (see 3.2) (Figure 16B). Protein extracts derived from wt cells and cells transduced with the transfer vector (LVTH) alone served as controls. The analysis yielded a single immunosignal at ~280 kDa, with the lysates of Lrrk2-knockdown cells displaying a decreased signal intensity (lanes 3 and 4) compared to those of wt and LVTH-transduced cells (lanes 1 and 2). Hence, the anti-Lrrk2 clone 1E11 was proved to be specific in western blot and further experiments were conducted with the affinity purified antibody (provided by Dr. E. Kremmer).

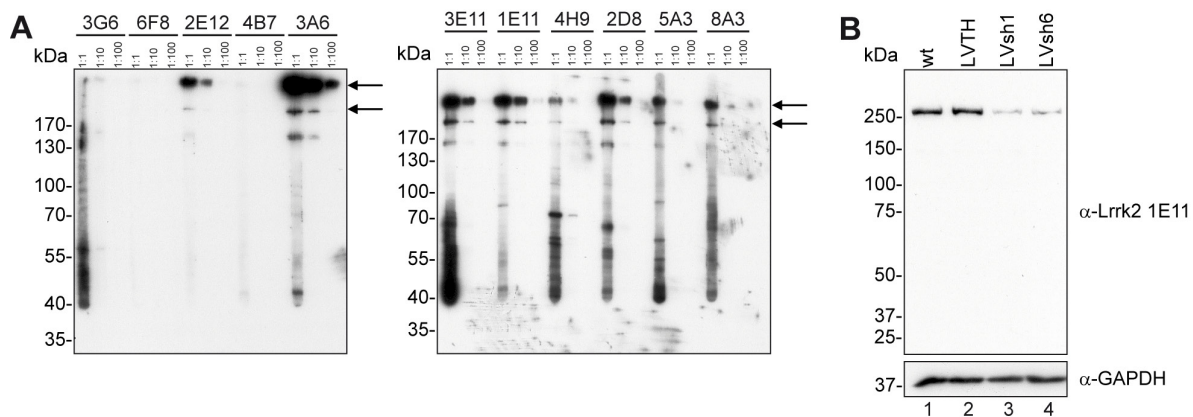


Figure 16: Lrrk2-specificity of monoclonal anti-Lrrk2 antibody clones in western blot analysis.

(A) Peptide-based antibodies produced from stable hybridomas were analyzed for their specificity in western blot analysis using protein extracts of NIH3T3 cells. Cell lysates were subjected to SDS-PAGE and probed with 10-fold serial dilutions of the different antibody clones. 8 of them displayed an immunosignal at ~280 kDa, correlating to the expected molecular mass of Lrrk2 (lower arrow). An additional signal was obtained in the molecular mass range above ~280 kDa (upper arrow), resulting from the dimerization of Lrrk2 upon denaturing of the protein samples by heating to 96°C. (B) Lrrk2 specificity of the anti-Lrrk2 antibody clone 1E11 was analyzed on lysates from NIH3T3 cells expressing shRNAs targeting Lrrk2 (LVsh1 and LVsh6). Cells transduced with the empty transfer vector (LVTH) and wt cells served as controls. A single immunosignal was detected at ~280 kDa whose intensity was decreased in the Lrrk2-knockdown samples (lanes 3 and 4) compared to the controls (lanes 1 and 2). A GAPDH western blot served as loading control.

2.2 Establishment of the immunoprecipitation of endogenous Lrrk2

The characterization of proteins that interact with a specific target protein yields important indications for the functional characterization of the protein. Antibody-based IP represents a key technique for the extraction of the endogenous target protein and its associated complex partners. Lrrk2-specificity for several of the generated anti-Lrrk2 mAbs was already demonstrated in western blot analysis. However, this only proved the ability of the antibodies to recognize the SDS-denatured epitope of the protein. IP is though performed under native conditions to preserve non-covalent PPIs, so that the antibody has to be capable to bind the native protein. Therefore, the suitability of the Lrrk2-specific mAbs produced by stable hybridomas to precipitate the native, endogenous protein was verified. At first, a streptavidin-biotin-based screening assay was performed to identify antibody clones that were able to extract Lrrk2 from NIH3T3 cell lysates. The efficiency of selected clones in an IP was then determined using a classical approach. A disadvantage of such a classical IP and co-IP is that the conditions used to elute the precipitated protein also release the antibody, resulting in a contamination of the antigen that interferes with the downstream

analysis by SDS-PAGE and MS. To overcome this issue, the Lrrk2-specific antibody was immobilized on a support resin by covalent coupling or cross-linking. For the mass spectrometric analysis of the precipitated proteins, optimization of the IP conditions was intended to reduce the amount of non-specifically bound proteins in the immunoprecipitates.

2.2.1 A streptavidin-biotin-based screening assay revealed specific precipitation of Lrrk2 by rat-monoclonal antibody clones

The ability of the Lrrk2-specific mAbs produced by stable hybridomas and three affinity-purified clones to precipitate the antigen was tested in a streptavidin-biotin-based assay using protein extracts derived from NIH3T3 cells. In principle, the antibodies were linked to streptavidin-coated microtiter plates through biotin-conjugated anti-rat IgGs and subsequently incubated with the protein extract. After elution of the anti-Lrrk2 bound target antigen, proteins were subjected to SDS-PAGE and analyzed by western blotting utilizing the anti-Lrrk2 antibody clone 1E11. For the identification of non-specific protein binding, samples without an anti-Lrrk2 antibody were used as negative control. NIH3T3 cell lysates separated on SDS gels served as positive control for western blot analysis.

Table 17: Optimization of the streptavidin-biotin-based screening assay.

	Original protocol	Optimized protocol
Washing of streptavidin-coated plates with PBS	1 x 400 μ L	1 x 400 μ L
Incubation with biotin-conjugated anti-rat IgGs (50 μ L/well; 1:200 in PBS)	30 min, room temperature	30 min, room temperature, 700 rpm
Washing with PBS	1 x 400 μ L	2 x 400 μ L
Incubation with anti-Lrrk2 antibody clones (100 μ L/well)	30 min, room temperature	30 min, room temperature, 700 rpm
Washing with PBS	1 x 400 μ L	2 x 400 μ L
Incubation with NIH3T3 cell lysates (100 μ L/well; 0.3 μ g/ μ L)	2h, room temperature	overnight, 4°C, 700 rpm
Washing with PBS	2 x 400 μ L	1 x 400 μ L
Elution (5x Laemmli buffer; 20 μ L/well)	10 min, room temperature	1h, 4°C, 700 rpm
Figure	Figure 17A	Figure 17B

In an initial screen using the original protocol (provided by Dr. E. Kremmer; Table 17), western blot analysis did not reveal Lrrk2-specific immunosignals at ~280 kDa with any of the tested antibodies (Figure 17A). Only non-specific signals could be detected between 75 and 150 kDa with the clones 4H9, 3E11, 2D8, 3A6 (hybridoma medium and purified), 1E11 (hybridoma medium and purified), 6F8 and purified 2E12 (Figure 17A). Therefore, the assay was optimized (Table 17) by changing the incubation time and temperature of the plates with the cell lysate as well as for the elution of proteins. Additionally, the incubation steps with the biotinylated anti-rat IgGs, Lrrk2-specific antibodies, protein extracts and Laemmli buffer were performed under agitation.

Under the improved assay conditions, the purified anti-Lrrk2 antibody clones 2E12, 1E11 and 3A6 were able to extract Lrrk2 in a detectable amount as demonstrated by western

blot analysis, which revealed Lrrk2-specific bands at ~280 kDa (Figure 17B). Additional non-specific signals of unknown origin were noticed between 75 and 100 kDa. The negative control without antibody, however, displayed no immunosignals, thus excluding non-specific binding of the protein (Figure 17B). Therefore, the purified antibody clones 1E11 and 2E12 were selected for a further validation of their efficiency to immunoprecipitate endogenous Lrrk2 in a classical IP approach.

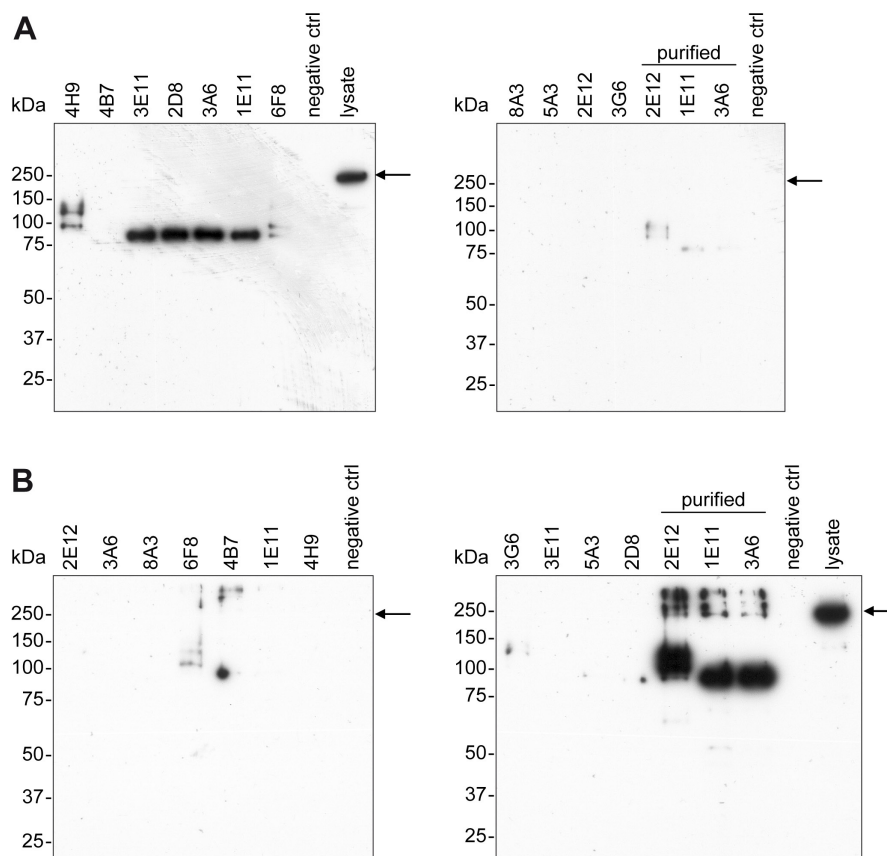


Figure 17: Streptavidin-biotin-based screening assay for the identification of anti-Lrrk2 monoclonal antibody clones suitable for the extraction of endogenous Lrrk2 from cellular lysates.

Lrrk2-specific antibodies produced by stable hybridomas and purified clones were linked to streptavidin-coated microtiterplates by biotinylated anti-rat IgGs. After incubation with NIH3T3 protein extracts, antibody-bound proteins were eluted and equal volumes were subjected to SDS-PAGE followed by western blot analysis using the anti-Lrrk2 antibody clone 1E11. For the identification of non-specifically bound proteins, negative controls without antibody were included. Samples of the cell lysates separated on SDS gels served as positive controls for the western blot analysis. (A) Utilizing the original assay protocol (provided by Dr. E. Kremmer), monoclonal Lrrk2-specific antibodies failed to extract Lrrk2 from the cell lysate. The western blot analysis revealed no immunoreactive bands that correspond to the antigen (arrow). (B) Optimization of the assay protocol resulted in the specific precipitation of Lrrk2 by the purified antibody clones 2E12, 1E11 and 3A6 as demonstrated by immunosignals at ~280 kDa (arrow). For the negative control (ctrl), no signals were obtained, excluding a non-specific binding of the protein in the samples.

2.2.2 The rat-monoclonal anti-Lrrk2 clones 1E11 and 2E12 efficiently immunoprecipitate endogenous Lrrk2 in a classic IP approach

The specificity and suitability of the Lrrk2-specific rat-monoclonal antibody clones 1E11 and 2E12 in IP was verified in a classic approach. Therefore, the purified antibodies were incubated with lysates of NIH3T3 cells to form an antigen-antibody complex, which was

precipitated using a Protein G resin. Proteins were released from the matrix under denaturing conditions, resolved by SDS-PAGE and analyzed by silver staining as well as western blotting using the anti-Lrrk2 1E11 antibody. As the amount of antibody needed for an efficient extraction of Lrrk2 was unknown, it was applied to the IP at different final concentrations (4, 8 and 10 $\mu\text{g}/\text{mL}$). Non-specific background resulting from proteins that cross-react with the antibody or bind non-specific to the resin was determined by a negative control without the anti-Lrrk2 antibody (bead control).

Western blot analysis of the antibody clone 1E11 and 2E12 immunoprecipitates identified Lrrk2-specific bands at ~ 280 kDa (Figure 18A and B, left panel, lanes 1-3). A final antibody concentration of 4 $\mu\text{g}/\text{mL}$ in both IPs was already capable to precipitate Lrrk2. The application of increasing amounts resulted in an augmented extraction of target protein from the lysates as demonstrated by an increase in the immunosignal's intensity. This correlated with a decrease of Lrrk2 in the respective IP-supernatants as the antibody concentration increased (Figure 18A and B, left panel, lanes 5-7). "IP-supernatant" denotes here and in the following the lysates after formation of the antigen-antibody complex. Compared to the band obtained for the supernatant of the bead control sample (Figure 18A and B, left panel, lane 8), those of the IPs displayed in general weaker signals, indicating an effective extraction of endogenous Lrrk2 from the lysates. Here, the clone 1E11 appeared to be more efficient than the clone 2E12 as the reduction in signal intensities in the IP using the former was more pronounced compared to utilizing the latter. A non-specific binding of Lrrk2 to the resin was excluded by the eluates from the bead control samples (Figure 18A and B, left panel, lane 4) where no immunosignal was detected. Moreover, western blotting of the immunoprecipitates revealed additional, strong immunoreactive signals at 50 and 25 kDa (Figure 18A and B, left panel, lanes 1-3), corresponding to the antibody's heavy and light chain, respectively.

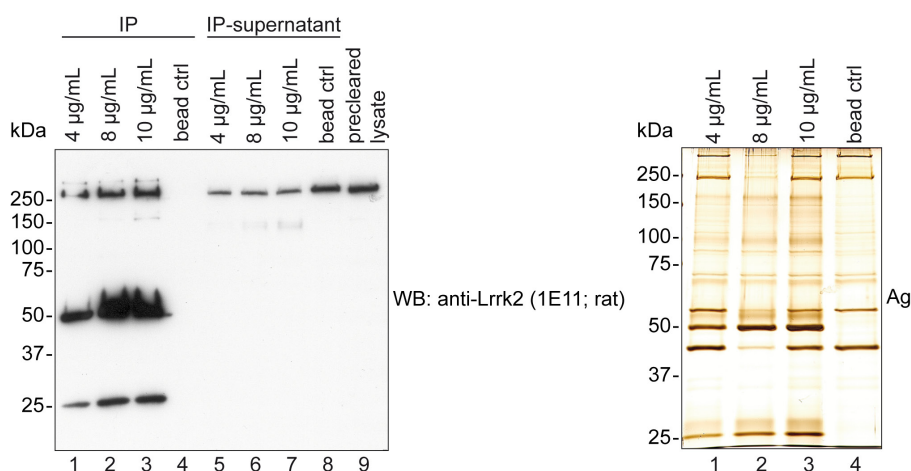
Visualization of the proteins by silver staining following separation of the IP eluates on SDS gels revealed a considerable number of non-specific bound proteins in both IPs as indicated by the bead control samples (Figure 18A and B, right panel, lane 4). An alignment of the IP samples with the bead control revealed no differences in the band pattern that could be correlated with Lrrk2-specific interactions. The strong signals at 50 and 25 kDa referred to the heavy and light chain of the antibody, respectively (Figure 18A and B, right panel, lanes 1-3). Although the western blot analysis of the IPs demonstrated a specific immunoprecipitation of Lrrk2 by both antibody clones, no bands that could be matched with the protein could be detected in silver stained gels.

Taken together, the results proved that the anti-Lrrk2 antibody clones 1E11 and 2E12 are able to immunoprecipitate endogenous Lrrk2. However, non-specific proteins that were coprecipitated generated a significant background and prevented an identification of Lrrk2-specific precipitated protein in silver stained gels. Additionally, the conditions used for the elution of protein complexes resulted in a contaminating release of the antibody. As the clone

1E11 was more efficient in the IP, it was selected for the establishment of IP approaches with an immobilized antibody that avoid its coelution (see 2.2.3 and 2.2.4).

A

IP: anti-Lrrk2 clone 2E12 (rat)

**B**

IP: anti-Lrrk2 clone 1E11 (rat)

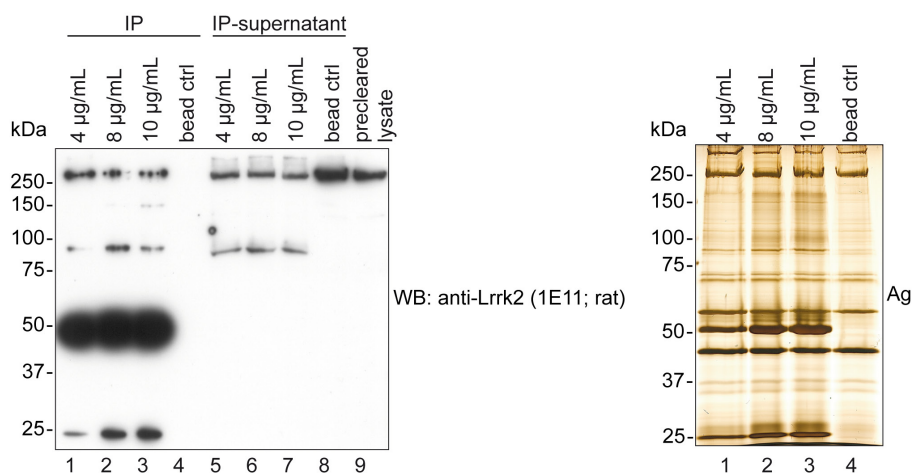


Figure 18: Precipitation of endogenous Lrrk2 in a classic IP approach by the rat-monoclonal anti-Lrrk2 antibody clones 1E11 and 2E12.

NIH3T3 protein extracts were subjected to a classic IP using the purified Lrrk2-specific rat-monoclonal antibody clones 2E12 (A) and 1E11 (B), each with a final concentration of 4, 8 or 10 µg/mL. Non-specific binding of proteins was monitored by a negative control without antibody (bead ctrl). Either 5/6 of the immunoprecipitates or 1/6 together with a lysate and IP-supernatant volume corresponding to 4% of the IP-input were separated by SDS-PAGE and analyzed by silver staining (Ag; right panel) or western blotting (WB; left panel). Both antibody clones were able to precipitate endogenous Lrrk2 efficiently as indicated by a specific immunoreactive signal at ~280 kDa in the immunoprecipitates (left panel, lanes 1-3). Accordingly, the Lrrk2 signal intensity in the IP-supernatants decreased compared to the bead control (left panel, lanes 5-8). Strong bands at 50 and 25 kDa in both western blot and silver staining (left and right panel, lanes 1-3) that corresponded to the heavy and light chains of the antibody revealed its release under the applied elution conditions. Visualization of the separated eluates following SDS-PAGE by silver staining exhibited a considerable amount of non-specific bound proteins in the bead control samples of both IPs (right panel, lane 4).

2.2.3 Lrrk2-specific immunoprecipitation using anti-Lrrk2 covalently coupled to CNBr-activated sepharose releases the antibody together with the precipitated proteins

As shown above, the rat-monoclonal anti-Lrrk2 antibody clone 1E11 efficiently immunoprecipitates endogenous Lrrk2 from cellular lysates in a classical IP approach. However, a significant amount of the antibody coeluted (see 2.2.2), thus contaminating the precipitated proteins and interfering with the downstream analysis. To prevent a release of antibody, it was ought to be immobilized onto a support matrix. In the first approach used, the purified Lrrk2-specific antibody (clone 1E11) was covalently coupled to a CNBr-activated sepharose matrix. To identify non-specific protein binding, total rat IgGs were coupled in parallel and used as negative control for the IP. In order to perform a capable and specific co-IP of Lrrk2 and associated protein complex components, the IP-conditions were optimized. That way, an efficient precipitation as well as elution of Lrrk2 and a low background caused by non-specific bound proteins and released antibody should be accomplished. This involved the modification of various IP parameters: the salt concentration in the lysis buffer, thus the conditions for the formation of the antigen-antibody complex, the preclearance conditions (lysate to matrix ratio, incubation time at 4°C) and the amount of protein, incubation time, washing stringency and elution. The most efficient protocol is described in Material and Method (see 2.2.1.3). The precipitated proteins were separated by SDS-PAGE and visualized by silver staining as well as analyzed by western blotting. As shown in Figure 19, endogenous Lrrk2 was successfully immunoprecipitated from cellular lysates using the immobilized antibody. Elution under reducing and denaturing conditions resulted in a Lrrk2-specific immunosignal at ~280 kDa in the western blot analysis for the Lrrk2-specific IP sample (left panel, lane 1), whereas the control IP using total rat IgGs revealed no signal (left panel, lane 2). Silver staining of the proteins following their separation on SDS gels showed a number of non-specific bound proteins in the control sample (right panel, lane 2). Additionally, the applied elution condition resulted in the release of a significant amount of antibody, indicated by strong bands at 50 and 25 kDa in both silver staining and western blot analysis that corresponded to the heavy and light antibody chains. An attempt to resolve this issue by different elution techniques revealed that Lrrk2 could only be detached from the antibody-complex under both denaturing and reducing conditions (data not shown). Although the application of denaturing as well as reducing conditions solely yielded a diminished release of the antibody, the recovery of Lrrk2 in the elution fraction was inefficient. Western blot analysis of the Lrrk2-specific IP samples revealed, moreover, immunosignals in a molecular mass range above 250 kDa (left panel, lane 1), resulting most likely from boiling of the samples for their denaturation (see 2.1), as well as at approximately 200 kDa, 140 kDa, 80 kDa and 37 kDa (left panel, lane 1). These bands may represent truncated species of Lrrk2 as described previously upon overexpression of the protein in HEK293 cells (156, 221) or non-specific signals.

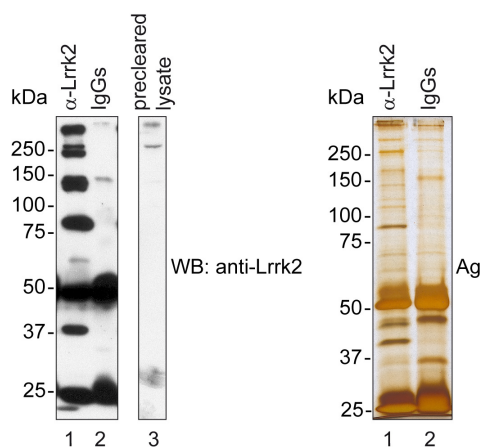


Figure 19: Optimized IP of endogenous Lrrk2 using the anti-Lrrk2 antibody covalently coupled to CNBr-activated sepharose.

The Lrrk2-specific rat-monoclonal antibody clone 1E11 was covalently coupled to CNBr-activated sepharose and endogenous Lrrk2 was immunoprecipitated from NIH3T3 cell lysates. Identically immobilized total rat IgGs were used to monitor non-specific binding of proteins. 1/6 and 5/6 of the eluates were subjected to SDS-PAGE followed by western blotting (WB; left panel) or silver staining (Ag; right panel). A precleared lysate volume corresponding to 1% of the IP input served as positive control in western blot analysis (left panel, lane 3). Western blotting revealed a successful precipitation of Lrrk2, indicated by a specific immunoreactive band at ~280 kDa in the IP fraction (left panel, lane 1). Immunoreactive bands at ~200 kDa, 140 kDa, 80 kDa

and 37 kDa may indicate truncated Lrrk2 species or non-specific signals. Visualization of the separated proteins by silver staining displayed a significant background caused by non-specific bound proteins in the control sample (right panel, lane 2). Strong signals detected at 25 and 50 kDa (lanes 1 and 2) correspond to the antibody's light and heavy chain.

As demonstrated, endogenous Lrrk2 could be successfully immunoprecipitated using the anti-Lrrk2 antibody covalently coupled to CNBr-activated sepharose. Although such immobilization of the antibody should prevent a contamination of the precipitated proteins with the antibody, the conditions established for an efficient co-IP of Lrrk2 and associated interaction partners yielded a considerable amount of the antibody in the elution fraction. Therefore, a second approach for the immobilization of the antibody was applied (see 2.2.4).

2.2.4 Cross-linking of the Lrrk2-specific antibody to a Protein G affinity resin efficiently precipitates endogenous Lrrk2 without a considerable contamination by the antibody

In order to precipitate the endogenous Lrrk2 complex without contamination by a vast amount of antibody for the identification of the protein's interaction partners by AP-MS, immobilization of antibody on a matrix was aimed. IP with the antibody covalently coupled to CNBr-activated sepharose resulted yet in a considerable high amount of antibody released from the resin (see 2.2.3). Therefore, immobilization was accomplished in a second approach by cross-linking the antibody to a Protein G sepharose matrix. A systematic comparison of different IP conditions was performed to optimize the approach for an analysis of the precipitated proteins by MS. This involved variations in the cross-linking density of the antibody, amount of total protein subjected to the IP, buffers used for the removal of unbound proteins and elution of the proteins as well as procedures to improve the IP specificity. The different conditions used for the optimization are outlined in Table 18, with the most efficient protocol (condition 11) described in detail in the Material and Method section 2.2.1.4.

Table 18: Conditions used to optimize the immunoprecipitation of endogenous Lrrk2 utilizing the anti-Lrrk2 antibody (clone 1E11) cross-linked to a sepharose resin.

		Condition 1	Condition 2	Condition 3	Condition 4	Condition 5
Protein samples	Cell type	NIH3T3	NIH3T3	Mouse brain	Mouse brain	Mouse brain
	Lysisbuffer	Buffer A ^{b)} +1% (v/v) NP-40	Buffer A +1% (v/v) NP-40	Buffer A +0.25 % (v/v) Brij-96	Buffer A +0.25 % (v/v) Brij-96	Buffer A +0.25 % (v/v) Brij-96
Matrix	Cross-linked IgGs	α -Lrrk2	α -Lrrk2/total rat IgG ^{g)}	α -Lrrk2/total rat IgG	α -Lrrk2/total rat IgG	α -Lrrk2/total rat IgG
	Coupling density	0.5 mg/mL matrix	1 mg/mL matrix	1 mg/mL matrix	1 mg/mL matrix	2 mg/mL matrix
Preclearance	Matrix:lysate ratio	1:10 ^{c)}	1:10	1:10	1:10	1:10
	Incubation at 4°C	30 min	30 min	30 min	30 min	30 min
IP	Protein conc.	2 μ g/ μ L	2 μ g/ μ L	2 μ g/ μ L	2 μ g/ μ L	2 μ g/ μ L
	Volume	0.5 mL	0.5 mL	0.5 mL	0.5 mL	0.5 mL
	Total protein amount	1 mg	1 mg	1 mg	1 mg	1 mg
	Matrix:lysate ratio	1:10	1:10	1:10	1:10	1:10
	Incubation at 4°	Overnight	Overnight	Overnight	Overnight	Overnight
	Washing buffer	HEPES buffer ^{d)} +0.1% (v/v) NP-40	HEPES buffer +0.1% (v/v) NP-40	HEPES buffer +0.1% (v/v) Brij-96	Buffer A +0.1% (v/v) Brij-96	HEPES buffer +0.1% (v/v) Brij-96
	Cycles	3	4	4	4	4
	Volume	500 μ L	500 μ L	500 μ L	500 μ L	500 μ L
Elution Step 1 ^{a)}	Buffer	Glycine buffer ^{e)} +0.1% (v/v) NP-40	Glycine buffer +0.1% (v/v) NP-40	Glycine buffer +0.1% (v/v) Brij-96	Glycine buffer +0.1% (v/v) Brij-96	Glycine buffer +0.1% (v/v) Brij-96
	Volume	100 μ L	100 μ L	100 μ L	100 μ L	100 μ L
	Conditions	5 min on ice	5 min on ice	5 min on ice	5 min on ice	5 min on ice
Elution Step 2	Buffer	1x Laemmli buffer ^{f)}	1x Laemmli buffer	1x Laemmli buffer	1x Laemmli buffer	1x Laemmli buffer
	Volume	50 μ L	50 μ L	50 μ L	50 μ L	50 μ L
	Conditions	15 min at 37°C	15 min at 37°C	15 min at 37°C	15 min at 37°C	15 min at 37°C
Figure		Figure 20	Figure 21A	Figure 21B	Figure 21C	Figure 22A

^{a)} Eluates were neutralized by the addition of 5% (v/v) 2 M Tris-HCL (pH 9).

^{b)} 30 mM Tris-HCl, pH 7.4, 150 mM NaCl, 10% (v/v) glycerol, 1x Roche complete protease inhibitor, 1x phosphatase inhibitor cocktail 1 and 2

^{c)} For preclearance, Protein G Fast Flow Sepharose was used.

^{d)} 20 mM HEPES-HCl, pH 7.5, 50 mM NaCl, 1x Roche complete protease inhibitor, 1x phosphatase inhibitor cocktail 1 and 2

^{e)} 200 mM glycine, pH 2.5, 500 mM NaCl

^{f)} 5x: 250 mM Tris-HCl, pH 6.8, 5% (w/v) SDS, 50% (v/v) glycerol, 500 mM β -mercaptoethanol and 0.025% (w/v) bromophenol blue; diluted 1:5 in ddH₂O. The buffer was supplemented with 5% (v/v) 2 M Tris-HCl (pH 9) for neutralization if an elution with glycine preceded.

^{g)} IgGs from rat serum (Sigma)

Table 18 (continued): Conditions used to optimize the immunoprecipitation of endogenous Lrrk2 utilizing the anti-Lrrk2 antibody (clone 1E11) cross-linked to a sepharose resin.

		Condition 6	Condition 7	Condition 8	Condition 9	Condition 10	Condition 11
Protein samples	Cell type	Mouse brain	Mouse brain	Mouse brain	Mouse brain	Mouse brain	Mouse brain
	Lysisbuffer	Buffer A +0.25 % (v/v) Brij-96	Buffer A +0.25 % (v/v) Brij-96	Buffer A +0.25 % (v/v) Brij-96	Buffer A +0.25 % (v/v) Brij-96	Buffer A +0.25 % (v/v) Brij-96	Buffer A +0.25 % (v/v) Brij-96
Matrix	Cross-linked IgGs	α -Lrrk2/total rat IgG	α -Lrrk2/total rat IgG	α -Lrrk2/total rat IgG	α -Lrrk2/total rat IgG	α -Lrrk2/rat IgG2a ^{j)}	α -Lrrk2/rat IgG2a
	Coupling density	2 mg/mL matrix	2 mg/mL matrix	2 mg/mL matrix	2 mg/mL matrix	1 mg/mL matrix	1 mg/mL matrix
Preclearance	Matrix:lysate ratio	1:10	1:10	1:10	1:10	1:10	1:10 ^{m)}
	Incubation at 4°C	30 min	30 min	30 min	30 min	1h	30 min
IP	Protein conc.	2 μ g/ μ L	2.25 μ g/ μ L	2 μ g/ μ L	2 μ g/ μ L	1 μ g/ μ L ^{k)}	1 μ g/ μ L ^{k)}
	Volume	1 mL	2 mL	2 mL	1 mL	1 mL	1 mL
	Total protein amount	2 mg	4.5 mg	4 mg	2 mg	1 mg	1 mg
	Matrix:lysate ratio	1:20	1:40	1:40 (preblocked) ^{h)}	1:20	1:20	1:40
	Incubation at 4°	Overnight	Overnight	Overnight	Overnight	Overnight	Overnight
	Washing buffer	HEPES buffer+0.1% (v/v) Brij-96	HEPES buffer+0.1% (v/v) Brij-96	HEPES buffer+0.1% (v/v) Brij-96	HEPES buffer+0.1% (v/v) Brij-96	HEPES buffer+0.1% (v/v) Brij-96	HEPES buffer +0.1% (v/v) NP-40
	Cycles	4	4	4	4	4	3
	Volume	500 μ L	500 μ L	500 μ L	500 μ L	500 μ L	500 μ L
Elution Step 1	Buffer	Glycine buffer +0.1% (v/v) Brij-96	Glycine buffer +0.1% (v/v) Brij-96	Glycine buffer +0.1% (v/v) Brij-96	340 μ g/ μ L Lrrk2 peptide ⁱ⁾	Glycine buffer +0.1% (v/v) Brij-96	
	Volume	100 μ L	100 μ L	100 μ L	200 μ L	100 μ L	
	Conditions	5 min on ice	5 min on ice	5 min on ice	10 min on ice	5 min on ice ^{l)}	
Elution Step 2	Buffer	1xLaemmli buffer	1xLaemmli buffer	1xLaemmli buffer	1xLaemmli buffer		1xLaemmli buffer
	Volume	50 μ L	50 μ L	50 μ L	50 μ L		50 μ L
	Conditions	15 min at 37°C	15 min at 37°C	15 min at 37°C	15 min at 37°C		15 min at 37°C
Figure	Figure 22B	Figure 22C	Figure 22D	Figure 22E	Figure 23A	Figure 23B	

^{h)} Lrrk2-specific and IgG-control matrix were preblocked with BSA to prevent non-specific binding of proteins. Thereto, 50 μ L of the resin was incubated in 10-fold matrix volume BSA (10 μ g/ μ L; New England Biolabs) diluted 1:1 in lysis buffer overnight at 4°C under agitation. Prior to use, the matrix was washed four times with 500 μ L lysis buffer.

ⁱ⁾ Peptide used for the production of rat-mono-clonal Lrrk2-specific antibodies. The elution was performed in 7-fold molar excess of the peptide versus the cross-linked antibody/IgG amount.

^{j)} Subclass-specific IgG control corresponding to anti-Lrrk2 antibody subclass IgG2a.

^{k)} Concentration of the protein sample was adjusted before preclearance.

^{l)} Elution of the proteins with glycine elution buffer was repeated two times. Prior to the analysis, all three fractions were combined and concentrated by centrifugation for 20 min at 14000 x g and 15°C using Microcon Centrifugal Filter Devices with a cut-off of 10 kDa (Millipore). To recover the samples, the Microcon unit was transferred bottom up to a fresh tube and centrifuged for 3 min at 1000 x g.

^{m)} For preclearance, Protein G Sepharose 4 Fast Flow was used.

Results

At first, two different protocols for cross-linking the antibody to Protein G sepharose were compared for their efficiency in immobilizing the antibody and IP of endogenous Lrrk2. Therefore, the Lrrk2-specific antibody (clone 1E11) was cross-linked to the affinity resin as detailed by Kriegsheim et al. (341) (Table 19, protocol 1) as well as according to Thermo Fisher Scientific as described elsewhere (291) (Table 19, protocol 2). Both prepared matrices were tested for their suitability to precipitate endogenous Lrrk2 from NIH3T3 lysates following the procedure described in Table 18 (condition 1). Proteins were eluted in a first step by incubation in glycine buffer (pH 2.5). Potentially remaining proteins were released from the matrix in a following second elution step using 1x Laemmli buffer. The precipitated proteins in both fractions were separated on SDS gels and analyzed by silver staining as well as western blot analysis.

Table 19: Protocols tested for cross-linking of the Lrrk2-specific antibody clone 1E11 to Protein G sepharose.

Step		Protocol 1 ^{a)}	Protocol 2 ^{b)}
Matrix equilibration	Buffer	20 mM HEPES, pH 7.5, 150 mM NaCl, 1% (v/v) NP-40, 2 mM EDTA	50 mM sodium borate, pH 8.2
	Volume	10-fold matrix volume	2.5-fold matrix volume
	Cycles	3	2
Antibody binding	Volume	10-fold matrix volume	2-fold matrix volume; diluted 1:1
	Buffer	20 mM HEPES, pH 7.5, 150 mM NaCl, 1% (v/v) NP-40, 2 mM EDTA	50 mM sodium borate, pH 8.2
	Density	0.5 mg/mL matrix	0.5–2 mg/mL matrix
	Incubation	2h, 4°C	30 min, room temperature
Removal of unbound antibody	Buffer	1. 20 mM HEPES, pH 7.5, 150 mM NaCl, 1% (v/v) NP-40, 2 mM EDTA 2. 100 mM HEPES, pH 8.5	50 mM sodium borate, pH 8.2
	Volume	10-fold matrix volume	2.5-fold matrix volume
	Cycles	1. 3 2. 2	2
Cross-linking	Buffer	100 mM HEPES, pH 8.5	0.2 M triethanolamine, pH 8.2
	DMP conc.	10 mg/mL	6.6 mg/mL
	Volume	10-fold matrix volume	2-fold matrix volume
	Incubation	1 h, room temperature	1 h, room temperature
Removal of surplus DMP	Buffer	100 mM HEPES, pH 8.5	0.2 M triethanolamine, pH 8.2
	Volume	10-fold matrix volume	2.5-fold matrix volume
	Cycles	2	2
Blocking of active sites	Buffer	100 mM Tris-HCl, pH 7.5	0.1 M ethanolamine, pH 8.2
	Volume	10-fold matrix volume	1-fold matrix volume
	Incubation	30 min, room temperature	10 min, room temperature
Washing step	Buffer	100 mM HEPES, pH 8.5	
	Volume	10-fold matrix volume	
Removal of non-cross-linked antibody	Volume	10-fold matrix volume	
	Cycles	2	1
	Buffer	200 mM glycine, pH 2.5, 500 mM NaCl, 0.1% (v/v) NP-40	200 mM glycine, pH 2.5, 500 mM NaCl, 0.1% (v/v) NP-40
Final wash	Volume	10-fold matrix volume	2.5-fold matrix volume
	Cycles	2	2
	Buffer	20 mM HEPES, pH 7.5, 150 mM NaCl, 1% (v/v) NP-40, 2 mM EDTA	50 mM sodium borate, pH 8.2

^{a)} Protocol according to Kriegsheim et al. (341).

^{b)} Protocol outlined by Thermo Fisher Scientific described elsewhere (291) (see 2.2.1.4).

As demonstrated by western blotting, mild elution conditions using acidic glycine in a buffer of high ionic strength did not release Lrrk2 from either of the two matrices used (Figure 20, left panel, lanes 1 and 3). In contrast, elution under denaturing and reducing conditions with 1x Laemmli buffer yielded a Lrrk2-specific immunosignal at ~280 kDa (Figure 20, left panel, lanes 2 and 4), indicating that the protein was efficiently immunoprecipitated by both matrices. Additionally, bands at 50 and 25 kDa that correspond to the heavy and light chain of the antibody were detected. However, the signal intensity of these bands was considerable less than compared to those in the IP using the classical approach (see 2.2.2, Figure 18) or the covalently coupled antibody (see 2.2.3, Figure 19). This was affirmed by visualization of the separated proteins on SDS gels by silver staining (Figure 20, right panel) where only the light chain generated a conspicuous signal at 25 kDa in the Laemmli fractions (lanes 2 and 4). Elution using the glycine buffer did not result in a contamination of the proteins by the antibody as no corresponding signals were detected in the western blot analysis (Figure 20, left panel, lanes 1 and 3) or silver staining (Figure 20, right panel, lanes 1 and 3).

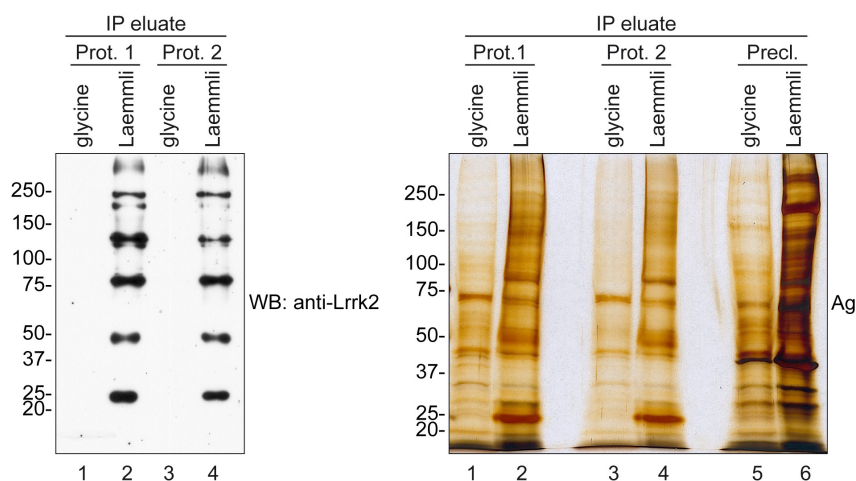


Figure 20: Evaluation of two cross-linking protocols for the immobilization of the anti-Lrrk2 antibody clone 1E11 to Protein G sepharose.

The Lrrk2-specific antibody was cross-linked to Protein G sepharose as described by Kriegsheim et al. (341) (Prot. 1) as well as according to Thermo Fisher Scientific described elsewhere (291) (Prot. 2). Both generated matrices were used for the immunoprecipitation of endogenous Lrrk2 from NIH3T3 cells (see Table 18; condition 1). Proteins were released from the matrix with acidic glycine (glycine) followed by incubation with Laemmli buffer (Laemmli). SDS gels were loaded with 10% or 50% of the eluate samples and separated proteins were analyzed by western blotting (WB; left panel) and visualized by silver staining (Ag; right panel), respectively. Using glycine for the elution of proteins prevented a release of Lrrk2 as well as of the antibody from both matrices as neither protein specific immunosignals nor bands corresponding to the heavy and light chain were detected in the western blot (left panel, lanes 1 and 3) or silver staining (right panel, lanes 1 and 3). Elution under denaturing and reducing conditions resulted in the release of Lrrk2 from both matrices as indicated by a corresponding immunoreactive signal at ~280 kDa in western blot analysis (left panel, lanes 2 and 4). The eluates contained also the antibody, demonstrated by analogous signals at 50 and 25 kDa in western blotting and silver staining, but in a considerable decreased amount than in the eluate fractions derived from the classic IP or IP using the covalently coupled antibody. Various non-specific bound proteins were identified by silver staining using eluates from the preclearance matrix (right panel, lanes 5 and 6).

The results revealed that both cross-linking protocols led to an efficient cross-linking of the antibody to the Protein G affinity resin that is suitable for the IP of endogenous Lrrk2. However, the elution fractions derived from the IP using the antibody cross-linked according to protocol 1 displayed a higher background likened to the corresponding ones using the matrix of protocol 2. This was indicated by a comparison with the glycine and Laemmli elution fraction of the matrix used for the preclearance of the lysates that were separated and silver stained in parallel (Figure 20, right panel, lanes 5 and 6). Bands detected in those fractions were also visible in a larger amount in the respective fractions of the IP using the protocol 1-matrix than utilizing the matrix cross-linked according to protocol 2, corresponding to proteins that bind non-specific to the matrix. Therefore, cross-linking of the antibody was performed hereafter according to protocol 2 as outlined in the Material and Method section 2.2.1.4.

The efficient immobilization of the anti-Lrrk2 antibody by cross-linking according to Thermo Fisher as described elsewhere (291) (Table 19, protocol 2) and the suitability of the obtained matrix in the IP of Lrrk2 from NIH3T3 lysates was verified in a second IP. Herein, the cross-linking density of the antibody was duplicated to 1 mg/mL to ameliorate the binding of Lrrk2 and a control matrix using total rat IgGs was prepared in parallel. The condition used for the IP was not further modified, except that the total rat IgG-matrix was used for the preclearance of the cell lysates, and corresponded to that used in the evaluation of the cross-linking protocol (Table 18, condition 2). The precipitated proteins were subjected to SDS-PAGE and analyzed by western blotting (Figure 21A, upper panel) and silver staining (Figure 21A, lower panel). Western blot analysis revealed that Lrrk2 was efficiently precipitated from the lysates, displayed by a decrease in the Lrrk2-specific immunosignal at ~280 kDa in the anti-Lrrk2 IP-supernatants (Figure 21A, upper panel, lane 5) compared to the supernatants of the control IP and the input lysate (Figure 21A, upper panel, lanes 6 and 7). As observed before, Lrrk2 was only released from the matrix under denaturing and reducing conditions, with a small amount of antibody coeluting with the proteins (Figure 21A, upper panel, lane 3). Herein, the protein was not detected in the eluate fraction derived from the control IP, thus indicating that it was specifically precipitated by the anti-Lrrk2 antibody (Figure 21A, upper panel, lanes 2 and 4). Elution with acidic glycine prevented a contamination of the proteins with the antibody but did not detach Lrrk2 from the matrix (Figure 21A, upper panel, lane 1). Silver staining of the resolved proteins showed a considerable high background of non-specifically bound proteins in the control immunoprecipitates (Figure 21A, lower panel, lanes 2 and 4) with a band pattern that was indiscernible from the respective ones of the Lrrk2-specific IP eluate fractions (Figure 21A, lower panel, lanes 1 and 3). Bands at 50 and 25 kDa in the Laemmli buffer eluates corresponded to the heavy and light chain of the coeluted antibody. The intensity of these bands as well as of the immunosignals in the western blotting analysis was considerably reduced compared to those in the classical IP (see 2.2.2)

or the IP using the covalently coupled antibody (see 2.2.3). Therefore, the cross-linking of the antibody successfully achieved its immobilization on the resin and decreased the quantity of antibody contaminating the precipitated proteins.

Due to the association of Lrrk2 with the neurodegenerative disorder PD, the identification of interaction partners in the brain represents a main concern. As demonstrated, immobilization of the anti-Lrrk2 antibody by cross-linking reduced the amount of antibody contamination in the precipitated proteins significantly, thus permitting an analysis of the IP eluates by MS. However, non-specific binding of proteins to the affinity matrix caused a high background that would interfere with the downstream analysis. Hence, the approach was further optimized utilizing mouse brain lysates.

At first, the IP of Lrrk2 from mouse brain lysates was conducted similar to that from NIH3T3 lysates, only the detergent in the washing buffer was changed to Brij-96 (Table 18, condition 3). Analysis of the precipitated proteins by western blotting revealed an efficient depletion of Lrrk2 from the lysates in the Lrrk2-specific IP compared to the control IP (Figure 21B, upper panel, lanes 5 and 6) and its release from the matrix that was only mediated by Laemmli buffer (Figure 21B, upper panel, lane 3) but not by acidic glycine (Figure 21B, upper panel, lane 1). Visualization of the resolved proteins on SDS gels by silver staining demonstrated a significant amount of non-specific bound proteins in the control samples (Figure 21B, lower panel, lanes 2 and 4), preventing the identification of specific bands in the Lrrk2 immunoprecipitates (Figure 21B, lower panel, lanes 1 and 3). Therefore, the buffer used to wash the matrix following the formation of the antigen-antibody-complex was changed for the next IP, with the HEPES buffer replaced by lysis buffer containing 0.1% (v/v) Brij-96 (Table 18, condition 4). Although Lrrk2 was precipitated from the lysates in a comparable amount to the prior IP (Figure 21B and C, upper panel, lanes 5 and 6 or 5-7), the quantity of Lrrk2 that was recovered in the Laemmli eluate fraction was markedly decreased (Figure 21B and C, upper panel, lane 3). Furthermore, a significant background was detectable in the control samples (Figure 21C, lower panel, lane 4) that was even higher than using HEPES buffer to wash the matrix (Figure 21B, lower panel, lane 4). Therefore, the HEPES buffer was utilized to remove non-specific bound proteins in the further optimization of the IP.

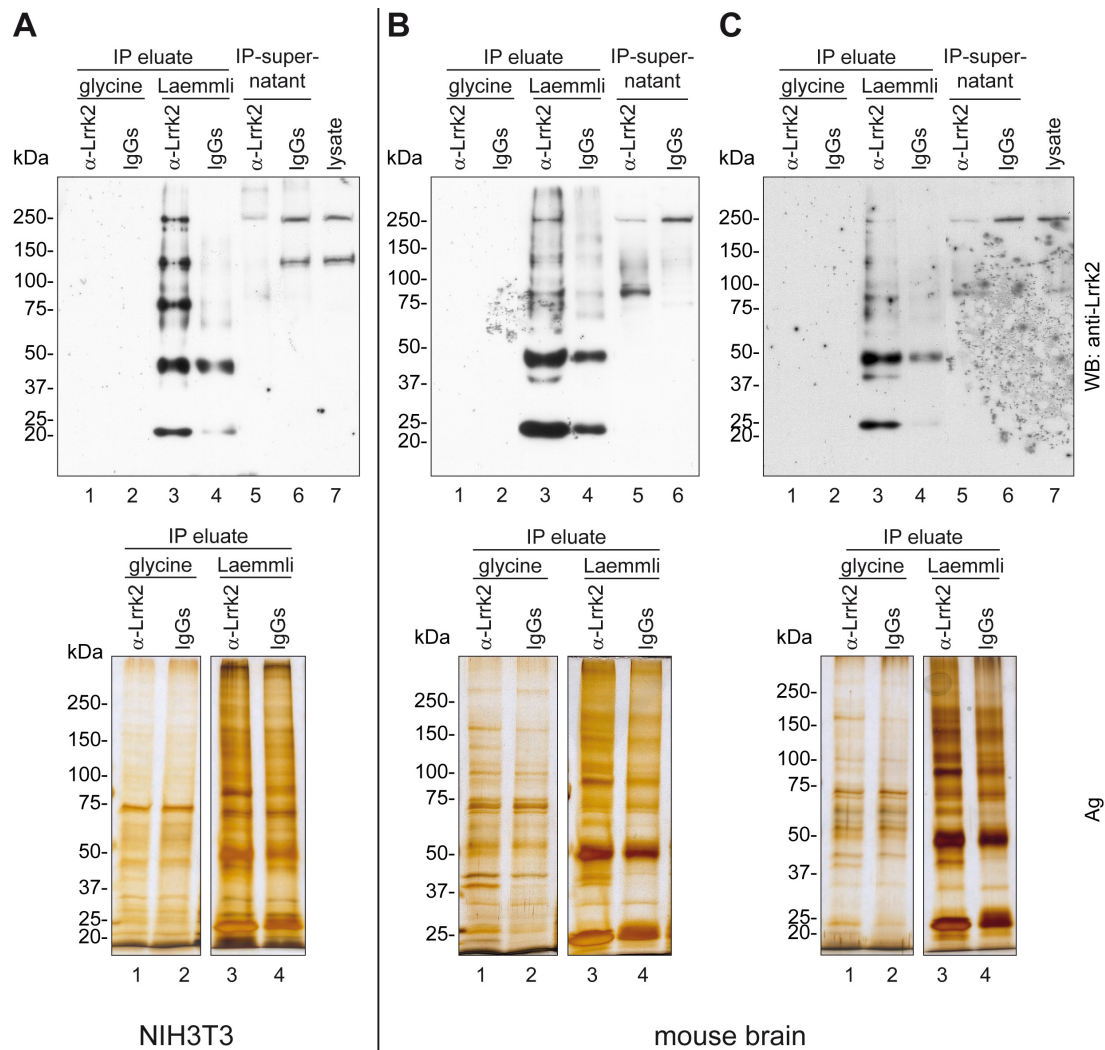


Figure 21: The anti-Lrrk2 antibody (clone 1E11) cross-linked to Protein G sepharose precipitated endogenous Lrrk2 efficiently from both NIH3T3 cell lysates and mouse brain lysates.

The anti-Lrrk2 antibody was cross-linked to Protein G sepharose at a density of 1 mg/mL matrix according to Thermo Fisher Scientific as described (291) and applied to the IP of endogenous Lrrk2 from NIH3T3 cell lysates (A) and mouse brain lysates (B and C). 10% or 50% of the eluates were resolved on SDS gels and subjected to the analysis by western blotting (WB; upper panels) or silver staining (Ag; lower panels). For western blotting, a lysate and IP-supernatant volume corresponding to 3% of the input was loaded. The specific precipitation of endogenous Lrrk2 with the cross-linked antibody from NIH3T3 (A) as well as mouse brain lysates (B and C) was confirmed. Western blotting revealed that the protein was efficiently depleted from the lysates (upper panels, lanes 5-7) and was only released from the matrix using denaturing and reducing conditions (upper panels, lane 3) together with a small amount of antibody coeluting (upper and lower panels, lanes 3 and 4). Although usage of acetic glycine for elution prevented a contamination of the eluates with antibody (upper and lower panels, lanes 1 and 2), Lrrk2 was not present (upper panels, lane 1). Silver staining of the resolved proteins showed a significant background generated by non-specific bound proteins (lower panels, lanes 2 and 4). Modification of the washing condition in the IPs from mouse brain lysates using HEPES buffer (see Table 18, condition 3) (B) instead of buffer A (see Table 18, condition 4) (C), both supplemented with 0.1% (v/v) Brij-96, yielded an increased amount of Lrrk2 recovered in the Laemmli eluate (upper panels, lane 3) and a decrease in background. However, the band pattern in the Lrrk2-specific IP samples was similar to that of the controls (lower panels, lanes 3 and 4).

In the next step of optimization, the density of the antibody and likewise the total rat IgGs cross-linked to the beads was elevated to 2 mg/mL matrix to improve the precipitation of Lrrk2 and thus related interaction partners. The initial IP using condition 5 (Table 18), which was similar to condition 3 except the antibody's cross-linking density, led again to numerous non-specifically precipitated proteins that were observed in the silver stained gels (Figure 22A, lower panel, lanes 2 and 4). No specific bands that could be correlated with

Lrrk2-related interactors were detectable in the Lrrk2 precipitates (Figure 22A, lower panel, lanes 1 and 3). Nevertheless, Lrrk2 was specifically precipitated with the antibody (Figure 22A, upper panel, lanes 5-7) and detached from the matrix with Laemmli buffer (Figure 22A, upper panel, lane 3). Also an enhanced amount of total protein applied to the IP of 2 mg (Table 18, condition 6) and 4.5 mg (Table 18, condition 7) with a concomitant decrease in the matrix to lysate ratio (1:20 and 1:40, respectively) did not result in an improvement. Although the extent of Lrrk2 that was precipitated by the anti-Lrrk2 antibody increased markedly (Figure 22B and C, upper panel, lane 3), no bands unique for the Lrrk2-specific IP were visible on silver stained SDS gels (Figure 22B and C, lower panel, lanes 1 and 3) compared to the total rat IgG control (Figure 22B and C, lower panel, lanes 2 and 4). In an attempt to impede the non-specific binding of proteins to the affinity resin, the matrix was blocked with BSA before it was applied to an IP with similar settings than used in condition 7 (Table 18, condition 8). As illustrated in the western blot analysis of the separated immunoprecipitates by SDS-PAGE, blocking of non-specific binding sites did not affect the efficiency of the IP. The amount of protein that was extracted by the Lrrk2-specific antibody from the lysate (Figure 22D, upper panel, lanes 5-7) and subsequently eluted in Laemmli buffer (Figure 22D, upper panel, lane 3) was in the range of condition 7. However, still a multitude of unspecific proteins was coprecipitated in the control as indicated by silver staining (Figure 22D, lower panel, lanes 2 and 4). The band pattern obtained for the Lrrk2-specific samples did not reveal any differences (Figure 22D, lower panel, lanes 1 and 3), so that neither Lrrk2 itself nor its interaction partners could be specified. Thus, both blocking of the affinity resin with BSA to prevent non-specific binding of proteins to the matrix and an augmented amount of total protein applied to the IP to increase the coprecipitation of Lrrk2 interactors did not enhance the ration between non-specific and specific precipitated protein that would admit an analysis of the precipitates by MS. In order to achieve a specific release of the Lrrk2 complex from the matrix without coelution of non-specific contaminants, Lrrk2 was attempted to detach from the antigen-antibody-complex by a gentle elution using the antibody-specific peptide. Herein, a 7-fold molar excess of the Lrrk2-peptide was used to displace endogenous Lrrk2 bound by the antibody (Table 18, condition 9). Silver stained SDS gels displayed distinct differences between the Lrrk2-specific IP and control IP, with the latter containing a reduced number of coeluted non-specific proteins (Figure 22E, lower panel, lanes 1 and 2). However, western blot analysis of the precipitates revealed that although efficiently depleted from the lysates (Figure 22E, upper panel, lanes 5-7) Lrrk2 could not be competitively eluted from the matrix (Figure 22E, upper panel, lane 1). Again, the protein was only released from the resin using denaturing and reducing conditions as proven by the Laemmli eluates (Figure 22E, upper panel, lane 3). The widespread, smeared immunosignal observed in the lower range (around 25 kDa) of the peptide elution fraction might be caused by the peptide itself (342).

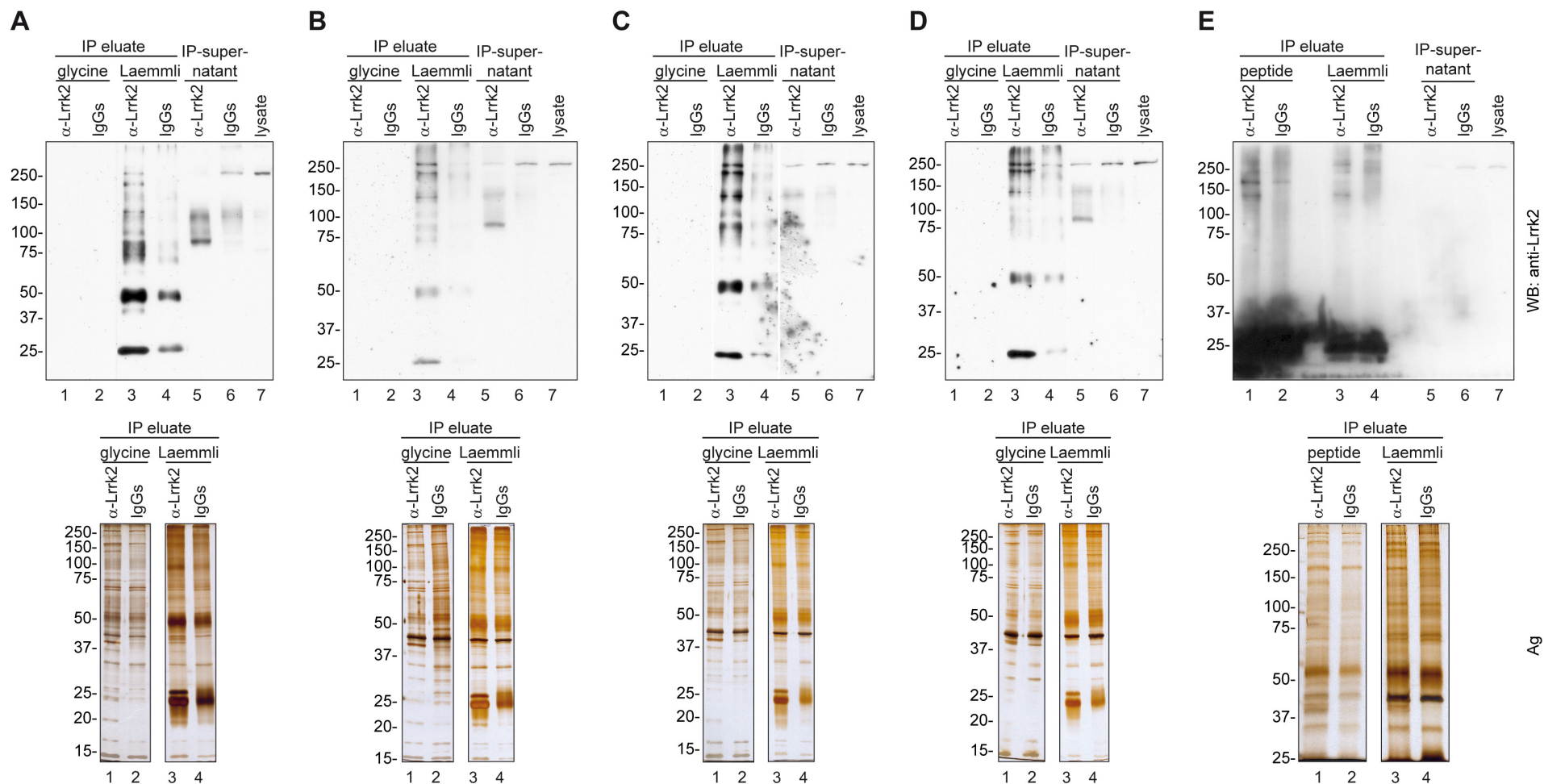


Figure 22: Different conditions assayed for their capability to optimize the IP of endogenous Lrrk2 from mouse brain lysates using the anti-Lrrk2 antibody (clone 1E11) cross-linked to Protein G sepharose.

The Lrrk2-specific antibody was immobilized with a density of 2 mg/mL matrix on Protein G sepharose and applied to the IP of endogenous Lrrk2 from mouse brain lysates using different conditions (see text and Table 18). Optimization of the approach to enhance the number of specific precipitated proteins comprised an increase in the amount of total protein applied to the IP (A-C, condition 5-7), blocking of non-specific binding sites on the resin with BSA (D, condition 8) and competitive elution of Lrrk2 using a 7-fold molar excess of the antibody-specific peptide (E, condition 9). For the analysis by western blotting (upper panels), 10% (A,B and E) or 5% (C and D) of the eluate fractions together with a lysate and IP-supernatant volume corresponding to 2% (A), 1% (B), 0.2% (C), 0.3% (D) or 0.5% (E) of the IP input were separated on SDS gels. 50% (A and B) or 25% (C-E) of the precipitated

Using total rat IgGs in the control to monitor the number of non-specific coprecipitated proteins provides the option that a certain amount of proteins bind to another IgG subclass than to the anti-Lrrk2-matched one, thereby causing a background additional to that generated by the subclass-specific IgGs and the resin. To increase the specificity of the control experiments, subclass-specific rat IgGs corresponding to the anti-Lrrk2 antibody clone 1E11 subclass IgG2a were therefore cross-linked to Protein G sepharose at a density of 1 mg/mL matrix, corresponding to that of the antibody. Both control and the Lrrk2-specific affinity matrix were subjected to the IP using mouse brain lysates that were precleared for 1 h at 4°C instead of 30 min using the control matrix. In an attempt to accomplish the release of Lrrk2 from the resin using gentle elution conditions, thus avoiding a clearance of the antibody from the matrix completely, elution with acidic glycine in a buffer of high ionic strength was repeated three times and the fractions were subsequently combined (Table 18, condition 10).

The IgG2a control samples still displayed a considerable high amount of non-specifically precipitated proteins in silver stained SDS gels (Figure 23A, right panel, lane 2). A similar band pattern was observed for the samples derived from the anti-Lrrk2 IP that did not admit the identification of bands correlating with potential Lrrk2 interactors (Figure 23A, right panel, lane 1). Moreover, western blot analysis of the precipitates showed that also a sequential elution with acetic glycine did not cause an elution of Lrrk2 (Figure 23A, left panel, lane 1), although the protein was efficiently cleared from the lysates by the antibody (Figure 23A, left panel, lanes 3-5). As demonstrated by a final IP (Table 18, condition 11), Lrrk2 could only be recovered in the IP eluates when using denaturing and reducing conditions (Figure 23B, lane 1). It illustrated further that Lrrk2 itself could not be extracted by the rat IgG2as (Figure 23B, lanes 2 and 4), thus proving that the anti-Lrrk2 antibody specifically precipitated endogenous Lrrk2 (Figure 23B, lanes 1 and 3).

In total, the results demonstrated that the Lrrk2-specific antibody specifically precipitated endogenous Lrrk2 from NIH3T3 lysates as well as mouse brain lysates when cross-linked to Protein G sepharose. The protein was only released from the matrix under denaturing and reducing conditions, which caused also a coelution of the antibody. The extent of antibody contaminating the elution fraction was, however, significantly reduced compared to the eluates in the classic IP or in the IP using the covalently bound antibody, with a quantity that would not interfere with a downstream analysis by LC-MS/MS. However,

(Figure 22 continued): proteins were subjected to SDS-PAGE and visualized by silver staining (lower panels). The anti-Lrrk2 antibody efficiently depleted endogenous Lrrk2 from the brain lysates (A-E, upper panels, lanes 5-6) that was only released from the resin under denaturing and reducing conditions (Laemmli; A-E, upper panels, lane 3). Mild conditions utilizing either acetic glycine in a buffer of high ionic strength (glycine; A-D) or the antibody-specific peptide in high molar excess (E) did not cause the elution of the protein (upper panels, lane 1). In addition, numerous unspecific coprecipitated proteins were observed under all conditions used for the elution of proteins in the silver stained gels (lower panels) as indicated by the control IPs (A-E, lanes 2 and 4). Compared to the controls, the band pattern obtained for the Lrrk2-specific immunoprecipitates did not reveal any differences that could be correlated with interactors, independent from any modification of the IP conditions (A-D, lower panels, lane 1 and 3).

the background caused by non-specifically bound proteins was considerable high, thus preventing an identification of Lrrk2 interaction partners by both gel-based and direct, non-quantitative MS strategies. Various modification of the IP conditions such as an increased amount of cross-linked antibody, enhanced amounts of total protein applied to the IP, preblocking of non-specific binding sites with BSA and competitive elution with the anti-Lrrk2 antibody specific peptide, did not result in an improvement. Nevertheless, the established Lrrk2-specific IP (Table 18, condition 11) is a suitable tool for the extraction of the complex from both cell line and brain lysates and a hypothesis-driven identification of interaction partners by western blotting. Although the obtained precipitates were not applicable for the *de novo* characterization of the Lrrk2 interactome by standard AP-MS, they constituted the prerequisite for the adapted AP-MS strategy QUICK (293) (see 4.1).

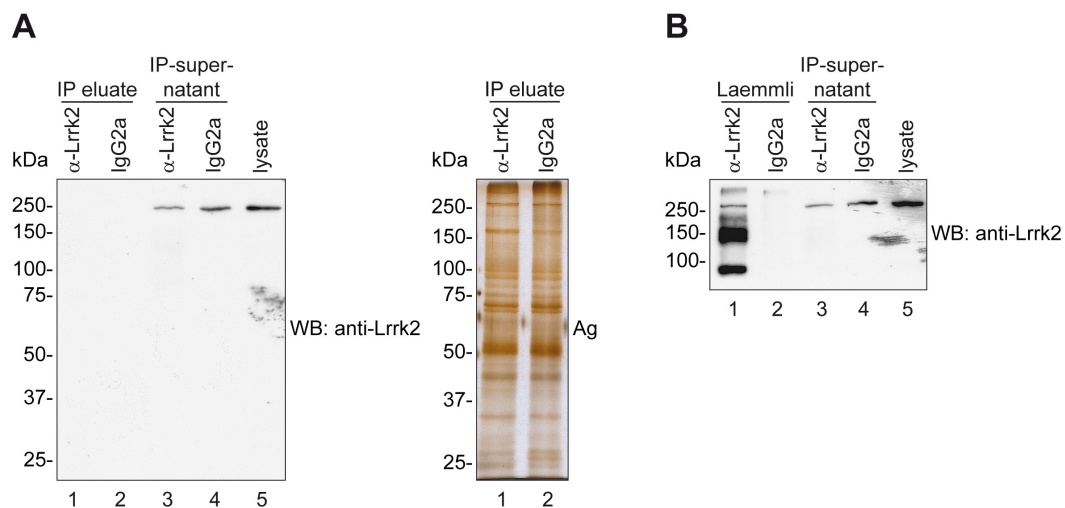


Figure 23: IP of endogenous Lrrk2 from mouse brain lysates using the cross-linked anti-Lrrk2 antibody and matched subclass-specific IgG2as for the identification of non-specific coprecipitated proteins.

The Lrrk2-specific antibody (clone 1E11) and matched subclass-specific IgGs (IgG2a) were cross-linked to Protein G sepharose at a density of 1 mg/mL matrix. IP of endogenous Lrrk2 was performed using mouse brain lysates. 5% of the IP eluates and a lysate as well as IP-supernatant volume corresponding to 1% (A) or 2% (B) of the input were separated by SDS-PAGE and analyzed by western blotting (WB; left panel in A). For the visualization of separated proteins by silver staining (Ag; right panel in A), 25% of the precipitated proteins was resolved. (A) Lrrk2 was specifically depleted from the lysate with an efficient amount (left panel, lanes 3-5), but repeated elution with acidic glycine did not release the protein from the affinity resin (left panel, lane 1). In addition, silver staining of the SDS gel did not identify protein bands that were specific for the Lrrk2-IP within the significant amount of non-specific coeluted proteins (right panel, lanes 1 and 2). (B) Lrrk2, specifically extracted from the lysates by the antibody (lane 3-5), was only recovered in the eluates under denaturing and reducing conditions using Laemmli buffer.

2.3 Lrrk2 antibodies are non-specific in immunofluorescence labeling of cells

Having validated the suitability of the Lrrk2-specific mAbs generated in the laboratory for western blot analysis and IP of the endogenous protein and established the respective assays, two basic tools to study the proteins function were implemented. IF staining of cells represents an additional technique for the characterization of a target protein. Therefore, several antibodies were tested for their ability to detect endogenous Lrrk2 in NIH3T3 cells compared to Lrrk2 knockdown cells (control) (see 3.2 and 3.3). In this study, only the affinity-purified Lrrk2-specific mAb clones 1E11, 2E12 and 3A6 were evaluated for their suitability in

an IF labeling. All three antibodies revealed a ubiquitous staining distributed throughout the cells. However, the staining intensity as well as the staining pattern was equal in both wt and Lrrk2 knockdown cells, thus indicating that the antibodies caused non-specific signals (Figure 24A). Modification of the routinely used staining conditions described in the Material and Methods section 2.6.7 by permeabilizing the cells for 5 min with PBST (PBS containing 0.1% (v/v) Tween20) prior to blocking non-specific binding sites with 1% (v/v) BSA or 3% (v/v) goat serum in PBST, removal of non-specific bound proteins with PBST and dilution of both the primary and the secondary antibody in 1% (v/v) BSA/PBST or 1% (v/v) goat serum/PBST yielded no improvement (data not shown). Besides the antibody clones tested here, all the other generated mAbs against Lrrk2 were evaluated for their suitability in IF in the laboratory using cortical cells derived from embryonic mice (wt and Lrrk2 knockdown controls). Although various fixation techniques, such as PFA and methanol fixation, as well as staining protocols were applied, only non-specific signals could be detected using the monoclonal anti-Lrrk2 antibodies (personal communication, Dr. G. Piccoli, Helmholtz Zentrum München). mAbs are generally thought to be more specific in IF and to generate less significant background as they detect only one epitope of the target protein. However, this makes them at the same time less tolerant towards changes in the antigen nature that might be caused by the fixation or processing of the cells to be labeled, preventing the antibodies to bind. Therefore, several commercial polyclonal antibodies that became available during the study and were raised to a number of distinct epitopes located within the protein (Table 20) were assayed on NIH3T3 cells.

Table 20: Summary of commercial antibodies against Lrrk2 tested for their suitability in immunocytochemistry.

Antibody	Species	Peptide origin	Peptide location
Alexis AT106	Rabbit-polyclonal	Recombinant human Lrrk2	aa 1838-2133 (COR/Kinase)
Lifespan LS-B505	Rabbit-polyclonal	Synthetic peptide of human Lrrk2	aa 2500-2527 (C-term)
Cell Signaling 2567	Rabbit-polyclonal	Synthetic peptide of human Lrrk2	around Gly2090 (WD40)
Abcam ab60937	Rabbit-polyclonal	Synthetic peptide of human Lrrk2	aa 2527-2577 (C-term)
Santa Cruz N-15	Goat-polyclonal	Murine Lrrk2	N-term

None of the tested antibodies could specifically detect the endogenous Lrrk2 protein. Using the modified staining protocol described above, the antibodies Cell Signaling 2567, Abcam ab60937 and Santa Cruz N-15 revealed no immunosignals (data not shown). The antibody Alexis AT106 displayed a non-specific staining in the Lrrk2 knockdown cells indiscernible from that in the wt cultures (data not shown). Likewise, the application of the Lifespan LS-B505 antibody led only to the detection of non-specific signals (Figure 24B).

In addition to the commercially available anti-Lrrk2 antibodies, rabbit-polyclonal ones directed against the C-term of murine Lrrk2 were generated in the laboratory in cooperation with Eurogentec. The purified antibodies 820 (peptide spanning amino acids 2501-2514) (146) and 821 (peptide spanning amino acids 2513-2527) were monitored for their suitability

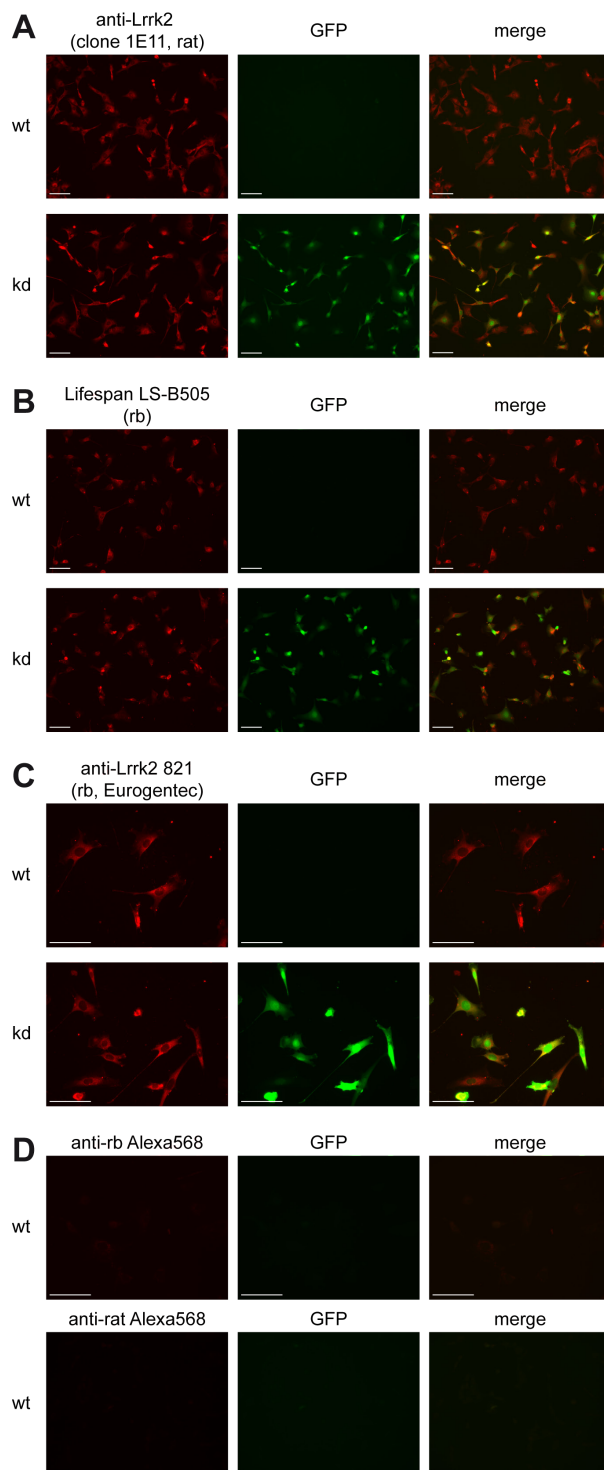


Figure 24: Antibodies directed against Lrrk2 did not detect the endogenous protein in IF staining.

Representative images of the immunocytochemical analysis of endogenous Lrrk2 on NIH3T3 cells (wt) using different Lrrk2 antibodies. Lrrk2 knockdown cells (kd) served as negative controls. The pictures illustrate immunostaining of cells using the antibodies anti-Lrrk2 clone 1E11 (A), Lifespan LS-B505 (B) and anti-Lrrk2 821 (C) (left column). Non-specific binding of the Alexa Fluor 568-conjugated secondary anti-rabbit (rb) and anti-rat antibodies was monitored by incubating the cells with them solely (D). GFP expression (center column) indicated cells expressing Lrrk2-targeting first (A) or second generation (B and C) shRNAs. Immunosignals detected with the outlined antibodies were indiscernible in pattern and intensity on wt cells compared to the knockdown controls, indicating a non-specific staining. Scale bar: 50 μm.

in IF labeling of endogenous Lrrk2 using NIH3T3 cells. Again, a non-specific staining was observed when either of the two antibodies was applied to the analysis using the standard protocol. Representative images are given in Figure 24C, with the antibody 821 being utilized. Therefore, the staining procedure was varied and cells were fixed with ice-cold methanol for 10 min at -20°C prior to the immunocytochemical assay according to Biskup et al. (146) with minor modifications. The used TBS buffer was replaced by a PBS buffer throughout the protocol and primary as well as secondary antibodies were diluted in PBS containing 0.1% (v/v) Triton X-100 and 1% (v/v) BSA instead of 10% (v/v) normal serum. However, both anti-Lrrk2 antibodies were non-specific in the IF staining, yielding immunosignals in wt and Lrrk2 knockdown cells that possessed an equal staining intensity as well as distribution within the cells (data not shown).

Although various self-generated as well as commercial antibodies to the Lrrk2 protein, monoclonal and polyclonal ones, were tested for their specificity in IF using wt NIH3T3 cells and Lrrk2 knockdown cells as control, none of the antibodies was able to detect the endogenous mouse protein.

3. Lentiviral-mediated knockdown of *Lrrk2* *in vitro*

RNAi is an evolutionary conserved mechanism that permits the selective post-transcriptional down-regulation of a target gene in cells and thus represents a generic technique to assess the function of an endogenously expressed protein in its native cellular environment. In the present study, the depletion of *Lrrk2* from *in vitro* cell systems was central to the functional characterization of the endogenous protein. Here, the long term-sustained knockdown of *Lrrk2* expression was aimed at by the lentiviral-mediated delivery of *Lrrk2*-specific shRNAs. Therefore, several suitable target sequences within the murine *Lrrk2* mRNA transcript were identified and the corresponding shRNAs were tested for their knockdown efficiency in a reporter-based assay system. The potential of the thus preselected shRNAs in RNAi experiments was then verified on cellular basis to ensure the validity of the obtained data, giving some indication of the physiological role of *Lrrk2*.

3.1 Evaluation of shRNA sequences targeting murine *Lrrk2* for their knockdown efficiency

One obstacle in the application of RNAi for determining and dissecting a protein's function is that not all siRNAs cognate to a given target mRNA are equally efficient in the down-regulation of protein expression. Even small positional shifts along the target mRNA sequence are sufficient to alter siRNA function and efficacy in an apparently unpredictable manner (343, 344). Hence, it appears reasonable to verify the efficiency of designed shRNAs prior to embark on the labor-intense lentiviral-mediated RNAi experiments. Although various computational tools are available to select efficient and specific siRNAs, these resources are yet imperfect and do not alleviate the need for experimental validation (344).

To identify potent shRNAs targeting *Lrrk2* among the eight selected hairpin constructs (see Material and Methods, 2.4.1), a reporter-based assay was applied, where a plasmid that carried the target sequence fused to a reporter gene was cointroduced into cells together with one of the target-specific shRNA constructs. The expression of the reporter could subsequently be correlated with the depletion of the target sequence. To this end, HEK293T cells were transiently cotransfected with a plasmid carrying a 3.5 kb-fragment of murine *Lrrk2* (AY792512: 50-3487) that comprised the siRNA target sequences fused 3' to eGFP (peGFP-EK-*Lrrk2* (3.5 kb)) and a shRNA expression plasmids (pBC/H1sh1-sh8) at a 1:9 ratio. Cells transfected with peGFP-EK-*Lrrk2* (3.5 kb) and the empty pBC KS+(Clal)-H1 plasmid in the same ratio, with either of the vectors solely and non-transfected cells served as controls. Two days after transfection, the amount of GFP-positive cells was determined by flow cytometry. In addition, GFP expression was analyzed by western blotting.

Among the eight tested shRNAs, four constructs led to a significant decrease in the relative amount of GFP-positive HEK293T cells compared to the control 2 (c2), transfected with the empty pBC KS+(Clal)-H1 vector together with peGFP-EK-*Lrrk2* (3.5 kb). Herein, the

expression of sh1 and sh6 was most effective, resulting in a reduction of GFP-positive cells to $19.83 \pm 4.00\%$ ($p < 0.001$ vs. c2, n=3, one-way ANOVA, Tukey's post-hoc test) and $34.17 \pm 7.70\%$ ($p < 0.01$ vs. c2, n=3, one-way ANOVA), respectively (Figure 25A). The diminished fraction of GFP-expressing cells within the respective cultures was accompanied by a corresponding reduction in GFP protein content as revealed by western blot analysis (Figure 25B, lanes 1 and 6). The cotransfection of either pBC/H1-sh3 or -sh5 led also to a decreased quantity of GFP protein detected on western blots (Figure 25B, lanes 3 and 5) as well as to a significant decline in the amount of GFP-expressing cells to $44.31 \pm 7.73\%$ (sh3; $p < 0.01$ vs. c2, n=3, one-way ANOVA) or $54.64 \pm 4.04\%$ (sh5; $p < 0.05$, vs. c2, n=3, one-way ANOVA) (Figure 25A). Both were, however, marked less pronounced compared to sh1 and sh6. In contrast, the depression in GFP-positive cells observed upon expression of shRNAs sh2, sh4, sh7 and sh8 was statistically not significant ($p > 0.05$ vs. c2, n=3, one-way ANOVA) (Figure 25A), correlating with only a slight reduction in GFP protein levels observed in the western blot analysis (Figure 25B, lanes 2, 4, 7 and 8).

Applying an artificial test system for the evaluation of the eight designed shRNAs targeting *Lrrk2* regarding their suitability in RNAi experiments, the two hairpins sh1 and sh6 appeared to be most efficient and were thus selected for the lentiviral-mediated knockdown of endogenous *Lrrk2* *in vitro*.

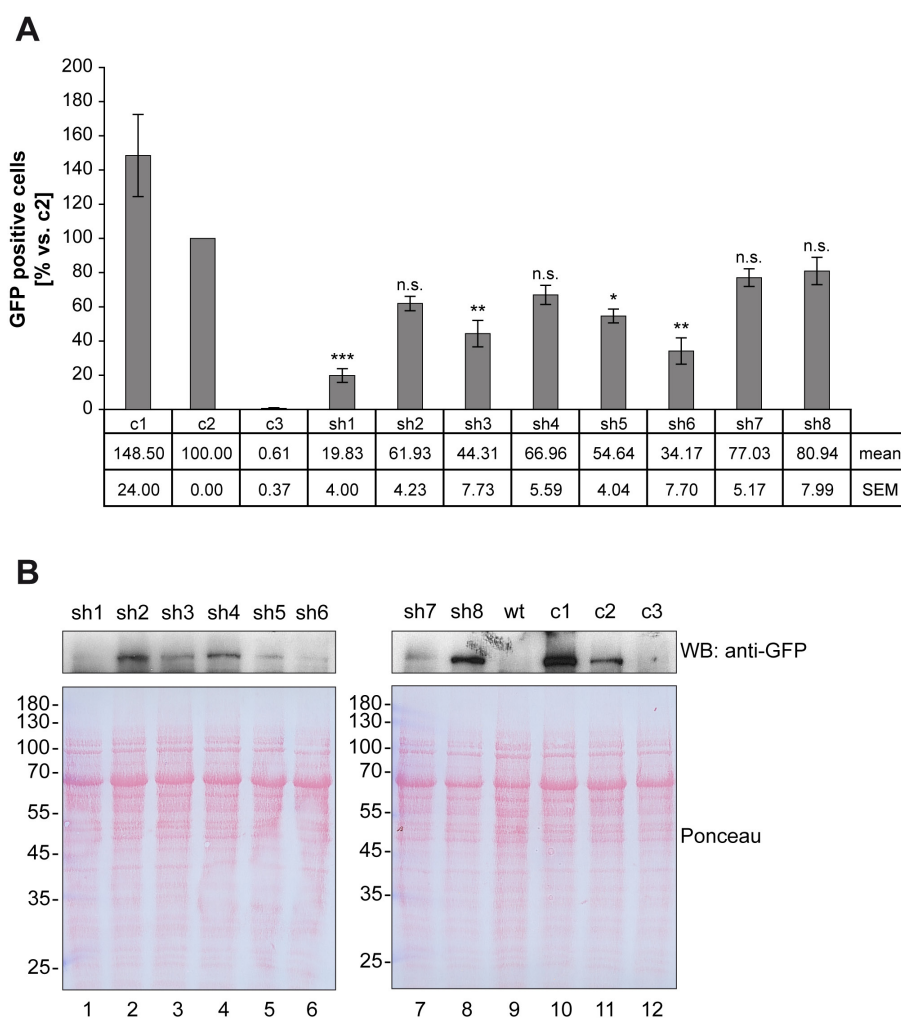


Figure 25: Identification of functional shRNAs targeting *Lrrk2* in a reporter-based *in vitro* assay.

HEK293T cells were transiently cotransfected with a vector carrying a 3.5 kb fragment of murine *Lrrk2* (AY792512: 50-3487), encompassing the siRNA target sequences, fused 3' to eGFP (peGFP-EK-*Lrrk2* (3.5 kb)) and an expression plasmid for the eight selected and designed shRNAs (pBC/H1sh1-sh8) in a 1:9 ratio by calcium phosphate precipitation. Controls were prepared in parallel by the transfection of peGFP-EK-*Lrrk2* (3.5 kb) together with the empty pBC KS+(Clal)-H1 vector in the same ration (c2), peGFP-EK-*Lrrk2* (3.5 kb) (c1) or pBC KS+(Clal)-H1 (c3) solely as well as using non-transfected cells (wt). Two days after transfection, cells were harvested and one half was utilized to determine the amount of GFP-positive cells by flow cytometry, whereas the second half was applied to western blot analysis of GFP protein levels. (A) Relative amount of GFP-positive cells within the cultures compared to c2. Out of the eight shRNAs targeting *Lrrk2*, only four led to a statistical significant decrease in the relative amount of GFP-positive cells, with sh1 and sh6 being the most efficient (vs. c2, *** $p < 0.001$, ** $p < 0.01$, * $p < 0.05$, n.s. $p > 0.05$, $n=3$, one-way ANOVA, Tukey's post-hoc test). (B) Western blot analysis revealed that the decline in GFP-positive cells is accompanied by a corresponding reduction in the GFP protein content. The Ponceau S-stained membranes served as loading control. WB: western blot.

3.2 Activation of a non-specific cellular innate immune response upon expression of first generation shRNAs against *Lrrk2* in primary VM cultures

The prevalidation of shRNA sequences using an artificial test system represents a suitable tool to evaluate their RNAi efficiency and to facilitate the selection of functional silencing constructs, but it does not replace the experimental verification within the applied cellular system. Given the pathological association between *Lrrk2* and PD, which predominantly affects DA neurons of the SNpc, the efficient lentiviral-mediated knockdown of *Lrrk2* by shRNA expression was aimed in primary VM cultures derived from embryonic mice. Containing authentic DA neurons with relevance to PD in the context of their naturally

occurring neighboring cell types in a yet controlled environment, they represent an established *in vitro* model of the DA system to study pathophysiological mechanism in PD (345).

First, the two preselected (see 3.1), independent first generation shRNA constructs sh1 and sh6 under the control a human H1 promoter were cloned into the lentiviral transfer vector LVTH and respective lentiviral supernatants were obtained. Primary VM cultures derived from E12.5 mouse embryos were transduced with the lentiviral vectors LVsh1 (MOI 0.5) or LVsh6 (MOI 2) one day after plating (DIV1). Cultures transduced with the empty vector (LVTH, MOI 0.5) or non-transduced wt cultures served as negative controls. The delivery of the two *Lrrk2* targeting shRNAs at the selected MOIs resulted in a similar efficient repression of *Lrrk2* on mRNA as well as protein levels at DIV9 (Figure 26A and B). Cultures expressing sh1 or sh6 displayed a significant decrease in *Lrrk2* mRNA levels compared to wt controls ($p < 0.01$, one-way ANOVA, Tukey's post-hoc test) as detected by semiquantitative real-time PCR (Figure 26A). In these cultures, the relative *Lrrk2* expression ratio amounted to 0.44 ± 0.16 (LVsh1, n=3) and 0.51 ± 0.09 (LVsh6, n=3) (Figure 26A), respectively. LVTH control cultures showed no alterations in the relative *Lrrk2* expression compared to non-transduced cells (1.00 ± 0.06 , n=4). The reduction in *Lrrk2* mRNA content upon expression of both silencing constructs was associated with an analogous decrease in *Lrrk2* protein levels (Figure 26B). However, a decline of the lentiviral vector-driven expression of GFP, which can be correlated with the quantity of transduced cells, in both sh1 and sh6 expressing cultures compared to the LVTH-transduced controls was detected, although equal (LVsh1) or even 4-fold (LVsh6) amounts of lentiviral particles were applied for the infection (Figure 26B). This suggested a marked decline in cell numbers within the knockdown cultures rather than a poor transduction efficiency of the silencing constructs.

As reported previously on primary cortical cultures, the expression of shRNAs from lentiviral vectors is capable of inducing an innate cellular immune response (346). Activation of INF signaling and ISG expression in the response to dsRNAs ultimately induces cell death (274). To determine whether the expression of both sh1 and sh6 triggered a cellular immune response in the primary VM cultures, semiquantitative real-time PCR for mRNA encoding *Oas1*, a classic interferon target gene, was conducted. At DIV9, *Oas1* mRNA levels were increased in both *Lrrk2* knockdown cultures (LVsh1 and LVsh6) compared to the wt control, with relative expression ratios of 4.37 ± 0.39 (LVsh1, n=3) and 2.6 ± 0.99 (LVsh6, n=2), whereas the LVTH vector alone had no effect (0.89 ± 0.10 , n=3) (Figure 26C). In addition to cultures cultivated until DIV9, LVTH- and LVsh1-transduced primary VM cultures were analyzed 13 days after lentiviral delivery (DIV14). Again, the transduction with LVsh1 led to a significant decline in levels of *Lrrk2* gene expression ($p < 0.001$, one-way ANOVA) to an expression ratio of 0.33 ± 0.06 (n=4) relative to the wt control (Figure 26A) and a concomitant decrease in *Lrrk2* protein levels (Figure 26B). The already at DIV 9 observed reduction of

GFP expression in cultures transduced with LVsh1 could also be monitored at DIV14 but with a higher degree of severity (Figure 26B). Likewise, the expression of *Oas1* induced upon delivery of the sh1 silencing construct exceeded that detected at DIV9, with a respective relative mRNA level increased approximately nine-fold compared to the wt control (8.78 ± 1.13 , $n=4$) (Figure 26C). LVTH control displayed again no alterations in the relative *Oas1* expression level (1.18 ± 0.09 , $n=4$) (Figure 26C).

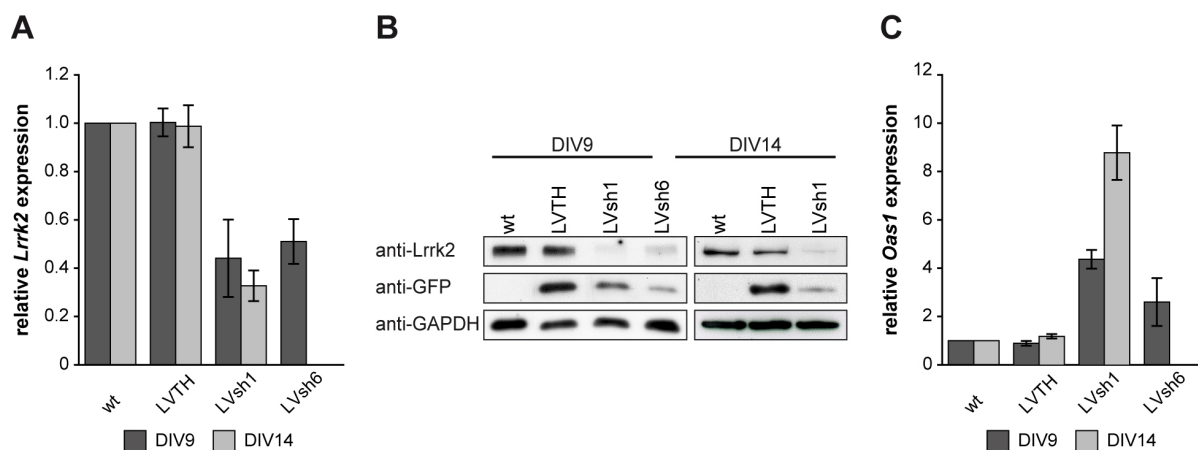


Figure 26: Induction of an IFN response by first generation shRNA constructs targeting *Lrrk2* in primary VM cultures.

Primary VM cultures derived from E12.5 mouse embryos were transduced with lentiviral vectors encoding *Lrrk2* targeting first generation shRNAs (LVsh1 or LVsh6) at DIV1. Transduction with the empty transfer vector LVTH and wt cells served as negative controls for transduction-associated effects. Cultures were analyzed at DIV9 or DIV14. (A) Semiquantitative real-time PCR revealed a decrease of *Lrrk2* mRNA levels in LVsh1- and LVsh6-transduced cultures relative to the wt controls. (B) Sh1 and sh6 expressing cultures exhibited a reduced *Lrrk2* protein content and, compared to the LVTH control, a decrease in the lentiviral vector-driven GFP expression as detected by western blot analysis. GAPDH western blotting served as protein loading control. (C) Semiquantitative real-time PCR was conducted to monitor the expression of the interferon-responsive gene *Oas1*. The expression of both *Lrrk2* silencing constructs led to a marked increase in *Oas1* mRNA levels relative to the wt control, indicative for the induction of an INF response.

For the immunocytochemical analysis of primary VM cultures expressing the first generation shRNA constructs sh1 or sh6, cells were fixed, dopaminergic neurons were identified by TH-immunoreactivity and examined by fluorescence microscopy. Cell counts at DIV9 revealed that silencing of *Lrrk2* by the expression of either sh1 or sh6 led to a significant decrease in the amount of TH-ir neurons in the cultures relative to untransduced wt controls. Here, a reduction to $30.25 \pm 7.22\%$ (LVsh1) and $29.86 \pm 2.21\%$ (LVsh6) ($p < 0.001$ vs. wt, $n=4$ and 2, one-way ANOVA) in the relative cell counts was observed, which remained unaltered in the LVTH control expressing cultures ($96.00 \pm 5.827\%$; $p > 0.05$ vs. wt, $n=4$, one-way ANOVA) (Figure 27A). Cultivation of LVsh1-transduced cultures until DIV14 resulted in further depression in the relative number of TH-ir cells to $10.83 \pm 3.34\%$ ($p < 0.001$ vs. wt, $n=3$, one-way ANOVA) (Figure 27A). LVTH control cultures displayed a small decrease in relative cell counts to $90.01 \pm 6.27\%$, which was not statistically significant ($p > 0.05$ vs. wt, $n=4$, one-way ANOVA) (Figure 27A). Morphological inspection of sh1 (Figure 27B) and sh6 (data not shown) expressing cell cultures at DIV9 revealed an

abnormal, degeneration-like cell shape of the remaining TH-ir neurons upon silencing of *Lrrk2*. Besides an irregular and distorted morphology, the neurons exhibited a rarefaction as well as collapse and/or complete loss of neurites in contradistinction to the healthy TH-ir cells with long, branched neural processes in the wt and LVTH control (Figure 27B). Cultivation of the *Lrrk2* knockdown cultures (LVsh1 and LVsh6) until DIV14 led to an increased severity of the phenotype (data not shown). Although transduction of primary VM cultures with the first generation shRNA constructs designed to target endogenous *Lrrk2* led to a significant repression of *Lrrk2* mRNA as well as protein levels, the observed decrease in lentiviral vector-driven GFP expression in combination with the markedly increased *Oas1* expression, the substantial net loss of TH-ir neurons and the abnormal phenotype of the remaining DA neurons strongly indicated a cellular immune response rather than a specific silencing effect induced by the two shRNAs. These results reflected the findings of a study published by Bauer et al. (324) where the first generation sh1 construct was observed to induce the activation of an interferon response in primary cortical cultures.

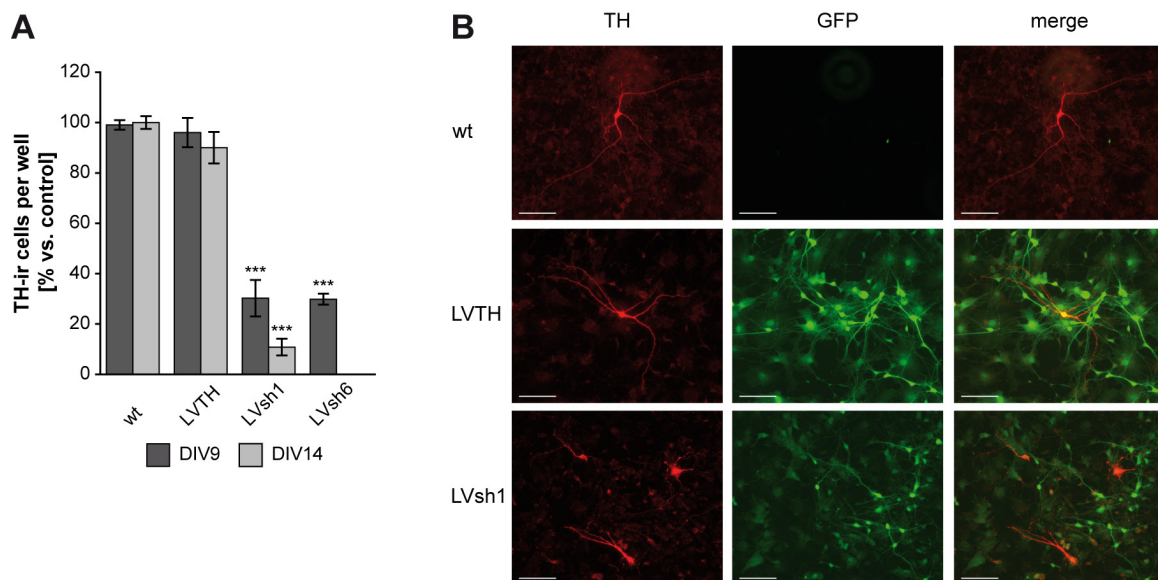


Figure 27: Cytotoxic effects of *Lrrk2* targeting first generation shRNAs in primary VM cultures.

Primary VM cultures were transduced with lentiviruses encoding first generation *Lrrk2* silencing constructs (LVsh1 or LVsh6) or containing the transfer vector (LVTH) alone. Dopaminergic (DA) neurons were visualized by tyrosine hydroxylase (TH-) immunocytochemistry. (A) A significant decline of TH-ir neurons was evident in *Lrrk2* shRNA expressing cultures at DIV9 and DIV14. (B) Immunocytochemical analysis of the TH-ir neurons (left panel) revealed an abnormal morphology of these cells in LVsh1-transduced cultures at DIV9. Cells in the wt and LVTH control cultures displayed the characteristic morphology of healthy neurons, including long branched neuronal processes. Overlay of the GFP-reporter (center column) and TH expression (right column, merge) indicates transduced DA neurons. Scale bar: 50 μ m.

3.3 Second generation silencing constructs accomplish the efficient knockdown of *Lrrk2* without the induction of an IFN response in primary VM cultures

At the beginning of the study, simple hairpin-structured first generation shRNAs were employed for the lentiviral-mediated knockdown of *Lrrk2* as they have been shown to represent an efficient system for stable gene silencing (323, 347). In addition, the same system was successfully applied for the knockdown of delta-like 1 (DIK1) in primary VM

cultures within the laboratory (336). However, as the expression of *Lrrk2*-targeting shRNAs induced a cellular immune response in primary VM cultures (see 3.2) - and also in primary cortical cultures (324) -, an alternative strategy for the design of the silencing triggers had to be applied. Here, the backbone structure of the hairpin stem within a shRNA was modified by the implementation of design features of the endogenously expressed primary miR-30 transcript. The natural configuration of such second generation shRNA (shRNA^{mir}) constructs was reported to be more efficient in target gene silencing than simple hairpin designs and suspected to avoid the induction of an INF response (325, 326). The shRNA^{mir} construct miB3, generated for the knockdown of *Lrrk2* on the basis of sh1 (see Figure 12), was shown to efficiently silence the target gene without provoking an interferon-stimulated gene expression in primary cortical cultures (324). In the present study, a second, independent shRNA^{mir} construct directed against *Lrrk2*, derived from the first generation shRNA sh6, was designed (miB4). Both silencing sequences, miB3 and miB4, were cloned into lentiviral vectors and the respective viral supernatants were obtained.

The lentiviral-mediated knockdown of *Lrrk2* by shRNA^{mir} expression was applied to primary VM cultures derived from E12.5 mouse embryos. Thereto, the cultures were transduced with lentiviral vectors encoding the *Lrrk2* targeting shRNA^{mir}s (LVmiB3 and LVmiB4) or the empty vector (LVTH) one day after plating with an MOI of 0.5 and were analyzed at DIV9 or DIV14. Transduction of the VM cultures with LVmiB3 and LVmiB4 resulted in a significant decrease of *Lrrk2* mRNA levels relative to wt cultures ($p < 0.001$, one-way ANOVA) (Figure 28A) and led to a relative *Lrrk2* expression ratio of 0.50 ± 0.03 (LVmiB3, n=5) and 0.52 ± 0.03 (LVmiB4, n=3) at DIV9 and 0.45 ± 0.04 (LVmiB3, n=5) and 0.51 ± 0.01 (LVmiB4, n=4) at DIV14 (Figure 28A). The decline in *Lrrk2* mRNA levels after expression of the two silencing constructs was accompanied by a corresponding reduction in *Lrrk2* protein content (Figure 28B). In contrast to cultures expressing first generation silencing constructs (see 3.2, Figure 26B), lentiviral vector-driven GFP expression in the shRNA^{mir}-transduced cultures was not reduced compared to that in the LVTH controls (Figure 28B). To monitor a possible induction of an INF response, the expression of *Oas1* was analyzed in the transduced primary VM cultures. Semiquantitative real-time PCR analysis revealed no meaningful changes in *Oas1* mRNA levels (Figure 28C). At DIV9, its expression level in the shRNA^{mir} transduced cultures achieved 2.04 ± 0.08 (LVmiB3, n=4) and 1.36 ± 0.32 (LVmiB4, n=3), respectively, and remained unaltered in the LVTH control (1.02 ± 0.16 , n=5) relative to the wt control. Also at DIV14, the knockdown of *Lrrk2* provoked only a small increase in the relative *Oas1* expression, varying between 2.56 ± 0.24 for LVmiB3 (n=4) and 1.77 ± 0.34 for LVmiB4 (n=4), which was far below of those induced by the expression of sh1 (see 3.2, Figure 26C) and unlikely to interfere with the downstream analysis (348). LVTH control cultures displayed a relative *Oas1* mRNA level of 1.21 ± 0.08 (n=5).

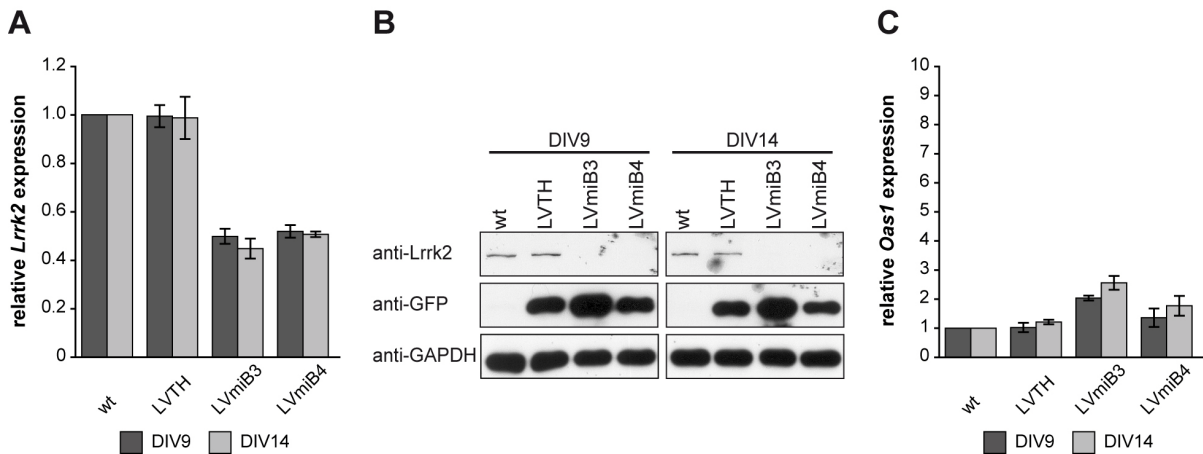


Figure 28: Second generation designed shRNA^{mir} constructs mediate the efficient knockdown of Lrrk2 in primary VM cultures without the induction of an INF response.

VM tissue was isolated from E12.5 mouse embryos, cells were transduced at DIV1 with LVTH, LVmiB3 or LVmiB4 and analyzed at DIV9 or DIV14. (A) Semiquantitative real-time PCR displayed reduced Lrrk2 mRNA levels in primary VM cultures transduced with the two independent shRNA^{mir}-constructs LVmiB3 and LVmiB4. (B) Western blot analysis revealed that the transduction with LVmiB3 and LVmiB4 resulted in decreased Lrrk2 protein levels at both time points. GFP and GAPDH western blots served as controls for transduction efficiency and protein load, respectively. (C) To rule out any effects due to antiviral defense mechanisms, the expression of the interferon responsive gene *Oas1* was determined by semiquantitative real-time PCR in transduced cultures. At both time points, the expression of the two constructs did not have an effect on the induction of *Oas1*. This research (A and B) was originally published in *Molecular and Cellular Proteomics* (349). © The American Society for Biochemistry and Molecular Biology.

Examination of TH-immunostained primary VM cultures revealed that the population of dopaminergic cells within these cultures was efficiently transduced with both the lentiviral transfer vector and the Lrrk2 targeting shRNA^{mir} encoding vectors. Moreover, a long-term sustained lentiviral-mediated gene expression could be assured. About 90% of the TH-ir neurons displayed the expression of the lentiviral vector-encoded reporter GFP at both time points, with $92.37 \pm 0.83\%$ (LVTH), $92.63 \pm 0.70\%$ (LVmiB3) and $90.40 \pm 1.07\%$ (LVmiB4) at DIV9 and $90.31 \pm 0.70\%$ (LVTH), $91.88 \pm 0.67\%$ (LVmiB3) and $88.83 \pm 1.02\%$ (LVmiB4) at DIV14 (Figure 29A). This observation correlated with the constant and uniform expression of GFP within the LVmiB3 and LVmiB4 transduced cultures compared to the LVTH control at DIV9 and DIV14 as detected by western blot analysis (Figure 28B). In addition, the amount of TH-ir cells relative to non-transduced wt cultures was quantified. Unlike after the delivery of first generation shRNAs (see 3.2, Figure 27A), no significant alterations in the relative number of TH-ir neurons was observed here at DIV9 ($p > 0.05$ vs. wt, $n = 4-5$, one-way ANOVA; wt: $99.28 \pm 1.20\%$, LVTH: $102.12 \pm 3.64\%$; LVmiB3: $102.16 \pm 3.22\%$ and LVmiB4: $97.34 \pm 8.37\%$) (Figure 29B). As recently as at DIV14, transduction of the cultures with either LVmiB3 or LVmiB4 caused a significant decrease in relative cell counts to $78.38 \pm 4.18\%$ and $74.92 \pm 5.40\%$, respectively ($p < 0.01$ vs. wt, $n = 3-5$, one-way ANOVA) (Figure 29B). However, this decline was far smaller than following the expression of sh1 (see 3.2, Figure 27A). The relative amount of TH-ir neurons in the LVTH control expressing cultures revealed a reduction to $89.46 \pm 5.79\%$, which was, however, not statistically significant ($p > 0.05$ vs. wt, $n = 4$, one-way ANOVA).

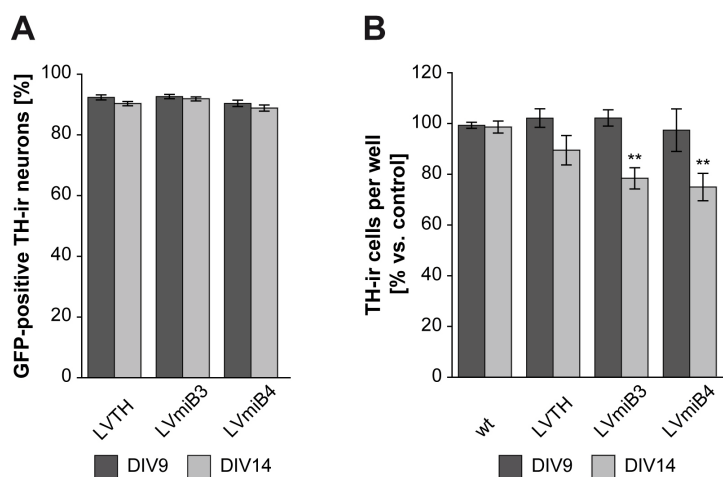


Figure 29: Efficient lentiviral delivery and persisted expression of shRNA^{mir} sequences within viable DA neurons.

Lrrk2 expression in primary VM cultures was depleted by lentiviral delivery of two independent silencing constructs (LVmiB3 and LVmiB4). Non-transduced (wt) or LVTH-transduced cells served as negative controls, and cultures were analyzed at DIV9 or DIV14. (A) Determination of the relative amount of TH-ir cells expressing the lentiviral reporter GFP revealed the efficient transduction of the dopaminergic cell population within the VM cultures as well as a sustained long-term expression of lentiviral-vector encoded sequences. (B) Cell counts of TH-ir cells per well. No differences in the amount of DA neurons occurred between

the conditions at DIV9, whereas the knockdown of Lrrk2 led to a decrease in TH-ir cell counts at DIV14 (** $p < 0.01$ vs. wt DIV14, $n=3-5$, one-way ANOVA, Tukey's post-hoc test). This research (B) was originally published in *Molecular and Cellular Proteomics* (349). © The American Society for Biochemistry and Molecular Biology.

The results demonstrated a Lrrk2 mRNA and protein reduction using the miR-30-based shRNAs miB3 and miB4. Of note, these Lrrk2 silencing constructs avoided the induction of the interferon-response gene *Oas1*, which was otherwise observed when first generation designed shRNAs were used (see 3.2), thus preventing any off-target effects based on the activation of an INF response. This was further supported by the preservation of viable VM cultures following the expression of the shRNA^{mir} constructs, indicated by non-considerable changes in TH-ir cell counts relative to wt controls. Hence, in accordance with published RNAi guidelines (348, 350), an efficient system for the lentiviral-mediated knockdown of endogenous Lrrk2 within primary VM cultures with two different, independent silencing constructs was established.

3.4 Silencing of endogenous Lrrk2 affects cellular morphology

3.4.1 The knockdown of Lrrk2 in primary VM cultures leads to an impaired neurite outgrowth of developing DA neurons.

Based on the implication of Lrrk2 in the etiology of the neurodegenerative disorder PD, the consequences of an experimentally downregulation of *Lrrk2* gene expression, indicative of the protein's biological function and associated cellular pathways, were investigated in neuronal cells. Therefore, the lentiviral-mediated knockdown of Lrrk2 was applied to primary VM cultures by the delivery of the two independent second generation designed silencing constructs LVmiB3 and LVmiB4 (see 3.3).

For the phenotypic analysis of shRNA^{mir} expressing primary VM cultures, cells were fixed, DA neurons were visualized by TH-IF and examined by fluorescence microscopy. Figure 30 shows representative images and camera lucida drawings of untreated wt, LVTH control and Lrrk2 knockdown (LVmiB3 and LVmiB4) cultures at DIV9 and DIV14. TH-ir neurons in the wt and LVTH control cultures displayed a typical neuronal morphology with small bi- or multipolar cell bodies. In addition, they extended long neuritic processes with

complex neuritic arborization, with both features becoming stronger apparent at DIV14 than at DIV9 (Figure 30). Although the overall appearance of the shRNA^{mir} expressing neurons was similar to the controls, the knockdown of Lrrk2 led to shortened neurites as early as at DIV9 (Figure 30A and B), which was even more pronounced at DIV14 (Figure 30C and D).

Quantitative measurements of the neurite length at DIV9 confirmed the immunocytochemical observations and revealed that the transduction with LVmiB3 led to a significant shift in the neurite length distribution ($p < 0.001$ vs. wt, χ^2) to shorter neurites (Figure 31B). Expression of the LVmiB4 construct led also to a shift towards lower value, although it was not significant ($p > 0.05$ vs. wt, χ^2). However, the population of neurites with a length of 40 μm or shorter increased significantly compared to wt cultures ($p < 0.001$, $n=4-5$, two-way ANOVA; wt: $24.04 \pm 0.71\%$, LVmiB4: $33.29 \pm 1.01\%$). Furthermore, the relative amount of processes with a length between 40-80 μm and 80-120 μm decreased from $22.68 \pm 0.91\%$ and $22.39 \pm 0.81\%$ (wt) to $19.51 \pm 1.24\%$ and $19.55 \pm 0.89\%$ (LVmiB4) ($p < 0.05$ vs. wt, $n=4-5$, two-way ANOVA). The alterations in neurite length distributions were reflected in a significant decrease in the average length of neurite extensions of TH-ir neurons expressing shRNA^{mir}s targeting Lrrk2 over wt control ($p < 0.001$ vs. wt, $n=4-5$, one-way ANOVA) (Figure 31A). The outgrowth declined from $90.60 \pm 0.98 \mu\text{m}$ in wt cultures to $58.92 \pm 0.58 \mu\text{m}$ (-35.0%) in LVmiB3-transduced and $82.20 \pm 1.89 \mu\text{m}$ (-9.4%) in LVmiB4-transduced cultures. In the LVTH control, no alterations in the frequency distribution and average neurite length ($91.54 \pm 1.34 \mu\text{m}$) were observed. Neurons cultivated until DIV14 possessed on average significantly longer processes than at DIV9 ($p < 0.001$ DIV9 vs. DIV14, $n=3-5$, two-way ANOVA), regardless of whether they expressed shRNA constructs or not (Figure 31A). However, the average neurite length of LVmiB3- or LVmiB4-transduced TH-ir neurons at DIV14 was still significantly decreased compared to the wt or LVTH condition ($p < 0.001$ vs. wt, $n=3-5$, one-way ANOVA; wt: $122.03 \pm 1.71 \mu\text{m}$, LVTH: $120.45 \pm 2.81 \mu\text{m}$, LVmiB3: $69.73 \pm 1.03 \mu\text{m}$ (-42.9%), LVmiB4: $103.65 \pm 2.35 \mu\text{m}$ (-15.1%)) (Figure 31A). The corresponding neurite length distributions displayed a shifting to lower values, which was significant for both Lrrk2 targeting shRNA constructs ($p < 0.001$ LVmiB3 vs. wt, $p < 0.01$ LVmiB4 vs. wt, χ^2) (Figure 31B). Thus, depletion of Lrrk2 in primary VM cultures resulted in an impaired outgrowth of developing DA neurites.

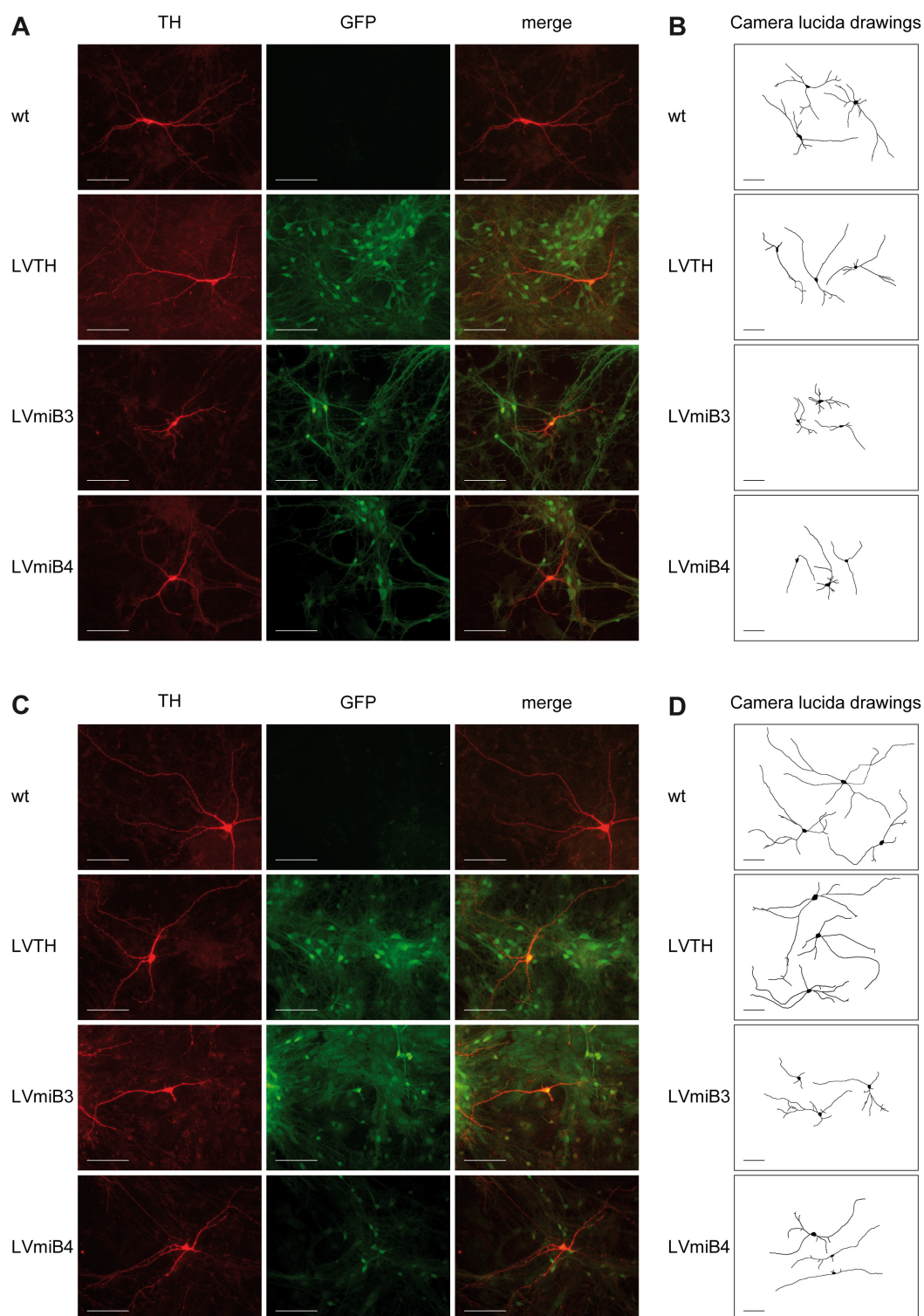


Figure 30: TH-ir neurons expressing *Lrrk2* mRNA targeting shRNA^{mir}s.

Primary VM progenitor cultures were transduced with lentiviruses encoding *Lrrk2* silencing shRNA^{mir} constructs (LVmiB3 and LVmiB4) or containing the transfer vector (LVTH) alone as indicated. (A and C) DA neurons were visualized using immunofluorescent labeling for tyrosine hydroxylase (TH) (left columns) at DIV9 (A) or DIV14 (C). The fluorescence of the reporter GFP (center columns) indicated infected neurons. The combination of TH and GFP fluorescence (right panel; merge) demonstrated efficient transduction of DA neurons. (B and D) Camera lucida drawing of representative, randomly selected GFP-positive TH-ir cells at DIV9 (B) and DIV14 (D). Drawings were obtained by manually tracing of the neuron in NeuronJ. TH-ir neurons in miB3- and miB4-expressing cultures exhibited shorter neurites compared to non-transduced (wt) or LVTH-transduced neurons at DIV9 and DIV14. Scale bar: 50 μ m. This research was originally published in *Molecular and Cellular Proteomics* (349). © The American Society for Biochemistry and Molecular Biology.

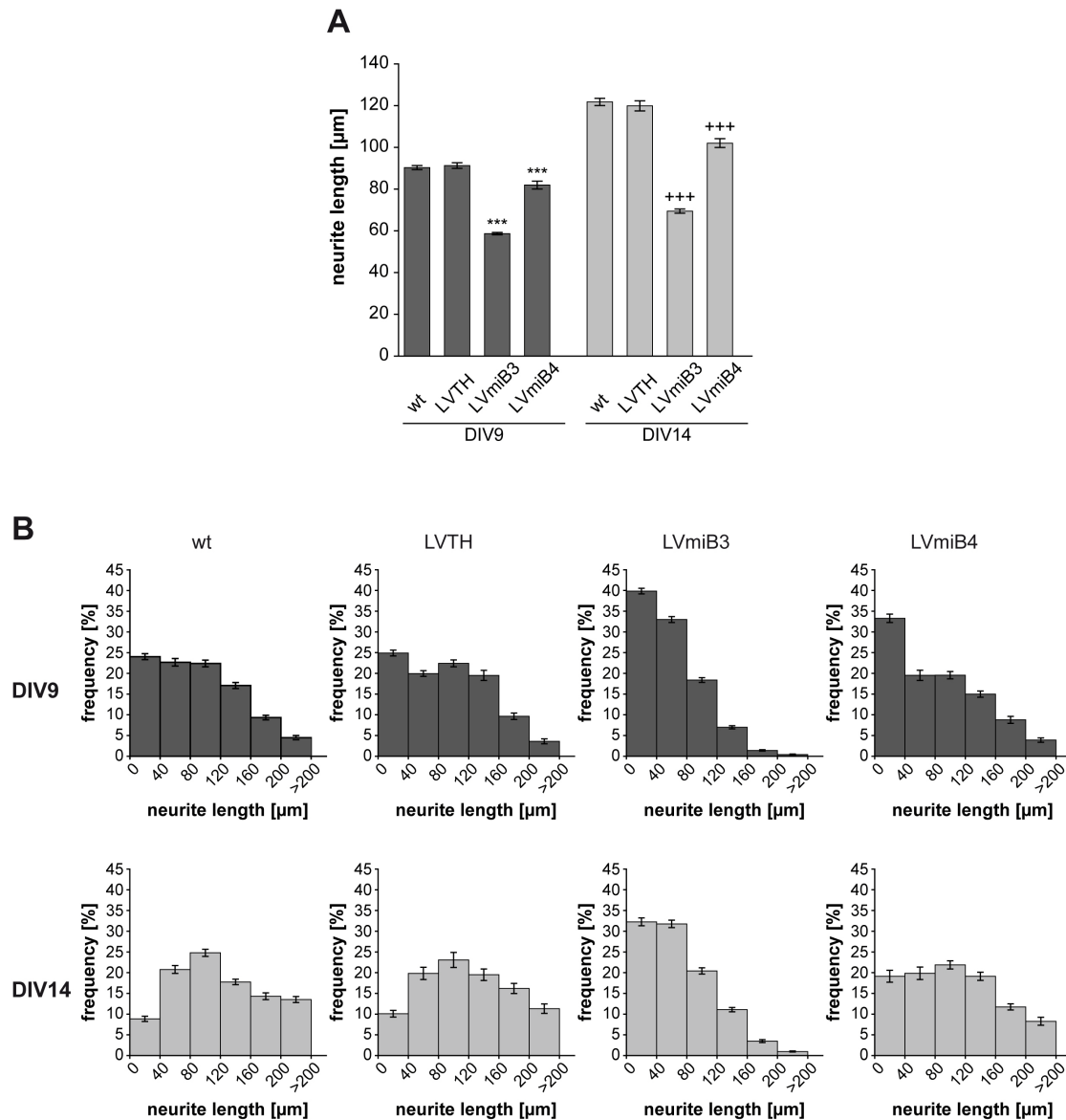


Figure 31: Silencing of *Lrrk2* results in a significant decrease in dopaminergic neurite length.

VM tissue was isolated from E12.5 mouse embryos and transduced with lentiviral vectors encoding the *Lrrk2* targeting shRNA^{mir}s (LVmiB3 and LVmiB4) or the empty vector one day after plating and analyzed at DIV9 or DIV14. (A) Quantification of neurite length of TH-ir neurons. Knockdown of *Lrrk2* led to a significant decrease in the average neurite length at DIV9 and DIV14 (*** $p < 0.001$ vs. wt DIV9, $n=4-5$, +++ $p < 0.001$ vs. wt DIV14, $n=3-5$, one-way ANOVA, Tukey's post-hoc test). (B) Corresponding frequency distributions of neurite length for the different treatment groups (wt, LVTH, LVmiB3 and LVmiB4) at DIV9 and DIV14. Absolute neurite lengths were grouped into 40 μm bins of increasing size and were calculated as percentage of DA neurites of given length. The expression of miB3 and miB4 resulted at both time points in a shifted distribution towards shorter processes compared to wt and LVTH-control cultures, reflecting an increase in the number of shorter neurites and a decrease of longer neurites. This research was originally published in *Molecular and Cellular Proteomics* (349). © The American Society for Biochemistry and Molecular Biology.

3.4.2 Modifications in the cellular shape of NIH3T3 following *Lrrk2* depletion

The knockdown of *Lrrk2* in primary dissociated ventral mesencephalic cultures demonstrated that the protein's depletion interfered with the outgrowth of DA neuron processes during maturation. A crucial factor for neuritic outgrowth and maintenance of neuronal processes represents the cytoskeleton (351, 352). Therefore, it was worthwhile to speculate that the function of *Lrrk2* is connected to cytoskeleton integrity, especially to actin, whose disruption was shown to result in a much slower elongation rate of neurite extensions

(353). However, cellular heterogeneity (336, 345) and the small size of the VM culture system circumvented its application to pursue this hypothesis and to elucidate intracellular mechanisms that might account for the observed cellular phenotype in DA neurons. Therefore, we went back to an appropriate cell line model. Murine NIH3T3 cells were chosen for two reasons: first, they endogenously express *Lrrk2* (324) and second, fibroblasts are commonly used to study the mechanisms of cytoskeleton reorganization (354, 355).

Initially and similar to DA neurons, it was investigated whether *Lrrk2* depletion affected the cellular morphology of NIH3T3 cells. Although Bauer et al. (324) showed in a previous study that the expression of the *Lrrk2*-specific second generation shRNA^{mir} construct miB3 in NIH3T3 cells resulted in an efficient *Lrrk2* mRNA and protein decline without the induction of an immune response, these findings were revalidated in the present study. Therefore, NIH3T3 cells were transduced with LVTH and LVmiB3 one day after plating using a MOI of 5 and analyzed six days later. *Lrrk2* mRNA levels in the miB3 expressing cultures were significantly decreased ($p < 0.05$, one-way ANOVA) to an expression ratio of 0.29 ± 0.15 ($n=2$) relative to the untreated wt cells, whereas the expression ratio in the LVTH control was unaffected ($p > 0.05$, $n=2$, one way ANOVA; 1.247 ± 0.12) (Figure 32A). Accordingly, the *Lrrk2* protein content in the genetically modified cultures was notably reduced compared to the wt and LVTH-transduced counterparts (Figure 32B). Both LVTH- and LVmiB3-transduced cultures possessed an equal expression of the vector-encoded reporter GFP (Figure 32B). As detected by semiquantitative real-time PCR, expression of the shRNA^{mir} construct did not provoke the induction of *Oas1* that displayed a relative expression ratio of 0.75 ± 0.06 (Figure 32C).

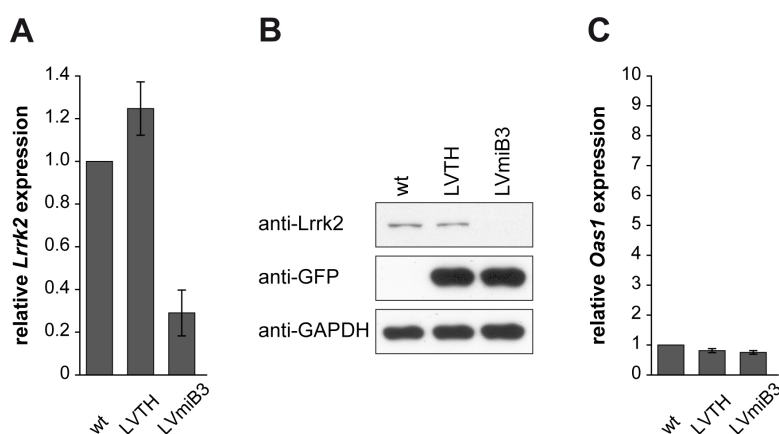


Figure 32: Efficient knockdown of *Lrrk2* in NIH3T3 cells.

NIH3T3 cells were plated onto 6-well plates and transduced the following day with lentiviral vectors encoding *Lrrk2* targeting shRNA^{mir} (miB3) or the transfer vector LVTH alone. Six days post-transduction the cultures were analyzed. (A) Quantification of *Lrrk2* mRNA levels by semiquantitative real-time PCR revealed a significant decline of the transcript in miB3 expressing cultures. (B) Efficient depletion of *Lrrk2* expression was accompanied by a decrease in protein content in LVmiB3-transduced cultures. GFP and GAPDH western blots served as controls for transduction efficiency and protein load, respectively. (C) The lentiviral delivery of the shRNA^{mir} silencing construct did not result in the induction of *Oas1* expression.

For the phenotypic analysis, wt, LVTH- and LVmiB3-transduced NIH3T3 cells were plated on glass coverslips five days post-transduction and serum-starved for 24 h. Upon silencing of *Lrrk2*, the cells displayed a change in morphology in terms of elongation and narrowing of the cell body, whereas the wt and LVTH-transduced controls had a typical fibroblast-like morphology (Figure 33A).

As a quantitative measure of cell shape, the ratio of perimeter to area (P:A-ratio) (338) was determined and both the average P:A-ratio (Figure 33B) and its frequency distribution (Figure 33C) calculated for the different conditions. Frequency distribution analysis confirmed the immunocytochemical observations. The P:A-ratio in all three conditions ranged from $0.05 \mu\text{m}^{-1}$ to greater than $0.40 \mu\text{m}^{-1}$ with the majority of cells falling in the range between $0.20 \mu\text{m}^{-1}$ and $0.35 \mu\text{m}^{-1}$ (Figure 33C). However, the distribution of the P:A-ratio revealed a shift towards higher values in the *Lrrk2* knockdown cultures (Figure 33C), indicating that a significant proportion of the cells showed cell body elongation and narrowing. The proportions of cells in the ranges of $0.15\text{-}0.2 \mu\text{m}^{-1}$ and $0.2\text{-}0.25 \mu\text{m}^{-1}$ were significantly reduced in the shRNA^{mir}-treated cultures ($p < 0.001$ vs. wt, $n=4$, two-way-ANOVA, Bonferroni post-hoc test; wt: $12.06 \pm 1.0\%$ and $27.07 \pm 1.0\%$; LVTH: $12.00 \pm 1.3\%$ and $27.59 \pm 0.9\%$; LVmiB3: $8.53 \pm 0.8\%$ and $23.28 \pm 1.0\%$), whereas the percentage of cells with a ratio greater than $0.4 \mu\text{m}^{-1}$ was significantly increased ($p < 0.001$ vs. wt, $n=4$, two-way ANOVA; wt: $10.07 \pm 0.7\%$, LVTH: $10.68 \pm 1.1\%$ and LVmiB3: $16.07 \pm 1.5\%$). This resulted in an increase in the average P:A-ratio of NIH3T3 cells expressing the miB3 silencing construct from $0.286 \pm 0.004 \mu\text{m}^{-1}$ and $0.286 \pm 0.005 \mu\text{m}^{-1}$ for wt and LVTH-control cells, respectively, to $0.309 \pm 0.005 \mu\text{m}^{-1}$ for LVmiB3 cells ($p < 0.01$ vs. wt, $n=4$, one-way ANOVA, Tukey's post-hoc test) (Figure 33B). These results denote that NIH3T3 cells underwent marked alterations in cell morphology upon *Lrrk2* knockdown.

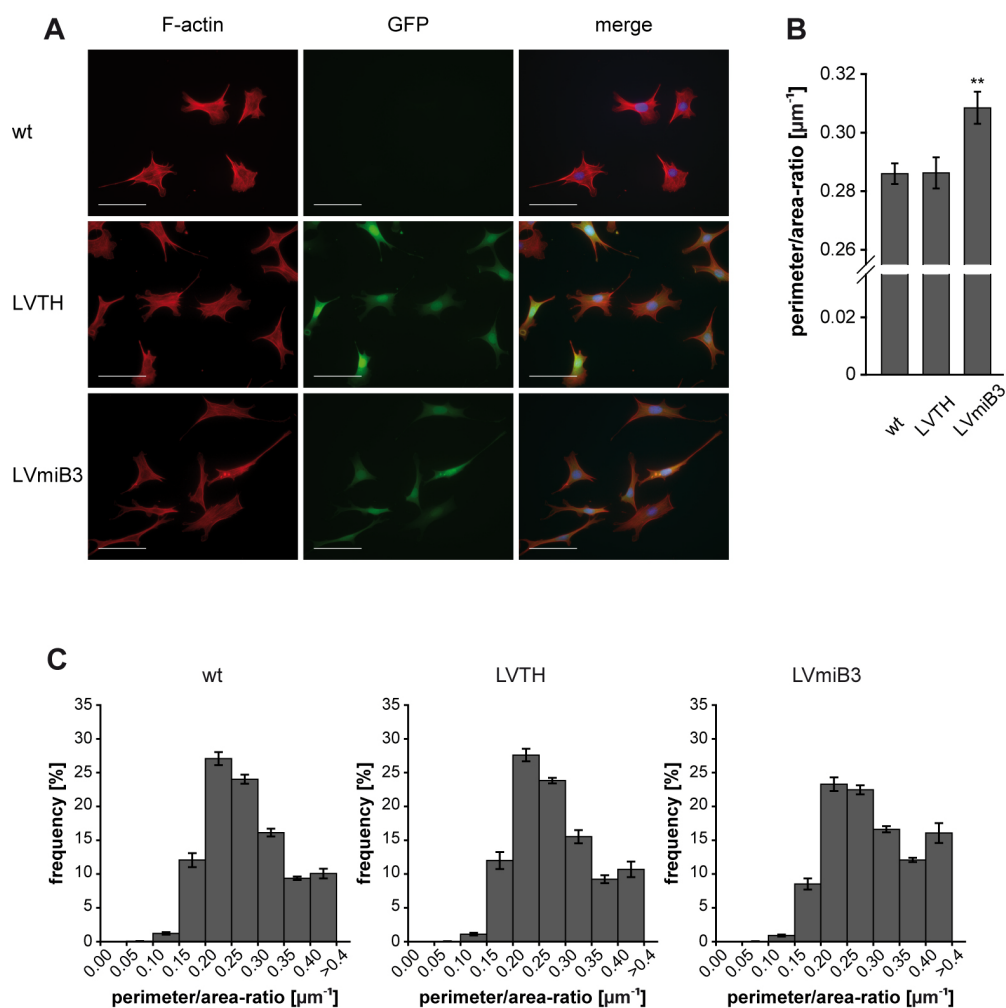


Figure 33: Knockdown of Lrrk2 alters the morphology of NIH3T3 cells.

NIH3T3 cells, wt as well as LVmiB3- or LVTH-transduced as indicated, were replated at a density of 5-10% on glass coverslips five days after transduction and serum-starved for 24 h prior to the analysis. (A) To visualize cell shape, cells were immunostained for F-actin. LVmiB3-transduced NIH3T3 cells displayed a shifting in their morphology, namely cell body elongation and narrowing. Scale bar: 50 μm . (B) To quantify the observed alterations in cell shape, the perimeter to area ratio (P:A-ratio) was determined. Silencing of Lrrk2 resulted in a significant increase of this ratio (** $p < 0.01$ vs. wt, $n=4$, one-way ANOVA, Tukey's post-hoc test). (C) Relative frequency distributions of P:A-ratios for wt, LVTH- or LVmiB3-transduced NIH3T3 cells. Ratios were grouped into consecutive bins increasing by $0.05 \mu\text{m}^{-1}$, ranging from 0.05 to $> 0.4 \mu\text{m}^{-1}$, and were calculated as percentage of cells with a given ratio. The knockdown of Lrrk2 led to a shift of the P:A-ratio towards higher values, denotative for an increase in the amount of cells exhibiting an enhanced P:A-ratio. This research was originally published in Molecular and Cellular Proteomics (349). © The American Society for Biochemistry and Molecular Biology.

4. Analysis and evaluation of the Lrrk2 interactome

4.1 Lrrk2 interacts with components of the actin cytoskeleton

A common strategy for the functional assignment of an unclassified protein is the identification of its interaction partners, based on the concept that interacting proteins exert equal, or at least related, cellular functions (“guilt-by-association”) (356). Most frequently used approaches for the analysis of PPIs such as yeast 2-hybrid or pull-down assays using the tagged, overexpressed target protein harbor considerable drawbacks (293). Co-IP of the untagged protein at its endogenous level in combination with MS-analysis to identify the complex components still represents the gold standard assay for PPIs. However, several technical challenges limit the general applicability of such AP-MS analysis. The coprecipitation of non-specific proteins along with the target protein complex often impedes the identification of genuine interactors. Also in the present study, the IP of endogenous Lrrk2 was associated with a significant background of non-specifically precipitated proteins as shown by the control IPs using total rat IgGs or subclass-specific rat IgG2a (see 2.2.4), thus circumventing the identification of Lrrk2 interactors by a classical AP-MS approach. For the systematic analysis of the Lrrk2 interactome, the QUICK approach (293) was therefore conducted, which combines SILAC, RNAi-induced knockdown, co-IP and quantitative MS to screen for endogenous PPIs (see also Material and Methods, 2.2.2).

A prerequisite for the QUICK assay is the efficient depletion of the protein of interest within an appropriate cell type. As the expression of the Lrrk2-specific second generation shRNA^{mir} construct miB3 in NIH3T3 cells resulted in an efficient knockdown of Lrrk2 without the induction of an immune response (see 3.4.2, Figure 32), this system was utilized. For the metabolic labeling with SILAC, wt and LVmiB3-transduced NIH3T3 cells were grown in heavy or light medium for at least five passages before the corresponding protein extracts were generated. To exclude differences due to the labeling, crossover experiments with an inverted isotopic labeling were conducted.

To test whether the knockdown of Lrrk2 itself led to global changes in the proteome of NIH3T3 cells, equal amounts of protein from the whole cell lysates of both experimental conditions were combined, prefractionated by SDS-PAGE, subjected to tryptic in-gel cleavage and the resulting peptides were analyzed by LC-MS/MS (in cooperation with Dr. K. Boldt). The identified peptides were assigned to proteins and quantified with MaxQuant (301). A total of 1731 proteins were identified all of which exhibited an abundance ratio of around one (Figure 34A and Supplementary Table 1). Thus, no serious alterations appeared in the NIH3T3 cell’s proteome following shRNA^{mir} expression.

Within the QUICK approach, equal protein amounts of the heavy and light labeled samples were used for immunoprecipitation applying a rat-monoclonal anti-Lrrk2 antibody (see 2.2.4) and MS analysis of the eluates was done as described for the lysates. As shown in Figure 34B, a number of identified proteins were significantly enriched ($p \leq 0.05$; red

circles) in the precipitated wt samples compared to the Lrrk2 knockdown IPs. Among them, Lrrk2 could be identified to be significantly enriched (Figure 34B; enlarged red circle) and being 3.57 times more abundant (Table 21), indicative for both an efficient immunoprecipitation and knockdown of the endogenous protein. Moreover, we found 355 proteins being equally abundant in both conditions (Figure 34B and Supplementary Table 2) and hence corresponding to proteins that precipitated irrespective of the presence of Lrrk2. They were therefore considered to be non-specific contaminants.

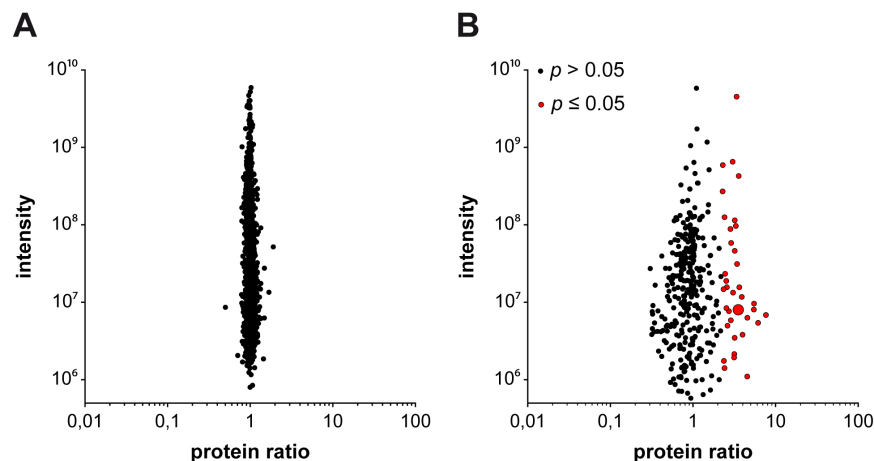


Figure 34: Scatter plots of protein ratios according to SILAC quantification.

Wt and Lrrk2-knockdown (LVmiB3-transduced) NIH3T3 cells were SILAC-labeled for five passages in cell culture. Equal amounts of proteins from corresponding protein extracts were directly analyzed by LC-MS/MS or subjected to an IP using a rat-monoclonal anti-Lrrk2 antibody cross-linked to Protein G Sepharose. Both combined total cell lysates and IP-eluates were prefractionated by SDS-PAGE prior to the analysis of the tryptic peptides on an OrbitrapXL and their quantification by MaxQuant. To exclude variations due to the isotopic labeling, crossover experiments with inversed labeling were performed. (A) Analysis of the whole cell lysates derived from wt and LVmiB3-transduced cells that were used for the IP revealed no alterations in the abundance ratio of the identified proteins, indicating that the lentiviral-mediated knockdown of Lrrk2 did not appear to induce major alterations in the proteome. (B) Within the QUICK assay, Lrrk2 (enlarged red circle) and 36 additional proteins (red circles) exhibited a significant increased abundance ratio ($p \leq 0.05$). The latter were thus identified as Lrrk2-specific interactors. In contrast, proteins with an abundance ratio of around 1 precipitated irrespective of the presence of Lrrk2 and were therefore considered to be non-specific contaminants.

Besides Lrrk2, 36 proteins with significantly increased abundance ratios ($p \leq 0.05$) were identified by QUICK (Table 21), which were considered to be potential Lrrk2 interaction partners. By literature-based curation, the Lrrk2 interactors were categorized according to their molecular function, with the majority of the identified proteins clustered into four groups and merely six of them possessing miscellaneous functions (group 5).

Results

Table 21: Summary of Lrrk2 interacting proteins identified by QUICK.

Proteins are categorized according to their molecular function as revealed by literature-based curation. Those that could not be differentiated by the MaxQuant software are grouped within the same cell. Ratio H/L: ratio heavy to light labeled peptides. This research was originally published in Molecular and Cellular Proteomics (349). © The American Society for Biochemistry and Molecular Biology.

Protein ^{a)}	Gene ^{b)}	UniProt ID ^{c)}	Normalized Ratio ^{d)}	Significance ^{e)}
Lrrk2				
Leucine-rich repeat serine/threonine-protein kinase 2	Lrrk2	Q5S006	3.57	0.010
actins				
Beta-actin-like protein 2	Actb12	Q8BFZ3	3.61	0.009
Actin, cytoplasmic 1 (β -actin)	Actb	P60710	3.24	0.015
Actin, cytoplasmic 2 (γ -actin)	Actg1	P63260	3.40	0.012
Actin, aortic smooth muscle (α -actin-2)	Acta2	P62737	3.05	0.019
Actin, gamma-enteric smooth muscle (γ -2-actin)	Actg2	P63268		
actin-regulatory				
Actin-related protein 2	Actr2	P61161	3.19	0.020
Actin-related protein 3	Actr3	Q99JY9	5.53	0.001
Actin-related protein 2/3 complex subunit 1B	Arpc1b	Q9WV32	4.02	0.006
Actin-related protein 2/3 complex subunit 2	Arpc2	Q9CVB6	4.59	0.003
Actin-related protein 2/3 complex subunit 4A	Arpc4	P59999	6.19	0.001
Actin-related protein 2/3 complex subunit 5	Arpc5	Q9CPW4	4.57	0.005
F-actin-capping protein subunit alpha-1	Capza1	P47753	2.59	0.036
F-actin-capping protein subunit alpha-2	Capza2	P47754	2.90	0.024
F-actin-capping protein subunit beta	Capzb	P47757	2.75	0.029
Tropomodulin-3	Tmod3	Q9JHJ0	3.08	0.018
Tropomyosin alpha-1 chain (α -Tropomyosin)	Tpm1	P58771	2.92	0.023
Tropomyosin alpha-3 chain (γ -Tropomyosin)	Tpm3	P21107	2.39	0.053
Tropomyosin beta chain (β -Tropomyosin)	Tpm2	P58774	2.56	0.038
LIM domain and actin-binding protein 1 (EPLIN)	Lima1	Q9ERG0	3.66	0.009
Drebrin	Dbn1	Q9QXS6	3.53	0.010
Ankyrin	Rai14	Q9EP71	2.55	0.038
Plectin-1	Plec1	Q9QXS1	2.32	0.053
myosins				
Myosin Ib	Myo1b	P46735	3.23	0.015
Myosin Ic	Myo1c	Q5ND46	2.30	0.054
Myosin Id	Myo1d	Q5SYD0	3.45	0.012
Myosin If	Myo1f	P70248	2.43	0.051
Myosin regulatory light chain 12B	Myl12b	Q3THE2	3.33	0.013
Myosin regulatory light chain 9	Myl9	Q9CQ19		
Myosin light polypeptide 6	Myl6	Q60605	2.43	0.045
myosin-regulatory				
Protein phosphatase 1 regulatory subunit 12A (MYPT1)	Ppp1r12a	Q9DBR7	2.37	0.049
Myosin phosphatase Rho-interacting protein (M-RIP)	Mrip	P97434	2.47	0.042
Calmodulin	Calm1	P62204	2.86	0.025
	Calm2			
	Calm3			
miscellaneous				
Guanine nucleotide-binding protein G(i), alpha-2 subunit	Gnai2	P08752	7.71	0.000
Guanine nucleotide-binding protein subunit alpha-12	Gna12	P27600	3.22	0.015
Guanine nucleotide-binding protein subunit alpha-13	Gna13	P27601		
Histone H3.1	Hist1h3a, Hist1h3g, Hist1h3h, Hist1h3i	P68433	5.50	0.001
Histone H3.2	Hist1h3b, Hist1h3c, Hist1h3d, Hist1h3e, Hist1h3f, Hist2h3b, Hist2h3c1, Hist2h3c2	P84228		
Histone H3.3	H3f3a, H3f3b	P84244		
Brain protein 44	Brp44	Q9D023	3.17	0.020
ATP synthase subunit g, mitochondrial	Atp5l	Q9CPQ8	2.64	0.033
Swiprosin-1	Efh2	Q9D8Y0	3.93	0.006

^{a)} Name of identified proteins according to the UniProt database.

^{b)} Name of the corresponding mouse gene according to the UniProt database.

^{c)} Accession numbers are derived from the UniProt database.

^{d)} Calculated by the quantitation algorithm in the MaxQuant software and correcting systematic deviations. All peptide ratios are normalized such that the mean of their log-transformed ratios are zero.

^{e)} Outlier significance score for protein ratios calculated by Max Quant software (significance B), corresponding to the probability of obtaining a value this large or larger by chance.

Group 1 represents proteins belonging to the actin family. The widely expressed cytoplasmic non-muscle actins β - and γ -actin in addition to beta-actin like protein 2 (κ -actin) and a smooth muscle actin isoform (α -actin-2 and/or γ -2-actin) were detected. The formation of actin filaments and their organization in structural higher-order networks is regulated by several actin-regulatory proteins (group 2). Herein we identified six out of seven subunits constituting the actin-related protein 2/3 (Arp2/3) complex, two α -subunit isoforms and the β -subunit of the heterodimeric CapZ complex, tropomodulin 3 (Tmod3) and three isoforms of tropomyosin (TM), α -TM, β -TM and γ -TM. Additionally, we found EPLIN (epithelial protein lost in neoplasm), ankyrbin, drebrin and plectin-1 associating with Lrrk2. Proteins belonging to the myosin superfamily are listed in the third group and involve four different isoforms of class I myosins, myosin Ib, myosin Ic, myosin Id and myosin If, one essential light chain (Myl6) and a regulatory light chain (Myl12B and/or Myl9) of class II myosins. Modulators of these actin-dependent motor proteins, calmodulin, myosin phosphatase-targeting subunit (MYPT1) and myosin phosphatase-Rho interacting protein (M-RIP) are categorized in group 4.

A selection of the identified Lrrk2 protein complex components was confirmed to interact with Lrrk2 by co-IP followed by western blot analysis (Figure 35). Cell extracts from wt and LVmiB3-transduced NIH3T3 cells, which were also cultivated for at least five passages, were prepared. Endogenous Lrrk2 was immunoprecipitated with the anti-Lrrk2 antibody covalently coupled to a Protein G Sepharose matrix. Western blot analysis with anti-myosin Id, anti-Arp3 and anti-tropomyosin revealed specific signals for wt cells compared to shRNA expressing NIH3T3, displaying no or weak bands, and thus confirming the results of the QUICK assay. In addition, a specific interaction of Lrrk2 with two heavy chain isoforms of class II myosins, myosin IIa and myosin IIb could be shown. Both proteins exhibited an increased abundance ratio in the QUICK assay of 1.5 (myosin IIa) and 1.8 (myosin IIb), which was, however, not significant ($p > 0.05$) under the applied analysis conditions (Supplementary Table 2).

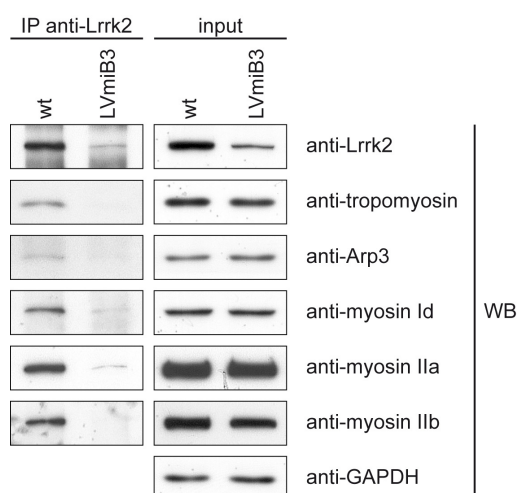


Figure 35: Verification of Lrrk2 interaction partners identified by QUICK using co-IP.

Equal volumes of cell lysates with identical protein amounts from wt and LVmiB3-transduced NIH3T3 cells were immunoprecipitated using the anti-Lrrk2 antibody covalently coupled to Protein G Sepharose. 50% of the immunoprecipitates and a lysate volume corresponding to 2% of the IP-input were separated by SDS-PAGE. Lrrk2 protein complex components found in the QUICK assay were verified by detecting selected proteins by western blotting using the antibodies indicated. IP: immunoprecipitation antibody; WB: western blotting antibody. This figure was modified from the research originally published in *Molecular and Cellular Proteomics* (349). © The American Society for Biochemistry and Molecular Biology.

The putative Lrrk2 interactors identified in the QUICK assay were further analyzed using Pathway Palette. First, a KEGG pathway enrichment analysis was performed to obtain an unbiased indication of overrepresented cellular process categories in the set of Lrrk2 complex components. In addition to the literature-based curation, it provides a second, independent approach for the functional annotation of the proteins that permits an inference of the physiological role of Lrrk2. The analysis yielded the highest enrichment for proteins annotated to the “regulation of actin cytoskeleton” pathway (KEGG pathway entry #hsa04810), with the by far strongest significance of $p < 10^{-10.35}$ (Figure 36). In addition, the proteins could be mapped to several other, not necessarily independent pathways whose significance did, however, not exceed $10^{-3.6}$.

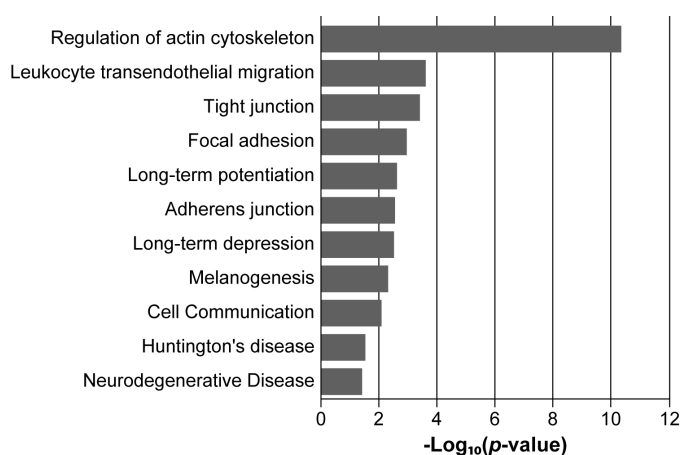


Figure 36: KEGG pathway enrichment analysis of proteins identified in the Lrrk2 complex.

The proteins identified to interact with Lrrk2 were subjected to a pathway enrichment analysis by using the KEGG database. Only significantly enriched KEGG functional categories ($p < 0.05$) are depicted according to their p -value ($-\log_{10}(p\text{-value})$). The analysis yielded a strong significance for proteins associated with the “regulation of actin cytoskeleton” pathway (KEGG pathway entry #hsa04810). This research was originally published in *Molecular and Cellular Proteomics* (349). © The American Society for Biochemistry and Molecular Biology.

Interactions between the identified Lrrk2 complex partners were then parsed and visualized using Pathway Palette, applying interaction data stored in the HPRD and BioGRID database. The analysis was performed in an evaluated and prioritized manner, based on the “evidence” for an interaction, referring to the experimental method used for its detection, hold by the databases. Therein, interactions were ranked according to the following categorization: (I) “BioGRID: Low-Throughput” or “HPRD: in-vivo”, (II) “BioGRID: HTP/complex” or “HPRD: in-vitro” and (III) “BioGRID: HTP/Pairwise” or “HPRD: yeast 2-hybrid”. In principal, edges arising from the first category are indicative for a reliable interaction of two proteins *in vivo* as the performed experiment types assure that the proteins are truly interacting in a mammalian cell. The second class comprises experimental settings that do not admit the conclusion that the interaction is subsident in a mammalian cell, thus occurring *in vitro*. Although yeast 2-hybrid and similar experiments test interactions in the context of a yeast cell and are therefore technically *in vivo*, they were annotated specifically in a separate group (III) because of the greater degree of false positive interactions seen with this method. The resulting network edges, however, do not necessarily signify binary interactions but rather denote that the proteins co-occur within the same complex. Admittedly, this approach does not allow distinguishing between direct and indirect interactions but facilitates the analysis of the Lrrk2 complex, whereon the emphasis in this

study was on.

Within the group of 37 specific interactors (nodes), the analysis identified 36 previously reported interactions (edges) between 20 individual nodes (Figure 37A). To evaluate the physical cohesiveness of the inferred interaction network, a PIE analysis (307) was applied in cooperation with Dr. M. Askenazi (Harvard Medical School). Figure 37B shows the frequency distribution of edge numbers within the simulated protein sets ($n=1000000$ simulated networks). As 37 proteins were significantly identified within the QUICK assay, sets of size 37 were used. The analysis yielded a PIE score of 1.78 and a p -value $< 10^{-6}$, thus revealing significant physical cohesiveness for the proteins identified within the QUICK assay. This means that they interact with one another at a significantly higher frequency than a random set of proteins with the same node degree distribution.

According to database searches for PPIs, interactions of proteins with Lrrk2 could not be automatically covered in the network. However, based on the experimental results within both the QUICK assay and co-IP experiments, these associations were manually added, resulting in a Lrrk2 interaction network (Figure 37A) that illustrates the close relationship between the identified proteins.

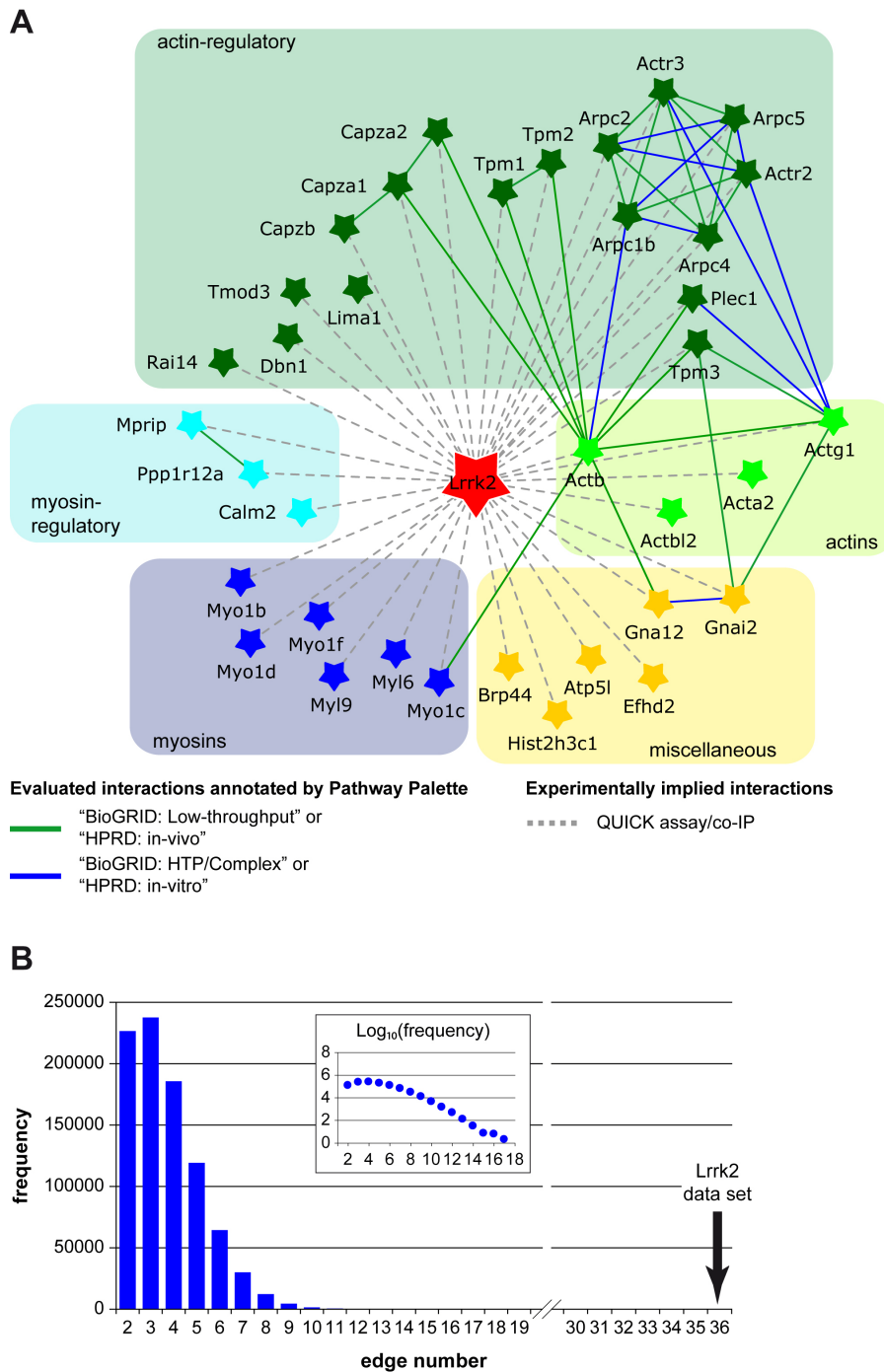


Figure 37: Network of Lrrk2 interacting proteins.

Known interactions among the proteins identified by QUICK were analyzed and visualized by Pathway Palette. The obtained network is significantly enriched in previously validated interactions. (A) Out of the 36 proteins identified as specific Lrrk2 interactors, 20 of them had previously been described as connected through 36 interactions. Interactions of proteins with Lrrk2 were added manually, based on their identification in the QUICK assay and verification by co-IP experiments. Proteins within the network are depicted by star-shaped nodes and colored according to their molecular function as classified in Table 21: actins, light green; actin-regulatory, dark green; myosins, dark blue; myosin-regulatory; light blue; miscellaneous, yellow; Lrrk2, red. Protein groups are further indicated by colored boxes, using the same coloring-scheme. Solid lines denote known protein interactions from the HPRD and BioGRID database prioritized and qualified according to their "evidence", referring to the PPI detection method, as reflected by a corresponding color-scheme of the edges: "BioGRID: Low-Throughput" or "HPRD: in-vivo" type (green) and "BioGRID: HTP/Complex" or "HPRD: in-vitro" type (blue). Manually added interactions are figured as dashed gray lines. Proteins are indicated by their gene names, with their full names shown in Table 21. (B) Distribution of interactions within a million randomly selected sets of proteins (set size 37) with the same node degree as those of the QUICK set. The graph insert represents the logarithmic depiction of interaction frequencies. The Lrrk2 data set gave significantly more interactions compared with the randomly selected sets. This research was originally published in *Molecular and Cellular Proteomics* (349). © The American Society for Biochemistry and Molecular Biology.

To further analyze the connectivity between the Lrrk2 complex components, the network was expanded by linking pairs of proteins through interconnecting proteins using interaction data from the HPRD and BioGRID database (Figure 38). Beyond the 36 interactions between 20 of the 36 Lrrk2 interacting proteins, 400 interactions were found using first-order shared neighbors (path length of one intermediate protein and two edges), enabling the mapping of 10 additional proteins from the QUICK set into the network. To assess fidelity of the network, all extensions were manually evaluated in a literature-based fashion by extracting functional information from peer-reviewed publications (Supplementary Table 3). The analysis revealed that the interconnecting neighbors predominantly comprise proteins that are associated with the actin cytoskeleton and/or affect its modulation as well as myosins and their regulators. Thus, the extended network strengthens an inherent correlation among the identified Lrrk2 interacting proteins.

Taken together, the results of the interactome analysis strongly indicated an association of Lrrk2 with the actin cytoskeleton and/or its dynamic regulation. Further support for this hypothesis could be achieved from the morphological analysis of NIH3T3 cells that showed significant alterations in the cellular shape following Lrrk2 knockdown. The actin cytoskeleton plays a fundamental role in eukaryotic cells and is a major determinant of cell morphology. Thus alterations in the cell shape are a consequence of modifications in the organization of this particular cytoskeletal component. Moreover, the actin-based cytoskeleton represents a crucial element in the development of the nervous system, including the extension of neurites that relies on an organized actin polymerization. Therefore, the observed decrease in neurite length of DA neurons after Lrrk2 depletion additionally militates for a function of Lrrk2 in the modulation of actin structures.

Figure 38 (page 168): Extended network of Lrrk2 interacting proteins.

The network of the 36 Lrrk2 interacting proteins was extended through the addition of first-order shared neighbors based on interaction data in the HPRD and BioGRID database using Pathway Palette. To reduce the network's complexity, interactions between the interconnecting proteins were not displayed. A total of 153 intermediate proteins and 408 additional edges were found to connect the proteins of the Lrrk2 complex, thereby linking 400 protein pairs through first-order shared neighbors in addition to the 36 direct interactions between 20 of the proteins. Thus, additional 10 proteins could be mapped into the network based on previously reported protein interactions. Star-shaped nodes represent the proteins identified by QUICK, with a color-scheme corresponding to their molecular function as classified in Table 21: actins, light green; actin-regulatory, dark green; myosins, dark blue; myosin-regulatory; light blue; miscellaneous, yellow; Lrrk2, red. First-order interconnecting proteins are depicted as grey diamonds. Interactions between the proteins, as curated in the HPRD and BioGRID database, were prioritized and evaluated according to their "evidence", referring to the PPI detection method, and are reflected by a corresponding color-scheme of the edges: "BioGRID: Low-Throughput" or "HPRD: in-vivo" type (green), "BioGRID: HTP/Complex" or "HPRD: in-vitro" type (blue) and "BioGRID: HTP/Pairwise" or "HPRD: yeast 2-hybrid" (red). Manually added interactions are figured as dashed gray lines. Proteins are indicated by their gene names, with their full names shown in Supplementary Table 3. This research was originally published in *Molecular and Cellular Proteomics* (349). © The American Society of Biochemistry and Molecular Biology.

Evaluated interactions annotated by Pathway Palette

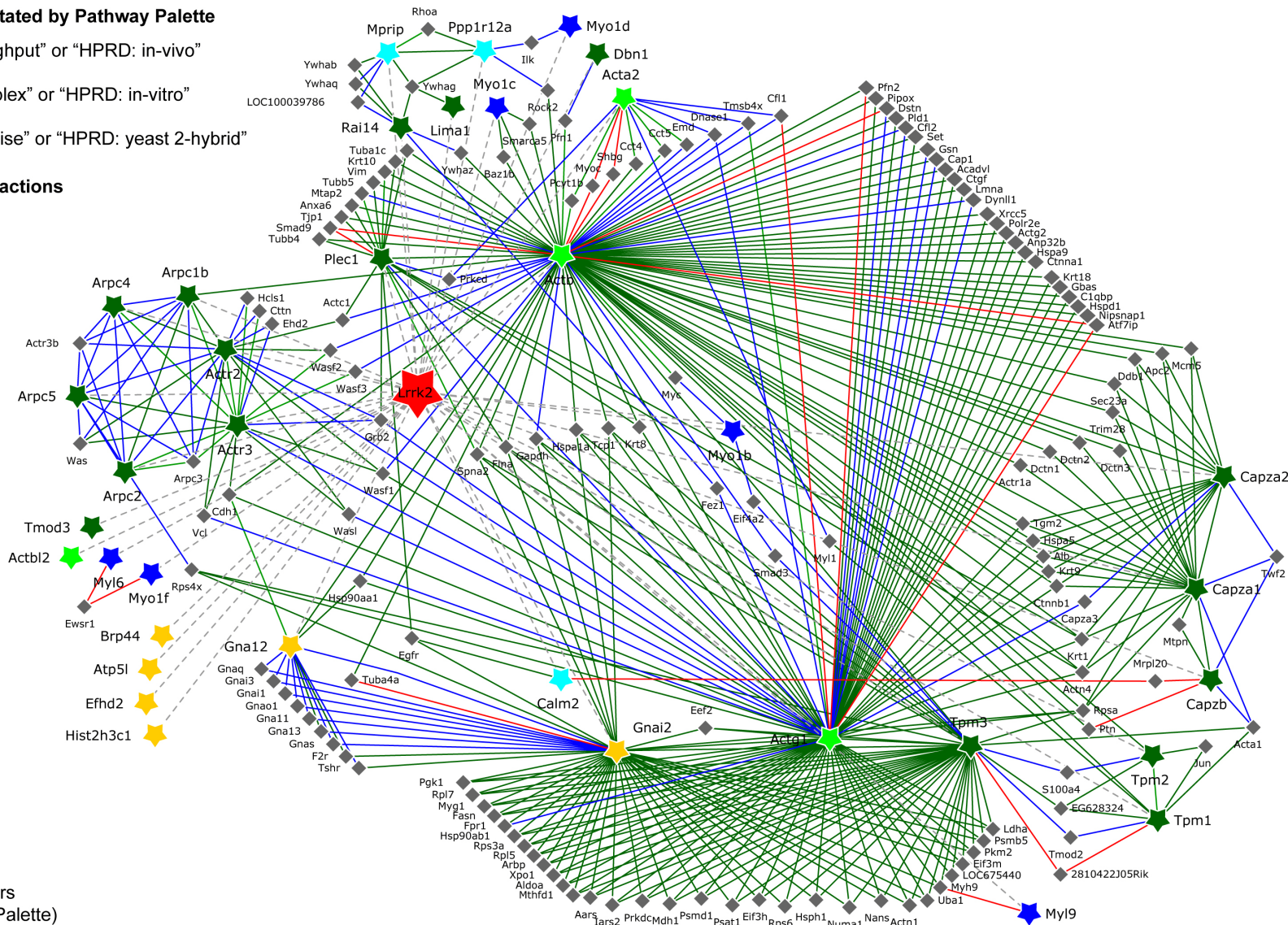
- "BioGRID: Low-throughput" or "HPRD: in-vivo"
- "BioGRID: HTP/Complex" or "HPRD: in-vitro"
- "BioGRID: HTP/Pairwise" or "HPRD: yeast 2-hybrid"

Experimentally implied interactions

- QUICK assay/co-IP

Protein groups

- ★ actins
- ★ actin-regulatory
- ★ myosins
- ★ myosin-regulatory
- ★ miscellaneous
- ◆ first-order direct neighbors (annotated by Pathway Palette)



4.2 Lrrk2 binds F-actin and affects its polymerization *in vitro*

The finding that Lrrk2 interacted with actin isoforms and other cytoskeletal proteins suggested a possible association between Lrrk2 and F-actin. In cooperation with Prof. M. van Troys (Ghent University) and Dr. C.J. Gloeckner, the F-actin binding of Lrrk2 was therefore assessed *in vitro* in a cosedimentation assay using recombinant SF-TAP tagged Lrrk2 purified from HEK293 cells. After incubating a constant amount of actin (3 μ M) with different concentrations of Lrrk2 (150 nM and 300 nM) under constant buffer conditions, actin was sedimented by centrifugation at steady-state level of polymerization. The pellets and supernatants, containing polymerized and unpolymerized actin, respectively, were analyzed by SDS-PAGE followed by Coomassie brilliant blue staining (Figure 39A, upper panel). (Co)sedimentation of Lrrk2 was visualized by western blotting using an anti-Flag antibody (Figure 39A, lower panel). Based hereupon, the amount of both Lrrk2 and actin present in the supernatants or pellets was quantified (Figure 39B and C). In the absence of actin, Lrrk2 was only present in the supernatant, indicating that Lrrk2 did not self-aggregate forming pellets (Figure 39A, upper panel, condition 5). Coomassie brilliant blue staining following SDS-PAGE of the purified protein revealed the purity of the affinity preparation (Figure 39A, upper panel, condition 5) as demonstrated in a previous study (173). In the presence of actin, Lrrk2 localized to the pellet fractions (Figure 39A, lower panel, conditions 3 and 4; Figure 39B). As the quantification data with the two applied protein batches used slightly displayed quantitative (not qualitative) differences (Figure 39B), the results of the separate, independent experiments were reported instead of a mean over the experiments performed. With increasing concentrations of Lrrk2 incubated with actin, a concentration-dependent recovery of Lrrk2 in the pellet fraction was consistently observed (Figure 39B). Depending on the protein batch, the amount of Lrrk2 in the pellet increased between 1.3 and 2.3-fold using an added concentration of 300 nM versus 150 nM Lrrk2. Lrrk2 led, furthermore, to a significant increase in actin present in the supernatants as shown by the quantification of Coomassie stained gels (Figure 39A and C). Whereas in the control samples the majority of actin sedimented (Figure 39A, upper panel, conditions 1 and 2; Figure 39C), the addition of substoichiometric amounts of Lrrk2 decreased the amount of polymerized actin (Figure 39A, upper panel, conditions 3 and 4; Figure 39C). As demonstrated in Figure 39C, the shift in the G-/F-actin ratio towards the monomeric form (in the supernatant) is statistically significant in the presence of increasing Lrrk2 ($p < 0.01$ and 0.001 vs. SB buffer control, $n=4$, one-way ANOVA, Holm-Sidak post-hoc test). At a concentration of 300 nM, Lrrk2 induced a ~1:1 distribution of actin between supernatant ($48.00 \pm 2.54\%$) and pellet ($52.00 \pm 2.54\%$) (Figure 39C).

Overall, the results demonstrate an association of Lrrk2 to F-actin. Moreover, under the *in vitro* conditions used, the G-actin/F-actin balance at equilibrium is altered in favor of G-actin, indicating that Lrrk2 affects actin polymerization.

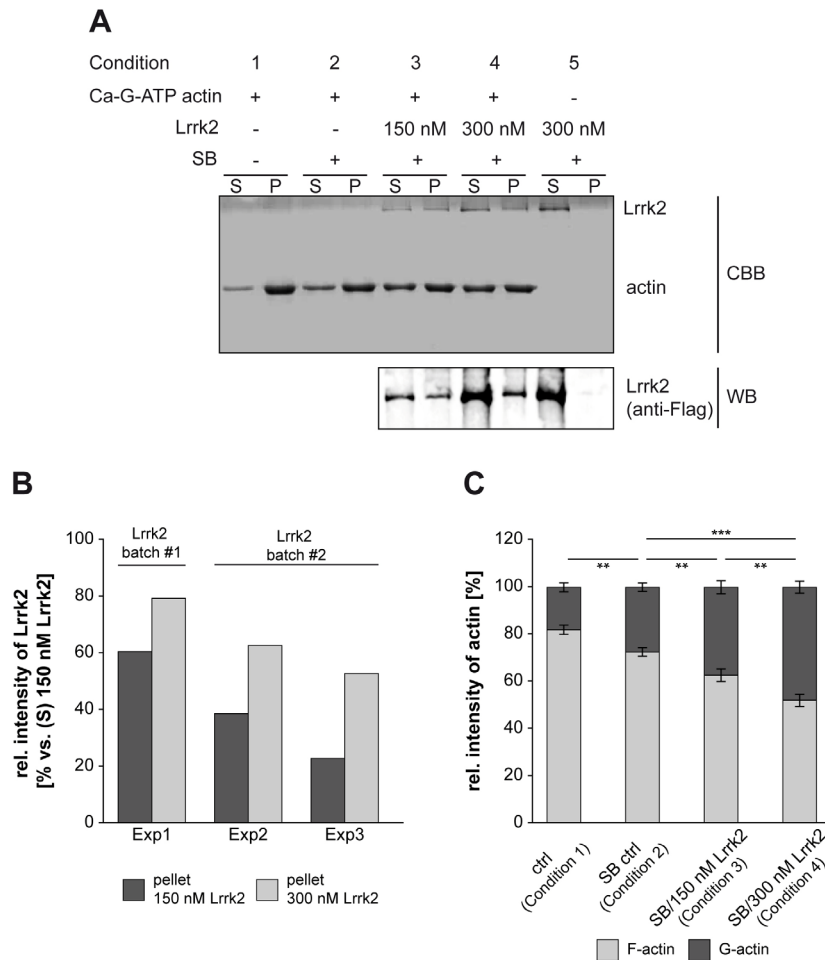


Figure 39: Lrrk2 binds directly to F-actin and affects its polymerization/depolymerization *in vitro*.

(A) F-actin cosedimentation experiments were performed by incubating 3 μM Ca-G-ATP actin under polymerizing conditions with 150 nM (condition 3) or 300 nM (condition 4) SF-TAP tagged Lrrk2 purified from HEK293 cells in storage buffer (SB). Samples without Lrrk2 and SB (condition 1), with only SB (condition 2) or containing 300 nM Lrrk2 in the absence of actin (condition 5) served as controls (ctrl). Samples with SB or Lrrk2/SB always contained a constant amount of the SB components, ensuring identical conditions. G-actin was allowed to polymerize until equilibrium was reached and sedimented by high speed centrifugation. The pellets (P) and supernatants (S) were analyzed by SDS-PAGE followed by Coomassie brilliant blue staining (upper panel) or western blot using an anti-Flag antibody (lower panel). The results of a representative experiment are shown. Lrrk2 cosedimented with actin (conditions 3 and 4), while in the absence of actin, Lrrk2 was only detected in the supernatant (condition 5). CBB: Coomassie brilliant blue; WB: western blot. (B) Relative amounts of Lrrk2 in the pellet upon incubation of 150 or 300 nM Lrrk2 with 3 μM actin for three experiments (Exp1 – Exp3) using two different protein purifications (batch #1 and batch #2), based on quantification of western blots as in A (lower panel). At the higher concentration, an increased amount of cosedimented Lrrk2 was consistently detected. (C) Quantification of actin in the supernatant (G-actin) and pellet (F-actin) in the absence of SB (ctrl, condition 1), presence of SB (SB ctrl, condition 2) or Lrrk2 (150 or 300 nM) in SB (condition 3 and 4). The addition of Lrrk2 led to a significant shift of actin from the pellet fraction to the supernatant (** $p < 0.01$, *** $p < 0.001$, $n=4$, one-way ANOVA, Holm-Sidak post-hoc test). Whereas in Lrrk2 deficient samples the majority of actin was detected in the pellet fraction, a decrease in sedimented actin accompanied by a corresponding increase in unpolymerized actin in the supernatant was found in the presence of Lrrk2. This research was originally published in *Molecular and Cellular Proteomics* (349). © The American Society for Biochemistry and Molecular Biology.

V. DISCUSSION

Since the first linkage of Lrrk2 to PD in 2004 (130, 131), mutations in Lrrk2 turned out to be collectively the most common cause of autosomal-dominant inherited and idiopathic PD (5). So far, however, little is known about its involvement in the molecular pathogenesis of the disease, primarily due to a limited understanding on the protein's physiological function. The present study thus aimed at elucidating Lrrk2-associated cellular processes and biological pathways. To this end, the effects of Lrrk2 depletion in two mammalian cell culture models were determined and the endogenous interactome of Lrrk2 was systematically analyzed.

1. Performance of Lrrk2-specific antibodies in immunological assays

As commercial Lrrk2-specific antibodies for immunological assays such as western blotting, IP and IF were missing at the beginning of this study, mAbs and pAbs generated within the laboratory had to be validated for their utilization in such basic research approaches that had to be optimized to some extent in the following. In western blot application, the rat-monoclonal antibody clone 1E11 was proven to be specific towards endogenous Lrrk2 (see Results, 2.1). Using protein extracts from wt NIH3T3 cells, the antibody revealed a single immunoreactive signal for Lrrk2 at ~280 kDa whose intensity was markedly decreased for lysates derived from Lrrk2-knockdown cells. The depletion of Lrrk2 in these cells was, however, achieved with first generation silencing constructs that turned out to induce an innate immune response in primary VM cultures (see Results, 3.2) and which might suggest a decline in Lrrk2 protein levels due to a detrimental antiviral defense. This possibility can though be excluded in NIH3T3 cells as a MOI of 5 was used for their lentiviral transduction, and even cells transduced with LVsh1 at a MOI of up to 10 did not show the induction of an INF response (324). The Lrrk2-specific antibody 1E11, furthermore, efficiently immunoprecipitated the endogenous protein from cellular lysates (see Results, 2.2), thereby forming the basis for the MS-based identification of Lrrk2 protein complex partners, which was one of the central purposes of the study. However, under the established assay condition for the classical IP approach, the precipitates became contaminated by a significant amount of coeluted antibody (see Results, 2.2.2) that can interfere with the downstream analysis (292). The first attempt to immobilize the antibody by its covalent coupling to CNBr-activated sepharose did not prevent the release of immunoglobulin peptides from the support matrix (see Results, 2.2.3). Although this method is frequently used for the immobilization of antibodies, the formed isourea bonds are known to be unstable and thus facilitating ligand leakage (357). In contrast, cross-linking of the antibody to Protein G sepharose for its immobilization markedly decreased the amount of antibody present in the IP precipitate to an extent that would not significantly interfere with subsequent MS analysis (see Results, 2.2.4). Though western blot analysis revealed that Lrrk2 could be efficiently and specifically

precipitated from cellular lysates (NIH3T3 cells and mouse brain), the protein itself and potential interaction partners could not be discriminated from the non-specific background by comparison to the control experiments on silver stained gels. Here, the limited separation power of one-dimensional SDS-PAGE to resolve protein mixtures with medium to high complexity (287, 358) as well as the confined detection capacity of the staining reagent could have hampered the resolution and detection of Lrrk2 complex components. Moreover, the abundance of the target protein in the cellular protein pool as well as the affinity/avidity of the antibody represent crucial factors for the purification of specific protein complexes by co-IP and subsequent MS analysis (359-361). The low level of Lrrk2 protein expression noted for several cell lines and brain tissue (154, 157) in combination with a degree of antibody affinity that is potentially not optimal for co-IP may thus have complicated the precipitation of Lrrk2 and its interaction partners, providing a yield that was indistinguishable from or covered by the background. These technical difficulties thus impeded the *de novo* identification of Lrrk2 interactors by a conventional gel-based co-IP/MS strategy. LC-MS/MS-based approaches exhibit a higher sensitivity compared to gel-based assays (340) as well as a significantly higher resolution, enabling in-depth analysis of complex protein samples. However, the low amount of enriched Lrrk2 in the excess of background proteins within the sample would also have hampered the detection of true Lrrk2 complex components by a direct, non-quantitative approach. Given the significant advantage of quantitative proteomic approaches to determine specific PPIs, the implemented protocol for the IP of endogenous Lrrk2 from cellular lysates could be successfully applied to the protein's interactome analysis by QUICK (see Results, 4.1). Utilizing quantitative MS analyses and side-by-side co-IPs from samples that only differ in the presence or absence of the target protein, this assay enables the differentiation between specific interactors and the non-specific background (290, 293). In addition, and as demonstrated by the successful verification of selected Lrrk2 protein complex components identified by QUICK (see Figure 35), the established Lrrk2-specific co-IP is suitable to identify interaction partners by candidate-driven western blot analysis.

Within the study, neither self-generated mAbs and pAbs nor commercial antibodies were able to specifically detect the endogenous mouse Lrrk2 protein in IF (see Results, 2.3). Despite some reports that, however, did not benefit from Lrrk2-knockdown or -knockout controls (146, 149, 152, 229), the specificity of commercial antibodies against mouse Lrrk2 has been challenged previously (172). Although not serving as an absolute standardization application for antibody binding in IF (362), a panel of commercially available antibodies has additionally been shown to generally fail in the recognition of the endogenous mouse Lrrk2 protein in western blot analysis (154). Among them the Cell Signaling 2567 antibody that also yielded no signals in the IF staining performed here. To the contrary, the antibody Alexis AT106 detected endogenous mouse Lrrk2 on western blots (154) but exhibited a non-specific staining in IF, with a pattern in Lrrk2 wt and knockdown cells indiscernible from each

other. As indicated by the western blot results that displayed numerous additional bands besides the Lrrk2-specific one (154), the antibody recognizes cross-reactive protein species that might mask the endogenous protein in the IF application.

One can only speculate about the reasons why the antibodies tested here do not specifically recognize endogenous Lrrk2 in the immunocytochemical approach. As such, insufficient affinity of the antibody might account for the absence of immunoreactivity. Conversely, simple cross-reactivity to other antigens or binding of the IgGs to various, unidentified cellular constituents, in particular after fixation, produces a non-specific (background)staining that occurs also in cells devoid of the target protein (363, 364). Furthermore, the fixation procedure can impact on the antigenicity as it modifies the chemical properties of cellular constituents and changes the three-dimensional protein conformation. Thereby, the accessibility to the epitope can be limited and thus masked, novel epitopes can - although less common - be generated or non-specific background staining evoked (363, 364). A further complicating factor might be that all tested antibodies are raised against peptides. Despite providing the advantage of knowing the amino acid sequence, peptides do not necessarily reproduced the native epitope conformation or a post-translational modification pattern, thus preventing the detection of the target epitope by the respective antibody in IF stainings (365, 366). In addition, the size, three dimensional structure and charge of the selected epitope region in the fixed protein might be recapitulated by regions within other proteins that are of entirely different primary sequences (364). Although mAbs possess the advantage of a higher specificity over pAbs, the latter hold a higher probability for antigen detection through a multiplicity of epitope recognition based on the pool of antibodies against the immunogen that they represent. Simultaneously, this increases the likelihood for cross-reactivity (362, 365, 366). Moreover, antibody generation to the same immunogen can vary in quality between individual animals of the same species (365). This might explain why the rabbit-polyclonal antibody 820 failed to detect endogenous murine Lrrk2 in IF, although an antibody raised against the same peptide sequence in rabbits was reported to function in such an approach, whose specificity was albeit just confirmed by western blot analysis (146). A further issue that exacerbates the detection of endogenous Lrrk2 protein against the backdrop of the afore mentioned obstacles in IF staining is its inherent low expression level (154).

Although the present study did not achieve to establish an IF labeling for the detection of endogenous mouse Lrrk2 protein *in cellulo*, the successful implementation of western blot analysis and IP constituted the basis for functional studies on the protein.

2. Second generation shRNA^{mir} design of Lrrk2-specific RNAi triggers block immunostimulatory effects of simple hairpin-structured shRNAs

To investigate its physiological relevance, a persistent RNAi-based *in vitro* knockdown of Lrrk2 via lentiviral-mediated expression of shRNAs should be established. Given that Lrrk2-associated PD is characterized by the degeneration of DA neurons in the SNpc (143), primary progenitor VM cultures derived from embryonic mice were utilized as cellular model system. At the beginning, two independent simple hairpin-structured first generation silencing constructs with a perfect base-paired 21-nt stem (LVsh1 and LVsh6) were generated for the target-specific mRNA depletion, as this system was already successfully implemented in the laboratory (336). Expression of both shRNAs in primary VM cultures resulted in an efficient knockdown of Lrrk2 on mRNA as well as protein level (see Figure 26A and B) but caused marked cytotoxic effects in primary DA neurons as indicated by a significant decrease in the amount of TH-ir cell counts and abnormal morphology of the remaining DA neurons (see Figure 27). The observed increase in the expression level of the classic IFN target gene *Oas1* (see Figure 26C) implies the activation of an innate immune response via ISG induction as being causative rather than an over-saturation of the endogenous miRNA biogenesis pathway as a consequence of excessive shRNA expression or unintentional silencing of key cellular genes through off-targeting (367, 368). Also a study of Bauer et al. reported similar results upon lentiviral delivery of the first generation shRNA construct sh1 to primary cortical cultures, leading to the initiation of an IFN response that was associated with a significant decline of neurons, rarefaction of neurites as well as fragmented and condensed nuclei at DIV7 (324). Even though numerous studies successfully applied the plasmid-derived synthesis of shRNAs for an efficient and specific silencing of gene expression (323, 347), stimulation of the immune system by ectopic shRNA expression has already been observed previously (346, 369). The delivery of shRNAs by lentiviral vector transduction has admittedly been reported to reduce their IFN-inducing capacity (370), but the present study as well as the one by Kenworthy and colleagues (371) indicate that this may not be universally applicable to all shRNAs. The toxic effects observed here do, however, not originate from the viral vector utilized for delivery of RNAi as the empty vector applied in the control experiments did not evoke an immune response. As such, expression of the shRNA itself appears to elicit toxicity. Whereas the pathways by which externally delivered synthetic siRNAs can cause toxic side effects as well as activate the immune system are in part characterized (372, 373), generic features of IFN-triggering shRNAs as well as the underlying mechanisms are only poorly studied and knowledge thus limited. Endogenously expressed shRNAs, which are processed to functional siRNAs within the cytoplasm, should bypass the sequence-dependent, endosomal TLR-sensing pathway and be detected by cytoplasmic PPRs (373). Indeed, RIG1 was found to mediate the induction of an IFN response by lentiviral-mediated shRNA expression (371). The specific binding and activation

of RIG1 is triggered by certain structural characteristics of the RNA including blunt ends and 5'-triphosphate groups that are absent from cellular RNAs as a result of capping or cleavage prior to their cytoplasmic occurrence (374, 375). The silencing constructs utilized here are designed to yield functional siRNAs with 3'-overhangs but their shRNA precursors are generated as Pol III transcripts from an H1 promoter and are thus neither processed nor capped at their 5'-end. They hence present an unmodified 5'-triphosphate (376), suggesting a contribution of RIG1 activation to the observed innate immune response. Whether also PKR was activated is uncovered. Initially, activation of PKR was thought to require >30 bp dsRNAs but also 21-mer duplexes have the potential to mediate this pathway in a concentration-dependent manner (277, 377). The utilized Pol III promoter H1 is known to be strong and thus to generate a huge amount of shRNA transcription products (376). A dose-dependent effect of shRNAs on the induction of an immune response has correspondingly been reported (346). Hence, a large concentration of Lrrk2-specific shRNAs might have evoked the IFN response registered here, possibly through PKR activation. To encounter this effect, one could have reduced the magnitude of shRNA expressing vector from an MOI of 0.5 for LVsh1 and 2 for LVsh6 to the lowest efficient one. The study by Bauer and colleagues, however, demonstrated that LVsh1 still induce an IFN response in primary cortical cultures when its viral titer was decreased to a MOI of 0.25 (324), indicative for alternative shRNA characteristics triggering toxicity. Given that the same strategy for target gene silencing utilized here was successfully applied in a previous study to knock down the expression of the gene *Dlk1* in primary VM cultures without the induction on an IFN response (336), it appears reasonable to take sequence-specific effects similar to the recognition of synthetic siRNAs by TLR receptors (277, 373, 378) into account. Although the detection of RNAs by cytoplasmic receptors is so far considered to be sequence-independent (277), Kenworthy and colleagues provided experimental evidence for sequence requirements in shRNAs for an efficient RIG1 recognition and innate immune activation (371) in addition to the structural characteristics described above. The authors did, however, not characterize such features of the shRNA nucleotide sequence more precisely. Despite the immunostimulatory potency of the two shRNA constructs LVsh1 and LVsh6 in the study presented here, both silencing triggers are unrelated in sequence. Any sequence characteristics that may contribute to a shRNA-mediated IFN response activation, if any, has yet to be determined. As this was not a subject of the thesis, a sequence-dependence of the ISG induction observed here thus remains speculative. Innate immune system activation by shRNAs is, however, not only mediated by the transcript itself but is also dependent on the cell type, its origin and developmental stage (267, 271, 379). While shRNA expression in several established cell lines, including NIH3T3, does not induce an IFN response, the same constructs are toxic in primary cultures (267, 271), inducing *Oas1* expression and adverse cellular phenotypes (324). The same effect could be observed for the Lrrk2-targeting shRNA

construct sh1. Transduction of NIH3T3 cells with the corresponding lentiviral vectors using an MOI of up to 10 did not result in the induction of Oas1 (324). Contrarily, expression levels of the IFN target gene were markedly increased in primary VM cultures transduced with LVsh1 at an MOI of only 0.5, which was accompanied with detrimental effects on the survival of DA neurons. Whether the observed decline of DA neurons resulted directly from an activation of immune response pathways in these cells or was based on a secondary effect in consequence of IFN induction in other cell types present in the cultures can, however, not be distinguished. The latter might be indicated by the observation that ISG expression was only induced in primary cultures while it was absent in the NIH3T3 cell line, with glial activation potentially contributing to the IFN response mediated by Lrrk2-specific shRNAs. Besides microglia as the major immune cells in the CNS (380), also astrocytes can act as important mediators of the cerebral innate immune response (381). Both types of glial cells are, moreover, sensitive to siRNA-triggered immunostimulation (382-384). As the midbrain area encompassing the SNpc possesses a high density of both microglia and astrocytes (385, 386), primary VM cultures comprise also these glial cells as non-neuronal component, with their proportion dependent on the surgical isolation and cell culture condition (345, 387, 388). Although their amount was not explicitly determined, the presence of glia in the VM cultures utilized in here may confer enhanced susceptibility to a shRNA-mediated immune response that may also impact on the DA neurons by inducing neurodegeneration.

To overcome the immunostimulatory side effects initiated by the Lrrk2-specific first generation silencing constructs, miRNA-based shRNAs were applied as an alternative design strategy. Expression systems using these second generation shRNAs (shRNA^{mir}s) have been shown to provide functional siRNAs, triggering the destruction of complementary target mRNAs (389, 390) and applied by several studies for an efficient target-gene silencing (270). Intriguingly, embedding siRNA duplexes into a miRNA context has been shown to reduce the risk of an immune response. When sequences that were toxic in the context of shRNAs were placed into artificial miRNA expression systems, their immunostimulative capacity was attenuated (324, 383). In particular, the study by Bauer et al. demonstrated that the induction of Oas1 upon expression of the Lrrk2-specific shRNA silencing construct sh1 in primary cortical cultures is abrogated with an endogenous pri-miRNA as a scaffold for the RNAi trigger (324). Therefore, the same construct, LVmiB3, where the Lrrk2-targeting sequence of sh1 was incorporated into the backbone of the miR-30 primary transcript, was utilized for the lentiviral-mediated knockdown of Lrrk2 in primary VM cultures here. In addition, a second, independent shRNA^{mir} construct (miB4) was designed on the basis of miR-30 with the targeting sequence of sh6 incorporated. In accordance with the findings from Bauer and colleagues and compared with the LVTH controls, an efficient decline in Lrrk2 protein and mRNA levels without a meaningful increase of Oas1 expression was observed in either LVmiB3- or LVmiB4-transduced VM cultures at both DIV9 and DIV14 (see Figure 28)

as well as in NIH3T3 cells (see Figure 32). The reasons why second generation silencing constructs do not evoke an innate immune response are still unclear. As they possess structure and sequence similarities to the corresponding endogenous transcript, they may be recognized by the cell as self (271). A multitude of endogenous expressed miRNAs is present in cells that do not evoke adverse effects other than their designated cellular function (391). These cell-derived short dsRNA species may thus hold some selectively evolved characteristics that allow cytoplasmic PPRs to discriminate between self and non-self dsRNA-species and avoid thereby triggering of an innate immune response. For instance, the secondary structure of endogenous miRNA precursors exhibit characteristic bulges and mismatches in the stem-loop structure (261) that may preclude an activation of an IFN-response by cellular pre-miRNAs (326). As such, the differences in perfection of the precursor stem between shRNA and shRNA^{mir} silencing constructs generated by the implementation of design features that are invariably present in miRNA precursors into gene-targeting shRNAs may account for the prevention of dsRNA-dependent ISG activation by second generation RNAi systems (267, 348). As outlined above, another critical feature to distinguish foreign RNA from host nucleic acids and that determines the activation of dsRNA signaling is the status of the RNA's 5'-end. pri-miRNA transcripts are processed by the action of Drosha before they appear in the cytoplasm, so that the miRNAs possess a monophosphate at their 5'-end (392). Likewise, shRNA^{mir} silencing triggers that are expressed as primary transcripts like the miR-30-based constructs used here may therefore remain silent to innate immunity by following the miRNA biosynthesis pathway. As an additional indication for viability of the VM cultures transduced with lentiviral vectors encoding the second generation Lrrk2-specific shRNAs miB3 and miB4, the relative amount of DA neurons remained unaltered upon Lrrk2 silencing at DIV9 (see Figure 29B). It is known that the development of DA neurons *in vivo* proceeds in two broad phases: during the prenatal phase, the population of DA neurons is established, and in the second phase, beginning in the perinatal period and extending in the postnatal phase, the DA neurons form interactions with other neuronal groups by extending their processes and generating synapses. In the context of developing target interactions, a natural cell death (NCD) event takes place among DA neurons of the SN (393, 394). The NCD is present during the first 14 days of life (395), which is regulated by target-derived neurotrophic factors, and determines the number of neurons surviving into maturity (396). The observed decrease in DA survival at DIV14 (see Figure 29B), corresponding roughly to postnatal day 5, may therefore result from the reduced neurite outgrowth (see Figure 30 and Figure 31) that impaired a successful projecting of the neurons. Consequently, forming of target contact was insufficient and NCD occurred.

In accordance with published RNAi guidelines (348, 350), the study showed Lrrk2 mRNA and protein reduction with two different, independent Lrrk2-silencing constructs and ruled out any gene deregulation due to nonspecific interferon-associated antiviral response.

Thus, specificity of the utilized RNAi approach and hence the validity of the observed silencing phenotypes was assured.

3. Lrrk2 as a modulator of the actin cytoskeleton

Subsequent to the finding that Lrrk2 is associated with PD, much attention has been drawn on the enzymatic activity of Lrrk2 and its modulation by mutations rather than on the physiological function of the protein in intact cells and tissues. Thus, knowledge about the endogenous role of Lrrk2 and Lrrk2-mediated signaling pathways is still limited. Within cells, many processes are in general not only directed by the mere presence of a protein but also by its rapid and transient association with other proteins into protein complexes. The analysis of interaction partners of a functionally uncharacterized protein is thus suggestive for its biological function and related molecular pathways according to the “guilt-by-association” principle (356, 397, 398). Correspondingly, identification of the Lrrk2 complex partners is a crucial step in elucidating its *in vivo* functions. Studies on the analysis of Lrrk2 protein interactions published so far are based on either yeast two-hybrid screens and/or the overexpression of the tagged protein (128, 216-219, 221, 227, 229, 230). However, several limitations are linked to these approaches. Although yeast two-hybrid assays facilitate the detection of weak and transient interactions, they only allow mapping of binary or pair-wise interactions (284, 287). Components of a larger complex that do not necessarily interact directly with each other are thus missed (399). Moreover, the method often yields high false positive (biological and technical) as well as false negative rates (284, 399-401). By analyzing PPIs outside their cellular environment, the heterologous yeast two-hybrid systems omit the specific subcellular localization and may additionally prevent post-transcriptional modifications and proper protein folding (293, 399, 401). Conversely, by overexpression of the affinity-tagged target protein in a suitable cell line, it is placed into a biological relevant setting. Thereby, post-transcriptional modifications and the association with physiological targets by allowing the protein’s correct subcellular localization are enabled (284). Nevertheless, the protein tag may interfere with proper protein folding and function which can alter or impact complex formation (284, 361, 397). In addition, the tag as well as the overexpression of the protein might yet affect its intracellular localization, so that the protein may not bind to its physiological targets or interact with non-physiological partners (284, 288). The formation of non-specific protein interactions by overexpression can also be encouraged through the altered stoichiometric ration between the target protein and its physiological interaction partners (288, 397). Furthermore, misfolding of the bait protein upon overexpression causes its association with chaperones and heat shock proteins (284, 288).

The present study describes the application of QUICK (293), a robust assay for the specific identification of PPIs, to systematically screen for Lrrk2 protein complex partners, based on the endogenous, untagged protein at its physiological expression level. Integrating

RNAi-mediated knockdown and co-IP, both of which has been implemented for Lrrk2 within the present study, as well as SILAC and quantitative MS technologies that are established within the laboratory, this assay allowed to overcome the technical issues in the detection of Lrrk2 protein interactions by conventional (gel-based) co-IP/MS methods (see 1.). By quantitative MS, the distinction of Lrrk2 interacting proteins from background proteins was enabled, resulting in the identification of 36 potential complex partners (see Table 21). Their vast majority is functionally linked to the actin cytoskeleton, its rearrangement, dynamics, and maintenance as indicated by both literature-based curation (see Table 21) and KEGG pathway enrichment analysis (see Figure 36). According to their molecular function extracted from peer-reviewed publications, the majority of potential interactors clustered into four defined categories and only six proteins exert miscellaneous functions (group 5).

A wealth of actin-binding proteins (ABPs), which were subdivided into actin-regulatory proteins (group 2) and myosins (group 3) here, control the spatial organization and dynamic assembly of monomeric actin into different filamentous structures of the actin cytoskeleton (239, 259, 402) on which numerous vital cellular processes rely (403). Besides some actin isoforms (group 1), a number of actin-regulatory proteins that are known to modulate actin dynamics by regulating the assembly and disassembly of actin filaments and their organization in structural higher-order networks (group 2) were found to be components of the Lrrk2 protein complex. Herein, six out of seven subunits comprising the Arp2/3 complex, which has emerged as a key component in the formation of dynamic actin networks as it is unique in its ability to both nucleate filaments and to organize them into branched networks, were detected (246, 404). With Tmod3 (405), the widely expressed isoform of the most-prominent pointed-end capping protein tropomodulin was found to interact with Lrrk2. Besides the Arp2/3 complex, tropomodulins are the only known proteins that bind to the slow growing end of actin filaments and inhibit polymerization/depolymerization of actin monomers at this end (239). Tmod3 performs a negative regulatory functions in dynamic actin networks, but the mechanisms underlying this function are poorly understood (245). In addition to its pointed end capping capacity, the protein is able to bind to actin monomers and sequester them from polymerization (406). As any other tropomodulin isoform, Tmod3 can, moreover, bind specifically to tropomyosins, so that the capping activity is targeted to and stimulated by tropomyosin-coated actin filaments (405, 406). In the screen, three isoforms of tropomyosin, α -, β - and γ -TM, were found as potential Lrrk2 interactors. Tropomyosins are homo- or heterodimers and polymerize into helical fibrous molecules that localize along the actin filament's length (248, 407). In general, tropomyosin is thought to exert its pivotal function in regulating actin properties by stabilizing the filaments. This is accomplished either through the nature of the tropomyosin-binding to F-actin, a protective effect towards other ABPs (see below) or by preventing the dissociation of G-actin from the filament's pointed end in the absence of tropomodulin (245, 407, 408). Furthermore, the two vertebrate's α -subunit

isoforms and the β -subunit of the α/β -heterodimeric CapZ complex were identified as Lrrk2 protein complex components (409). Both subunits are required for an efficient binding of this predominant barbed-end capping protein to F-actin, thereby preventing the addition and loss of G-actin at that end (409, 410). As a key component in the dendritic nucleation model, which accounts for the assembly of branched actin networks and generation of protrusive forces at the leading edge of cells, CapZ “funnels” polymerization-competent actin monomers to a subset of filament barbed ends near the membrane and promotes their individual rapid elongation (409, 410). The in the QUICK assay detected proteins EPLIN, ankyrbin, drebrin and plectin also associate to the actin cytoskeleton and control cellular actin dynamics, although they are less well characterized than the ABPs described above. The ability of EPLIN to cross-link and bundle actin filaments facilitates the formation of stable actin structures. By inhibiting the depolymerization of F-actin, EPLIN regulates or rather inhibits, moreover, actin filament turnover (247). Likewise, plectin acts as a cross-linker. Being the most versatile cytoskeletal linker and scaffolding protein, it features prominently in the organization and stabilization of cytoskeletal network structures by cross-linking within as well as between the various polymer systems (F-actin, MTs and intermediate filaments), thus providing cells with mechanical strength (411). The protein is also considered as an important regulator of actin dynamics and related cellular processes where it controls filament polymerization and/or depolymerization by sequestering monomeric actin (411, 412). The precise function of ankyrbin is unknown but suggested to be involved in the maintenance and/or organization of actin cytoskeletal structures. Its association to F-actin is though supposed to be indirectly through an unidentified factor (413). The spatial organization and dynamic assembly of the actin cytoskeleton is, however, not only affected by an individual regulation of protein activities but mainly by their coordination and integration. Tropomyosin for instance promotes its stabilizing properties by regulating the access of ABPs to actin filaments and increasing the binding affinity of tropomodulin towards F-actin. As such, it protects against the action of depolymerizing and severing proteins. Furthermore, it prevents the assembly of new actin filaments to the pre-existing network through restricting the nucleation activity of the Arp2/3 complex (405, 407, 408). Likewise, also EPLIN affects the formation of new actin filaments by inhibiting the action of the Arp2/3 complex, thereby circumventing a remodeling of the actin-based cytoskeleton (247). Drebrin binds in a competitive manner with tropomyosin to actin filaments, making them available for actin-depolymerizing factors and therefore facilitating their destabilization, maintaining them in a dynamic state (414). Additionally, it also competes with actin-bundling proteins for interaction with actin (414, 415).

Besides actin and its regulating proteins, members of the myosin I and II (group 3) family and modulators of these actin-dependent motor proteins (group 4) were identified. Myosins generally use actin filaments as a track along which they move, thereby promoting

contractility or cell motility and vesicular transport (236), but their involvement in the assembly/disassembly and remodeling of actin filaments has also been shown. Based on the domain structure of their terminal tail region, members of the myosin I family (unconventional myosins) can be subdivided into long-tailed and short-tailed. By QUICK, three short-tailed (myosin 1b, 1c and 1d) and one long-tailed (myosin 1f) class I myosins were detected (416). The ability of all class I myosins to bind simultaneously to cellular membranes and actin filaments implicates that they exert their physiological function at the interface between membranes and the actin cytoskeleton. Serving as divalent cross-linkers, they may physically connect and generate forces between F-actin and the membrane, thus controlling processes involving membrane movement, deformation and bending, e.g. plasma membrane tension, vesicle release, endocytosis and exocytosis (417, 418). Studies in yeast and *Dictyostelium discoideum* suggest, moreover, a more active role of long-tailed myosins in the regulation of actin dynamics. Being able to associate directly to the Arp2/3 complex but also indirectly through ligands of the Src homology domain 3 (SH3) in their tail region, long-tailed class I myosins may control Arp2/3-dependent actin assembly via the formation of complexes with regulators of actin nucleation (418, 419). In addition, myosin I may enrich actin monomers locally through its SH3 domain interaction partners (418). The participation of myosin I in the complex with actin nucleating proteins is still unclear but it may move the nucleation machinery along the filaments towards sites of actin assembly, involving either clusters of membrane-bound myosin I and adaptor proteins that link to Arp2/3 or the “free” complex (418, 419). The enzymatic activity as well as the mechanical activities of vertebrate class I myosins is predominantly regulated by the interaction with calmodulin, also found to participate in the Lrrk2-associated complex, but the underlying mechanisms are poorly understood. Serving as myosin I light chains (416, 420) and constituting a Ca^{2+} -activated switch protein (421), calmodulin regulates the activity as well as the ability of unconventional myosins to translocate actin filaments in a Ca^{2+} -dependent manner (416, 420). Besides members of the class I myosins, subunits comprising members of the myosin II superfamily (422, 423) were found within the Lrrk2 protein complex. Here, one essential light chain (Myl6) and one regulatory light chain (Myl12B or Myl9) of these heterohexameric proteins were identified by QUICK and two non-muscle heavy chains (NMHC IIa and NMHC IIb) by means of co-IP. Although non-muscle class II myosins (NM II) do not participate in the physical organization of actin network structures directly, using their actin-bundling and contractile properties, they affect actin cytoskeleton assembly. NM II for instance generates the retrograde flow of actin and promotes cell-matrix adhesion, two processes involved in the dynamic remodeling of the actin cytoskeleton and interaction of the cell with its environment that drive cell migration (253, 423). The phosphorylation level of the regulatory light chain (RLC) is an important factor in myosin II regulation and depends on the relative activities of several kinases and myosin phosphatase (MP). Inhibition imposed on myosin II by the

unphosphorylated RLC is reversed by RLC-phosphorylation, promoting actin-activated ATPase activity, filament formation and contractile activity (422-424). Most properties of MP, the only phosphatase catalyzing the dephosphorylation of myosin II's RLC, are due to its target/regulatory subunit MYPT1 (myosin phosphatase-targeting subunit 1), which was also identified in the QUICK approach. It targets the catalytic subunit of type 1 phosphatase δ isoform (PP1c δ) to its substrate phospho-RLC and effects an activation of PP1c δ (424). Comprising multiple protein interaction domains, MYPT1 serves, moreover, as a platform for various PPIs, and several kinases as well as signaling pathways inhibiting MP activity by MYPT1-phosphorylation have been discovered, including RhoA/Rho kinase (424-426). Here, the myosin phosphatase-Rho interacting protein (M-RIP), also detected in the screen, functions as an important component in the regulation of RhoA signaling and MP activity. Besides acting as a scaffolding protein that targets the MP complex to actomyosin structures, promoting specificity and efficiency of the MP activity towards myosin, M-RIP links RhoA signaling to MP regulation, inactivating the RhoA/Rho kinase pathway (427, 428).

The assembled PPI network based on the putative Lrrk2 complex partners identified in the study (see Figure 37A) proved to be significantly enriched in previously validated interactions as curated by the HPRD and BioGRID database (see Figure 37B). In general, the employed PIE analysis assesses the physical cohesiveness of interacting proteins in a given set of (experimentally verified) proteins. By circumventing interaction enrichment biases for proteins that are often studied in context-specific networks derived from general PPI networks, PIE improved the reliability of the experimentally inferred network (307). The set of the identified Lrrk2 interactors displayed a remarkable physical cohesiveness in the sense of being enriched with PPIs regardless of pathway assignment. Statistical analysis of the network density provides confidence that the proteins are significantly linked. The significant physical cohesiveness of the Lrrk2 complex partners thus reflects their biological coherence and functional interdependence, thereby reinforcing the validity of the remaining, novel Lrrk2 interactions implied by the experimental results. The inferred Lrrk2 PPI network, which links Lrrk2 to proteins that are involved in the assembly of actin-based structures and/or cellular mechanisms relying on their dynamic nature, therefore indicates that the function of Lrrk2 is related to the actin cytoskeleton, its dynamic regulation and interrelated processes. This is further supported by the extension of the network through the incorporation of first-order shared neighbors, revealing a high degree of connectivity between the Lrrk2 interacting proteins by intermediate proteins (see Figure 38). A functional evaluation of the extensions in a literature-based fashion demonstrated that the interconnecting proteins are predominantly closely associated with the actin cytoskeleton, its modulation and/or the actin-dependent myosins (see Supplementary Table 3), affirming the network's fidelity. Therefore, Lrrk2 protein complex partners and consequently Lrrk2 itself can be mapped into an evolutionary and functionally conserved PPI network regulating the

actin-based cytoskeleton. The indicated role of Lrrk2 in actin-based biological processes is in line with previous studies that suggest an association of Lrrk2's biological function with the actin cytoskeleton (158, 187, 429). It was demonstrated in a cell-free kinase substrate tracking and elucidation (KESTREL) screening that Lrrk2 phosphorylates members of the ERM family (187), which link the actin cytoskeleton to the plasma membrane (430). Lrrk2 was also shown to be located in the neck of membrane microdomains, whose formation involve the reorganization of the underlying actin cytoskeletal network and is partially regulated by ERM proteins (431), whereupon a regulative role of Lrrk2 in actin cytoskeleton reorganization was suggested (158). Furthermore, microarray experiments after Lrrk2 knockdown in SH-SY5Y cells revealed alterations in the expression levels of some proteins participating in actin cytoskeleton signaling (429). Although the study of Häbig and colleagues reports that the knockdown of Lrrk2 results in the differential expression of genes involved in actin cytoskeleton signaling in SH-SY5Y cells (429), the knockdown does not affect the proteome of NIH3T3 cells, as no significant alterations in the protein ratios could be detected here (see Figure 34A and Supplementary Table 1). As such, SH-SY5Y cells may react differentially to Lrrk2 knockdown, at least on mRNA level on which the results of Häbig et al. were based. However, the findings of the two studies are not mutually exclusive. Studies on the transcriptome and proteome analyze two different levels of a biological system (here also in different cell types). Divergent expression levels of mRNA and proteins within them are well-known in the literature, being most likely the result of posttranslational regulatory mechanisms (432, 433). Thus, besides integrating genomic and proteomic data sets, their meaningful interpretation requires functional annotation and consideration in the context of biological pathways and functional processes (433). In fact, both studies, the one of Häbig et al. and the work presented here, assign the same cellular function to Lrrk2 based on the respective experimental findings and associate it with the actin-based cytoskeleton.

Utilizing the non-neuronal cell line NIH3T3 in the QUICK approach represents a limitation insofar that potential brain-specific interactors escape identification. The application of a cellular model with more relevance to neuronal degeneration would have been indeed interesting in that it assists the specific analysis of Lrrk2 function in neurons and would thus provide more intrinsic indications on the impact of Lrrk2 in PD-related neurodegeneration. However, the prior aim of the study was to analyze the Lrrk2 interactome based on the endogenous protein at its physiological expression level which was not reported before. For this purpose NIH3T3 cells were chosen as they express significant levels of the Lrrk2 protein and can be analyzed quantitatively with high confidence using lentiviral-mediated knockdown of Lrrk2. Considering Lrrk2's multidomain structure and its expression in both CNS and peripheral tissues, it is reasonable that the interactome obtained here represents systemic and physiological relationships of Lrrk2 that do relate to general cellular mechanisms and signaling cascades. The identified proteins by QUICK suggest that Lrrk2 is involved in basic

cellular pathways regulating actin structure and dynamics. Although neuron-specific interactions and thus Lrrk2 function cannot be excluded, an involvement of Lrrk2 in such more basic functional pathway is indicated by the findings in actin cosedimentation assays as well as on the morphology of NIH3T3 cells. Yet, the experiments carried out in primary VM cultures demonstrate that Lrrk2 activity is also relevant for neuronal cells.

The actin cosedimentation assay demonstrated the ability of affinity purified Lrrk2 to associate with F-actin *in vitro* (see Figure 39), emphasizing the suggested functional link of Lrrk2 with actin cytoskeletal structures. Beyond that and under the stoichiometric conditions tested *in vitro*, Lrrk2 increased the amount of unpolymerized actin at steady state. The thus altered G-actin/F-actin ratio in favor of the monomer may indicate that Lrrk2 itself can function as a direct modulator of F-actin assembly by exerting an at least basal regulatory activity on actin polymerization. In the *in vitro* context, it might act either in sequestering monomers or, given its substoichiometric activity, capping of filaments barbed ends. Both regulatory processes affect the dynamic assembly of actin filaments by controlling their turnover (239). At the same time, the Lrrk2/actin stoichiometry used *in vitro* (1/10 to 1/20) needs to be considered. Given the cellular abundance of actin, it may be higher than one can expect *in vivo*. However, it cannot be excluded that local Lrrk2 to actin ratios within cells may be sufficiently high at actin filaments or, given the observation that Lrrk2 is associated to membranous structures (146, 155), close to membranes. It is likewise possible that a modified form of Lrrk2 (e.g. phosphorylated) is more active in exerting its modulating function within the cell. In conjunction with its identified interactors, an alternative scenario can be considered, where Lrrk2 is assigned to a more “passive operator” of the actin filamentous network, acting as a connector that localizes and scaffolds/cooperates with the actin-regulatory and motor proteins. Due to the complexity by which proteins can modulate actin dynamics, further analysis is needed to clarify how Lrrk2 itself or along with its interaction partners affects actin dynamics as well as the mechanisms underlying the observed effects of Lrrk2 on the G-actin/F-actin ratio. Nevertheless, the study provides initial mechanistic insights.

The cellular relevance of Lrrk2 in actin cytoskeleton-based processes was affirmed by the findings obtained in the functional analysis of Lrrk2 on the cellular level that determined the effects of a lentiviral-mediated knockdown of Lrrk2 by second generation shRNA expression in NIH3T3 cells as well as in primary VM cultures. Given that the actin cytoskeleton plays a fundamental role in the generation and maintenance of cell morphology, alterations in cell shape result from modifications in the organization of cytoskeletal structures (434). The depletion of Lrrk2 in NIH3T3 cells by RNAi led to significant morphological alterations, with cells displaying elongation and narrowing of the cell body (see Figure 33) and reflecting a general perturbation of normal cytoskeleton organization. Nevertheless, Lrrk2-associated PD is a neurodegenerative disorder characterized by the loss

of DA neurons in the SNpc like in the idiopathic disease (144). Assaying primary VM cultures derived from embryonic mice, the study thus considers also a model system with more relevance to the pathophysiology of PD. Depletion of *Lrrk2* caused a decrease in the average neurite length of developing DA neurons, the prime cellular target site in PD, as a consequence of an impaired neurite outgrowth (see Figure 30 and Figure 31). Specificity of the phenotype was controlled by using lentiviruses encoding two different, independent *Lrrk2*-targeting shRNA^{mir} constructs as well as monitoring *Oas1* expression. Due to the fact that the delivery of silencing vectors did not induce the expression of *Oas1* (see Figure 28C), it can be excluded that the observed phenotype resulted from off-target effects by innate antiviral response pathways following shRNA expression, which has been reported to alter the neuronal morphology in hippocampal cultures (435) as well as to cause rarefaction of cortical neurites *in vitro* (324). Moreover, the neurites of shRNA^{mir} expressing DA neurons displayed a proceeding outgrowth from DIV9 to DIV14 though it was diminished compared to the wt or control (see Figure 31). This reveals further that the neurites were subjected to an attenuated outgrowth ability rather than to a retraction process. A physiological relevance of *Lrrk2* on neurite outgrowth was also demonstrated by others. Gillardon recently showed that neurons derived from *Lrrk2*-deficient mouse ES cells also exhibit significantly shorter neurites than wt neurons (215). A converse effect of *Lrrk2* on neurite length was observed after transduction of rat cortical neurons with *Lrrk2* shRNA vectors, which led to an increase in neurite length (436). This discrepancy is difficult to conciliate. One point that might contribute to the conflicting results is the difference in cell culture, namely primary progenitor VM cultures and ES cell derived neurons from mouse versus cortical cultures derived from P1 rat brains. Besides the two various animal models that were used, the developmental stage of the neurons represented by the cellular systems also differs. Both the progenitor VM cultures and the ES cell derived neurons mimic the prenatal phase of neuronal development, whereas the cortical cultures represent the postnatal period. The knockdown of *Lrrk2* at DIV1 in the dopaminergic system and permanent knock-out in ES cells versus depletion at DIV7 in postnatal cortical cultures interferes therefore with two different developmental stages of the neurons. Consequently, the studies analyzed the impact of *Lrrk2* on neurite process formation during neuronal development or on neurite maintenance in mature neurons.

The actin-based cytoskeleton is not only critical for a wide range of fundamental processes in non-neuronal cells but is also a crucial element in the development of the nervous system. Migration of neurons as well as initiation and extension of neurites rely on an organized actin polymerization (437). Here, the regulative mechanisms postulated to underlie the dynamic spatiotemporal organization and reorganization of the actin cytoskeleton in migrating non-neuronal cells are in general assumed to be also applicable to the protrusion of growth cones in the generation of neurites and their outgrowth, with cytoskeletal proteins representing the important endogenous factors for regulation (251, 259,

437, 438). Numerous ABPs have been identified in neurons, but the precise regulatory mechanisms for the actin cytoskeleton during neurite outgrowth are still unclear (251, 259). Notwithstanding, the importance of several ABPs that were found to participate in the Lrrk2-associated protein complex in the regulation of these events could be demonstrated, including the Arp2/3 complex (439), tropomodulin (438), tropomyosin (440, 441) and members of the myosin class I (442) and II (443-445) family. As various aspects of actin cytoskeleton organization and dynamics in the growth cone are controlled through the coordinated action of ABPs (259, 446), perturbation of this regulative cellular system may certainly cause abnormalities in neurite extension. The identified interactors of Lrrk2 as well as its link to actin filaments implicated by the *in vitro* experiments may support the effects observed upon Lrrk2 knockdown *in cellulo*. The findings collectively suggest that Lrrk2 impacts on the cytoskeletal integrity mediated by variations in actin-based dynamics, either most likely in concert with its complex partners or – which cannot be yet excluded – in part directly. Being placed in the functional network of proteins that are essential for a proper assembly of the actin filamentous network during neurite outgrowth in conjunction with the observed reduction in neurite length of developing DA neurons following Lrrk2 depletion indicates, furthermore, that Lrrk2 exerts a modulating function in neurite extension.

Neurite outgrowth is the result of numerous extracellular stimuli targeting the actin cytoskeleton of each individual neuron. Small Rho GTPases are essential components that link these stimuli to actin but their neuronal downstream effectors binding to actin or responsible for scaffolding are largely opaque (447). Lrrk2 being a GTPase-dependent kinase, harboring both protein interaction domains (LRR and WD40) as well as enzymatic domains (ROC and MAPKKK), may be involved in such processes and serve as a scaffold protein within signaling pathways controlling the dynamic actin cytoskeleton organization. Several LRR-containing proteins such as flightless I protein (Flii), tropomodulin and the *Dictyostelium* Lrrk2 homologous proteins GbpC (cyclic guanosine monophosphate binding protein) and Pats1 (protein associated with the transduction of signal 1) participate in the functional assembly of the actin network (245, 448-450). Interestingly, besides GbpC and Pats1 one further member of the ROCO protein superfamily, death-associated protein kinase (DAPk), seems to be involved in cytoskeletal rearrangement by affecting myosin II function (448, 449, 451), making Lrrk2 not the first member of this family to be associated with components of the cytoskeleton.

Lrrk2 being involved in actin network assembly, it may influence various interrelated cellular processes. Figure 40 presents a model for the physiological function of Lrrk2 within neuronal networks proposed on the basis of the present study. The findings obtained upon Lrrk2 depletion in primary VM cultures demonstrate that the protein impacts on the outgrowth of neuronal processes. Along with the generation of neurites and their guidance, neurite extension is essential to the formation of neuronal morphology and circuitry within the CNS,

with each event relying on the actin-based cytoskeleton (351, 452). As a consequence of a reduction in neurite length, Lrrk2 deficient neurons may establish fewer connections to other neurons, implicating that Lrrk2 may be involved in the determination of neuronal connectivity, which is a major defining factor for neuronal survival (453). The *in cellulo* results of the present study indicate that this can be at least applicable to DA neurons. Lrrk2 is, however, not only expressed in the DA neurons of the SNpc but also and in part at even higher levels in other brain regions, including the nuclei of the basal ganglia motor circuit (see Introduction, 2.3). It may thus influence the formation of projections not only from but also to nigral neurons as well as between other neuronal populations with relevance to PD pathogenesis. While this scenario has been suggested previously on the basis of functional assays (454), the present study provides a feasible molecular explanation on how Lrrk2 may direct neurite circuit formation, demonstrating its specific interaction with the actin filament network and the cellular machinery controlling actin dynamics. The actin-based cytoskeleton holds also a fundamental function in the formation, organization and maintenance of synapses as well as a physiological role in the mature synapse. Here, actin cytoskeletal structures are involved in the regulation of the synaptic vesicle cycle in the presynapse and thus affect neurotransmission, albeit each step of the process - consisting of synaptic vesicle clustering, mobilization, fusion and recycling - is influenced to a different extent by actin filaments (455). Interestingly, recent studies indicated an involvement of Lrrk2 in presynaptic functioning. In this context, Lrrk2 has been implicated in the regulation of synaptic vesicle endocytosis by its interaction with Rab5b that is known to play a major role in the transport of endocytotic vesicles in the presynapse. Disturbance of endocytosis, however, may cause alterations in the synaptic transmission (229). Indeed, several studies consistently revealed abnormalities in the nigrostriatal system (e.g. DA release, striatal DA content and uptake) of R1441C- and G2019S-Lrrk2 bacterial artificial chromosome (BAC) transgenic mice as well as of R1441C knockin mice, providing evidence that Lrrk2 might be involved in DA neurotransmission (456-458). Moreover, (ultra)structural and electrophysiological analysis of cortical synapses upon Lrrk2 knockdown suggested a function of Lrrk2 in regulating trafficking and distribution of synaptic vesicles. The identification of presynaptic proteins, including actin, as interactors implied that Lrrk2 operates as a component of a functional protein network that controls the dynamics between the vesicle pools inside the presynapse (459). Based on the results of the present work, it is worth to speculate that Lrrk2 participates in the physiology of the presynapse not only through mechanisms proposed by the studies presented above. As a potential modifier of F-actin polymerization/depolymerization, Lrrk2 might assist presynaptic integrity and neurotransmitter release that depend in a large part on organized actin cytoskeletal structures by regulating their dynamic assembly. Changes in both neuronal connectivity and presynaptic functioning, which are essential to CNS integrity, induced by perturbations of the cytoskeleton may represent a pathogenic trigger preceding DA

neurodegeneration in PD. Even if Lrrk2 knockout animals were reported to survive normally and not to develop neurodegeneration or motor dysfunctions (219, 458, 460, 461), the work presented here indicates that a loss of Lrrk2 interferes with neuronal integrity. The absence of neurodegeneration and neuropathological changes in the animals, consistent with reports on the disruption of other PD-related genes, might be explained by a negligible role of the protein during neuronal development. The cellular function of Lrrk2 may thus become important as recently as at the mature state. Considering the developmental expression profile of Lrrk2 (154) and both the phenotype in developing DA neurons following Lrrk2 knockdown *in vitro* observed here as well as in ES cell derived neurons from Lrrk2-deficient mice (215), the protein appears to hold a function during maturation. Alternatively, other molecules, including Lrrk2's paralog Lrrk1, may compensate for the loss of Lrrk2 *in vivo*, which is supported by studies in the nematode and fly where the deletion of the single Lrrk2 paralogs *lrrk-1* and *dLrrk* had no effect on the viability of DA neurons (461).

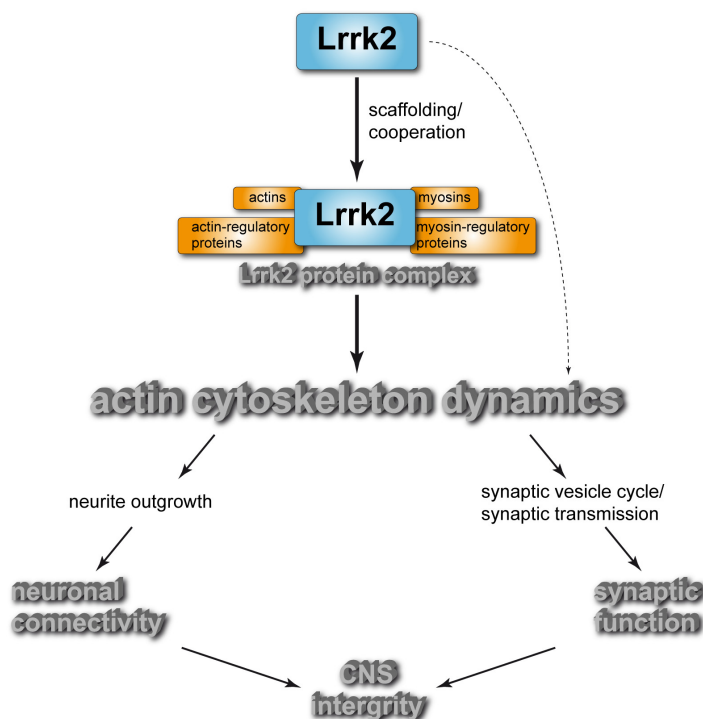


Figure 40: Lrrk2 function and CNS integrity – a model.

The present study indicates that Lrrk2 is involved in the dynamic assembly and organization of the actin-based cytoskeleton. Here, Lrrk2 can exert a modulatory function either directly (dashed line) or, more likely, by scaffolding or cooperating with its specific interactors, representing components of the actin cytoskeletal network and its regulators (bold line). Through its participation in actin cytoskeleton dynamics, Lrrk2 impacts on neurite outgrowth as shown for DA neurons upon Lrrk2 knockdown in primary VM cultures and may thus influence neuronal circuit formation by effecting neuronal connectivity. Additionally, previous studies suggest that Lrrk2 operates in the synaptic vesicle cycle and/or synaptic transmission. Given that these processes rely on an organized actin cytoskeletal structure, Lrrk2 might be involved in synaptic functioning. Both neuronal connectivity and neurotransmitter release are critical to CNS integrity. See text for further details.

Also several other proteins that are related to autosomal dominant forms of PD have been linked to the dynamic regulation of actin cytoskeletal networks. Parkin has been shown to be associated with the actin-based cytoskeleton and to be involved in its dynamic assembly (462, 463). PINK1 that is assumed to participate together with parkin in the same cellular pathway (28), has also been implicated in the modulation of actin filament assembly, possibly through the same mechanistic pathway as parkin (464). In addition, α -synuclein was demonstrated to bind to actin and to exert presumably monomer sequestration activity, which induces a decrease in actin polymerization and facilitation of depolymerization. Additionally, α -synuclein is able to initiate the formation of actin bundles. These actions by whose α -

synuclein modulates the actin cytoskeleton are, however, significantly altered in the pathogenic A30P mutant, impairing actin cytoskeletal organization (465). The link between actin dynamics or rather its impairment and the pathogenesis of PD revealed by these findings thus supports the biological significance of Lrrk2 function in the assembly of the cytoskeletal network reported in the work presented here.

Interestingly, the dynamic state of the actin cytoskeleton has been indicated as an elicitor for mitochondrial ROS release and apoptosis (466). Several mechanisms have been suggested that may couple actin cytoskeletal structures, ROS release and cell death pathways. F-actin dynamics may for instance regulate the activity of several ion channels with relevance for ROS release and/or apoptosis or is coupled to signaling pathways regulating longevity where it acts in feedback mechanisms as a sensor of cellular integrity (466). Of note, increased ROS production and apoptosis are also implicated in PD-associated pathogenic pathways (see Introduction, 1.3.4.2).

The proteomic approach applied in the present study in conjunction with the molecular and cellular analyses of Lrrk2 provides novel and critical aspects on the endogenous function of the protein. The molecular interactions as well as the biological role of Lrrk2 appeared to be closely associated with the organization and dynamics of the actin-based cytoskeleton. Clearly, further research has to determine the specific role of Lrrk2 in the assembly of actin filamentous networks along with its interaction partners and its involvement in actin-related cellular pathways. It is equally probable that Lrrk2 is capable to accomplish additional, different biochemical functions as it is a multidomain protein, possessing besides a catalytic core several protein interaction domains that are likely to facilitate various PPIs. The results of several studies support this notion by demonstrating that Lrrk2 participates in various, not necessarily independent, physiological processes. This includes kinase signaling, vesicle transport, regulation of microtubules, cytoskeleton assembly and the chaperone system (180). Nevertheless, the functional proteomic analysis of Lrrk2 in its normal physiological environment provided new insights on how Lrrk2 may interact with the cytoskeletal machinery controlling actin network assembly on the molecular level. A direct influence of Lrrk2 on filament dynamics was observed *in vitro*. Within cells, however, Lrrk2 may also act, and maybe mainly, as a molecular hub that regulates both actin filament assembly and stability by scaffolding or connecting associated actin-regulatory and motor proteins. On the cellular level, the loss of Lrrk2 expression specifically affects the generation and/or maintenance of cell morphology in non-neuronal cells and compromises neurite outgrowth of DA neurons. Consistent with previous studies (187, 429) the findings obtained here, therefore, indicate that Lrrk2 functions in actin-related cellular processes that do not only specify fundamental properties of a cell but are likewise essential for neuronal functioning and integrity. Their impairment may thus be relevant to the pathogenic mechanisms in PD and contribute to neurodegeneration associated with the disease.

4. Perspectives

Given the prevalence of Lrrk2 mutations in both idiopathic and familial PD, the protein is in the focus of intensive research in the Parkinson's field but its physiological and pathophysiological function remained largely elusive. The study presented here indicates that the endogenous role of Lrrk2 is linked to the dynamic organization of the actin-based cytoskeleton and related biological processes. Based on these findings as well as work by others discussed above, future research will not only aim at unrevealing the specific, regulative action of Lrrk2 along with its interaction partners in this specific context but will also be extended by studies on PD-associated Lrrk2 variants. Comparative analyses of cellular wt, Lrrk2 knockdown (loss-of-function) and Lrrk2 mutant models will hopefully provide essential clues towards Lrrk2-associated pathophysiology.

In future experiments, the power of quantitative MS-based proteomics may be utilized to address the influence of mutant Lrrk2 on its interaction network. A systematic interactome analysis of pathogenic Lrrk2 variants shall reveal whether mutations impact on the qualitative and/or quantitative composition of protein complexes associated with the different protein mutants. Complementing the results by a kinase-dead control can further disclose a potential regulatory role of Lrrk2's kinase activity in the complex formation. On the cellular level, the influence of Lrrk2 as well as of its mutants on the organization of the actin cytoskeleton and associated proteins by tracking selected candidates of the Lrrk2 interactome may be studied.

As proven by the present work, NIH3T3 cells constitute a powerful model system to study the impact of Lrrk2 on the actin cytoskeleton. For comparative analyses with the wt and Lrrk2 knockdown model, knockdown cells complemented with PD-associated Lrrk2 variants and the kinase-dead control can be generated that exhibit protein expression levels similar to the endogenous protein. Additionally, differentiated iPS cells derived from human Lrrk2 mutation carriers and their genetically corrected counterparts, generated in the laboratory of Prof. T. Gasser (University of Tübingen), may be utilized, as they represent the closest model to the human disease.

The detection of endogenous Lrrk2 in immunocytochemical assays is a still persisting problem for the analysis of the murine protein in the established model system (NIH3T3 cells and primary VM cultures), primarily due to lack of antibodies of sufficient specificity. Colocalization studies of Lrrk2 and its suggested complex partners can not only confirm the proteomic and biochemical results but also affirm and specify the association between Lrrk2 and the actin cytoskeleton. It is, moreover, conceivable that mutations in Lrrk2 interfere with the protein's localization and thus with its functioning in actin dynamics. Establishing a protocol for the detection of endogenous Lrrk2 by IF is thus of great interest. The Lrrk2-specific antibodies offered by the Michael J. Fox Foundation hold promise. They have been shown to specifically detect the endogenous protein in western blot analysis by several laboratories including our own and perform in IF on mouse brain by one group.

VI. REFERENCES

1. Mattson, M. P., Chan, S. L., and Duan, W. (2002) Modification of brain aging and neurodegenerative disorders by genes, diet, and behavior. *Physiol Rev* 82 (3), 637-672
2. Mattson, M. P., and Magnus, T. (2006) Ageing and neuronal vulnerability. *Nat Rev Neurosci* 7 (4), 278-294
3. Oeppen, J., and Vaupel, J. W. (2002) Demography. Broken limits to life expectancy. *Science* 296 (5570), 1029-1031
4. Parkinson, J. (2002) An essay on the shaking palsy. 1817. *J Neuropsychiatry Clin Neurosci* 14 (2), 223-236; discussion 222
5. Lesage, S., and Brice, A. (2009) Parkinson's disease: from monogenic forms to genetic susceptibility factors. *Hum Mol Genet* 18 (R1), R48-59
6. Alves, G., Forsaa, E. B., Pedersen, K. F., Dreetz Gjerstad, M., and Larsen, J. P. (2008) Epidemiology of Parkinson's disease. *J Neurol* 255 Suppl 5, 18-32
7. Dauer, W., and Przedborski, S. (2003) Parkinson's disease: mechanisms and models. *Neuron* 39 (6), 889-909
8. Fahn, S. (2003) Description of Parkinson's disease as a clinical syndrome. *Ann N Y Acad Sci* 991, 1-14
9. Jankovic, J. (2008) Parkinson's disease: clinical features and diagnosis. *J Neurol Neurosurg Psychiatry* 79 (4), 368-376
10. Chaudhuri, K. R., Healy, D. G., and Schapira, A. H. (2006) Non-motor symptoms of Parkinson's disease: diagnosis and management. *Lancet Neurol* 5 (3), 235-245
11. Poewe, W. (2008) Non-motor symptoms in Parkinson's disease. *Eur J Neurol* 15 Suppl 1, 14-20
12. Shults, C. W. (2006) Lewy bodies. *Proc Natl Acad Sci U S A* 103 (6), 1661-1668
13. Halliday, G. M., and McCann, H. (2010) The progression of pathology in Parkinson's disease. *Ann N Y Acad Sci* 1184, 188-195
14. Braak, H., Del Tredici, K., Rub, U., de Vos, R. A., Jansen Steur, E. N., and Braak, E. (2003) Staging of brain pathology related to sporadic Parkinson's disease. *Neurobiol Aging* 24 (2), 197-211
15. Braak, H., Ghebremedhin, E., Rub, U., Bratzke, H., and Del Tredici, K. (2004) Stages in the development of Parkinson's disease-related pathology. *Cell Tissue Res* 318 (1), 121-134
16. Galvan, A., and Wichmann, T. (2008) Pathophysiology of parkinsonism. *Clin Neurophysiol* 119 (7), 1459-1474
17. Brotchie, J., and Fitzer-Attas, C. (2009) Mechanisms compensating for dopamine loss in early Parkinson disease. *Neurology* 72 (7 Suppl), S32-38
18. Zigmond, M. J., Abercrombie, E. D., Berger, T. W., Grace, A. A., and Stricker, E. M. (1990) Compensations after lesions of central dopaminergic neurons: some clinical and basic implications. *Trends Neurosci* 13 (7), 290-296
19. Bartels, A. L., and Leenders, K. L. (2009) Parkinson's disease: the syndrome, the pathogenesis and pathophysiology. *Cortex* 45 (8), 915-921
20. Obeso, J. A., Rodriguez-Oroz, M. C., Rodriguez, M., Lanciego, J. L., Artieda, J., Gonzalo, N., and Olanow, C. W. (2000) Pathophysiology of the basal ganglia in Parkinson's disease. *Trends Neurosci* 23 (10 Suppl), S8-19
21. Moore, D. J., West, A. B., Dawson, V. L., and Dawson, T. M. (2005) Molecular pathophysiology of Parkinson's disease. *Annu Rev Neurosci* 28, 57-87
22. Di Monte, D. A. (2001) The role of environmental agents in Parkinson's disease. *Clinical Neuroscience Research* 1 (6), 419-426
23. Hindle, J. V. (2010) Ageing, neurodegeneration and Parkinson's disease. *Age Ageing* 39 (2), 156-161
24. de Lau, L. M., and Breteler, M. M. (2006) Epidemiology of Parkinson's disease. *Lancet Neurol* 5 (6), 525-535
25. Lai, B. C., Marion, S. A., Teschke, K., and Tsui, J. K. (2002) Occupational and environmental risk factors for Parkinson's disease. *Parkinsonism Relat Disord* 8 (5), 297-309
26. Logroscino, G. (2005) The role of early life environmental risk factors in Parkinson disease: what is the evidence? *Environ Health Perspect* 113 (9), 1234-1238
27. Thomas, B., and Beal, M. F. (2007) Parkinson's disease. *Hum Mol Genet* 16 Spec No. 2, R183-194
28. Hatano, T., Kubo, S., Sato, S., and Hattori, N. (2009) Pathogenesis of familial Parkinson's disease: new insights based on monogenic forms of Parkinson's disease. *J Neurochem* 111 (5), 1075-1093
29. Bekris, L. M., Mata, I. F., and Zabetian, C. P. (2010) The genetics of Parkinson disease. *J Geriatr Psychiatry Neurol* 23 (4), 228-242
30. Ibanez, P., Bonnet, A. M., Debarges, B., Lohmann, E., Tison, F., Pollak, P., Agid, Y., Durr, A.,

- and Brice, A. (2004) Causal relation between alpha-synuclein gene duplication and familial Parkinson's disease. *Lancet* 364 (9440), 1169-1171
31. Kruger, R., Kuhn, W., Muller, T., Woitalla, D., Graeber, M., Kosel, S., Przuntek, H., Epplen, J. T., Schols, L., and Riess, O. (1998) Ala30Pro mutation in the gene encoding alpha-synuclein in Parkinson's disease. *Nat Genet* 18 (2), 106-108
32. Polymeropoulos, M. H., Lavedan, C., Leroy, E., Ide, S. E., Dehejia, A., Dutra, A., Pike, B., Root, H., Rubenstein, J., Boyer, R., Stenroos, E. S., Chandrasekharappa, S., Athanassiadou, A., Papapetropoulos, T., Johnson, W. G., Lazzarini, A. M., Duvoisin, R. C., Di Iorio, G., Golbe, L. I., and Nussbaum, R. L. (1997) Mutation in the alpha-synuclein gene identified in families with Parkinson's disease. *Science* 276 (5321), 2045-2047
33. Singleton, A. B., Farrer, M., Johnson, J., Singleton, A., Hague, S., Kachergus, J., Hulihan, M., Peuralinna, T., Dutra, A., Nussbaum, R., Lincoln, S., Crawley, A., Hanson, M., Maraganore, D., Adler, C., Cookson, M. R., Muentert, M., Baptista, M., Miller, D., Blancato, J., Hardy, J., and Gwinn-Hardy, K. (2003) alpha-Synuclein locus triplication causes Parkinson's disease. *Science* 302 (5646), 841
34. Zarranz, J. J., Alegre, J., Gomez-Esteban, J. C., Lezcano, E., Ros, R., Ampuero, I., Vidal, L., Hoenicka, J., Rodriguez, O., Atares, B., Llorens, V., Gomez Tortosa, E., del Ser, T., Munoz, D. G., and de Yébenes, J. G. (2004) The new mutation, E46K, of alpha-synuclein causes Parkinson and Lewy body dementia. *Ann Neurol* 55 (2), 164-173
35. Levy, O. A., Malagelada, C., and Greene, L. A. (2009) Cell death pathways in Parkinson's disease: proximal triggers, distal effectors, and final steps. *Apoptosis* 14 (4), 478-500
36. Abeliovich, A., Schmitz, Y., Farinas, I., Choi-Lundberg, D., Ho, W. H., Castillo, P. E., Shinsky, N., Verdugo, J. M., Armanini, M., Ryan, A., Hynes, M., Phillips, H., Sulzer, D., and Rosenthal, A. (2000) Mice lacking alpha-synuclein display functional deficits in the nigrostriatal dopamine system. *Neuron* 25 (1), 239-252
37. Guo, J. T., Chen, A. Q., Kong, Q., Zhu, H., Ma, C. M., and Qin, C. (2008) Inhibition of vesicular monoamine transporter-2 activity in alpha-synuclein stably transfected SH-SY5Y cells. *Cell Mol Neurobiol* 28 (1), 35-47
38. Larsen, K. E., Schmitz, Y., Troyer, M. D., Mosharov, E., Dietrich, P., Quazi, A. Z., Savalle, M., Nemani, V., Chaudhry, F. A., Edwards, R. H., Stefanis, L., and Sulzer, D. (2006) Alpha-synuclein overexpression in PC12 and chromaffin cells impairs catecholamine release by interfering with a late step in exocytosis. *J Neurosci* 26 (46), 11915-11922
39. Yavich, L., Tanila, H., Vepsäläinen, S., and Jakala, P. (2004) Role of alpha-synuclein in presynaptic dopamine recruitment. *J Neurosci* 24 (49), 11165-11170
40. Lee, V. M., and Trojanowski, J. Q. (2006) Mechanisms of Parkinson's disease linked to pathological alpha-synuclein: new targets for drug discovery. *Neuron* 52 (1), 33-38
41. Spillantini, M. G., Schmidt, M. L., Lee, V. M., Trojanowski, J. Q., Jakes, R., and Goedert, M. (1997) Alpha-synuclein in Lewy bodies. *Nature* 388 (6645), 839-840
42. Uversky, V. N., Li, J., and Fink, A. L. (2001) Evidence for a partially folded intermediate in alpha-synuclein fibril formation. *J Biol Chem* 276 (14), 10737-10744
43. Weinreb, P. H., Zhen, W., Poon, A. W., Conway, K. A., and Lansbury, P. T., Jr. (1996) NACP, a protein implicated in Alzheimer's disease and learning, is natively unfolded. *Biochemistry* 35 (43), 13709-13715
44. Uversky, V. N. (2007) Neuropathology, biochemistry, and biophysics of alpha-synuclein aggregation. *J Neurochem* 103 (1), 17-37
45. Lashuel, H. A., Hartley, D., Petre, B. M., Walz, T., and Lansbury, P. T., Jr. (2002) Neurodegenerative disease: amyloid pores from pathogenic mutations. *Nature* 418 (6895), 291
46. Smith, W. W., Jiang, H., Pei, Z., Tanaka, Y., Morita, H., Sawa, A., Dawson, V. L., Dawson, T. M., and Ross, C. A. (2005) Endoplasmic reticulum stress and mitochondrial cell death pathways mediate A53T mutant alpha-synuclein-induced toxicity. *Hum Mol Genet* 14 (24), 3801-3811
47. Hsu, L. J., Sagara, Y., Arroyo, A., Rockenstein, E., Sisk, A., Mallory, M., Wong, J., Takenouchi, T., Hashimoto, M., and Masliah, E. (2000) alpha-synuclein promotes mitochondrial deficit and oxidative stress. *Am J Pathol* 157 (2), 401-410
48. Cuervo, A. M., Stefanis, L., Fredenburg, R., Lansbury, P. T., and Sulzer, D. (2004) Impaired degradation of mutant alpha-synuclein by chaperone-mediated autophagy. *Science* 305 (5688), 1292-1295
49. Tanaka, Y., Engelender, S., Igarashi, S., Rao, R. K., Wanner, T., Tanzi, R. E., Sawa, A., V. L. D., Dawson, T. M., and Ross, C. A. (2001) Inducible expression of mutant alpha-synuclein decreases proteasome activity and increases sensitivity to mitochondria-dependent apoptosis. *Hum Mol Genet* 10 (9), 919-926
50. Cappai, R., Leck, S. L., Tew, D. J., Williamson, N. A., Smith, D. P., Galatis, D., Sharples, R. A., Curtain, C. C., Ali, F. E., Cherny, R. A., Culvenor, J. G., Bottomley, S. P., Masters, C. L., Barnham, K. J., and Hill, A. F. (2005) Dopamine promotes alpha-synuclein aggregation into SDS-

- resistant soluble oligomers via a distinct folding pathway. *FASEB J* 19 (10), 1377-1379
51. Conway, K. A., Rochet, J. C., Bieganski, R. M., and Lansbury, P. T., Jr. (2001) Kinetic stabilization of the alpha-synuclein protofibril by a dopamine-alpha-synuclein adduct. *Science* 294 (5545), 1346-1349
 52. Norris, E. H., Giasson, B. I., Hodara, R., Xu, S., Trojanowski, J. Q., Ischiropoulos, H., and Lee, V. M. (2005) Reversible inhibition of alpha-synuclein fibrillization by dopaminochrome-mediated conformational alterations. *J Biol Chem* 280 (22), 21212-21219
 53. Xu, J., Kao, S. Y., Lee, F. J., Song, W., Jin, L. W., and Yankner, B. A. (2002) Dopamine-dependent neurotoxicity of alpha-synuclein: a mechanism for selective neurodegeneration in Parkinson disease. *Nat Med* 8 (6), 600-606
 54. West, A. B., and Maidment, N. T. (2004) Genetics of parkin-linked disease. *Hum Genet* 114 (4), 327-336
 55. Imai, Y., Soda, M., and Takahashi, R. (2000) Parkin suppresses unfolded protein stress-induced cell death through its E3 ubiquitin-protein ligase activity. *J Biol Chem* 275 (46), 35661-35664
 56. Shimura, H., Hattori, N., Kubo, S., Mizuno, Y., Asakawa, S., Minoshima, S., Shimizu, N., Iwai, K., Chiba, T., Tanaka, K., and Suzuki, T. (2000) Familial Parkinson disease gene product, parkin, is a ubiquitin-protein ligase. *Nat Genet* 25 (3), 302-305
 57. Zhang, Y., Gao, J., Chung, K. K., Huang, H., Dawson, V. L., and Dawson, T. M. (2000) Parkin functions as an E2-dependent ubiquitin-protein ligase and promotes the degradation of the synaptic vesicle-associated protein, CDCrel-1. *Proc Natl Acad Sci U S A* 97 (24), 13354-13359
 58. Sriram, S. R., Li, X., Ko, H. S., Chung, K. K., Wong, E., Lim, K. L., Dawson, V. L., and Dawson, T. M. (2005) Familial-associated mutations differentially disrupt the solubility, localization, binding and ubiquitination properties of parkin. *Hum Mol Genet* 14 (17), 2571-2586
 59. Olanow, C. W., and McNaught, K. S. (2006) Ubiquitin-proteasome system and Parkinson's disease. *Mov Disord* 21 (11), 1806-1823
 60. West, A. B., Dawson, V. L., and Dawson, T. M. (2007) The role of PARKIN in Parkinson's disease. In: Dawson, T. M. (ed.) *Parkinson's disease: genetics and pathogenesis*, vol., 199-218, Informa Healthcare USA, Inc., New York
 61. Greene, J. C., Whitworth, A. J., Kuo, I., Andrews, L. A., Feany, M. B., and Pallanck, L. J. (2003) Mitochondrial pathology and apoptotic muscle degeneration in Drosophila parkin mutants. *Proc Natl Acad Sci U S A* 100 (7), 4078-4083
 62. Palacino, J. J., Sagi, D., Goldberg, M. S., Krauss, S., Motz, C., Wacker, M., Klose, J., and Shen, J. (2004) Mitochondrial dysfunction and oxidative damage in parkin-deficient mice. *J Biol Chem* 279 (18), 18614-18622
 63. Pesah, Y., Pham, T., Burgess, H., Middlebrooks, B., Verstreken, P., Zhou, Y., Harding, M., Bellen, H., and Mardon, G. (2004) Drosophila parkin mutants have decreased mass and cell size and increased sensitivity to oxygen radical stress. *Development* 131 (9), 2183-2194
 64. Kuroda, Y., Mitsui, T., Kunishige, M., Shono, M., Akaike, M., Azuma, H., and Matsumoto, T. (2006) Parkin enhances mitochondrial biogenesis in proliferating cells. *Hum Mol Genet* 15 (6), 883-895
 65. Tanaka, A. (2010) Parkin-mediated selective mitochondrial autophagy, mitophagy: Parkin purges damaged organelles from the vital mitochondrial network. *FEBS Lett* 584 (7), 1386-1392
 66. Olzmann, J. A., and Chin, L. S. (2008) Parkin-mediated K63-linked polyubiquitination: a signal for targeting misfolded proteins to the aggresome-autophagy pathway. *Autophagy* 4 (1), 85-87
 67. Banerjee, R., Starkov, A. A., Beal, M. F., and Thomas, B. (2009) Mitochondrial dysfunction in the limelight of Parkinson's disease pathogenesis. *Biochim Biophys Acta* 1792 (7), 651-663
 68. LaVoie, M. J., Ostaszewski, B. L., Weihofen, A., Schlossmacher, M. G., and Selkoe, D. J. (2005) Dopamine covalently modifies and functionally inactivates parkin. *Nat Med* 11 (11), 1214-1221
 69. Kubo, S., Hattori, N., and Mizuno, Y. (2006) Recessive Parkinson's disease. *Mov Disord* 21 (7), 885-893
 70. Silvestri, L., Caputo, V., Bellacchio, E., Atorino, L., Dallapiccola, B., Valente, E. M., and Casari, G. (2005) Mitochondrial import and enzymatic activity of PINK1 mutants associated to recessive parkinsonism. *Hum Mol Genet* 14 (22), 3477-3492
 71. Valente, E. M., Abou-Sleiman, P. M., Caputo, V., Muqit, M. M., Harvey, K., Gispert, S., Ali, Z., Del Turco, D., Bentivoglio, A. R., Healy, D. G., Albanese, A., Nussbaum, R., Gonzalez-Maldonado, R., Deller, T., Salvi, S., Cortelli, P., Gilks, W. P., Latchman, D. S., Harvey, R. J., Dallapiccola, B., Auburger, G., and Wood, N. W. (2004) Hereditary early-onset Parkinson's disease caused by mutations in PINK1. *Science* 304 (5674), 1158-1160
 72. Sim, C. H., Lio, D. S., Mok, S. S., Masters, C. L., Hill, A. F., Culvenor, J. G., and Cheng, H. C. (2006) C-terminal truncation and Parkinson's disease-associated mutations down-regulate the protein serine/threonine kinase activity of PTEN-induced kinase-1. *Hum Mol Genet* 15 (21), 3251-3262
 73. Vila, M., Ramonet, D., and Perier, C. (2008) Mitochondrial alterations in Parkinson's disease: new

- clues. *J Neurochem* 107 (2), 317-328
74. Xiong, H., Wang, D., Chen, L., Choo, Y. S., Ma, H., Tang, C., Xia, K., Jiang, W., Ronai, Z., Zhuang, X., and Zhang, Z. (2009) Parkin, PINK1, and DJ-1 form a ubiquitin E3 ligase complex promoting unfolded protein degradation. *J Clin Invest* 119 (3), 650-660
75. Abou-Sleiman, P. M., Muqit, M. M., and Wood, N. W. (2006) Expanding insights of mitochondrial dysfunction in Parkinson's disease. *Nat Rev Neurosci* 7 (3), 207-219
76. Tao, X., and Tong, L. (2003) Crystal structure of human DJ-1, a protein associated with early onset Parkinson's disease. *J Biol Chem* 278 (33), 31372-31379
77. Canet-Aviles, R. M., Wilson, M. A., Miller, D. W., Ahmad, R., McLendon, C., Bandyopadhyay, S., Baptista, M. J., Ringe, D., Petsko, G. A., and Cookson, M. R. (2004) The Parkinson's disease protein DJ-1 is neuroprotective due to cysteine-sulfinic acid-driven mitochondrial localization. *Proc Natl Acad Sci U S A* 101 (24), 9103-9108
78. Mitsumoto, A., and Nakagawa, Y. (2001) DJ-1 is an indicator for endogenous reactive oxygen species elicited by endotoxin. *Free Radic Res* 35 (6), 885-893
79. Andres-Mateos, E., Perier, C., Zhang, L., Blanchard-Fillion, B., Greco, T. M., Thomas, B., Ko, H. S., Sasaki, M., Ischiropoulos, H., Przedborski, S., Dawson, T. M., and Dawson, V. L. (2007) DJ-1 gene deletion reveals that DJ-1 is an atypical peroxiredoxin-like peroxidase. *Proc Natl Acad Sci U S A* 104 (37), 14807-14812
80. Taira, T., Saito, Y., Niki, T., Iguchi-Ariga, S. M., Takahashi, K., and Ariga, H. (2004) DJ-1 has a role in antioxidative stress to prevent cell death. *EMBO Rep* 5 (2), 213-218
81. Kim, R. H., Peters, M., Jang, Y., Shi, W., Pintilie, M., Fletcher, G. C., DeLuca, C., Liepa, J., Zhou, L., Snow, B., Binari, R. C., Manoukian, A. S., Bray, M. R., Liu, F. F., Tsao, M. S., and Mak, T. W. (2005) DJ-1, a novel regulator of the tumor suppressor PTEN. *Cancer Cell* 7 (3), 263-273
82. Lev, N., Ickowicz, D., Melamed, E., and Offen, D. (2008) Oxidative insults induce DJ-1 upregulation and redistribution: implications for neuroprotection. *Neurotoxicology* 29 (3), 397-405
83. Shendelman, S., Jonason, A., Martinat, C., Leete, T., and Abeliovich, A. (2004) DJ-1 is a redox-dependent molecular chaperone that inhibits alpha-synuclein aggregate formation. *PLoS Biol* 2 (11), e362
84. Zhou, W., Zhu, M., Wilson, M. A., Petsko, G. A., and Fink, A. L. (2006) The oxidation state of DJ-1 regulates its chaperone activity toward alpha-synuclein. *J Mol Biol* 356 (4), 1036-1048
85. Leroy, E., Boyer, R., Auburger, G., Leube, B., Ulm, G., Mezey, E., Harta, G., Brownstein, M. J., Jonnalagada, S., Chernova, T., Dehejia, A., Lavedan, C., Gasser, T., Steinbach, P. J., Wilkinson, K. D., and Polymeropoulos, M. H. (1998) The ubiquitin pathway in Parkinson's disease. *Nature* 395 (6701), 451-452
86. Healy, D. G., Abou-Sleiman, P. M., and Wood, N. W. (2004) Genetic causes of Parkinson's disease: UCHL-1. *Cell Tissue Res* 318 (1), 189-194
87. Saigoh, K., Wang, Y. L., Suh, J. G., Yamanishi, T., Sakai, Y., Kiyosawa, H., Harada, T., Ichihara, N., Wakana, S., Kikuchi, T., and Wada, K. (1999) Intragenic deletion in the gene encoding ubiquitin carboxy-terminal hydrolase in gad mice. *Nat Genet* 23 (1), 47-51
88. Maraganore, D. M., Farrer, M. J., Hardy, J. A., Lincoln, S. J., McDonnell, S. K., and Rocca, W. A. (1999) Case-control study of the ubiquitin carboxy-terminal hydrolase L1 gene in Parkinson's disease. *Neurology* 53 (8), 1858-1860
89. Tan, E. K., Puong, K. Y., Fook-Chong, S., Chua, E., Shen, H., Yuen, Y., Pavanni, R., Wong, M. C., Puvan, K., and Zhao, Y. (2006) Case-control study of UCHL1 S18Y variant in Parkinson's disease. *Mov Disord* 21 (10), 1765-1768
90. Liu, Y., Fallon, L., Lashuel, H. A., Liu, Z., and Lansbury, P. T., Jr. (2002) The UCH-L1 gene encodes two opposing enzymatic activities that affect alpha-synuclein degradation and Parkinson's disease susceptibility. *Cell* 111 (2), 209-218
91. Nishikawa, K., Li, H., Kawamura, R., Osaka, H., Wang, Y. L., Hara, Y., Hirokawa, T., Manago, Y., Amano, T., Noda, M., Aoki, S., and Wada, K. (2003) Alterations of structure and hydrolase activity of parkinsonism-associated human ubiquitin carboxyl-terminal hydrolase L1 variants. *Biochem Biophys Res Commun* 304 (1), 176-183
92. Strauss, K. M., Martins, L. M., Plun-Favreau, H., Marx, F. P., Kautzmann, S., Berg, D., Gasser, T., Wszolek, Z., Muller, T., Bornemann, A., Wolburg, H., Downward, J., Riess, O., Schulz, J. B., and Kruger, R. (2005) Loss of function mutations in the gene encoding Omi/HtrA2 in Parkinson's disease. *Hum Mol Genet* 14 (15), 2099-2111
93. Lautier, C., Goldwurm, S., Durr, A., Giovannone, B., Tsiaras, W. G., Pezzoli, G., Brice, A., and Smith, R. J. (2008) Mutations in the GIGYF2 (TNRC15) gene at the PARK11 locus in familial Parkinson disease. *Am J Hum Genet* 82 (4), 822-833
94. Plun-Favreau, H., Klupsch, K., Moiso, N., Gandhi, S., Kjaer, S., Frith, D., Harvey, K., Deas, E., Harvey, R. J., McDonald, N., Wood, N. W., Martins, L. M., and Downward, J. (2007) The mitochondrial protease HtrA2 is regulated by Parkinson's disease-associated kinase PINK1. *Nat Cell Biol* 9 (11), 1243-1252

95. Park, H. M., Kim, G. Y., Nam, M. K., Seong, G. H., Han, C., Chung, K. C., Kang, S., and Rhim, H. (2009) The serine protease HtrA2/Omi cleaves Parkin and irreversibly inactivates its E3 ubiquitin ligase activity. *Biochem Biophys Res Commun* 387 (3), 537-542
96. Paisan-Ruiz, C., Bhatia, K. P., Li, A., Hernandez, D., Davis, M., Wood, N. W., Hardy, J., Houlden, H., Singleton, A., and Schneider, S. A. (2009) Characterization of PLA2G6 as a locus for dystonia-parkinsonism. *Ann Neurol* 65 (1), 19-23
97. Di Fonzo, A., Dekker, M. C., Montagna, P., Baruzzi, A., Yonova, E. H., Correia Guedes, L., Szczerbinska, A., Zhao, T., Dubbel-Hulsman, L. O., Wouters, C. H., de Graaff, E., Oyen, W. J., Simons, E. J., Breedveld, G. J., Oostra, B. A., Horstink, M. W., and Bonifati, V. (2009) FBXO7 mutations cause autosomal recessive, early-onset parkinsonian-pyramidal syndrome. *Neurology* 72 (3), 240-245
98. Laman, H. (2006) Fbxo7 gets proactive with cyclin D/cdk6. *Cell Cycle* 5 (3), 279-282
99. Goldberg, A. L. (2003) Protein degradation and protection against misfolded or damaged proteins. *Nature* 426 (6968), 895-899
100. Jung, T., Catalgol, B., and Grune, T. (2009) The proteasomal system. *Mol Aspects Med* 30 (4), 191-296
101. Sherman, M. Y., and Goldberg, A. L. (2001) Cellular defenses against unfolded proteins: a cell biologist thinks about neurodegenerative diseases. *Neuron* 29 (1), 15-32
102. Glickman, M. H., and Ciechanover, A. (2002) The ubiquitin-proteasome proteolytic pathway: destruction for the sake of construction. *Physiol Rev* 82 (2), 373-428
103. Bennett, M. C., Bishop, J. F., Leng, Y., Chock, P. B., Chase, T. N., and Mouradian, M. M. (1999) Degradation of alpha-synuclein by proteasome. *J Biol Chem* 274 (48), 33855-33858
104. Chen, L., Thiruchelvam, M. J., Madura, K., and Richfield, E. K. (2006) Proteasome dysfunction in aged human alpha-synuclein transgenic mice. *Neurobiol Dis* 23 (1), 120-126
105. Lindersson, E., Beedholm, R., Hojrup, P., Moos, T., Gai, W., Hendil, K. B., and Jensen, P. H. (2004) Proteasomal inhibition by alpha-synuclein filaments and oligomers. *J Biol Chem* 279 (13), 12924-12934
106. Snyder, H., Mensah, K., Theisler, C., Lee, J., Matouschek, A., and Wolozin, B. (2003) Aggregated and monomeric alpha-synuclein bind to the S6' proteasomal protein and inhibit proteasomal function. *J Biol Chem* 278 (14), 11753-11759
107. Stefanis, L., Larsen, K. E., Rideout, H. J., Sulzer, D., and Greene, L. A. (2001) Expression of A53T mutant but not wild-type alpha-synuclein in PC12 cells induces alterations of the ubiquitin-dependent degradation system, loss of dopamine release, and autophagic cell death. *J Neurosci* 21 (24), 9549-9560
108. McNaught, K. S., Belizaire, R., Isacson, O., Jenner, P., and Olanow, C. W. (2003) Altered proteasomal function in sporadic Parkinson's disease. *Exp Neurol* 179 (1), 38-46
109. Zeng, B. Y., Medhurst, A. D., Jackson, M., Rose, S., and Jenner, P. (2005) Proteasomal activity in brain differs between species and brain regions and changes with age. *Mech Ageing Dev* 126 (6-7), 760-766
110. Floor, E., and Wetzel, M. G. (1998) Increased protein oxidation in human substantia nigra pars compacta in comparison with basal ganglia and prefrontal cortex measured with an improved dinitrophenylhydrazine assay. *J Neurochem* 70 (1), 268-275
111. Kikuchi, S., Shinpo, K., Tsuji, S., Takeuchi, M., Yamagishi, S., Makita, Z., Niino, M., Yabe, I., and Tashiro, K. (2003) Effect of proteasome inhibitor on cultured mesencephalic dopaminergic neurons. *Brain Res* 964 (2), 228-236
112. Li, Z., Jansen, M., Pierre, S. R., and Figueiredo-Pereira, M. E. (2003) Neurodegeneration: linking ubiquitin/proteasome pathway impairment with inflammation. *Int J Biochem Cell Biol* 35 (5), 547-552
113. Jesenberger, V., and Jentsch, S. (2002) Deadly encounter: ubiquitin meets apoptosis. *Nat Rev Mol Cell Biol* 3 (2), 112-121
114. Kroemer, G., Galluzzi, L., and Brenner, C. (2007) Mitochondrial membrane permeabilization in cell death. *Physiol Rev* 87 (1), 99-163
115. van Loo, G., Saelens, X., van Gurp, M., MacFarlane, M., Martin, S. J., and Vandenabeele, P. (2002) The role of mitochondrial factors in apoptosis: a Russian roulette with more than one bullet. *Cell Death Differ* 9 (10), 1031-1042
116. Turrens, J. F. (2003) Mitochondrial formation of reactive oxygen species. *J Physiol* 552 (Pt 2), 335-344
117. Miyazaki, I., and Asanuma, M. (2008) Dopaminergic neuron-specific oxidative stress caused by dopamine itself. *Acta Med Okayama* 62 (3), 141-150
118. Jenner, P., Dexter, D. T., Sian, J., Schapira, A. H., and Marsden, C. D. (1992) Oxidative stress as a cause of nigral cell death in Parkinson's disease and incidental Lewy body disease. The Royal Kings and Queens Parkinson's Disease Research Group. *Ann Neurol* 32 Suppl, S82-87
119. Devi, L., Raghavendran, V., Prabhu, B. M., Avadhani, N. G., and Anandatheerthavarada, H. K.

- (2008) Mitochondrial import and accumulation of alpha-synuclein impair complex I in human dopaminergic neuronal cultures and Parkinson disease brain. *J Biol Chem* 283 (14), 9089-9100
120. Lee, H. J., Shin, S. Y., Choi, C., Lee, Y. H., and Lee, S. J. (2002) Formation and removal of alpha-synuclein aggregates in cells exposed to mitochondrial inhibitors. *J Biol Chem* 277 (7), 5411-5417
121. Parihar, M. S., Parihar, A., Fujita, M., Hashimoto, M., and Ghafourifar, P. (2008) Mitochondrial association of alpha-synuclein causes oxidative stress. *Cell Mol Life Sci* 65 (7-8), 1272-1284
122. Volles, M. J., Lee, S. J., Rochet, J. C., Shtilerman, M. D., Ding, T. T., Kessler, J. C., and Lansbury, P. T., Jr. (2001) Vesicle permeabilization by protofibrillar alpha-synuclein: implications for the pathogenesis and treatment of Parkinson's disease. *Biochemistry* 40 (26), 7812-7819
123. Sullivan, P. G., Dragicevic, N. B., Deng, J. H., Bai, Y., Dimayuga, E., Ding, Q., Chen, Q., Bruce-Keller, A. J., and Keller, J. N. (2004) Proteasome inhibition alters neural mitochondrial homeostasis and mitochondria turnover. *J Biol Chem* 279 (20), 20699-20707
124. Hoglinger, G. U., Carrard, G., Michel, P. P., Medja, F., Lombes, A., Ruberg, M., Friguet, B., and Hirsch, E. C. (2003) Dysfunction of mitochondrial complex I and the proteasome: interactions between two biochemical deficits in a cellular model of Parkinson's disease. *J Neurochem* 86 (5), 1297-1307
125. Bogaerts, V., Theuns, J., and van Broeckhoven, C. (2008) Genetic findings in Parkinson's disease and translation into treatment: a leading role for mitochondria? *Genes Brain Behav* 7 (2), 129-151
126. Yao, Z., and Wood, N. W. (2009) Cell death pathways in Parkinson's disease: role of mitochondria. *Antioxid Redox Signal* 11 (9), 2135-2149
127. Cook, C., and Petrucelli, L. (2009) A critical evaluation of the ubiquitin-proteasome system in Parkinson's disease. *Biochim Biophys Acta* 1792 (7), 664-675
128. Gandhi, P. N., Chen, S. G., and Wilson-Delfosse, A. L. (2009) Leucine-rich repeat kinase 2 (LRRK2): a key player in the pathogenesis of Parkinson's disease. *J Neurosci Res* 87 (6), 1283-1295
129. Funayama, M., Hasegawa, K., Kowa, H., Saito, M., Tsuji, S., and Obata, F. (2002) A new locus for Parkinson's disease (PARK8) maps to chromosome 12p11.2-q13.1. *Ann Neurol* 51 (3), 296-301
130. Paisan-Ruiz, C., Jain, S., Evans, E. W., Gilks, W. P., Simon, J., van der Brug, M., Lopez de Munain, A., Aparicio, S., Gil, A. M., Khan, N., Johnson, J., Martinez, J. R., Nicholl, D., Carrera, I. M., Pena, A. S., de Silva, R., Lees, A., Marti-Masso, J. F., Perez-Tur, J., Wood, N. W., and Singleton, A. B. (2004) Cloning of the gene containing mutations that cause PARK8-linked Parkinson's disease. *Neuron* 44 (4), 595-600
131. Zimprich, A., Biskup, S., Leitner, P., Lichtner, P., Farrer, M., Lincoln, S., Kachergus, J., Hulihan, M., Uitti, R. J., Calne, D. B., Stoessl, A. J., Pfeiffer, R. F., Patenge, N., Carbajal, I. C., Vieregge, P., Asmus, F., Muller-Myhsok, B., Dickson, D. W., Meitinger, T., Strom, T. M., Wszolek, Z. K., and Gasser, T. (2004) Mutations in LRRK2 cause autosomal-dominant parkinsonism with pleomorphic pathology. *Neuron* 44 (4), 601-607
132. <http://www.molgen.ua.ac.be/PDmutDB/>
133. Paisan-Ruiz, C. (2009) LRRK2 gene variation and its contribution to Parkinson disease. *Hum Mutat* 30 (8), 1153-1160
134. Haugarvoll, K., and Wszolek, Z. K. (2009) Clinical features of LRRK2 parkinsonism. *Parkinsonism Relat Disord* 15 Suppl 3, S205-208
135. Ross, O. A., Spanaki, C., Griffith, A., Lin, C. H., Kachergus, J., Haugarvoll, K., Latsoudis, H., Plaitakis, A., Ferreira, J. J., Sampaio, C., Bonifati, V., Wu, R. M., Zabetian, C. P., and Farrer, M. J. (2009) Haplotype analysis of Lrrk2 R1441H carriers with parkinsonism. *Parkinsonism Relat Disord* 15 (6), 466-467
136. Kumari, U., and Tan, E. K. (2009) LRRK2 in Parkinson's disease: genetic and clinical studies from patients. *FEBS J* 276 (22), 6455-6463
137. Healy, D. G., Falchi, M., O'Sullivan, S. S., Bonifati, V., Durr, A., Bressman, S., Brice, A., Aasly, J., Zabetian, C. P., Goldwurm, S., Ferreira, J. J., Tolosa, E., Kay, D. M., Klein, C., Williams, D. R., Marras, C., Lang, A. E., Wszolek, Z. K., Berciano, J., Schapira, A. H., Lynch, T., Bhatia, K. P., Gasser, T., Lees, A. J., and Wood, N. W. (2008) Phenotype, genotype, and worldwide genetic penetrance of LRRK2-associated Parkinson's disease: a case-control study. *Lancet Neurol* 7 (7), 583-590
138. Lesage, S., Patin, E., Condroyer, C., Leutenegger, A. L., Lohmann, E., Giladi, N., Bar-Shira, A., Belarbi, S., Hecham, N., Pollak, P., Ouvrard-Hernandez, A. M., Bardien, S., Carr, J., Benhassine, T., Tomiyama, H., Pirkevi, C., Hamadouche, T., Cazeneuve, C., Basak, A. N., Hattori, N., Durr, A., Tazir, M., Orr-Urtreger, A., Quintana-Murci, L., and Brice, A. (2010) Parkinson's disease-related LRRK2 G2019S mutation results from independent mutational events in humans. *Hum Mol Genet* 19 (10), 1998-2004

139. Tan, E. K., Shen, H., Tan, L. C., Farrer, M., Yew, K., Chua, E., Jamora, R. D., Puvan, K., Puong, K. Y., Zhao, Y., Pavanni, R., Wong, M. C., Yih, Y., Skipper, L., and Liu, J. J. (2005) The G2019S LRRK2 mutation is uncommon in an Asian cohort of Parkinson's disease patients. *Neurosci Lett* 384 (3), 327-329
140. Kachergus, J., Mata, I. F., Hulihan, M., Taylor, J. P., Lincoln, S., Aasly, J., Gibson, J. M., Ross, O. A., Lynch, T., Wiley, J., Payami, H., Nutt, J., Maraganore, D. M., Czystewski, K., Styczynska, M., Wszolek, Z. K., Farrer, M. J., and Toft, M. (2005) Identification of a novel LRRK2 mutation linked to autosomal dominant parkinsonism: evidence of a common founder across European populations. *Am J Hum Genet* 76 (4), 672-680
141. Zabetian, C. P., Hutter, C. M., Yearout, D., Lopez, A. N., Factor, S. A., Griffith, A., Leis, B. C., Bird, T. D., Nutt, J. G., Higgins, D. S., Roberts, J. W., Kay, D. M., Edwards, K. L., Samii, A., and Payami, H. (2006) LRRK2 G2019S in families with Parkinson disease who originated from Europe and the Middle East: evidence of two distinct founding events beginning two millennia ago. *Am J Hum Genet* 79 (4), 752-758
142. Haugarvoll, K., Rademakers, R., Kachergus, J. M., Nuytemans, K., Ross, O. A., Gibson, J. M., Tan, E. K., Gaig, C., Tolosa, E., Goldwurm, S., Guidi, M., Riboldazzi, G., Brown, L., Walter, U., Benecke, R., Berg, D., Gasser, T., Theuns, J., Pals, P., Cras, P., De Deyn, P. P., Engelborghs, S., Pickut, B., Uitti, R. J., Foroud, T., Nichols, W. C., Hagenah, J., Klein, C., Samii, A., Zabetian, C. P., Bonifati, V., Van Broeckhoven, C., Farrer, M. J., and Wszolek, Z. K. (2008) Lrrk2 R1441C parkinsonism is clinically similar to sporadic Parkinson disease. *Neurology* 70 (16 Pt 2), 1456-1460
143. Wider, C., Dickson, D. W., and Wszolek, Z. K. (2010) Leucine-rich repeat kinase 2 gene-associated disease: redefining genotype-phenotype correlation. *Neurodegener Dis* 7 (1-3), 175-179
144. Giasson, B. I., and Van Deerlin, V. M. (2008) Mutations in LRRK2 as a cause of Parkinson's disease. *Neurosignals* 16 (1), 99-105
145. Higashi, S., Biskup, S., West, A. B., Trinkaus, D., Dawson, V. L., Faull, R. L., Waldvogel, H. J., Arai, H., Dawson, T. M., Moore, D. J., and Emson, P. C. (2007) Localization of Parkinson's disease-associated LRRK2 in normal and pathological human brain. *Brain Res* 1155, 208-219
146. Biskup, S., Moore, D. J., Celsi, F., Higashi, S., West, A. B., Andrabi, S. A., Kurkinen, K., Yu, S. W., Savitt, J. M., Waldvogel, H. J., Faull, R. L., Emson, P. C., Torp, R., Ottersen, O. P., Dawson, T. M., and Dawson, V. L. (2006) Localization of LRRK2 to membranous and vesicular structures in mammalian brain. *Ann Neurol* 60 (5), 557-569
147. Galter, D., Westerlund, M., Carmine, A., Lindqvist, E., Sydow, O., and Olson, L. (2006) LRRK2 expression linked to dopamine-innervated areas. *Ann Neurol* 59 (4), 714-719
148. Higashi, S., Moore, D. J., Colebrooke, R. E., Biskup, S., Dawson, V. L., Arai, H., Dawson, T. M., and Emson, P. C. (2007) Expression and localization of Parkinson's disease-associated leucine-rich repeat kinase 2 in the mouse brain. *J Neurochem* 100 (2), 368-381
149. Melrose, H., Lincoln, S., Tyndall, G., Dickson, D., and Farrer, M. (2006) Anatomical localization of leucine-rich repeat kinase 2 in mouse brain. *Neuroscience* 139 (3), 791-794
150. Simon-Sanchez, J., Herranz-Perez, V., Olucha-Bordonau, F., and Perez-Tur, J. (2006) LRRK2 is expressed in areas affected by Parkinson's disease in the adult mouse brain. *Eur J Neurosci* 23 (3), 659-666
151. Taymans, J. M., Van den Haute, C., and Baekelandt, V. (2006) Distribution of PINK1 and LRRK2 in rat and mouse brain. *J Neurochem* 98 (3), 951-961
152. Han, B. S., Iacovitti, L., Katano, T., Hattori, N., Seol, W., and Kim, K. S. (2008) Expression of the LRRK2 gene in the midbrain dopaminergic neurons of the substantia nigra. *Neurosci Lett* 442 (3), 190-194
153. Zechel, S., Meinhardt, A., Unsicker, K., and von Bohlen Und Halbach, O. (2010) Expression of leucine-rich-repeat-kinase 2 (LRRK2) during embryonic development. *Int J Dev Neurosci* 28 (5), 391-399
154. Biskup, S., Moore, D. J., Rea, A., Lorenz-Deperieux, B., Coombes, C. E., Dawson, V. L., Dawson, T. M., and West, A. B. (2007) Dynamic and redundant regulation of LRRK2 and LRRK1 expression. *BMC Neurosci* 8, 102
155. Hatano, T., Kubo, S., Imai, S., Maeda, M., Ishikawa, K., Mizuno, Y., and Hattori, N. (2007) Leucine-rich repeat kinase 2 associates with lipid rafts. *Hum Mol Genet* 16 (6), 678-690
156. Gloeckner, C. J., Kinkl, N., Schumacher, A., Braun, R. J., O'Neill, E., Meitinger, T., Kolch, W., Prokisch, H., and Ueffing, M. (2006) The Parkinson disease causing LRRK2 mutation I2020T is associated with increased kinase activity. *Hum Mol Genet* 15 (2), 223-232
157. West, A. B., Moore, D. J., Biskup, S., Bugayenko, A., Smith, W. W., Ross, C. A., Dawson, V. L., and Dawson, T. M. (2005) Parkinson's disease-associated mutations in leucine-rich repeat kinase 2 augment kinase activity. *Proc Natl Acad Sci U S A* 102 (46), 16842-16847
158. Alegre-Abarrategui, J., Christian, H., Lufino, M., Mutihac, R., Lourenco Venda, L., Ansorge, O.,

- and Wade-Martins, R. (2009) LRRK2 regulates autophagic activity and localises to specific membrane microdomains in a novel human genomic reporter cellular model. *Hum Mol Genet* 18 (21), 4022-4034
159. Brown, D. A., and London, E. (1998) Functions of lipid rafts in biological membranes. *Annu Rev Cell Dev Biol* 14, 111-136
160. Maxfield, F. R. (2002) Plasma membrane microdomains. *Curr Opin Cell Biol* 14 (4), 483-487
161. Parton, R. G., and Simons, K. (2007) The multiple faces of caveolae. *Nat Rev Mol Cell Biol* 8 (3), 185-194
162. Bosgraaf, L., and Van Haastert, P. J. (2003) Roc, a Ras/GTPase domain in complex proteins. *Biochim Biophys Acta* 1643 (1-3), 5-10
163. Marin, I. (2006) The Parkinson disease gene LRRK2: evolutionary and structural insights. *Mol Biol Evol* 23 (12), 2423-2433
164. Mata, I. F., Wedemeyer, W. J., Farrer, M. J., Taylor, J. P., and Gallo, K. A. (2006) LRRK2 in Parkinson's disease: protein domains and functional insights. *Trends Neurosci* 29 (5), 286-293
165. Marin, I. (2008) Ancient origin of the Parkinson disease gene LRRK2. *J Mol Evol* 67 (1), 41-50
166. Groves, M. R., and Barford, D. (1999) Topological characteristics of helical repeat proteins. *Curr Opin Struct Biol* 9 (3), 383-389
167. Li, J., Mahajan, A., and Tsai, M. D. (2006) Ankyrin repeat: a unique motif mediating protein-protein interactions. *Biochemistry* 45 (51), 15168-15178
168. Kobe, B., and Kajava, A. V. (2001) The leucine-rich repeat as a protein recognition motif. *Curr Opin Struct Biol* 11 (6), 725-732
169. Li, D., and Roberts, R. (2001) WD-repeat proteins: structure characteristics, biological function, and their involvement in human diseases. *Cell Mol Life Sci* 58 (14), 2085-2097
170. West, A. B., Moore, D. J., Choi, C., Andrabi, S. A., Li, X., Dikeman, D., Biskup, S., Zhang, Z., Lim, K. L., Dawson, V. L., and Dawson, T. M. (2007) Parkinson's disease-associated mutations in LRRK2 link enhanced GTP-binding and kinase activities to neuronal toxicity. *Hum Mol Genet* 16 (2), 223-232
171. Manning, G., Whyte, D. B., Martinez, R., Hunter, T., and Sudarsanam, S. (2002) The protein kinase complement of the human genome. *Science* 298 (5600), 1912-1934
172. Biskup, S., and West, A. B. (2009) Zeroing in on LRRK2-linked pathogenic mechanisms in Parkinson's disease. *Biochim Biophys Acta* 1792 (7), 625-633
173. Gloeckner, C. J., Boldt, K., von Zweydford, F., Helm, S., Wiesent, L., Sarioglu, H., and Ueffing, M. (2010) Phosphopeptide analysis reveals two discrete clusters of phosphorylation in the N-terminus and the Roc domain of the Parkinson-disease associated protein kinase LRRK2. *J Proteome Res* 9 (4), 1738-1745
174. Greggio, E., Taymans, J. M., Zhen, E. Y., Ryder, J., Vancaenenbroeck, R., Beilina, A., Sun, P., Deng, J., Jaffe, H., Baekelandt, V., Merchant, K., and Cookson, M. R. (2009) The Parkinson's disease kinase LRRK2 autophosphorylates its GTPase domain at multiple sites. *Biochem Biophys Res Commun* 389 (3), 449-454
175. Kamikawaji, S., Ito, G., and Iwatsubo, T. (2009) Identification of the autophosphorylation sites of LRRK2. *Biochemistry* 48 (46), 10963-10975
176. Qi, M., and Elion, E. A. (2005) MAP kinase pathways. *J Cell Sci* 118 (Pt 16), 3569-3572
177. Stenmark, H., and Olkkonen, V. M. (2001) The Rab GTPase family. *Genome Biol* 2 (5), REVIEWS3007
178. Lesage, S., Condroyer, C., Lannuzel, A., Lohmann, E., Troiano, A., Tison, F., Damier, P., Thobois, S., Ouvrard-Hernandez, A. M., Rivaud-Pechoux, S., Brefel-Courbon, C., Destee, A., Tranchant, C., Romana, M., Leclere, L., Durr, A., and Brice, A. (2009) Molecular analyses of the LRRK2 gene in European and North African autosomal dominant Parkinson's disease. *J Med Genet* 46 (7), 458-464
179. Smith, W. W., Pei, Z., Jiang, H., Dawson, V. L., Dawson, T. M., and Ross, C. A. (2006) Kinase activity of mutant LRRK2 mediates neuronal toxicity. *Nat Neurosci* 9 (10), 1231-1233
180. Anand, V. S., and Braithwaite, S. P. (2009) LRRK2 in Parkinson's disease: biochemical functions. *FEBS J* 276 (22), 6428-6435
181. Gloeckner, C. J., Schumacher, A., Boldt, K., and Ueffing, M. (2009) The Parkinson disease-associated protein kinase LRRK2 exhibits MAPKKK activity and phosphorylates MKK3/6 and MKK4/7, in vitro. *J Neurochem* 109 (4), 959-968
182. Li, X., Tan, Y. C., Poulouse, S., Olanow, C. W., Huang, X. Y., and Yue, Z. (2007) Leucine-rich repeat kinase 2 (LRRK2)/PARK8 possesses GTPase activity that is altered in familial Parkinson's disease R1441C/G mutants. *J Neurochem* 103 (1), 238-247
183. Greggio, E., and Cookson, M. R. (2009) Leucine-rich repeat kinase 2 mutations and Parkinson's disease: three questions. *ASN Neuro* 1 (1)
184. Imai, Y., Gehrke, S., Wang, H. Q., Takahashi, R., Hasegawa, K., Oota, E., and Lu, B. (2008) Phosphorylation of 4E-BP by LRRK2 affects the maintenance of dopaminergic neurons in

- Drosophila. *EMBO J* 27 (18), 2432-2443
185. Anand, V. S., Reichling, L. J., Lipinski, K., Stochaj, W., Duan, W., Kelleher, K., Pungaliya, P., Brown, E. L., Reinhart, P. H., Somberg, R., Hirst, W. D., Riddle, S. M., and Braithwaite, S. P. (2009) Investigation of leucine-rich repeat kinase 2 : enzymological properties and novel assays. *FEBS J* 276 (2), 466-478
 186. Luzon-Toro, B., Rubio de la Torre, E., Delgado, A., Perez-Tur, J., and Hilfiker, S. (2007) Mechanistic insight into the dominant mode of the Parkinson's disease-associated G2019S LRRK2 mutation. *Hum Mol Genet* 16 (17), 2031-2039
 187. Jaleel, M., Nichols, R. J., Deak, M., Campbell, D. G., Gillardon, F., Knebel, A., and Alessi, D. R. (2007) LRRK2 phosphorylates moesin at threonine-558: characterization of how Parkinson's disease mutants affect kinase activity. *Biochem J* 405 (2), 307-317
 188. Seol, W. (2010) Biochemical and molecular features of LRRK2 and its pathophysiological roles in Parkinson's disease. *BMB Rep* 43 (4), 233-244
 189. Greggio, E., Jain, S., Kingsbury, A., Bandopadhyay, R., Lewis, P., Kaganovich, A., van der Brug, M. P., Beilina, A., Blackinton, J., Thomas, K. J., Ahmad, R., Miller, D. W., Kesavapany, S., Singleton, A., Lees, A., Harvey, R. J., Harvey, K., and Cookson, M. R. (2006) Kinase activity is required for the toxic effects of mutant LRRK2/dardarin. *Neurobiol Dis* 23 (2), 329-341
 190. Heo, H. Y., Park, J. M., Kim, C. H., Han, B. S., Kim, K. S., and Seol, W. (2010) LRRK2 enhances oxidative stress-induced neurotoxicity via its kinase activity. *Exp Cell Res* 316 (4), 649-656
 191. Liou, A. K., Leak, R. K., Li, L., and Zigmond, M. J. (2008) Wild-type LRRK2 but not its mutant attenuates stress-induced cell death via ERK pathway. *Neurobiol Dis* 32 (1), 116-124
 192. Guo, L., Gandhi, P. N., Wang, W., Petersen, R. B., Wilson-Delfosse, A. L., and Chen, S. G. (2007) The Parkinson's disease-associated protein, leucine-rich repeat kinase 2 (LRRK2), is an authentic GTPase that stimulates kinase activity. *Exp Cell Res* 313 (16), 3658-3670
 193. Ito, G., Okai, T., Fujino, G., Takeda, K., Ichijo, H., Katada, T., and Iwatsubo, T. (2007) GTP binding is essential to the protein kinase activity of LRRK2, a causative gene product for familial Parkinson's disease. *Biochemistry* 46 (5), 1380-1388
 194. Lewis, P. A., Greggio, E., Beilina, A., Jain, S., Baker, A., and Cookson, M. R. (2007) The R1441C mutation of LRRK2 disrupts GTP hydrolysis. *Biochem Biophys Res Commun* 357 (3), 668-671
 195. Haebig, K., Gloeckner, C. J., Miralles, M. G., Gillardon, F., Schulte, C., Riess, O., Ueffing, M., Biskup, S., and Bonin, M. (2010) ARHGEF7 (Beta-PIX) acts as guanine nucleotide exchange factor for leucine-rich repeat kinase 2. *PLoS One* 5 (10), e13762
 196. Gotthardt, K., Weyand, M., Kortholt, A., Van Haastert, P. J., and Wittinghofer, A. (2008) Structure of the Roc-COR domain tandem of *C. tepidum*, a prokaryotic homologue of the human LRRK2 Parkinson kinase. *EMBO J* 27 (16), 2239-2249
 197. Greggio, E., Zambrano, I., Kaganovich, A., Beilina, A., Taymans, J. M., Daniels, V., Lewis, P., Jain, S., Ding, J., Syed, A., Thomas, K. J., Baekelandt, V., and Cookson, M. R. (2008) The Parkinson disease-associated leucine-rich repeat kinase 2 (LRRK2) is a dimer that undergoes intramolecular autophosphorylation. *J Biol Chem* 283 (24), 16906-16914
 198. Klein, C. L., Rovelli, G., Springer, W., Schall, C., Gasser, T., and Kahle, P. J. (2009) Homo- and heterodimerization of ROCO kinases: LRRK2 kinase inhibition by the LRRK2 ROCO fragment. *J Neurochem* 111 (3), 703-715
 199. Sen, S., Webber, P. J., and West, A. B. (2009) Dependence of leucine-rich repeat kinase 2 (LRRK2) kinase activity on dimerization. *J Biol Chem* 284 (52), 36346-36356
 200. Deng, J., Lewis, P. A., Greggio, E., Sluch, E., Beilina, A., and Cookson, M. R. (2008) Structure of the ROC domain from the Parkinson's disease-associated leucine-rich repeat kinase 2 reveals a dimeric GTPase. *Proc Natl Acad Sci U S A* 105 (5), 1499-1504
 201. Komander, D., Garg, R., Wan, P. T., Ridley, A. J., and Barford, D. (2008) Mechanism of multi-site phosphorylation from a ROCK-I:RhoE complex structure. *EMBO J* 27 (23), 3175-3185
 202. Bretscher, A., Edwards, K., and Fehon, R. G. (2002) ERM proteins and merlin: integrators at the cell cortex. *Nat Rev Mol Cell Biol* 3 (8), 586-599
 203. Paglini, G., Kunda, P., Quiroga, S., Kosik, K., and Caceres, A. (1998) Suppression of radixin and moesin alters growth cone morphology, motility, and process formation in primary cultured neurons. *J Cell Biol* 143 (2), 443-455
 204. Parisiadou, L., Xie, C., Cho, H. J., Lin, X., Gu, X. L., Long, C. X., Lobbstaal, E., Baekelandt, V., Taymans, J. M., Sun, L., and Cai, H. (2009) Phosphorylation of ezrin/radixin/moesin proteins by LRRK2 promotes the rearrangement of actin cytoskeleton in neuronal morphogenesis. *J Neurosci* 29 (44), 13971-13980
 205. Gingras, A. C., Raught, B., and Sonenberg, N. (2001) Regulation of translation initiation by FRAP/mTOR. *Genes Dev* 15 (7), 807-826
 206. Teleman, A. A., Chen, Y. W., and Cohen, S. M. (2005) 4E-BP functions as a metabolic brake used under stress conditions but not during normal growth. *Genes Dev* 19 (16), 1844-1848
 207. Tettweiler, G., Miron, M., Jenkins, M., Sonenberg, N., and Lasko, P. F. (2005) Starvation and

- oxidative stress resistance in *Drosophila* are mediated through the eIF4E-binding protein, d4E-BP. *Genes Dev* 19 (16), 1840-1843
208. Yamaguchi, S., Ishihara, H., Yamada, T., Tamura, A., Usui, M., Tominaga, R., Munakata, Y., Satake, C., Katagiri, H., Tashiro, F., Aburatani, H., Tsukiyama-Kohara, K., Miyazaki, J., Sonenberg, N., and Oka, Y. (2008) ATF4-mediated induction of 4E-BP1 contributes to pancreatic beta cell survival under endoplasmic reticulum stress. *Cell Metab* 7 (3), 269-276
209. Kumar, A., Greggio, E., Beilina, A., Kaganovich, A., Chan, D., Taymans, J. M., Wolozin, B., and Cookson, M. R. (2010) The Parkinson's disease associated LRRK2 exhibits weaker in vitro phosphorylation of 4E-BP compared to autophosphorylation. *PLoS One* 5 (1), e8730
210. Hsu, C. H., Chan, D., Greggio, E., Saha, S., Guillily, M. D., Ferree, A., Raghavan, K., Shen, G. C., Segal, L., Ryu, H., Cookson, M. R., and Wolozin, B. (2010) MKK6 binds and regulates expression of Parkinson's disease-related protein LRRK2. *J Neurochem* 112 (6), 1593-1604
211. Garrington, T. P., and Johnson, G. L. (1999) Organization and regulation of mitogen-activated protein kinase signaling pathways. *Curr Opin Cell Biol* 11 (2), 211-218
212. Whitmarsh, A. J. (2006) The JIP family of MAPK scaffold proteins. *Biochem Soc Trans* 34 (Pt 5), 828-832
213. Hsu, C. H., Chan, D., and Wolozin, B. (2010) LRRK2 and the stress response: interaction with MKKs and JNK-interacting proteins. *Neurodegener Dis* 7 (1-3), 68-75
214. Lee, Y. J., Cho, H. N., Soh, J. W., Jhon, G. J., Cho, C. K., Chung, H. Y., Bae, S., Lee, S. J., and Lee, Y. S. (2003) Oxidative stress-induced apoptosis is mediated by ERK1/2 phosphorylation. *Exp Cell Res* 291 (1), 251-266
215. Gillardon, F. (2009) Leucine-rich repeat kinase 2 phosphorylates brain tubulin-beta isoforms and modulates microtubule stability--a point of convergence in parkinsonian neurodegeneration? *J Neurochem* 110 (5), 1514-1522
216. Smith, W. W., Pei, Z., Jiang, H., Moore, D. J., Liang, Y., West, A. B., Dawson, V. L., Dawson, T. M., and Ross, C. A. (2005) Leucine-rich repeat kinase 2 (LRRK2) interacts with parkin, and mutant LRRK2 induces neuronal degeneration. *Proc Natl Acad Sci U S A* 102 (51), 18676-18681
217. Ding, X., and Goldberg, M. S. (2009) Regulation of LRRK2 stability by the E3 ubiquitin ligase CHIP. *PLoS One* 4 (6), e5949
218. Ko, H. S., Bailey, R., Smith, W. W., Liu, Z., Shin, J. H., Lee, Y. I., Zhang, Y. J., Jiang, H., Ross, C. A., Moore, D. J., Patterson, C., Petrucelli, L., Dawson, T. M., and Dawson, V. L. (2009) CHIP regulates leucine-rich repeat kinase-2 ubiquitination, degradation, and toxicity. *Proc Natl Acad Sci U S A* 106 (8), 2897-2902
219. Wang, L., Xie, C., Greggio, E., Parisiadou, L., Shim, H., Sun, L., Chandran, J., Lin, X., Lai, C., Yang, W. J., Moore, D. J., Dawson, T. M., Dawson, V. L., Chiosis, G., Cookson, M. R., and Cai, H. (2008) The chaperone activity of heat shock protein 90 is critical for maintaining the stability of leucine-rich repeat kinase 2. *J Neurosci* 28 (13), 3384-3391
220. Pearl, L. H., and Prodromou, C. (2006) Structure and mechanism of the Hsp90 molecular chaperone machinery. *Annu Rev Biochem* 75, 271-294
221. Dachsel, J. C., Taylor, J. P., Mok, S. S., Ross, O. A., Hinkle, K. M., Bailey, R. M., Hines, J. H., Szutu, J., Madden, B., Petrucelli, L., and Farrer, M. J. (2007) Identification of potential protein interactors of Lrrk2. *Parkinsonism Relat Disord* 13 (7), 382-385
222. McDonough, H., and Patterson, C. (2003) CHIP: a link between the chaperone and proteasome systems. *Cell Stress Chaperones* 8 (4), 303-308
223. Ho, C. C., Rideout, H. J., Ribe, E., Troy, C. M., and Dauer, W. T. (2009) The Parkinson disease protein leucine-rich repeat kinase 2 transduces death signals via Fas-associated protein with death domain and caspase-8 in a cellular model of neurodegeneration. *J Neurosci* 29 (4), 1011-1016
224. Li, J., and Yuan, J. (2008) Caspases in apoptosis and beyond. *Oncogene* 27 (48), 6194-6206
225. Iaccarino, C., Crosio, C., Vitale, C., Sanna, G., Carri, M. T., and Barone, P. (2007) Apoptotic mechanisms in mutant LRRK2-mediated cell death. *Hum Mol Genet* 16 (11), 1319-1326
226. Kruidering, M., and Evan, G. I. (2000) Caspase-8 in apoptosis: the beginning of "the end"? *IUBMB Life* 50 (2), 85-90
227. Sancho, R. M., Law, B. M., and Harvey, K. (2009) Mutations in the LRRK2 Roc-COR tandem domain link Parkinson's disease to Wnt signalling pathways. *Hum Mol Genet* 18 (20), 3955-3968
228. Baskys, A., Bayazitov, I., Zhu, E., Fang, L., and Wang, R. (2007) Rab-mediated endocytosis: linking neurodegeneration, neuroprotection, and synaptic plasticity? *Ann N Y Acad Sci* 1122, 313-329
229. Shin, N., Jeong, H., Kwon, J., Heo, H. Y., Kwon, J. J., Yun, H. J., Kim, C. H., Han, B. S., Tong, Y., Shen, J., Hatano, T., Hattori, N., Kim, K. S., Chang, S., and Seol, W. (2008) LRRK2 regulates synaptic vesicle endocytosis. *Exp Cell Res* 314 (10), 2055-2065
230. Gandhi, P. N., Wang, X., Zhu, X., Chen, S. G., and Wilson-Delfosse, A. L. (2008) The Roc domain of leucine-rich repeat kinase 2 is sufficient for interaction with microtubules. *J Neurosci*

- Res 86 (8), 1711-1720
231. Guzik, B. W., and Goldstein, L. S. (2004) Microtubule-dependent transport in neurons: steps towards an understanding of regulation, function and dysfunction. *Curr Opin Cell Biol* 16 (4), 443-450
 232. Poulain, F. E., and Sobel, A. (2010) The microtubule network and neuronal morphogenesis: Dynamic and coordinated orchestration through multiple players. *Mol Cell Neurosci* 43 (1), 15-32
 233. Gillardon, F. (2009) Interaction of elongation factor 1-alpha with leucine-rich repeat kinase 2 impairs kinase activity and microtubule bundling in vitro. *Neuroscience* 163 (2), 533-539
 234. Nichols, R. J., Dzamko, N., Morrice, N. A., Campbell, D. G., Deak, M., Ordureau, A., Macartney, T., Tong, Y., Shen, J., Prescott, A. R., and Alessi, D. R. (2010) 14-3-3 binding to LRRK2 is disrupted by multiple Parkinson's disease-associated mutations and regulates cytoplasmic localization. *Biochem J* 430 (3), 393-404
 235. Morrison, D. K. (2009) The 14-3-3 proteins: integrators of diverse signaling cues that impact cell fate and cancer development. *Trends Cell Biol* 19 (1), 16-23
 236. Winder, S. J., and Ayscough, K. R. (2005) Actin-binding proteins. *J Cell Sci* 118 (Pt 4), 651-654
 237. Khaitlina, S. Y. (2001) Functional specificity of actin isoforms. *Int Rev Cytol* 202, 35-98
 238. dos Remedios, C. G., and Chhabra, D. (2008) Actin: An Overview of Its Structure and Function. In: Atassi, M. Z., Berliner, L. J., Chang, R. J.-Y., Jörmvall, H., Kenyon, G. L., and Wittman-Liebold, B. (eds.), *Actin-Binding Proteins and Disease*, vol. 8, 1-15, Springer New York
 239. dos Remedios, C. G., Chhabra, D., Kekic, M., Dedova, I. V., Tsubakihara, M., Berry, D. A., and Nosworthy, N. J. (2003) Actin binding proteins: regulation of cytoskeletal microfilaments. *Physiol Rev* 83 (2), 433-473
 240. Carlier, M. F. (1990) Actin polymerization and ATP hydrolysis. *Adv Biophys* 26, 51-73
 241. Pollard, T. D., and Cooper, J. A. (1986) Actin and actin-binding proteins. A critical evaluation of mechanisms and functions. *Annu Rev Biochem* 55, 987-1035
 242. Carlier, M. F., and Pantaloni, D. (1997) Control of actin dynamics in cell motility. *J Mol Biol* 269 (4), 459-467
 243. Disanza, A., Steffen, A., Hertzog, M., Frittoli, E., Rottner, K., and Scita, G. (2005) Actin polymerization machinery: the finish line of signaling networks, the starting point of cellular movement. *Cell Mol Life Sci* 62 (9), 955-970
 244. Zigmond, S. H. (2004) Beginning and ending an actin filament: control at the barbed end. *Curr Top Dev Biol* 63, 145-188
 245. Fischer, R. S., and Fowler, V. M. (2003) Tropomodulins: life at the slow end. *Trends Cell Biol* 13 (11), 593-601
 246. Campellone, K. G., and Welch, M. D. (2010) A nucleator arms race: cellular control of actin assembly. *Nat Rev Mol Cell Biol* 11 (4), 237-251
 247. Maul, R. S., Song, Y., Amann, K. J., Gerbin, S. C., Pollard, T. D., and Chang, D. D. (2003) EPLIN regulates actin dynamics by cross-linking and stabilizing filaments. *J Cell Biol* 160 (3), 399-407
 248. Perry, S. V. (2001) Vertebrate tropomyosin: distribution, properties and function. *J Muscle Res Cell Motil* 22 (1), 5-49
 249. Condeelis, J. (2001) How is actin polymerization nucleated in vivo? *Trends Cell Biol* 11 (7), 288-293
 250. Revenu, C., Athman, R., Robine, S., and Louvard, D. (2004) The co-workers of actin filaments: from cell structures to signals. *Nat Rev Mol Cell Biol* 5 (8), 635-646
 251. Pak, C. W., Flynn, K. C., and Bamburg, J. R. (2008) Actin-binding proteins take the reins in growth cones. *Nat Rev Neurosci* 9 (2), 136-147
 252. Geraldo, S., and Gordon-Weeks, P. R. (2009) Cytoskeletal dynamics in growth-cone steering. *J Cell Sci* 122 (Pt 20), 3595-3604
 253. Brown, J., and Bridgman, P. C. (2003) Role of myosin II in axon outgrowth. *J Histochem Cytochem* 51 (4), 421-428
 254. Lowery, L. A., and Van Vactor, D. (2009) The trip of the tip: understanding the growth cone machinery. *Nat Rev Mol Cell Biol* 10 (5), 332-343
 255. Letourneau, P. C., Shattuck, T. A., and Ressler, A. H. (1987) "Pull" and "push" in neurite elongation: observations on the effects of different concentrations of cytochalasin B and taxol. *Cell Motil Cytoskeleton* 8 (3), 193-209
 256. Goldberg, J. L. (2003) How does an axon grow? *Genes Dev* 17 (8), 941-958
 257. Nicholson-Dykstra, S., Higgs, H. N., and Harris, E. S. (2005) Actin dynamics: growth from dendritic branches. *Curr Biol* 15 (9), R346-357
 258. Pollard, T. D., Blanchoin, L., and Mullins, R. D. (2000) Molecular mechanisms controlling actin filament dynamics in nonmuscle cells. *Annu Rev Biophys Biomol Struct* 29, 545-576
 259. Ishikawa, R., and Kohama, K. (2007) Actin-binding proteins in nerve cell growth cones. *J Pharmacol Sci* 105 (1), 6-11
 260. Suter, D. M., and Forscher, P. (2000) Substrate-cytoskeletal coupling as a mechanism for the

References

- regulation of growth cone motility and guidance. *J Neurobiol* 44 (2), 97-113
261. Carthew, R. W., and Sontheimer, E. J. (2009) Origins and Mechanisms of miRNAs and siRNAs. *Cell* 136 (4), 642-655
262. Malone, C. D., and Hannon, G. J. (2009) Small RNAs as guardians of the genome. *Cell* 136 (4), 656-668
263. Cullen, B. R. (2005) RNAi the natural way. *Nat Genet* 37 (11), 1163-1165
264. Meister, G., and Tuschl, T. (2004) Mechanisms of gene silencing by double-stranded RNA. *Nature* 431 (7006), 343-349
265. Kim, V. N. (2003) RNA interference in functional genomics and medicine. *J Korean Med Sci* 18 (3), 309-318
266. Scherr, M., and Eder, M. (2007) Gene silencing by small regulatory RNAs in mammalian cells. *Cell Cycle* 6 (4), 444-449
267. Bauer, M. (2010) Strategies to Prevent siRNA-Triggered Cellular Toxicity. In: Erdmann, V. A., and Barciszewski, J. (eds.), *RNA Technologies and Their Applications*, vol., 93-106, Springer Berlin Heidelberg
268. Dykxhoorn, D. M., Novina, C. D., and Sharp, P. A. (2003) Killing the messenger: short RNAs that silence gene expression. *Nat Rev Mol Cell Biol* 4 (6), 457-467
269. Tuschl, T. (2003) Mammalian RNA interference. In: Hannon, G. J. (ed.) *RNAi: A Guide to Gene Silencing*, vol., 265-295, Cold Spring Harbor Laboratory Press, Cold Spring Harbor, NY, USA
270. Marquez, R. T., and McCaffrey, A. P. (2008) Advances in microRNAs: implications for gene therapists. *Hum Gene Ther* 19 (1), 27-38
271. Olejniczak, M., Galka, P., and Krzyzosiak, W. J. (2010) Sequence-non-specific effects of RNA interference triggers and microRNA regulators. *Nucleic Acids Res* 38 (1), 1-16
272. Li, C. X., Parker, A., Menocal, E., Xiang, S., Borodyansky, L., and Fruehauf, J. H. (2006) Delivery of RNA interference. *Cell Cycle* 5 (18), 2103-2109
273. de Veer, M. J., Sledz, C. A., and Williams, B. R. (2005) Detection of foreign RNA: implications for RNAi. *Immunol Cell Biol* 83 (3), 224-228
274. Gantier, M. P., and Williams, B. R. (2007) The response of mammalian cells to double-stranded RNA. *Cytokine Growth Factor Rev* 18 (5-6), 363-371
275. Karpala, A. J., Doran, T. J., and Bean, A. G. (2005) Immune responses to dsRNA: implications for gene silencing technologies. *Immunol Cell Biol* 83 (3), 211-216
276. Sadler, A. J., and Williams, B. R. (2008) Interferon-inducible antiviral effectors. *Nat Rev Immunol* 8 (7), 559-568
277. Robbins, M., Judge, A., and MacLachlan, I. (2009) siRNA and innate immunity. *Oligonucleotides* 19 (2), 89-102
278. Bradford, M. M. (1976) A rapid and sensitive method for the quantitation of microgram quantities of protein utilizing the principle of protein-dye binding. *Anal Biochem* 72, 248-254
279. Laemmli, U. K. (1970) Cleavage of structural proteins during the assembly of the head of bacteriophage T4. *Nature* 227 (5259), 680-685
280. Switzer, R. C., 3rd, Merrill, C. R., and Shifrin, S. (1979) A highly sensitive silver stain for detecting proteins and peptides in polyacrylamide gels. *Anal Biochem* 98 (1), 231-237
281. Rabilloud, T., Carpentier, G., and Tarroux, P. (1988) Improvement and simplification of low-background silver staining of proteins by using sodium dithionite. *Electrophoresis* 9 (6), 288-291
282. Towbin, H., Staehelin, T., and Gordon, J. (1979) Electrophoretic transfer of proteins from polyacrylamide gels to nitrocellulose sheets: procedure and some applications. *Proc Natl Acad Sci U S A* 76 (9), 4350-4354
283. Gravel, P., and Golaz, O. (1996) Protein Blotting by the Semidry Method. In: Walker, J. M. (ed.) *The Protein Protocols Handbook*, vol., 249-260
284. Berggard, T., Linse, S., and James, P. (2007) Methods for the detection and analysis of protein-protein interactions. *Proteomics* 7 (16), 2833-2842
285. Kuroda, K., Kato, M., Mima, J., and Ueda, M. (2006) Systems for the detection and analysis of protein-protein interactions. *Appl Microbiol Biotechnol* 71 (2), 127-136
286. Phizicky, E. M., and Fields, S. (1995) Protein-protein interactions: methods for detection and analysis. *Microbiol Rev* 59 (1), 94-123
287. Zhou, M., and Veenstra, T. D. (2007) Proteomic analysis of protein complexes. *Proteomics* 7 (16), 2688-2697
288. Gingras, A. C., Gstaiger, M., Raught, B., and Aebersold, R. (2007) Analysis of protein complexes using mass spectrometry. *Nat Rev Mol Cell Biol* 8 (8), 645-654
289. Kaboord, B., and Perr, M. (2008) Isolation of Proteins and Protein Complexes by Immunoprecipitation. In: Posch, A. (ed.) *2D PAGE: Sample Preparation and Fractionation*, vol. 424, 349-364
290. Braun, P., Cusick, M. E., and Vidal, M. (2006) QUICKstep and GS-TAP: new moves for protein-interaction analysis. *Nat Methods* 3 (12), 975-976

291. Liu, W. Z., Boucias, D. G., and McCoy, C. W. (1995) Extraction and characterization of the insecticidal toxin hirsutellin A produced by *Hirsutella thompsonii* var. *thompsonii*. *Exp Mycol* 19 (4), 254-262
292. Gingras, A. C., Aebersold, R., and Raught, B. (2005) Advances in protein complex analysis using mass spectrometry. *J Physiol* 563 (Pt 1), 11-21
293. Selbach, M., and Mann, M. (2006) Protein interaction screening by quantitative immunoprecipitation combined with knockdown (QUICK). *Nat Methods* 3 (12), 981-983
294. Ong, S. E., Blagoev, B., Kratchmarova, I., Kristensen, D. B., Steen, H., Pandey, A., and Mann, M. (2002) Stable isotope labeling by amino acids in cell culture, SILAC, as a simple and accurate approach to expression proteomics. *Mol Cell Proteomics* 1 (5), 376-386
295. Yates, J. R., Ruse, C. I., and Nakorchevsky, A. (2009) Proteomics by mass spectrometry: approaches, advances, and applications. *Annu Rev Biomed Eng* 11, 49-79
296. Steen, H., and Mann, M. (2004) The ABC's (and XYZ's) of peptide sequencing. *Nat Rev Mol Cell Biol* 5 (9), 699-711
297. Vermeulen, M., Hubner, N. C., and Mann, M. (2008) High confidence determination of specific protein-protein interactions using quantitative mass spectrometry. *Current Opinion in Biotechnology* 19 (4), 331-337
298. Scigelova, M., and Makarov, A. (2006) Orbitrap mass analyzer--overview and applications in proteomics. *Proteomics* 6 Suppl 2, 16-21
299. Olsen, J. V., de Godoy, L. M., Li, G., Macek, B., Mortensen, P., Pesch, R., Makarov, A., Lange, O., Horning, S., and Mann, M. (2005) Parts per million mass accuracy on an Orbitrap mass spectrometer via lock mass injection into a C-trap. *Mol Cell Proteomics* 4 (12), 2010-2021
300. Blagoev, B., Kratchmarova, I., Ong, S. E., Nielsen, M., Foster, L. J., and Mann, M. (2003) A proteomics strategy to elucidate functional protein-protein interactions applied to EGF signaling. *Nat Biotechnol* 21 (3), 315-318
301. Cox, J., and Mann, M. (2008) MaxQuant enables high peptide identification rates, individualized p.p.b.-range mass accuracies and proteome-wide protein quantification. *Nat Biotechnol* 26 (12), 1367-1372
302. Askenazi, M., Li, S., Singh, S., and Marto, J. A. (2010) Pathway Palette: a rich internet application for peptide-, protein- and network-oriented analysis of mass spectrometry data. *Proteomics* 10 (9), 1880 - 1885
303. Kanehisa, M., and Goto, S. (2000) KEGG: kyoto encyclopedia of genes and genomes. *Nucleic Acids Res* 28 (1), 27-30
304. Mishra, G. R., Suresh, M., Kumaran, K., Kannabiran, N., Suresh, S., Bala, P., Shivakumar, K., Anuradha, N., Reddy, R., Raghavan, T. M., Menon, S., Hanumanthu, G., Gupta, M., Upendran, S., Gupta, S., Mahesh, M., Jacob, B., Mathew, P., Chatterjee, P., Arun, K. S., Sharma, S., Chandrika, K. N., Deshpande, N., Palvankar, K., Raghavnath, R., Krishnakanth, R., Karathia, H., Rekha, B., Nayak, R., Vishnupriya, G., Kumar, H. G., Nagini, M., Kumar, G. S., Jose, R., Deepthi, P., Mohan, S. S., Gandhi, T. K., Harsha, H. C., Deshpande, K. S., Sarker, M., Prasad, T. S., and Pandey, A. (2006) Human protein reference database--2006 update. *Nucleic Acids Res* 34 (Database issue), D411-414
305. Stark, C., Breitkreutz, B. J., Reguly, T., Boucher, L., Breitkreutz, A., and Tyers, M. (2006) BioGRID: a general repository for interaction datasets. *Nucleic Acids Res* 34 (Database issue), D535-539
306. Peri, S., Navarro, J. D., Amanchy, R., Kristiansen, T. Z., Jonnalagadda, C. K., Surendranath, V., Niranjan, V., Muthusamy, B., Gandhi, T. K., Gronborg, M., Ibarrola, N., Deshpande, N., Shanker, K., Shivashankar, H. N., Rashmi, B. P., Ramya, M. A., Zhao, Z., Chandrika, K. N., Padma, N., Harsha, H. C., Yatish, A. J., Kavitha, M. P., Menezes, M., Choudhury, D. R., Suresh, S., Ghosh, N., Saravana, R., Chandran, S., Krishna, S., Joy, M., Anand, S. K., Madavan, V., Joseph, A., Wong, G. W., Schiemann, W. P., Constantinescu, S. N., Huang, L., Khosravi-Far, R., Steen, H., Tewari, M., Ghaffari, S., Blobel, G. C., Dang, C. V., Garcia, J. G., Pevsner, J., Jensen, O. N., Roepstorff, P., Deshpande, K. S., Chinnaiyan, A. M., Hamosh, A., Chakravarti, A., and Pandey, A. (2003) Development of human protein reference database as an initial platform for approaching systems biology in humans. *Genome Res* 13 (10), 2363-2371
307. Sama, I. E., and Huynen, M. A. (2010) Measuring the physical cohesiveness of proteins using physical interaction enrichment. *Bioinformatics* 26 (21), 2737-2743
308. Dale, J. W., and Greenaway, P. J. (1984) Bacterial Transformation (Kushner Method). In: Walker, J. M. (ed.) *Methods in Molecular Biology* vol. 2, 241-244
309. Hanahan, D., Jessee, J., and Bloom, F. (1985) Techniques for transformation of *E. coli*. In: Glover, D. M. (ed.) *DNA cloning: a practical approach*, vol. 1, 109-135
310. Sanger, F., Nicklen, S., and Coulson, A. R. (1977) DNA sequencing with chain-terminating inhibitors. *Biotechnology* 24, 104-108
311. Saiki, R. K., Gelfand, D. H., Stoffel, S., Scharf, S. J., Higuchi, R., Horn, G. T., Mullis, K. B., and

References

- Erich, H. A. (1988) Primer-directed enzymatic amplification of DNA with a thermostable DNA polymerase. *Science* 239 (4839), 487-491
312. Ailles, L. E., and Naldini, L. (2002) HIV-1-derived lentiviral vectors. *Curr Top Microbiol Immunol* 261, 31-52
313. Srinivasakumar, N. (2001) HIV-1 vector systems. *Somat Cell Mol Genet* 26 (1-6), 51-81
314. Vigna, E., and Naldini, L. (2000) Lentiviral vectors: excellent tools for experimental gene transfer and promising candidates for gene therapy. *J Gene Med* 2 (5), 308-316
315. Wiznerowicz, M., and Trono, D. (2003) Conditional suppression of cellular genes: lentivirus vector-mediated drug-inducible RNA interference. *J Virol* 77 (16), 8957-8961
316. Zufferey, R., Donello, J. E., Trono, D., and Hope, T. J. (1999) Woodchuck hepatitis virus posttranscriptional regulatory element enhances expression of transgenes delivered by retroviral vectors. *J Virol* 73 (4), 2886-2892
317. Zufferey, R., Dull, T., Mandel, R. J., Bukovsky, A., Quiroz, D., Naldini, L., and Trono, D. (1998) Self-inactivating lentivirus vector for safe and efficient in vivo gene delivery. *J Virol* 72 (12), 9873-9880
318. Bantounas, I., Phylactou, L. A., and Uney, J. B. (2004) RNA interference and the use of small interfering RNA to study gene function in mammalian systems. *J Mol Endocrinol* 33 (3), 545-557
319. Tuschl, T. (2002) Expanding small RNA interference. *Nat Biotechnol* 20 (5), 446-448
320. Regulier, E., Zala, D., Aebischer, P., and Deglon, N. (2004) Lentiviral-mediated gene transfer to model triplet repeat disorders. *Methods Mol Biol* 277, 199-213
321. Delenda, C. (2004) Lentiviral vectors: optimization of packaging, transduction and gene expression. *J Gene Med* 6 Suppl 1, S125-138
322. Dull, T., Zufferey, R., Kelly, M., Mandel, R. J., Nguyen, M., Trono, D., and Naldini, L. (1998) A third-generation lentivirus vector with a conditional packaging system. *J Virol* 72 (11), 8463-8471
323. Brummelkamp, T. R., Bernards, R., and Agami, R. (2002) A system for stable expression of short interfering RNAs in mammalian cells. *Science* 296 (5567), 550-553
324. Bauer, M., Kinkl, N., Meixner, A., Kremmer, E., Riemenschneider, M., Forstl, H., Gasser, T., and Ueffing, M. (2009) Prevention of interferon-stimulated gene expression using microRNA-designed hairpins. *Gene Ther* 16 (1), 142-147
325. Boden, D., Pusch, O., Silbermann, R., Lee, F., Tucker, L., and Ramratnam, B. (2004) Enhanced gene silencing of HIV-1 specific siRNA using microRNA designed hairpins. *Nucleic Acids Res* 32 (3), 1154-1158
326. Cullen, B. R. (2006) Induction of stable RNA interference in mammalian cells. *Gene Ther* 13 (6), 503-508
327. Abbas-Terki, T., Blanco-Bose, W., Deglon, N., Pralong, W., and Aebischer, P. (2002) Lentiviral-mediated RNA interference. *Hum Gene Ther* 13 (18), 2197-2201
328. Agilent 2100 Bioanalyzer - 2100 Expert User's Guide. Edition November 2003
329. Schroeder, A., Mueller, O., Stocker, S., Salowsky, R., Leiber, M., Gassmann, M., Lightfoot, S., Menzel, W., Granzow, M., and Ragg, T. (2006) The RIN: an RNA integrity number for assigning integrity values to RNA measurements. *BMC Mol Biol* 7, 3
330. Simon, P. (2003) Q-Gene: processing quantitative real-time RT-PCR data. *Bioinformatics* 19 (11), 1439-1440
331. Holley, R. W., and Kiernan, J. A. (1968) "Contact inhibition" of cell division in 3T3 cells. *Proc Natl Acad Sci U S A* 60 (1), 300-304
332. Bendall, S. C., Hughes, C., Stewart, M. H., Doble, B., Bhatia, M., and Lajoie, G. A. (2008) Prevention of amino acid conversion in SILAC experiments with embryonic stem cells. *Mol Cell Proteomics* 7 (9), 1587-1597
333. Graham, F. L., and van der Eb, A. J. (1973) A new technique for the assay of infectivity of human adenovirus 5 DNA. *Virology* 52 (2), 456-467
334. Jordan, M., and Wurm, F. (2004) Transfection of adherent and suspended cells by calcium phosphate. *Methods* 33 (2), 136-143
335. (2005) Calcium phosphate-mediated transfection of eukaryotic cells. *Nat Meth* 2 (4), 319-320
336. Bauer, M., Szulc, J., Meyer, M., Jensen, C. H., Terki, T. A., Meixner, A., Kinkl, N., Gasser, T., Aebischer, P., and Ueffing, M. (2008) Delta-like 1 participates in the specification of ventral midbrain progenitor derived dopaminergic neurons. *J Neurochem* 104 (4), 1101-1115
337. Baldock, R., Bard, J., Burger, A., Burton, N., Christiansen, J., Feng, G., Hill, B., Houghton, D., Kaufman, M., Rao, J., Sharpe, J., Ross, A., Stevenson, P., Venkataraman, S., Waterhouse, A., Yang, Y., and Davidson, D. (2003) EMAP and EMAGE. *Neuroinformatics* 1 (4), 309-325
338. Chevallier, J., Koop, C., Srivastava, A., Petrie, R. J., Lamarche-Vane, N., and Presley, J. F. (2009) Rab35 regulates neurite outgrowth and cell shape. *FEBS Lett* 583 (7), 1096-1101
339. Spudich, J. A., and Watt, S. (1971) The regulation of rabbit skeletal muscle contraction. I. Biochemical studies of the interaction of the tropomyosin-troponin complex with actin and the proteolytic fragments of myosin. *J Biol Chem* 246 (15), 4866-4871

340. Gloeckner, C. J., Boldt, K., Schumacher, A., Roepman, R., and Ueffing, M. (2007) A novel tandem affinity purification strategy for the efficient isolation and characterisation of native protein complexes. *Proteomics* 7 (23), 4228-4234
341. Kriegsheim, A., Preisinger, C., and Kolch, W. (2008) Mapping of signaling pathways by functional interaction proteomics. *Methods Mol Biol* 484, 177-192
342. Schagger, H. (2006) Tricine-SDS-PAGE. *Nat Protoc* 1 (1), 16-22
343. Malik, I., Garrido, M., Bahr, M., Kugler, S., and Michel, U. (2006) Comparison of test systems for RNA interference. *Biochem Biophys Res Commun* 341 (1), 245-253
344. Pei, Y., and Tuschl, T. (2006) On the art of identifying effective and specific siRNAs. *Nat Methods* 3 (9), 670-676
345. Collier, T. J., Steece-Collier, K., McGuire, S., and Sortwell, C. E. (2003) Cellular models to study dopaminergic injury responses. *Ann N Y Acad Sci* 991, 140-151
346. Bridge, A. J., Pebernard, S., Ducraux, A., Nicoulaz, A. L., and Iggo, R. (2003) Induction of an interferon response by RNAi vectors in mammalian cells. *Nat Genet* 34 (3), 263-264
347. Paddison, P. J., Caudy, A. A., Bernstein, E., Hannon, G. J., and Conklin, D. S. (2002) Short hairpin RNAs (shRNAs) induce sequence-specific silencing in mammalian cells. *Genes Dev* 16 (8), 948-958
348. Cullen, B. R. (2006) Enhancing and confirming the specificity of RNAi experiments. *Nat Methods* 3 (9), 677-681
349. Meixner, A., Boldt, K., Van Troys, M., Askenazi, M., Gloeckner, C. J., Bauer, M., Marto, J. A., Ampe, C., Kinkl, N., and Ueffing, M. (2011) A QUICK screen for Lrrk2 interaction partners--leucine-rich repeat kinase 2 is involved in actin cytoskeleton dynamics. *Mol Cell Proteomics* 10 (1), M110 001172
350. Editorial in Nature Cell Biology (2003) Whither RNAi? *Nat Cell Biol* 5 (6), 489-490
351. Dent, E. W., and Gertler, F. B. (2003) Cytoskeletal dynamics and transport in growth cone motility and axon guidance. *Neuron* 40 (2), 209-227
352. van Veen, M. P., and van Pelt, J. (1994) Dynamic mechanisms of neuronal outgrowth. *Prog Brain Res* 102, 95-108
353. Marsh, L., and Letourneau, P. C. (1984) Growth of neurites without filopodial or lamellipodial activity in the presence of cytochalasin B. *J Cell Biol* 99 (6), 2041-2047
354. Castets, M., Schaeffer, C., Bechara, E., Schenck, A., Khandjian, E. W., Luche, S., Moine, H., Rabilloud, T., Mandel, J. L., and Bardoni, B. (2005) FMRP interferes with the Rac1 pathway and controls actin cytoskeleton dynamics in murine fibroblasts. *Hum Mol Genet* 14 (6), 835-844
355. Vardouli, L., Moustakas, A., and Stournaras, C. (2005) LIM-kinase 2 and cofilin phosphorylation mediate actin cytoskeleton reorganization induced by transforming growth factor-beta. *J Biol Chem* 280 (12), 11448-11457
356. Merico, D., Gfeller, D., and Bader, G. D. (2009) How to visually interpret biological data using networks. *Nat Biotechnol* 27 (10), 921-924
357. Kohn, J., and Wilchek, M. (1982) Mechanism of activation of Sepharose and Sephadex by cyanogen bromide. *Enzyme and Microbial Technology* 4 (3), 161-163
358. Miernyk, J. A., and Thelen, J. J. (2008) Biochemical approaches for discovering protein-protein interactions. *Plant J* 53 (4), 597-609
359. Harlow, E., and Lane, D. (1999) *Using Antibodies: A Laboratory Manual*, Cold Spring Harbor Laboratory Press, Cold Spring Harbor.
360. Park, H. R., Cockrell, L. M., Du, Y., Kasinski, A., Havel, J., Zhao, J., Reyes-Turcu, F., Wilkinson, K. D., and Fu, H. (2008) Protein-Protein Interactions. In: Walker, J. M., and Rapley, R. (eds.), *Molecular Biomethods Handbook*, vol., 463-494
361. Yang, W., Steen, H., and Freeman, M. R. (2008) Proteomic approaches to the analysis of multiprotein signaling complexes. *Proteomics* 8 (4), 832-851
362. Bordeaux, J., Welsh, A., Agarwal, S., Killiam, E., Baquero, M., Hanna, J., Anagnostou, V., and Rimm, D. (2010) Antibody validation. *Biotechniques* 48 (3), 197-209
363. Fritschy, J. M. (2008) Is my antibody-staining specific? How to deal with pitfalls of immunohistochemistry. *Eur J Neurosci* 28 (12), 2365-2370
364. Willingham, M. C. (1999) Conditional epitopes. is your antibody always specific? *J Histochem Cytochem* 47 (10), 1233-1236
365. Mighell, A. J., Hume, W. J., and Robinson, P. A. (1998) An overview of the complexities and subtleties of immunohistochemistry. *Oral Dis* 4 (3), 217-223
366. Ramos-Vara, J. A. (2005) Technical aspects of immunohistochemistry. *Vet Pathol* 42 (4), 405-426
367. Grimm, D. (2009) Small silencing RNAs: state-of-the-art. *Adv Drug Deliv Rev* 61 (9), 672-703
368. Martin, S. E., and Caplen, N. J. (2007) Applications of RNA interference in mammalian systems. *Annu Rev Genomics Hum Genet* 8, 81-108
369. Fish, R. J., and Kruihof, E. K. (2004) Short-term cytotoxic effects and long-term instability of

- RNAi delivered using lentiviral vectors. *BMC Mol Biol* 5, 9
370. Robbins, M. A., Li, M., Leung, I., Li, H., Boyer, D. V., Song, Y., Behlke, M. A., and Rossi, J. J. (2006) Stable expression of shRNAs in human CD34+ progenitor cells can avoid induction of interferon responses to siRNAs in vitro. *Nat Biotechnol* 24 (5), 566-571
371. Kenworthy, R., Lambert, D., Yang, F., Wang, N., Chen, Z., Zhu, H., Zhu, F., Liu, C., Li, K., and Tang, H. (2009) Short-hairpin RNAs delivered by lentiviral vector transduction trigger RIG-I-mediated IFN activation. *Nucleic Acids Res* 37 (19), 6587-6599
372. Judge, A., and MacLachlan, I. (2008) Overcoming the innate immune response to small interfering RNA. *Hum Gene Ther* 19 (2), 111-124
373. Marques, J. T., and Williams, B. R. (2005) Activation of the mammalian immune system by siRNAs. *Nat Biotechnol* 23 (11), 1399-1405
374. Hornung, V., Ellegast, J., Kim, S., Brzozka, K., Jung, A., Kato, H., Poeck, H., Akira, S., Conzelmann, K. K., Schlee, M., Endres, S., and Hartmann, G. (2006) 5'-Triphosphate RNA is the ligand for RIG-I. *Science* 314 (5801), 994-997
375. Marques, J. T., Devosse, T., Wang, D., Zamanian-Daryoush, M., Serbinowski, P., Hartmann, R., Fujita, T., Behlke, M. A., and Williams, B. R. (2006) A structural basis for discriminating between self and nonself double-stranded RNAs in mammalian cells. *Nat Biotechnol* 24 (5), 559-565
376. Manjunath, N., Wu, H., Subramanya, S., and Shankar, P. (2009) Lentiviral delivery of short hairpin RNAs. *Adv Drug Deliv Rev* 61 (9), 732-745
377. Sledz, C. A., Holko, M., de Veer, M. J., Silverman, R. H., and Williams, B. R. (2003) Activation of the interferon system by short-interfering RNAs. *Nat Cell Biol* 5 (9), 834-839
378. Jackson, A. L., and Linsley, P. S. (2010) Recognizing and avoiding siRNA off-target effects for target identification and therapeutic application. *Nat Rev Drug Discov* 9 (1), 57-67
379. Reynolds, A., Anderson, E. M., Vermeulen, A., Fedorov, Y., Robinson, K., Leake, D., Karpilow, J., Marshall, W. S., and Khvorova, A. (2006) Induction of the interferon response by siRNA is cell type- and duplex length-dependent. *RNA* 12 (6), 988-993
380. Rivest, S. (2009) Regulation of innate immune responses in the brain. *Nat Rev Immunol* 9 (6), 429-439
381. Farina, C., Aloisi, F., and Meinl, E. (2007) Astrocytes are active players in cerebral innate immunity. *Trends Immunol* 28 (3), 138-145
382. Gorina, R., Santalucia, T., Petegnief, V., Ejarque-Ortiz, A., Saura, J., and Planas, A. M. (2009) Astrocytes are very sensitive to develop innate immune responses to lipid-carried short interfering RNA. *Glia* 57 (1), 93-107
383. McBride, J. L., Boudreau, R. L., Harper, S. Q., Staber, P. D., Monteys, A. M., Martins, I., Gilmore, B. L., Burstein, H., Peluso, R. W., Polisky, B., Carter, B. J., and Davidson, B. L. (2008) Artificial miRNAs mitigate shRNA-mediated toxicity in the brain: implications for the therapeutic development of RNAi. *Proc Natl Acad Sci U S A* 105 (15), 5868-5873
384. Read, M. L., Mir, S., Spice, R., Seabright, R. J., Suggate, E. L., Ahmed, Z., Berry, M., and Logan, A. (2009) Profiling RNA interference (RNAi)-mediated toxicity in neural cultures for effective short interfering RNA design. *J Gene Med* 11 (6), 523-534
385. Kim, W. G., Mohny, R. P., Wilson, B., Jeohn, G. H., Liu, B., and Hong, J. S. (2000) Regional difference in susceptibility to lipopolysaccharide-induced neurotoxicity in the rat brain: role of microglia. *J Neurosci* 20 (16), 6309-6316
386. Savchenko, V. L., McKanna, J. A., Nikonenko, I. R., and Skibo, G. G. (2000) Microglia and astrocytes in the adult rat brain: comparative immunocytochemical analysis demonstrates the efficacy of lipocortin 1 immunoreactivity. *Neuroscience* 96 (1), 195-203
387. Gao, H. M., Hong, J. S., Zhang, W., and Liu, B. (2002) Distinct role for microglia in rotenone-induced degeneration of dopaminergic neurons. *J Neurosci* 22 (3), 782-790
388. Pardo, B., Paino, C. L., Casarejos, M. J., and Mena, M. A. (1997) Neuronal-enriched cultures from embryonic rat ventral mesencephalon for pharmacological studies of dopamine neurons. *Brain Res Brain Res Protoc* 1 (2), 127-132
389. McManus, M. T., Petersen, C. P., Haines, B. B., Chen, J., and Sharp, P. A. (2002) Gene silencing using micro-RNA designed hairpins. *RNA* 8 (6), 842-850
390. Zeng, Y., Wagner, E. J., and Cullen, B. R. (2002) Both natural and designed micro RNAs can inhibit the expression of cognate mRNAs when expressed in human cells. *Mol Cell* 9 (6), 1327-1333
391. Bushati, N., and Cohen, S. M. (2007) microRNA functions. *Annu Rev Cell Dev Biol* 23, 175-205
392. Liu, X., Fortin, K., and Mourelatos, Z. (2008) MicroRNAs: biogenesis and molecular functions. *Brain Pathol* 18 (1), 113-121
393. Burke, R. E. (2003) Postnatal developmental programmed cell death in dopamine neurons. *Ann N Y Acad Sci* 991, 69-79
394. Marti, M. J., James, C. J., Oo, T. F., Kelly, W. J., and Burke, R. E. (1997) Early developmental destruction of terminals in the striatal target induces apoptosis in dopamine neurons of the

- substantia nigra. *J Neurosci* 17 (6), 2030-2039
395. Oo, T. F., and Burke, R. E. (1997) The time course of developmental cell death in phenotypically defined dopaminergic neurons of the substantia nigra. *Brain Res Dev Brain Res* 98 (2), 191-196
396. Cowan, W. M., Fawcett, J. W., O'Leary, D. D., and Stanfield, B. B. (1984) Regressive events in neurogenesis. *Science* 225 (4668), 1258-1265
397. Monti, M., Orru, S., Pagnozzi, D., and Pucci, P. (2005) Functional proteomics. *Clin Chim Acta* 357 (2), 140-150
398. Ong, S. E., and Mann, M. (2005) Mass spectrometry-based proteomics turns quantitative. *Nat Chem Biol* 1 (5), 252-262
399. Bruckner, A., Polge, C., Lentze, N., Auerbach, D., and Schlattner, U. (2009) Yeast two-hybrid, a powerful tool for systems biology. *Int J Mol Sci* 10 (6), 2763-2788
400. Cusick, M. E., Klitgord, N., Vidal, M., and Hill, D. E. (2005) Interactome: gateway into systems biology. *Hum Mol Genet* 14 Spec No. 2, R171-181
401. Suter, B., Kittanakom, S., and Stagljar, I. (2008) Two-hybrid technologies in proteomics research. *Curr Opin Biotechnol* 19 (4), 316-323
402. Lambrechts, A., Van Troys, M., and Ampe, C. (2004) The actin cytoskeleton in normal and pathological cell motility. *Int J Biochem Cell Biol* 36 (10), 1890-1909
403. Pollard, T. D., and Cooper, J. A. (2009) Actin, a central player in cell shape and movement. *Science* 326 (5957), 1208-1212
404. May, R. C. (2001) The Arp2/3 complex: a central regulator of the actin cytoskeleton. *Cell Mol Life Sci* 58 (11), 1607-1626
405. Kostyukova, A. S. (2008) Tropomodulins and tropomodulin/tropomyosin interactions. *Cell Mol Life Sci* 65 (4), 563-569
406. Fischer, R. S., Yarmola, E. G., Weber, K. L., Speicher, K. D., Speicher, D. W., Bubb, M. R., and Fowler, V. M. (2006) Tropomodulin 3 binds to actin monomers. *J Biol Chem* 281 (47), 36454-36465
407. Wang, C. L., and Coluccio, L. M. (2010) New insights into the regulation of the actin cytoskeleton by tropomyosin. *Int Rev Cell Mol Biol* 281, 91-128
408. Cooper, J. A. (2002) Actin dynamics: tropomyosin provides stability. *Curr Biol* 12 (15), R523-525
409. Cooper, J. A., and Sept, D. (2008) New insights into mechanism and regulation of actin capping protein. *Int Rev Cell Mol Biol* 267, 183-206
410. Wear, M. A., and Cooper, J. A. (2004) Capping protein: new insights into mechanism and regulation. *Trends Biochem Sci* 29 (8), 418-428
411. Wiche, G. (1998) Role of plectin in cytoskeleton organization and dynamics. *J Cell Sci* 111 (Pt 17), 2477-2486
412. Andra, K., Nikolic, B., Stocher, M., Drenckhahn, D., and Wiche, G. (1998) Not just scaffolding: plectin regulates actin dynamics in cultured cells. *Genes Dev* 12 (21), 3442-3451
413. Peng, Y. F., Mandai, K., Sakisaka, T., Okabe, N., Yamamoto, Y., Yokoyama, S., Mizoguchi, A., Shiozaki, H., Monden, M., and Takai, Y. (2000) Ankyrcorbin: a novel actin cytoskeleton-associated protein. *Genes Cells* 5 (12), 1001-1008
414. Ishikawa, R., Hayashi, K., Shirao, T., Xue, Y., Takagi, T., Sasaki, Y., and Kohama, K. (1994) Drebrin, a development-associated brain protein from rat embryo, causes the dissociation of tropomyosin from actin filaments. *J Biol Chem* 269 (47), 29928-29933
415. Shirao, T. (1995) The roles of microfilament-associated proteins, drebrins, in brain morphogenesis: a review. *J Biochem* 117 (2), 231-236
416. Coluccio, L. M. (2008) Myosin I. In: Ridley, A., and Frampton, J. (eds.), *Myosins*, vol. 7, 95-124, Springer Netherlands, Dordrecht
417. McConnell, R. E., and Tyska, M. J. (2010) Leveraging the membrane - cytoskeleton interface with myosin-1. *Trends Cell Biol* 20 (7), 418-426
418. Soldati, T., and Kistler, C. (2004) Do Class I Myosins Exert Their Functions through Regulation of Actin Dynamics? In: Ridley, A., Peckham, M., and Clark, P. (eds.), *Cell Motility: From Molecules to Organisms*, vol., 39-59, John Wiley & Sons, Ltd, Chichester
419. Osherov, N., and May, G. S. (2000) In vivo function of class I myosins. *Cell Motil Cytoskeleton* 47 (3), 163-173
420. Barylko, B., Binns, D. D., and Albanesi, J. P. (2000) Regulation of the enzymatic and motor activities of myosin I. *Biochim Biophys Acta* 1496 (1), 23-35
421. Chin, D., and Means, A. R. (2000) Calmodulin: a prototypical calcium sensor. *Trends Cell Biol* 10 (8), 322-328
422. Conti, M. A., and Adelstein, R. S. (2008) Nonmuscle myosin II moves in new directions. *J Cell Sci* 121 (Pt 1), 11-18
423. Vicente-Manzanares, M., Ma, X., Adelstein, R. S., and Horwitz, A. R. (2009) Non-muscle myosin II takes centre stage in cell adhesion and migration. *Nat Rev Mol Cell Biol* 10 (11), 778-790
424. Ito, M., Nakano, T., Erdodi, F., and Hartshorne, D. J. (2004) Myosin phosphatase: structure,

- regulation and function. *Mol Cell Biochem* 259 (1-2), 197-209
425. Feng, J., Ito, M., Ichikawa, K., Isaka, N., Nishikawa, M., Hartshorne, D. J., and Nakano, T. (1999) Inhibitory phosphorylation site for Rho-associated kinase on smooth muscle myosin phosphatase. *J Biol Chem* 274 (52), 37385-37390
426. Kimura, K., Ito, M., Amano, M., Chihara, K., Fukata, Y., Nakafuku, M., Yamamori, B., Feng, J., Nakano, T., Okawa, K., Iwamatsu, A., and Kaibuchi, K. (1996) Regulation of myosin phosphatase by Rho and Rho-associated kinase (Rho-kinase). *Science* 273 (5272), 245-248
427. Koga, Y., and Ikebe, M. (2005) p116Rip decreases myosin II phosphorylation by activating myosin light chain phosphatase and by inactivating RhoA. *J Biol Chem* 280 (6), 4983-4991
428. Surks, H. K., Richards, C. T., and Mendelsohn, M. E. (2003) Myosin phosphatase-Rho interacting protein. A new member of the myosin phosphatase complex that directly binds RhoA. *J Biol Chem* 278 (51), 51484-51493
429. Habig, K., Walter, M., Poths, S., Riess, O., and Bonin, M. (2008) RNA interference of LRRK2-microarray expression analysis of a Parkinson's disease key player. *Neurogenetics* 9 (2), 83-94
430. Mangeat, P., Roy, C., and Martin, M. (1999) ERM proteins in cell adhesion and membrane dynamics. *Trends Cell Biol* 9 (5), 187-192
431. Tsukita, S., and Yonemura, S. (1999) Cortical actin organization: lessons from ERM (ezrin/radixin/moesin) proteins. *J Biol Chem* 274 (49), 34507-34510
432. Tian, Q., Stepaniants, S. B., Mao, M., Weng, L., Feetham, M. C., Doyle, M. J., Yi, E. C., Dai, H., Thorsson, V., Eng, J., Goodlett, D., Berger, J. P., Gunter, B., Linseley, P. S., Stoughton, R. B., Aebersold, R., Collins, S. J., Hanlon, W. A., and Hood, L. E. (2004) Integrated genomic and proteomic analyses of gene expression in Mammalian cells. *Mol Cell Proteomics* 3 (10), 960-969
433. Waters, K. M., Pounds, J. G., and Thrall, B. D. (2006) Data merging for integrated microarray and proteomic analysis. *Brief Funct Genomic Proteomic* 5 (4), 261-272
434. Lázaro-Diéguez, F., and Egea, G. (2007) Comparative study of the impact of the actin cytoskeleton on cell shape and membrane surface in mammalian cells in response to actin toxins. In: Méndez-Vilas, A., and Díaz, J. (eds.), *Modern research and educational topics in microscopy*, vol. 1, 362-369, Formatex, Badajoz
435. Alvarez, V. A., Ridenour, D. A., and Sabatini, B. L. (2006) Retraction of synapses and dendritic spines induced by off-target effects of RNA interference. *J Neurosci* 26 (30), 7820-7825
436. MacLeod, D., Dowman, J., Hammond, R., Leete, T., Inoue, K., and Abeliovich, A. (2006) The familial Parkinsonism gene LRRK2 regulates neurite process morphology. *Neuron* 52 (4), 587-593
437. Meyer, G., and Feldman, E. L. (2002) Signaling mechanisms that regulate actin-based motility processes in the nervous system. *J Neurochem* 83 (3), 490-503
438. Fath, T., Fischer, R. S., Dehmelt, L., Halpain, S., and Fowler, V. M. (2010) Tropomodulins are negative regulators of neurite outgrowth. *Eur J Cell Biol*
439. Korobova, F., and Svitkina, T. (2008) Arp2/3 complex is important for filopodia formation, growth cone motility, and neuritogenesis in neuronal cells. *Mol Biol Cell* 19 (4), 1561-1574
440. Fath, T., Agnes Chan, Y. K., Vrhovski, B., Clarke, H., Curthoys, N., Hook, J., Lemckert, F., Schevzov, G., Tam, P., Watson, C. M., Khoo, P. L., and Gunning, P. (2010) New aspects of tropomyosin-regulated neuritogenesis revealed by the deletion of Tm5NM1 and 2. *Eur J Cell Biol* 89 (7), 489-498
441. Schevzov, G., Bryce, N. S., Almonte-Baldonado, R., Joya, J., Lin, J. J., Hardeman, E., Weinberger, R., and Gunning, P. (2005) Specific features of neuronal size and shape are regulated by tropomyosin isoforms. *Mol Biol Cell* 16 (7), 3425-3437
442. Diefenbach, T. J., Latham, V. M., Yimlamai, D., Liu, C. A., Herman, I. M., and Jay, D. G. (2002) Myosin 1c and myosin IIB serve opposing roles in lamellipodial dynamics of the neuronal growth cone. *J Cell Biol* 158 (7), 1207-1217
443. Bridgman, P. C., Dave, S., Asnes, C. F., Tullio, A. N., and Adelstein, R. S. (2001) Myosin IIB is required for growth cone motility. *J Neurosci* 21 (16), 6159-6169
444. Wylie, S. R., and Chantler, P. D. (2003) Myosin IIA drives neurite retraction. *Mol Biol Cell* 14 (11), 4654-4666
445. Wylie, S. R., Wu, P. J., Patel, H., and Chantler, P. D. (1998) A conventional myosin motor drives neurite outgrowth. *Proc Natl Acad Sci U S A* 95 (22), 12967-12972
446. Letourneau, P. C. (2009) Actin in axons: stable scaffolds and dynamic filaments. *Results Probl Cell Differ* 48, 65-90
447. Luo, L. (2000) Rho GTPases in neuronal morphogenesis. *Nat Rev Neurosci* 1 (3), 173-180
448. Ahsyalh, J. C., Kuchnicki, L. L., and Larochele, D. A. (2003) The identification of pats1, a novel gene locus required for cytokinesis in Dictyostelium discoideum. *Mol Biol Cell* 14 (1), 14-25
449. Bosgraaf, L., Russcher, H., Smith, J. L., Wessels, D., Soll, D. R., and Van Haastert, P. J. (2002) A novel cGMP signalling pathway mediating myosin phosphorylation and chemotaxis in Dictyostelium. *EMBO J* 21 (17), 4560-4570

450. Davy, D. A., Ball, E. E., Matthaei, K. I., Campbell, H. D., and Crouch, M. F. (2000) The flightless I protein localizes to actin-based structures during embryonic development. *Immunol Cell Biol* 78 (4), 423-429
451. Cohen, O., Feinstein, E., and Kimchi, A. (1997) DAP-kinase is a Ca²⁺/calmodulin-dependent, cytoskeletal-associated protein kinase, with cell death-inducing functions that depend on its catalytic activity. *EMBO J* 16 (5), 998-1008
452. Luo, L. (2002) Actin cytoskeleton regulation in neuronal morphogenesis and structural plasticity. *Annu Rev Cell Dev Biol* 18, 601-635
453. Oppenheim, R. W. (1991) Cell-Death during Development of the Nervous-System. *Annual Review of Neuroscience* 14, 453-501
454. Taymans, J.-M., and Cookson, M. R. (2010) Mechanisms in dominant parkinsonism: The toxic triangle of LRRK2, α -synuclein, and tau. *Bioessays* 32 (3), 227-235
455. Dillon, C., and Goda, Y. (2005) The actin cytoskeleton: integrating form and function at the synapse. *Annu Rev Neurosci* 28, 25-55
456. Li, X., Patel, J. C., Wang, J., Avshalumov, M. V., Nicholson, C., Buxbaum, J. D., Elder, G. A., Rice, M. E., and Yue, Z. (2010) Enhanced striatal dopamine transmission and motor performance with LRRK2 overexpression in mice is eliminated by familial Parkinson's disease mutation G2019S. *J Neurosci* 30 (5), 1788-1797
457. Li, Y., Liu, W., Oo, T. F., Wang, L., Tang, Y., Jackson-Lewis, V., Zhou, C., Geghman, K., Bogdanov, M., Przedborski, S., Beal, M. F., Burke, R. E., and Li, C. (2009) Mutant LRRK2(R1441G) BAC transgenic mice recapitulate cardinal features of Parkinson's disease. *Nat Neurosci* 12 (7), 826-828
458. Tong, Y., Pisani, A., Martella, G., Karouani, M., Yamaguchi, H., Pothos, E. N., and Shen, J. (2009) R1441C mutation in LRRK2 impairs dopaminergic neurotransmission in mice. *Proc Natl Acad Sci U S A* 106 (34), 14622-14627
459. Piccoli, G., Condliffe, S. B., Bauer, M., Giesert, F., Boldt, K., De Astis, S., Meixner, A., Sarioglu, H., Vogt-Weisenhorn, D. M., Wurst, W., Gloeckner, C. J., Matteoli, M., Sala, C., and Ueffing, M. (2011) LRRK2 Controls Synaptic Vesicle Storage and Mobilization within the Recycling Pool. *J Neurosci* 31 (6), 2225-2237
460. Lin, X., Parisiadou, L., Gu, X. L., Wang, L., Shim, H., Sun, L., Xie, C., Long, C. X., Yang, W. J., Ding, J., Chen, Z. Z., Gallant, P. E., Tao-Cheng, J. H., Rudow, G., Troncoso, J. C., Liu, Z., Li, Z., and Cai, H. (2009) Leucine-rich repeat kinase 2 regulates the progression of neuropathology induced by Parkinson's-disease-related mutant alpha-synuclein. *Neuron* 64 (6), 807-827
461. Yue, Z. (2009) LRRK2 in Parkinson's disease: in vivo models and approaches for understanding pathogenic roles. *FEBS J* 276 (22), 6445-6454
462. Huynh, D. P., Scoles, D. R., Ho, T. H., Del Bigio, M. R., and Pulst, S. M. (2000) Parkin is associated with actin filaments in neuronal and nonneuronal cells. *Ann Neurol* 48 (5), 737-744
463. Lim, M. K., Kawamura, T., Ohsawa, Y., Ohtsubo, M., Asakawa, S., Takayanagi, A., and Shimizu, N. (2007) Parkin interacts with LIM Kinase 1 and reduces its cofilin-phosphorylation activity via ubiquitination. *Exp Cell Res* 313 (13), 2858-2874
464. Kim, K. H., and Son, J. H. (2010) PINK1 gene knockdown leads to increased binding of parkin with actin filament. *Neurosci Lett* 468 (3), 272-276
465. Sousa, V. L., Bellani, S., Giannandrea, M., Yousuf, M., Valtorta, F., Meldolesi, J., and Chieriegatti, E. (2009) {alpha}-synuclein and its A30P mutant affect actin cytoskeletal structure and dynamics. *Mol Biol Cell* 20 (16), 3725-3739
466. Gourlay, C. W., and Ayscough, K. R. (2005) The actin cytoskeleton: a key regulator of apoptosis and ageing? *Nat Rev Mol Cell Biol* 6 (7), 583-589

VII. ANNEX

1. Figure index

Figure 1: PD-related intraneuronal proteinaceous inclusion pathology.....	19
Figure 2: PD-related changes in the motor loop of the basal ganglia.....	21
Figure 3: Molecular pathways implicated in the pathogenesis of PD.	33
Figure 4: Lrrk2 multidomain structure.....	38
Figure 5: Actin-binding proteins.	49
Figure 6: Cytoskeletal organization and actin dynamics in growth cones.	52
Figure 7: RNAi-mediated post-transcriptional regulation of gene expression and sites of intervention with RNAi technology tools.....	56
Figure 8: Strategy to screen for endogenous PPIs by QUICK.....	83
Figure 9: Representative MS spectra of SILAC peptide doublets.....	88
Figure 10: Lentivirus vector-based delivery system for stable shRNA expression.....	100
Figure 11: Generation of multiple-attenuated and SIN HIV-1-derived lentiviral vectors based on a four-plasmid (third generation) system.....	102
Figure 12: Structure and design of shRNA-based silencing constructs (first and second generation).	104
Figure 13: Dissection of the ventral midbrain (VM) region from embryonic mouse brain.....	115
Figure 14: Actin cosedimentation assay.....	121
Figure 15: Schematic overview of the experimental procedure.	123
Figure 16: Lrrk2-specificity of monoclonal anti-Lrrk2 antibody clones in western blot analysis.....	125
Figure 17: Streptavidin-biotin-based screening assay for the identification of anti-Lrrk2 monoclonal antibody clones suitable for the extraction of endogenous Lrrk2 from cellular lysates.....	127
Figure 18: Precipitation of endogenous Lrrk2 in a classic IP approach by the rat-monoclonal anti- Lrrk2 antibody clones 1E11 and 2E12.	129
Figure 19: Optimized IP of endogenous Lrrk2 using the anti-Lrrk2 antibody covalently coupled to CNBr-activated sepharose.	131
Figure 20: Evaluation of two cross-linking protocols for the immobilization of the anti-Lrrk2 antibody clone 1E11 to Protein G sepharose.	135
Figure 21: The anti-Lrrk2 antibody (clone 1E11) cross-linked to Protein G sepharose precipitated endogenous Lrrk2 efficiently from both NIH3T3 cell lysates and mouse brain lysates. ...	138
Figure 22: Different conditions assayed for their capability to optimize the IP of endogenous Lrrk2 from mouse brain lysates using the anti-Lrrk2 antibody (clone 1E11) cross-linked to Protein G sepharose.	140
Figure 23: IP of endogenous Lrrk2 from mouse brain lysates using the cross-linked anti-Lrrk2 antibody and matched subclass-specific IgG2as for the identification of non-specific coprecipitated proteins.	142
Figure 24: Antibodies directed against Lrrk2 did not detect the endogenous protein in IF staining...	144
Figure 25: Identification of functional shRNAs targeting Lrrk2 in a reporter-based <i>in vitro</i> assay.	147
Figure 26: Induction of an IFN response by first generation shRNA constructs targeting Lrrk2 in primary VM cultures.	149
Figure 27: Cytotoxic effects of Lrrk2 targeting first generation shRNAs in primary VM cultures.	150
Figure 28: Second generation designed shRNA ^{mir} constructs mediate the efficient knockdown of Lrrk2 in primary VM cultures without the induction of an INF response.	152
Figure 29: Efficient lentiviral delivery and persisted expression of shRNA ^{mir} sequences within viable DA neurons.	153
Figure 30: TH-ir neurons expressing Lrrk2 mRNA targeting shRNA ^{mir} s.....	155
Figure 31: Silencing of Lrrk2 results in a significant decrease in dopaminergic neurite length.	156
Figure 32: Efficient knockdown of Lrrk2 in NIH3T3 cells.	157
Figure 33: Knockdown of Lrrk2 alters the morphology of NIH3T3 cells.	159
Figure 34: Scatter plots of protein ratios according to SILAC quantification.	161
Figure 35: Verification of Lrrk2 interaction partners identified by QUICK using co-IP.	163
Figure 36: KEGG pathway enrichment analysis of proteins identified in the Lrrk2 complex.	164
Figure 37: Network of Lrrk2 interacting proteins.....	166
Figure 38: Extended network of Lrrk2 interacting proteins.....	168
Figure 39: Lrrk2 binds directly to F-actin and affects its polymerization/depolymerization <i>in vitro</i>	170
Figure 40: Lrrk2 function and CNS integrity – a model.	188

2. Table index

Table 1: Genetic loci and genes associated with PD.	24
Table 2: Primer	63
Table 3: Oligonucleotides encoding first generation shRNA transcripts targeting Lrrk2.....	63
Table 4: Oligonucleotides encoding second generation shRNA (shRNA ^{mir}) transcripts targeting Lrrk2.....	64
Table 5: Plasmids	64
Table 6: Constructs	64
Table 7: Commercial primary antibodies	67
Table 8: Rat-monoclonal and rabbit-polyclonal antibody clones against Lrrk2.	67
Table 9: Secondary antibodies	68
Table 10: Immunoglobulins	68
Table 11: Gel solutions for SDS separating gels (10 mL).	73
Table 12: Gel solution for SDS stacking gels (5 mL).....	73
Table 13: Gel solutions for SDS gradient separating gels (30 mL).....	74
Table 14: Subdivision of BioGRID experimental evidence codes represented in Pathway Palette.	90
Table 15: siRNA target sequences for the specific knockdown of Lrrk2 expression.....	103
Table 16: DNA amount and reagent volumes for calcium phosphate precipitation on different cell culture surface areas.	114
Table 17: Optimization of the streptavidin-biotin-based screening assay.	126
Table 18: Conditions used to optimize the immunoprecipitation of endogenous Lrrk2 utilizing the anti-Lrrk2 antibody (clone 1E11) cross-linked to a sepharose resin.....	132
Table 19: Protocols tested for cross-linking of the Lrrk2-specific antibody clone 1E11 to Protein G sepharose.....	134
Table 20: Summary of commercial antibodies against Lrrk2 tested for their suitability in immunocytochemistry.....	143
Table 21: Summary of Lrrk2 interacting proteins identified by QUICK.....	162

3. Publications and poster presentations

3.1 Peer-reviewed publications

Piccoli, G., Condliffe, S. B., Bauer, M., Giesert, F., Boldt, K., De Astis, S., **Meixner, A.**, Sarioglu, H., Vogt-Weisenhorn, D. M., Wurst, W., Gloeckner, C. J., Matteoli, M., Sala, C., and Ueffing, M. (2011) LRRK2 Controls Synaptic Vesicle Storage and Mobilization within the Recycling Pool. *J Neurosci* 31 (6), 2225-2237.

Meixner, A., Boldt, K., Van Troys, M., Askenazi, M., Gloeckner, C. J., Bauer, M., Marto, J. A., Ampe, C., Kinkl, N., and Ueffing, M. (2011) A QUICK screen for Lrrk2 interaction partners--leucine-rich repeat kinase 2 is involved in actin cytoskeleton dynamics. *Mol Cell Proteomics* 10 (1), M110 001172.

Bauer, M., Kinkl, N., **Meixner, A.**, Kremmer, E., Riemenschneider, M., Forstl, H., Gasser, T., and Ueffing, M. (2009) Prevention of interferon-stimulated gene expression using microRNA-designed hairpins. *Gene Ther* 16 (1), 142-147.

Bauer, M., Szulc, J., Meyer, M., Jensen, C. H., Terki, T. A., **Meixner, A.**, Kinkl, N., Gasser, T., Aebischer, P., and Ueffing, M. (2008) Delta-like 1 participates in the specification of ventral midbrain progenitor derived dopaminergic neurons. *J Neurochem* 104 (4), 1101-1115.

3.2 Poster presentations

Meixner A, Boldt K, Van Troys M, Askenazi M, Gloeckner CJ, Bauer M, Marto JA, Ampe C, Kinkl N, Ueffing M. Interactome analysis and functional characterization reveals a role of Lrrk2 in actin cytoskeleton dynamics. 4th Annual Meeting of NGFN-Plus and NGFN-Transfer, Berlin, Germany, September 2011

Meixner A, Boldt K, Van Troys M, Askenazi M, Gloeckner CJ, Bauer M, Marto JA, Ampe C, Kinkl N, Ueffing M. Interactome analysis and functional characterization reveals a role of Lrrk2 in actin cytoskeleton dynamics. Alliance for Mental Health in an aging Society (HelMa) Interim Evaluation, Munich, Germany, February 2011

Meixner A, Boldt K, Van Troys M, Askenazi M, Gloeckner CJ, Bauer M, Marto JA, Ampe C, Kinkl N, Ueffing M. Interactome analysis and functional characterization reveals a role of Lrrk2 in actin cytoskeleton dynamics. "Functional Genomics of Parkinson's Disease" in conjunction with the 16th Annual Meeting of the German Society of Neurogenetics, Tübingen, Germany, November 2010

Gloeckner CJ, Boldt K, von Zweyendorf F, Helm S, **Meixner A**, Sarioglu H, Ueffing M. Mapping of LRRK2 phosphorylation sites – the GTPase domain Roc represents a primary target for autophosphorylation. 2nd World Parkinson Congress, Glasgow, Scotland/UK, September 2010

Meixner A, Bauer M, Ueffing M. Knockdown of Lrrk2 in developing DA neurons *in vitro*. 6th Human Brain Proteome Meeting SMP Proteomics within NGFN-2, Rauschholzhausen, Germany, January 2007

Bauer M, **Meixner A**, Ueffing M. Investigation of developmental and disease-related genes in primary neuronal systems using lentiviral vector-based technology. 5th Human Brain Proteome Meeting SMP Proteomics within NGFN-2, Rauschholzhausen, Germany, November 2005

Bauer M, **Meixner A**, Ueffing M. Investigation of developmental and disease-related genes in primary neuronal systems using lentiviral vector-based technology. NGFN meeting, Bonn, Germany, November 2005

4. Acknowledgements

Die vorliegende Arbeit wurde in der Abteilung für Proteinanalytik von Prof. Dr. Marius Ueffing (vor 2008 Arbeitsgruppe innerhalb des Instituts für Humangenetik von Prof. Dr. Thomas Meitinger) am Helmholtz Zentrum München durchgeführt. Die Betreuung und Vertretung der Arbeit an der Technischen Universität München erfolgte durch Prof. Dr. Wolfgang Wurst.

An dieser Stelle möchte ich mich bei all jenen bedanken, die mich auf unterschiedlichste Weise bei dieser Arbeit unterstützt haben.

Marius möchte ich dafür danken, dass er es mir ermöglicht hat, meine Doktorarbeit in seiner Abteilung durchzuführen und mir die notwendigen Freiräume für deren selbständige Bearbeitung gewährte. Auch wenn Lrrk2 nicht immer ein einfaches Forschungsobjekt war, hat Marius nie an meinen wissenschaftlichen Fähigkeiten gezweifelt. In Form von wissenschaftlichen Diskussionen, konstruktiver Kritik und Sachmitteln gab er mir wertvolle Unterstützung und Hilfe, ebenso durch die Möglichkeit an verschiedenen Kongressen und Fortbildungen teilzunehmen. Darüber hinaus werden die Einblicke, die ich in Projektförderung und –management erhalten habe, auf meinem weiteren wissenschaftlichen Weg von Nutzen sein.

Bei Prof. Dr. Wolfgang Wurst bedanke ich mich für die Übernahme der Betreuung und Vertretung der Arbeit an der Fakultät Wissenschaftszentrum Weihenstephan für Ernährung, Landnutzung und Umwelt der Technischen Universität München.

Weiterer Dank gilt Prof. Dr. Dieter Langosch und Prof. Dr. Jerzy Adamski für die Übernahme des Zweit- bzw. Drittgutachtens, sowie Prof. Dr. Siegfried Scherer für den Prüfungsvorsitz.

Bei Dr. Matthias Bauer bedanke ich mich für die Betreuung im ersten Jahr meiner Arbeit. Er hat mir die methodisch-technischen Grundlagen im Rahmen der Arbeiten mit primären neuronalen Zellkulturen und dem lentiviral-vermittelten Gen-Knockdown beigebracht. Sein Design der „second generation“ Silencing Konstrukte hat maßgeblich zum Gelingen dieser Arbeit beigetragen.

Ein besonderer Dank gilt Dr. Norbert Kinkl, dafür, dass er die Betreuung der Arbeit übernommen und mich auf vielfältigste Weise unterstützt hat. Er stand mir nicht nur in wissenschaftlichen, sondern auch administrativen Fragen immer mit Rat und Tat zur Seite. Darüber hinaus war er ein wertvoller Kritiker meiner Arbeit, diverser Paper-Versionen und letztlich der vorliegenden Dissertation. Seine stete und unermüdliche Diskussionsbereitschaft war immer eine große Hilfe.

Dr. Johannes Gloeckner, der weiß, was Lrrk2-Forschung bedeutet, danke ich für seine fortwährende Unterstützung meiner Arbeit und sein Wissen, das er mit mir teilte. Die Beantwortung unzähliger fachlicher Fragen und die Hilfeleistung bei Computerproblemen waren für mich von großem Nutzen.

Bei Dr. Karsten Boldt bedanke ich mich für seine Hilfe und Unterstützung bei den proteomischen Arbeiten, insbesondere bei der Durchführung und Auswertung der massenspektrometrischen Experimente, und den Korrekturen am Papermanuskript sowie der Dissertation. Er hat mir stets alle Fragen beantwortet und seine Erfahrung auf dem Gebiet quantitativer Proteomik und MS haben wesentlich zur erfolgreichen Analyse des endogenen Interaktoms von Lrrk2 beigetragen.

Prof. Dr. Christoph Ampe und Prof. Dr. Marleen von Troys (Universität Gent) danke ich für ihre Zusammenarbeit und ihren Einsatz bei den Kosedimentationsanalysen, sowie für die wertvollen Korrekturen des Papers. Dr. Jarrod A. Marto und Dr. Manor Askenazi (Harvard Medical School) für die Kooperation im Rahmen der Lrrk2-Proteinnetzwerkanalyse.

Bei Dr. Saskia Biskup und Dr. Andrea Huber-Brösamle bedanke ich mich für die Teilnahme an meinem Thesis Committee, die hilfreichen Diskussionen und die wertvollen Anregungen, die sie mir gaben.

Stephanie Schöffmann danke ich für die unzähligen Präparationen von VM Kulturen. Darüber hinaus war sie eine großartige Hilfe und hat mir viele grundlegende Methoden im Labor beigebracht.

Unsere Labor-Koordinatorinnen Saskia Hanf und Dr. Ursula Olazabal, die leider nicht mehr in unserer Abteilung arbeitet, haben die stets wachsende Arbeitsgruppe immer zusammengehalten und nie den Überblick verloren. Für ihre großartige Unterstützung und Hilfe bei administrativen Angelegenheiten danke ich ihnen ebenso wie für die Organisation diverser Weihnachtsfeiern, Retreats und Oktoberfestbesuchen.

Dankbar bin ich allen derzeitigen sowie ehemaligen Mitarbeitern der Arbeitsgruppe Proteinanalytik und der Core Facility Proteomics, die nicht nur auf fachlicher, sondern auch auf menschlicher Ebene eine gute Zusammenarbeit und Arbeitsatmosphäre geschaffen haben. Dr. Elöd Körtvely, Dr. Giovanni Piccoli, Dr. Matthias Bauer, Yves Texier und Matteo Gorza, die sich mit mir zeitweise unser kleines Büro geteilt haben, möchte ich für die nette Zeit und viele lustige Momente dort danken. Dr. Norbert Kinkl, Dr. Johannes Gloeckner, Dr. Hakan Sarioglu, Dr. Andreas Vogt, Dr. Stefanie Hauck, Dr. Elöd Körtvely, Dr. Giovanni Piccoli, Dr. Juliane Merl, Dr. Christine von Törne, Dr. Alice Ly, Dr. Kim Byung-Gyu, Dr. Matthias Bauer, Dr. Sibylle Regn, Dr. Ralf Braun, Dr. Monika Beer, Dr. Gabriele Dütsch, Dr. Ursula Olazabal, Saskia Hanf, Matteo Gorza, Ana Griciuc, Patricia del Rio Medina, Marcel Blindert, Johannes Dietter, Sandra Helm, Silke Becker, Alexander Schäfer, Joanna Kucharska, Yves Texier, Ludwig Wiesent, Felix von Zweyendorf, Jennifer Behler, Caroline Bobe, Stephanie Schöffmann, Annette Schumacher und Prof. Dr. Marius Ueffing danke ich für sämtliche Unterstützung und Hilfe, die ich erhalten habe, die schöne Zeit, die vielen netten Gespräche und produktiven Diskussionen.

Bei meinen Freunden und meiner Familie bedanke ich mich für das Leben neben der Wissenschaft, sowie den Rückhalt und die moralische Unterstützung die sie leisteten.

Insbesondere bei Jens, der mich durch alle Höhen und Tiefen die diese Arbeit mit sich gebracht haben geduldig begleitet hat.

Der größte Dank geht an meine Eltern. Ihre uneingeschränkte und bedingungslose Unterstützung haben meinen bisherigen Weg erst möglich gemacht. Sie standen mir zu jeder Zeit mit Rat und Tat zur Seite und auf ihre Rückendeckung konnte und kann ich immer bauen. Darüber hinaus haben sie die Promotion in all ihren Facetten mit durchlebt, haben mit gefiebert, sich mit gefreut und mir, wenn nötig, Mut gemacht. Danke – euch ist diese Arbeit gewidmet.

5. Curriculum vitae

Name	Andrea Meixner
Date of birth	July 22 nd 1980
Place of birth	Düsseldorf/Germany
Nationality	German

Education

02/05-present	PhD at the Technical University of Munich, Munich, Germany Institute of Developmental Genetics (Prof. Dr. Wolfgang Wurst)
10/99-01/05	Studies in Biology at the Heinrich Heine University, Düsseldorf, Germany Zoology, genetics and organic chemistry Qualification: Diploma Finale grade: 1.6
08/90-06/99	St. Ursula Gymnasium Düsseldorf, Germany Qualification: Abitur Finale grade: 2.0
09/86-07/90	Primary School (Katholische Grundschule Itterstraße) Düsseldorf, Germany

Research experience

06/11-present	Postdoctoral fellow at the Medical Proteome Center (Institute for Ophthalmic Research) of Prof. Dr. Marius Ueffing at the University of Tübingen, Tübingen, Germany
02/05-05/11	PhD thesis in the Department of Protein Science of Prof. Dr. Marius Ueffing at the Helmholtz Zentrum München, Munich, Germany Title: "Leucine-rich repeat kinase 2 (Lrrk2): Functional characterization and interactome analysis of a protein kinase associated with Parkinson's disease"
01/04-11/04	Diploma thesis in the Institute of Zoophysiology of Prof. Dr. Manfred K. Grieshaber at the Heinrich Heine University in Düsseldorf, Germany Titel: "Ungerichtete Mutagenese und Selektion rekombinanter Opin-Dehydrogenasen in <i>Escherichia coli</i> "
11/03-01/05	Student Assistant in the Institute of Zoophysiology of Prof. Dr. Manfred K. Grieshaber at the Heinrich Heine University in Düsseldorf, Germany
08/02-09/02	Internship in the Institute of Human Genetics of Prof. Dr. Thomas Meitinger at the Helmholtz Zentrum München, Munich, Germany

Meetings and conferences

4th Annual Meeting of NGFN-Plus and NGFN-Transfer, Berlin, Germany, September 2011

Alliance for Mental Health in an Aging Society (HelMA) Interim Evaluation, Munich, Germany, February 2011

“Functional Genomics of Parkinson’s Disease” in conjunction with the 16th Annual Meeting of the German Society of Neurogenetics, Tübingen, Germany, November 2010

2nd World Parkinson Congress, Glasgow, Scotland/UK, September 2010

HelMA Second Annual Meeting, Munich, Germany, July 2010

NGFNplus Parkinson Network Meeting: Genomics of Parkinson’s disease, Berlin, Germany, November 2009

HelMA First Annual Meeting, Munich, Germany, July 2009

HelMA Kick-Off Meeting, Munich, Germany, July 2008

6th Human Brain Proteome Meeting, SMP Proteomics within NGFN-2, Rauschholzhausen, Germany, January 2007

NGFN Meeting Heidelberg 2006, Heidelberg, Germany, November 2006

RETNET/Neurotrain Training Course, Tübingen, Germany, May 2006

NGFN NeuroNet Spring Meeting, Bonn, Germany, March 2006

5th Human Brain Proteome Meeting, SMP Proteomics within NGFN-2, Rauschholzhausen, Germany, November 2005

NGFN Meeting 2005, Bonn, Germany, November 2005

Honors

The identified and published interactome dataset for Lrrk2 has been nominated as “Dataset of the month November 2010” by the EMBL-European Bioinformatics Institute (<http://www.ebi.ac.uk/intact/main.xhtml>).

Language skills

German	first language
English	fluent in speech and writing
French	basic skills